



**THE EFFECT OF TOOL PROFILES ON HEAT  
GENERATION AND DISTRIBUTION DURING FRICTION  
STIR WELDING OF ALUMINIUM ALLOY**

Thesis submitted for the degree of

Doctor of Philosophy

At the University of Leicester

By

**BASIM M. A. AL-BHADLE**

Department of Engineering

University of Leicester

**2020**

## **Abstract**

# **THE EFFECT OF TOOL PROFILES ON HEAT GENERATION AND DISTRIBUTION DURING FRICTION STIR WELDING OF ALUMINIUM ALLOY**

**BASIM M. A. AL-BHADLE**

**University of Leicester, 2020**

Friction stir welding (FSW) is a solid-state joining process that uses a non-consumable tool to join metallic components. Heat is generated by friction between the rotating tool and the workpiece. In this study the effect of process parameters and tool geometry on heat generation during FSW is investigated through analytical and numerical modelling together experimental validation. Equations of tapered and straight tool profiles for triangular, square, pentagonal, hexagonal and octagonal geometries profiles have been derived first. The derived equations were then implemented in a finite element software package to model heat generation and thermal profile during FSW. Experimental validation was carried out using design of experimental (DOE) method for welding 6061-T6 aluminium alloy. The calculated thermal profiles agree with experimental data. It is found that the amount of heat generation increases with increasing number of flats, and taper ratio, and the highest temperature occurs in a straight octagonal tool profile which has 8 flats. The peak temperature increases around 19% by increase the number of probe flats from 3 to 8, and its taper ratio changes from 0.4 to 1. The tensile strength in experimental welded joints was tested to evaluate the effect of tool profile on mechanical properties. The transverse tensile strength increases approximately 33% by changing the tool profile from straight octagonal (SOct) to straight square (SSQ) due to producing defect free joints with symmetric hardness profiles. The tensile strength of SSQ joint is 79% of base metal strength were obtained using rotational speed of 1000 rpm and a welding speed of 200 mm/min.

## **PUBLICATIONS**

Basim M. A. Al Bhadle, Rafat A. A. Al Azzawi, R. Thornton, K. Beamish, S. Shi & H. B. Dong (2019) Equations of heat generation during friction stir welding for tapered polygonal tools, Science and Technology of Welding and Joining, 24:2, 93-100, DOI: [10.1080/13621718.2018.1495407](https://doi.org/10.1080/13621718.2018.1495407)

## SUPERVISOR'S CERTIFICATE

This is to certify that the entitled thesis “THE EFFECT OF TOOL PROFILES ON HEAT GENERATION AND DISTRIBUTION DURING FRICTION STIR WELDING OF ALUMINIUM ALLOY” has been prepared under my supervision at the Engineering department/ University of Leicester for the degree of PhD.

Signature: 

Supervisor: Prof. Hongbiao Dong

Date: 26<sup>th</sup> March 2020

Signature: 

Student: Basim AL-Bhadle

Date: 26-03-2020

## **STATEMENT**

All the work described in this thesis for the degree of Ph.D. entitled “THE EFFECT OF TOOL PROFILES ON HEAT GENERATION AND DISTRIBUTION DURING FRICTION STIR WELDING OF ALUMINIUM ALLOY” was conducted by the author in the Department of Engineering at the University of Leicester mainly during the period between January 2016 and March 2020.

The work in this thesis is original unless otherwise acknowledged in the text or by references and none of the work has been submitted for another degree at this or any other university.

## ACKNOWLEDGEMENT

I would like to thank my supervisory team: Prof. Hongbiao Dong, and Dr. Rob Thornton for all the support, guidance, patience, encouragement, knowledge, and concern to achieve a desirable work that helped me to finish this study. I also would like to thank all the members in mechanics of materials laboratory: Graham Clark, Vinay Patel and Alex Frost for their cooperation during my lab work.

I'm thankful to Dr Kathryn and Nathan Horrex from TWI for all the assistance in experiment work. I also would like to express my heartfelt gratitude to the mechanics of materials group and my dear friends Dr Mazin AL-Isawy, Rafat Alazzawi Dr Muhanad AL-Sabbagh, Dr Dhuha Albusalih, Mahmoud Ehresh, Dr Ramy Mesalam, Peter Polak, Dr. Baber Saleem, Dr Kevser Sevim, and Dr Amnani Binti, for all the help, sharing experience and for building a lovely atmosphere that ease the work throughout the whole PhD study.

My endless appreciation and gratitude to all family members: Jasim, Gisum, Abtasm, Ahlum, Sondos, Hazim, Mohammed, and Zaynab for pushing me forward during the very difficult time in this journey. Thanks and gratitude to my lovely wife Dr. Suad rauby who shared my concerns and supported me in all adversities. Many thanks to my sweet daughter Ruqaya and lovely son Jaffar, they are always motivating me to have a better future.

Finally, I would like to thank my sponsor, the ministry of higher education and scientific research for funding this project and providing the opportunity to have this experience.

Basim

March, 2020

## **DEDICATION**

*All Thanks and Praise to Allah for all His infinite blessings.*

I dedicate this thesis to the memory of my father, mum and first wife.

You were and still are an immense blessing. Although you are not amongst us anymore, with all you taught me and the precious cherished moments we shared, you are always in my heart and prayers.

## LIST OF ACRONYMS

AET	Average experimental temperature
AS	Advancing side
CCD	Central composite design
CNC	Computer numerical control
CT	Computed tomography
DOE	Design of experimental
FEM	Finite element method
FSW	Friction stir welding
HAZ	Heat-affected zone
Hex	Hexagonal taper tool
HTS	Heat transfer in solids
MCS	Moving coordinate system
MTTR	Mean tensile test results
MTTS	Mean transverse tensile strength results
MWZTS	Mean welding zone tensile strength results
Oct	Octagonal taper tool
Pen	Pentagonal taper tool
PFN	The polygon probe flats number
PIAS	Probe interface areas
RS	Retreating side
SD	Standard deviation
SEM	Standard error of the mean
SHex	Straight hexagonal tool
SIA	Shoulder interface area
SOct	The straight octagonal tool profile
SPen	Straight pentagonal tool
SQ	Square taper tool
SSQ	Straight square tool
STR	Straight triangular tool

TMAZ	Thermo-mechanically affected zone
Tp	Taper ratio
TR	The triangular taper tool
WZ	Welding zone

## LIST OF SYMBOLS

Symbol	Description	Unit
$AF$	Axial force	kN
$\sigma_y$	Tensile strength	MPa
$N$	Rotational speed	rpm
$S$	Welding speed	mm/min
PT	The peak temperature	K
$Q_1, Q_2$ and $Q_3$	Heat generated from shoulder, probe and probe tip	W
$Q_{total}$	Total heat generated	W
$Q$	Heat generated	W
$\omega$	Angular velocity	1/sec
$M$	Torque of the welding tool	N.m
$x$	Shear force arm	m
$F$	Force	N
$\tau_{contact}$	Contact shear stress	N/m <sup>2</sup>
$\tau_{friction}$	Friction shear stress	N/m <sup>2</sup>
$\tau_{sticking}$	Sticking shear stress	N/m <sup>2</sup>
$A$	Contact area	m <sup>2</sup>
$\mu$	Friction coefficient	
$P$	Axial pressure	N/m <sup>2</sup>
$\sigma_y$	Yield tensile stress	N/m <sup>2</sup>
$Q_b$	Heat generated form probe base area	W
$Q_{shoulder}$	Heat generated for shoulder	W
$A_{one}$	Area for one element	m <sup>2</sup>
$H_{Area}$	Height of area for one element	m
$a_b, a_t$	Probe base and tip area side length	m
$R_{shoulder}$	Shoulder radius	m
$R_{Probe}, R_{tip}$	Probe base and tip radius	m
$R_{Cb}, R_{Ct}$	Circumscribed radius at probe base and probe tip	m

$A_{Total}$	Total area	$m^2$
PN	Cross section parts number	
$H_{probe}$	Probe height	m
$P_F$	Probe geometry factor	
$F_T$	Taper radius factor	
$A_R$	Average of circumscribed radius for the tapered probe	
$F_1, F_2$ and $F_3$	Heat generation equation factors	
$F_R$	Radius factor	
$T$	Temperature	K
$c_p$	Heat capacity	J/(kg.K)
$\rho$	Density	kg/m <sup>3</sup>
$k$	Thermal conductivity	K.W/(m.K)
$S_B$	The Stefan-Boltzmann constant	W/m <sup>2</sup> .k <sup>4</sup>
$h_{up}$ and $h_{down}$	Convection coefficients for lower and upper-base Metal surfaces	W/(m <sup>2</sup> .K)
$\varepsilon$	The emissivity	
$T_i$	Initial temperature	K

## LIST OF FIGURES

Figure 2-1. The principle of FSW process a) Plates are rigidly clamped to prevent lateral moving, b) Friction interaction between tip probe and upper work piece surface, c) The temperature increases rapidly when the shoulder contacts the work piece surface and d) FSW tool feeds at contact welding speed along welding line [6].	6
Figure 2-2. The sources of the total heat generation [7].	7
Figure 2-3. The effect of shoulder diameter to the peak temperature [11].	8
Figure 2-4. Shoulder shapes and features, (A) Shoulder outer surface, (B) Shoulder end surface and (C) End surface [9].	9
Figure 2-5. View of tools: (a) Front view for all tools; (b) Bottom view of plane shoulder tool (PST); (c) Bottom view of concentric circles shoulder tool (CCST); (d) Bottom view of ridges shoulder tool (RST); (e) Bottom view of knurling shoulder tool (KST); (f) Bottom view of scroll shoulder tool (SST) [51].	10
Figure 2-6. Probes features, (A) Probe tip and (B) Probe surface [9].	11
Figure 2-7. Probe types developed at TWI for various material thicknesses and joint types [52].	12
Figure 2-8. Basic variants for the Whorl™ type probes [52].	13
Figure 2-9. Typical MX-Triflute™ probe [52].	13
Figure 2-10. (a) Tool diameters versus work piece thickness and (b) Relation between tool diameters [9].	14
Figure 2-11. Microstructural zone classification in a friction stir weld in Al 2024 alloy (A: Parent material, unaffected by process; B: HAZ, thermally affected but with no visible plastic deformation; C: TMAZ, affected by heat and plastic deformation) [57].	16
Figure 2-12. Characteristic defect types in friction stir welds [62].	17
Figure 2-13. Schematic view of FSW steps; plunging, first dwelling, welding, second dwelling, and extraction [13].	18
Figure 2-14. Predicted dynamic maximum temperature, total heat generation, and probe heat at FSW steps; plunge (period I); second plunge (period II); first dwell period (period III); weld period (period IV); second dwell period (period V); and cooling period (period VI) [64].	19
Figure 2-15. Heat fraction generated by the shoulder and probe [66].	19

Figure 2-16. Finite element mesh of the welding model [86].	23
Figure 2-17. Stir-welding temperatures as a function of welding speed [86].	24
Figure 2-18. Stir-welding temperatures as a function of rotational velocity [86].	24
Figure 2-19. Heat transfer in tool and workpiece in friction stir welding (One-half of the tool model is shown due to symmetry) [87].	25
Figure 2-20. Relative comparison of the numerically computed TMAZ with the corresponding experimentally determined geometry. The welding velocity is $2.11 \text{ mm s}^{-1}$ and the rotation speed was varied: (a) 150 rpm (b) 480 rpm and (c) 800 rpm [90].	28
Figure 2-21. Schematic view of configuration of 6 cases: left column = sliding condition, right column = sticking condition. First row: no probe heat generation (HG); second row: with probe H.G; third row: probe volume removed, H.G. in shear layer [91].	28
Figure 2-22. Calculated isothermals versus microstructure morphology [92].	29
Figure 2-23. Tool design showing geometric parameters [22].	29
Figure 2-24. Temperature profile in a $x-z$ section as a function of pin angle $\alpha$ ( $V_f = 100 \text{ mm/min}$ ) (a) $\alpha = 40^\circ$ , (b) $\alpha = 20^\circ$ and (c) $\alpha = 0^\circ$ .	30
Figure 2-25. Numerical and experimental temperature distribution for welding with conical tool pin [93].	30
Figure 2-26. Different heat generation regions [94].	31
Figure 2-27. Surface orientations and infinitesimal segment area for taper conical profile [94].	32
Figure 2-28. Effect of taper angle on peak temperature (a) AA 6061-T6, (b) AA 6061-T651 and (c) AA 6082-T6 [94].	32
Figure 3-1. TR tool profile.	36
Figure 3-2. Schematic drawing of surface orientations and infinitesimal segment areas for triangular taper tool (TR). (a) Shoulder surface area, (b) Probe surface area and (c) Probe base and tip cross-section area.	38
Figure 3-3. Schematic drawing for shoulder segment area.	39
Figure 3-4. Schematic drawing for probe base. (a) The triangular probe base cross section. (b) Schematic drawing for Position and dimensions of segment.	40
Figure 3-5. Schematic drawing of isosceles trapezoidal elements to probe surface.	43
Figure 3-6. The circumscribed radius at probe base and probe tip.	45
Figure 4-1. FSW Model geometry.	51

Figure 4-2. Temperature-dependent 0.2% offset yield strength for AA 6061-T6 [97].	54
Figure 4-3. Density as a function of temperature.	54
Figure 4-4. Thermal conductivity as a function of temperature.	55
Figure 4-5. Heat capacity as a function of temperature.	55
Figure 5-1. Square groove welding joint [98].	61
Figure 5-2. Triangular tool 0.7 taper ratio.	63
Figure 5-3. Square tool 0.6 taper ratio.	63
Figure 5-4. Square tool 0.8 taper ratio.	64
Figure 5-5. Pentagonal tool 0.4 taper ratio.	64
Figure 5-6. Pentagonal tool 0.7 taper ratio.	65
Figure 5-7. Straight pentagonal tool.	65
Figure 5-8. Hexagonal tool 0.6 taper ratio.	66
Figure 5-9. Hexagonal tool 0.8 taper ratio.	66
Figure 5-10. Octagonal tool 0.7 taper ratio.	67
Figure 5-11. Tool holder.	67
Figure 5-12. Straight square tool.	68
Figure 5-13. Straight hexagonal tool.	69
Figure 5-14. Straight octagonal tool.	69
Figure 5-15. The assembly tool and its parts.	70
Figure 5-16. Thermocouple locations.	72
Figure 5-17. Experimental set up for temperature measurements.	72
Figure 5-18. Location of the weld test specimens [98].	73
Figure 5-19. Positions of microhardness test indentations.	74
Figure 5-20. Dimensions of transverse welding tensile specimen [102].	75
Figure 5-21. Dimensions of a welding zone tensile specimen [102].	75
Figure 6-1. Axial force normal probability plot.	81
Figure 6-2. Scatter diagram of axial force (KN).	81
Figure 6-3. Contour plots for the effect of rotational speed and welding speed on axial force.	82
Figure 6-4. Response surface graphs for the effect of rotational speed and welding speed on axial force.	83
Figure 6-5. Contour plots for the effect of tool profile (PFN and Tp) on axial force.	84

Figure 6-6. Response surface graphs for the effect of tool profile (PFN and $T_p$ ) on axial force. ....	84
Figure 7-1. Isotherms temperature distribution (K) for different probe profiles: A-TR, B-SQ, C- Pen, D- Hex and E- Oct .....	87
Figure 7-2. Isotherms temperature distribution (K) for different probe profiles: A-TR, B-SQ, C- Pen, D- Hex and E- Oct .....	88
Figure 7-3. Change interfaces area by increasing flats number.....	89
Figure 7-4. Comparison between modelling results for present work.....	90
Figure 7-5. A schematic diagram illustrating the L5 position. ....	92
Figure 7-6. Experimental temperature data for Run 1. ....	92
Figure 7-7. Comparison the average experimental temperatures (AET) with calculated temperature (L5) for (A) Run1, (B) Run5, .....	93
Figure 7-8. Peak temperature normal probability plot.....	98
Figure 7-9. Scatter diagram of peak temperature (K).....	100
Figure 7-10. Contour plots for the effect of rotational speed and welding speed on peak temperature. ....	101
Figure 7-11. Response surface graphs for the effect of rotational speed and welding speed on peak temperature.....	101
Figure 7-12. Contour plots for the effect of tool profile (PFN and $T_p$ ) on peak temperature. ....	102
Figure 7-13. Response surface graph for the effect of tool profile (PFN and $T_p$ ) on peak temperature. ....	103
Figure 8-1. Tensile strength normal probability plot.....	111
Figure 8-2. Scatter diagram of tensile strength (MPa).....	111
Figure 8-3. Contour plots for the effect of rotational speed and welding speed on tensile strength.....	112
Figure 8-4. Response surface graphs for the effect of rotational speed and welding speed on tensile strength. ....	113
Figure 8-5. Contour plots for the effect of tool profile (PFN and $T_p$ ) on tensile strength. ....	114
Figure 8-6. Response surface graphs for the effect of tool profile (PFN and $T_p$ ) on tensile strength.....	114

Figure 9-1. Isotherms temperature distribution for different probe profiles: A-SSQ, B- SHex, and C- SOct (model 2). .....	117
Figure 9-2. Transverse tensile strength for welding joints by SSQ, SHex and SOct tools. ....	118
Figure 9-3. Comparison between the MTTTS of the joints welded by different tools with the tensile strength of base metal. ....	119
Figure 9-4. Tensile fracture appearances of FSW welds. ....	120
Figure 10-1. Corresponding 2D microhardness map for different tool profiles: (A) SOct, (B) SHex and (C) SSQ. ....	123
Figure 10-2. 2D images of Run2 (A) Microstructure and (B) CT scan. ....	124
Figure 10-3. 2D images of Run3 (A) Microstructure and (B) CT scan. ....	125
Figure 10-4. 2D images of Run18 (A) Microstructure and (B) CT scan. ....	125
Figure 10-5. 2D images of SSQ joint (A) Microstructure and (B) CT scan. ....	126
Figure 10-6. 2D images of SHex joint (A) Microstructure and (B) CT scan. ....	126
Figure 10-7. 2D images of SOct joint (A) Microstructure and (B) CT scan. ....	127
Figure 10-8. Microstructure of SSQ joints. ....	129
Figure 10-9. Welding zone tensile strength for welding joints by SSQ, SHex and SOct tools. ....	131
Figure 10-10. Comparison between MWZTS of the joints welded by different tools with the tensile strength of base metal. ....	132
Figure 10-11. Comparison among the MTTTS and MWZTS. ....	132
Figure 10-12. Temperature contours for STR joint at different planes in the work piece thickness: (A) 6mm, (B) 3mm and (C) 0 mm. ....	134
Figure 10-13. Temperature contours for SSQ joint at different planes in the work piece thickness: (A) 6mm, (B) 3mm and (C) 0 mm. ....	135
Figure 10-14. Temperature contours for SPen joint at different planes in the work piece thickness: (A) 6mm, (B) 3mm and (C) 0 mm. ....	136
Figure 10-15. Temperature contours for SHex joint at different planes in the work piece thickness: (A) 6mm, (B) 3mm and (C) 0 mm. ....	137
Figure 10-16. Temperature contours for SOct joint at different planes in the work piece thickness: (A) 6mm, (B) 3mm and (C) 0 mm. ....	138

## LIST OF TABLES

Table 2-1. Tool materials, geometries and welding variables used for FSW of several aluminium alloys [53].	15
Table 2-2. Definition of contact condition, velocity/shear relationship and state variable ..	26
Table 3-1. The heat generation equation factors for different taper tool profiles.	47
Table 3-2. The heat generation equation factors for different straight tool profiles.	49
Table 4-1. Welding parameters and materials properties used in Models 1 and 2. ....	53
Table 5-1. Levels of welding parameters and tool profiles for DOE matrix. ....	58
Table 5-2. FSW process variables for DOE matrix. ....	59
Table 5-3. Chemical composition (wt%) of AA6061-T6 aluminium alloy.....	60
Table 5-4. Mechanical properties of AA6061-T6 aluminium alloy. ....	60
Table 5-5. The required parts.....	62
Table 6-1. Design matrix for experimental value and predicted value of axial force. ....	77
Table 6-2. Calculated regression coefficients of axial force mathematical model.....	78
Table 6-3. Axial force ANOVA tests results. ....	80
Table 6-4. Coefficient of determination values for axial force model.....	80
Table 7-1. Values of welding parameters for different taper tool profiles. ....	86
Table 7-2. FSW process variables for selected runs.....	91
Table 7-3. Maximum temperatures and P&T values for selected runs. ....	92
Table 7-4. The variation between maximum temperatures for L5 and AET.....	94
Table 7-5. Design matrix for modelling and predicted values of peak temperature.....	95
Table 7-6. Calculated regression coefficients of peak temperature mathematical model. ...	97
Table 7-7. Peak temperature ANOVA test results.....	99
Table 7-8. Coefficient of determination values for peak temperature. ....	99
Table 8-1. MTTR, paired SD& SEM difference, T-value and level of significance.....	106
Table 8-2. Design matrix for experimental and predicted values of tensile strength. ....	107
Table 8-3. Calculated regression coefficients of tensile strength mathematical model.....	108
Table 8-4. Tensile strength ANOVA test results. ....	110
Table 8-5. Coefficient of determination values for tensile strength. ....	110
Table 9-1. Paired SD, SEM difference, T-value and level of significance of the axial force. .....	116

Table 9-2. Paired SD, SEM difference, T-value and level of significance of the peak temperature. ....	117
Table 9-3. Mean, paired difference (SD and SEM), T-value and level of significance of the tensile test results. ....	119
Table 9-4. Paired difference (SD and SEM), T-value and level of significance of the transverse tensile strength. ....	121
Table 10-1. MWZTS, paired difference (SD and SEM), T-value and level of significance. ....	130

# Table of Contents

<b>Chapter 1 : Introduction .....</b>	<b>1</b>
1.1 Background .....	1
1.2 Aim.....	2
1.3 Assumptions made in this study.....	2
1.4 Thesis structure .....	2
<b>Chapter 2 : Literature review on friction stir welding.....</b>	<b>5</b>
2.1 Friction Stir Welding (FSW).....	5
2.1.1 The principle of FSW.....	5
2.1.2 FSW tool .....	7
2.1.3 Microstructures in FSW .....	16
2.1.4 FSW defects .....	16
2.1.5 Thermal cycle of FSW .....	18
2.2 FSW of aluminium alloys .....	20
2.3 The heat generation at FSW .....	20
2.3.1 Heat generation in FSW .....	20
2.3.2 The effect of welding parameters on heat generation .....	21
2.3.3 The effect of FSW tool design on heat generation.....	21
2.3.4 Modelling and simulation of FSW thermal cycle .....	23
2.4 Summary .....	33
2.5 Gaps in literature.....	34
2.6 Objectives.....	34
<b>Chapter 3 : Analytical modelling of FSW.....</b>	<b>36</b>
3.1 Heat generation equations for FSW tools .....	36
3.1.1 Heat generation equations for taper tools.....	37
3.1.2 Heat generation equations for straight tools.....	47
<b>Chapter 4 : Numerical modelling of heat generation during FSW .....</b>	<b>50</b>
4.1 Introduction.....	50
4.2 Physical models.....	51

4.2.1	Welding joint.....	51
4.2.2	FSW tool .....	51
4.3	Heat generation equation.....	52
4.4	Modelling assumptions .....	52
4.5	Boundary conditions and initial condition .....	56
<b>Chapter 5 Methodology experimental work.....</b>		<b>57</b>
5.1	Introduction.....	57
5.2	DOE parameters and their levels.....	57
5.2.1	Experimental design matrix .....	58
5.3	Materials selection .....	60
5.3.1	Plate material.....	60
5.3.2	Tools Material .....	60
5.4	FSW joints fabrication .....	61
5.5	Tools manufacturing .....	62
5.5.1	DOE tools.....	62
5.5.2	DOE validation tools.....	68
5.5.3	FSW tools heat treatment .....	70
5.6	Experiential work.....	71
5.6.1	Temperature measurement .....	71
5.7	Welding quality.....	73
5.7.1	X-ray radiography .....	73
5.7.2	Macroscopic and Microscopic Evaluation .....	73
5.7.3	Microhardness test .....	74
5.7.4	Tensile test .....	74
5.7.5	Transverse and welding zone tensile test .....	75
<b>Chapter 6 : Effect of welding parameters and tool profile on axial force .....</b>		<b>76</b>
6.1	Introduction.....	76
6.2	Axial force DOE matrix .....	76
6.2.1	Data driven model for axial force .....	76
6.2.2	Adequacy of DOE model for AF .....	79
6.2.3	Effect of welding parameters and tool profile on axial force.....	82

6.3	Conclusion .....	85
<b>Chapter 7 : Effect of tool profiles on thermal profile .....</b>		<b>86</b>
7.1	Modelling results validation.....	91
7.2	Peak temperature DOE.....	94
7.2.1	Data driven model for peak temperature .....	96
7.2.2	Adequacy of DOE model for the peak temperature .....	97
7.2.3	Effect of welding parameters and tool profile on peak temperature .....	100
7.3	Conclusion .....	103
<b>Chapter 8 : Mechanical performance .....</b>		<b>105</b>
8.1	Tensile strength DOE.....	105
8.1.1	Data driven model for tensile strength .....	105
8.1.2	Adequacy of DOE model for tensile strength .....	109
8.1.3	Effect of welding parameters and tool profile on tensile strength.....	112
8.2	Conclusion .....	115
<b>Chapter 9 : Validation of DOE results.....</b>		<b>116</b>
9.1	Introduction.....	116
9.2	Validation axial force DOE results .....	116
9.3	Validation peak temperature DOE results.....	116
9.4	Validation tensile strength DOE results .....	118
9.5	Conclusion .....	121
<b>Chapter 10 : Effect of tool profile on heat distribution, microstructure and mechanical properties.....</b>		<b>122</b>
10.1	Introduction.....	122
10.2	Microhardness results.....	122
10.3	Macrostructure and CT scan .....	124
10.4	Microstructure for optimum condition trial .....	127
10.5	Weld zone tension testing .....	130
10.6	The effect of tool profile on temperature distribution.....	133

10.7	Conclusion .....	139
<b>Chapter 11</b>	<b>: Conclusion and future work .....</b>	<b>140</b>
11.1	Conclusion .....	140
11.2	Future work .....	141
<b>References</b> .....		<b>142</b>
<b>APPENDICES</b> .....		<b>151</b>

# Chapter 1 : Introduction

## 1.1 Background

Friction Stir Welding (FSW) was invented at TWI Ltd in the UK in 1991 and it was initially applied to join aluminium alloys [1, 2]. Comparing with other joining techniques FSW has many advantages, such as joining base metal without using filler metal and shielding gas, and the process is energy efficient, environment-friendly, low cost and high welding efficiency [3]. FSW has now been widely used in aerospace, automotive, electronics and shipbuilding [4].

During FSW, heat is generated from two sources, *i.e.* the heat friction and the deformation heat. The frictional heat is generated as a result of the frictional action at the interface between the FSW tool and base metal, and the deformational heat is generated from the deformation interactions between softening material layers when they rotate at different rates [5]. The frictional heat represents the primary heat source because it produces approximately 95% of the total heat generation during FSW [6].

Heat generated during FSW is not enough to melt the based metal, but it is enough to soften material at the edge of base metal, and the welding zones are then formed by flowing this softening material from front to back of tool under stirring action [7]. So, the heat generation during FSW is the major factor on the quality of the final performance of welding joints.

FSW thermal cycle can be practically measured, but this procedure has many challenges; one of them is that the thermocouples cannot be placed in the nugget zone because of high plastic deformation caused by stirring force from the rotating FSW tool. In addition, experimental measurements cannot give the full thermal profile of welding zone.

The heat generation relies on the profile of FSW tool, and the tool profile, welding parameters and material thermal properties are related [5]. So, it is important to study the relationship among these factors to evaluate the heat generation during FSW.

## 1.2 Aim

The aim of the proposed research is to improve the understanding of the effect of change FSW tool profiles from taper to straight on the amount of heat generated and distributed in FSW of aluminium alloy.

## 1.3 Assumptions made in this study

In the present work, the tool profile and welding parameters are listed below:

- ❖ The friction stir welding tools have following features:
  - The shoulder end surface is a flat.
  - The shoulder to probe diameter ratio is two.
  - The tool profiles are the polygonal tapered or straight. The polygon probe flats number (PFN) is changed from 3 to 8 while taper ratio ( $Tp$ ) is changed from 0.4 to 1.
  - The tool dimensions are:
    - Shoulder diameter is 12 mm.
    - Probe diameter is 6 mm.
    - Probe length is 6 mm.
- ❖ The range of welding parameters are:
  - Rotational speed (N) between 500 to 1400 rpm.
  - Welding speed (S) between 150 to 350 mm/min.

## 1.4 Thesis structure

This thesis is divided into the following chapters:

- ❖ **Chapter One:** Presents an overview of the study. It consists of a brief introduction, a statement of the aim of this work, and the structure of the thesis.

- ❖ **Chapter Two:** Comprises the theoretical background of the principles of the FSW with a review of the relevant literature on tool profile, process parameters, FSW defects, heat generation, gaps in literature and objectives.
- ❖ **Chapter Three:** Presents the analytical sequence to derive heat generation equations for taper and straight tools by dividing FSW tool into a shoulder-base metal interface, vertical probe surface-base metal interface and probe tip-base metal interface.
- ❖ **Chapter Four:** Presents the sequence of numerical implementation of FSW by using COMSOL 5.2 software under two model assumptions:
  - **Model 1 assumptions:** Density, thermal conductivity, thermal capacity and friction coefficient are assumed as constant while shear contact stress under sticking condition is a function of temperature according to yield stress as a function of temperature.
  - **Model 2 assumptions:** Density, thermal conductivity, thermal capacity, friction coefficient and shear contact stress under sticking condition are assumed as a function of temperature.
- ❖ **Chapter Five:** Comprises the procedures to carry out the welding trials by machining slots in 6061-T6 plates to place the thermocouples, as well as design and manufacturing FSW tools and heat treatment sequence to improving mechanical properties for FSW tools. Presents the preparing steps conducted to manufacture the tensile, microstructure, microstructure and microhardness test samples.
- ❖ **Chapter Six:** Presents the discussion and analysis DOE results for AF by explanation the effect of welding parameters and tool profiles.
- ❖ **Chapter Seven:** Presents the thermal profile during FSW by displaying model 1 and model 2 results and discussing the results of DOE for PT.
- ❖ **Chapter Eight:** Presents mechanical performance by discussion and analysis DOE results for  $\sigma_T$  to explain the effect of welding parameters and tool profiles.

- ❖ **Chapter Nine:** Presents the validation results of the DOE predicted equations for AF, PT and  $\sigma_T$ .
- ❖ **Chapter Ten:** Presents the effect of tool profile on microhardness, macrostructure, microstructure, weld zone tensile strength and heat distribution.
- ❖ **Chapter Eleven:** This is the last chapter which draws the conclusions from the work done in this thesis and presents future work.

## Chapter 2 : Literature review on friction stir welding

### 2.1 Friction Stir Welding (FSW)

In this part of literature review, the principle, tool, microstructures and thermal cycle in FSW will be reviewed.

#### 2.1.1 The principle of FSW

The principle of FSW process is shown in Figure 2-1. The axial force (forging force) is a normal force applied by FSW tool on plates which are rigidly clamped on the backing strip plate to prevent lateral moving (Figure 2-1(a)).

At the beginning, FSW tool rotates with a constant rotation rate which causes a friction force between tip probe and upper work piece surface (Figure 2-1(b)) and increases temperature between them. As a consequence of increasing temperature and axial force the FSW tool will plunge inside the softened material until the shoulder contacts the work piece surface.

At this moment, the temperature increases rapidly (Figure 2-1(c)) and when the temperature increases to sufficient value the FSW tool will move along a welding line with a constant speed (Figure 2-1 (d)).

FSW heat energy is generated by frictional and deformational heating. The frictional heating is primary source because it produces more than 95% from heat generation (the red line in Figure 2-2 represents the interface action of this source), the deformational heating is the secondary source because it produce approximately 4.4% from heat generation [5].

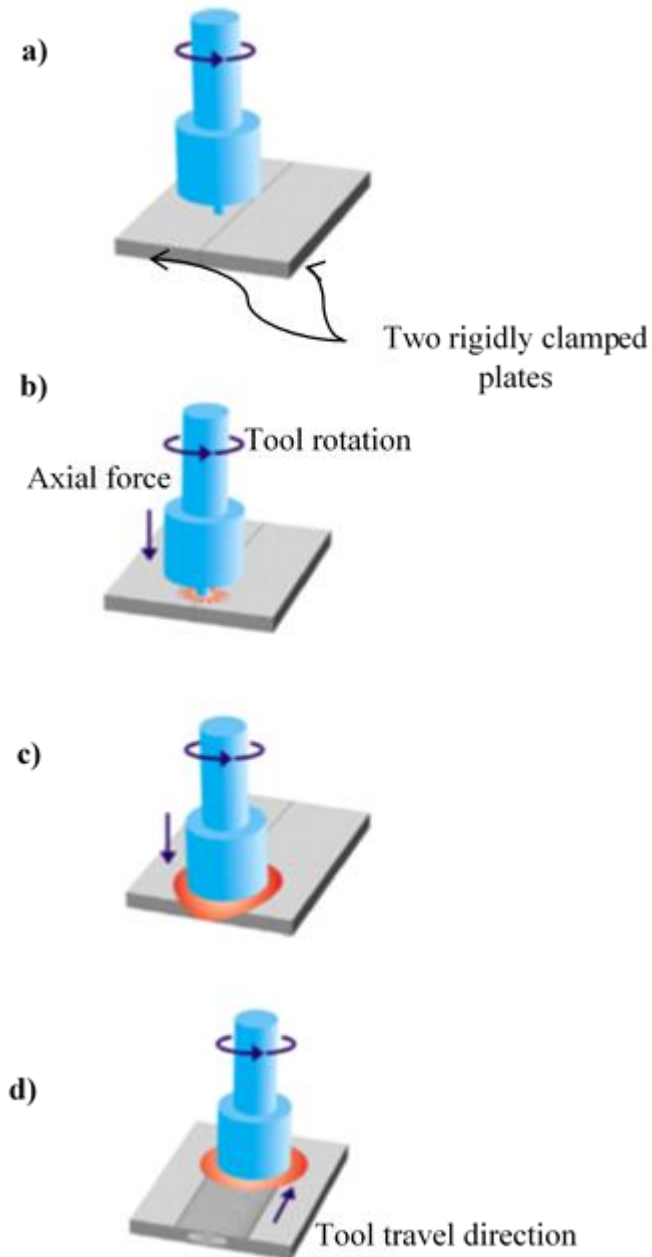


Figure 2-1. The principle of FSW process a) Plates are rigidly clamped to prevent lateral moving, b) Friction interaction between tip probe and upper work piece surface, c) The temperature increases rapidly when the shoulder contacts the work piece surface and d) FSW tool feeds at contact welding speed along welding line [6].

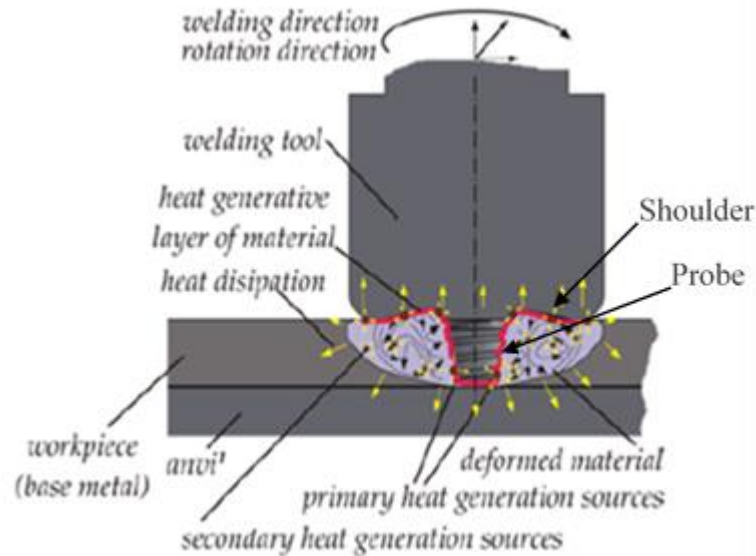


Figure 2-2. The sources of the total heat generation [7].

During welding, FSW tool will form welding zones by flowing thermally softened material from front to back of this tool. FSW tool slides and rotates on base metal with non-symmetric influence on base metal because FSW tool rotates in the same direction of the tool moving at advancing side while it rotates inverse that at the rear side [8].

### 2.1.2 FSW tool

FSW tools are designed to generate frictional heat at the interface with a workpiece, apply the downward forging force necessary for welding consolidation and constrain heated metal under the bottom shoulder surface [9]. These tools are still under development to cover the growth demand using FSW for joining several materials in various industries [10]. So, many adjustments are applied on tool design by adding several features. FSW tool has two effective parts *i.e.* shoulder and probe.

The functions of the tool shoulder generate the heat at the interface with work piece and capture the soft layer in welding zone. The heat input increases with increasing shoulder diameter because shoulder diameter significant effect to the amount of frictional heat as shown in Figure 2-3.

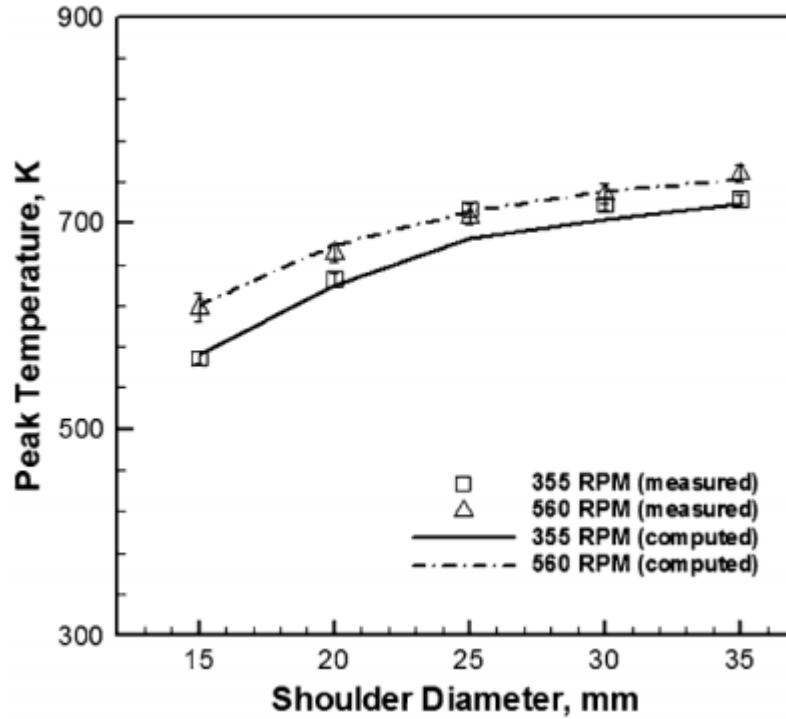


Figure 2-3. The effect of shoulder diameter to the peak temperature [11].

The shoulder has three features as shown in Figure 2-4. The shoulder outer surface has two common designs, cylindrical [12-14] and conical [15-18]; This feature does not have significant effect on welding quality because the shoulder plunge depth is so small to make change on welding quality (i.e. 1–5% of the base metal thickness) [1, 19].

However, shoulder end surface and end surface feature have a significant impact on mechanical properties of welding joints. There are three types of shoulder end surface convex, concave and flat [20-23], These features reduce the formation of material flash by capturing the softening material under shoulder surface during welding time [24], improving the surface conditions [25].

While there are several designs for the end surface feature used to improve the welding quality (some of them shows in Figure 2-4 and Figure 2-5) by regulation axial force, improving flow pattern around the friction stir welding tool and providing sufficient volume to capture softening layers under the shoulder.

In addition, shoulder end surface and end surface feature can also increase forging force and hydrostatic pressures, which may promote material mixing and produce sound joints [26, 27].

The stationary shoulder was recently used to join different materials [28-33], especially with low conductivity coefficient materials to solve poor weld quality which generates from a significant temperature gradient through the thickness [34, 35]. The heat is generated by the probe when it rotates at high rotational speed.

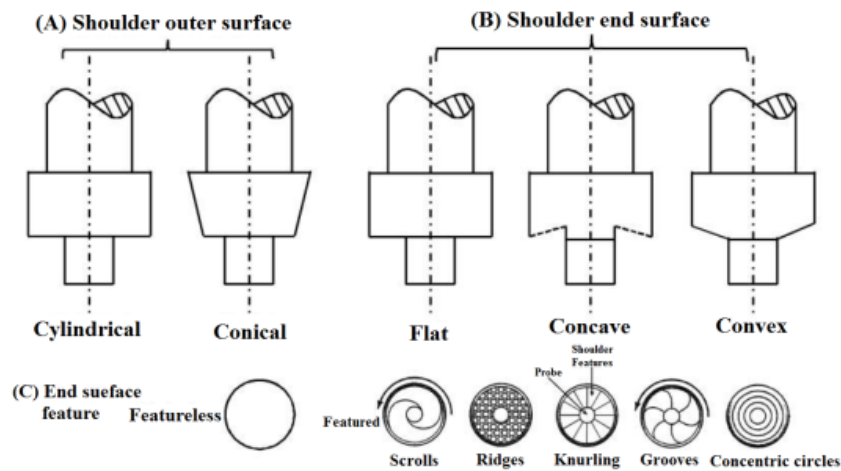


Figure 2-4. Shoulder shapes and features, (A) Shoulder outer surface, (B) Shoulder end surface and (C) End surface [9].

The probe features are probe end surface (probe tip) and probe outer surface (probe surface) as shown in Figure 2-6. The shape of probe tip depends on the probe design; so, the cylindrical probes have flat or domed tip shape [36, 37]. The change of probe tip design from flat to domed is increased tool life by reducing contact area at first contact between tool and work piece [38-40]. The tip shape for taper probes depend on the design of probe surface and taper angle.

The probe surface has many functions during FSW such as formation mixing zones and deformational heat and frictional heat. So, the probe surfaces develop by adding several features such as threads [41-43], flats [44-47] or flutes [48, 49] to improve the performance of these tools. The change of probe surface design increases the heat generation because of

increasing contact area [50]. Increasing flute radius affects the material flow pattern in stirring zone.

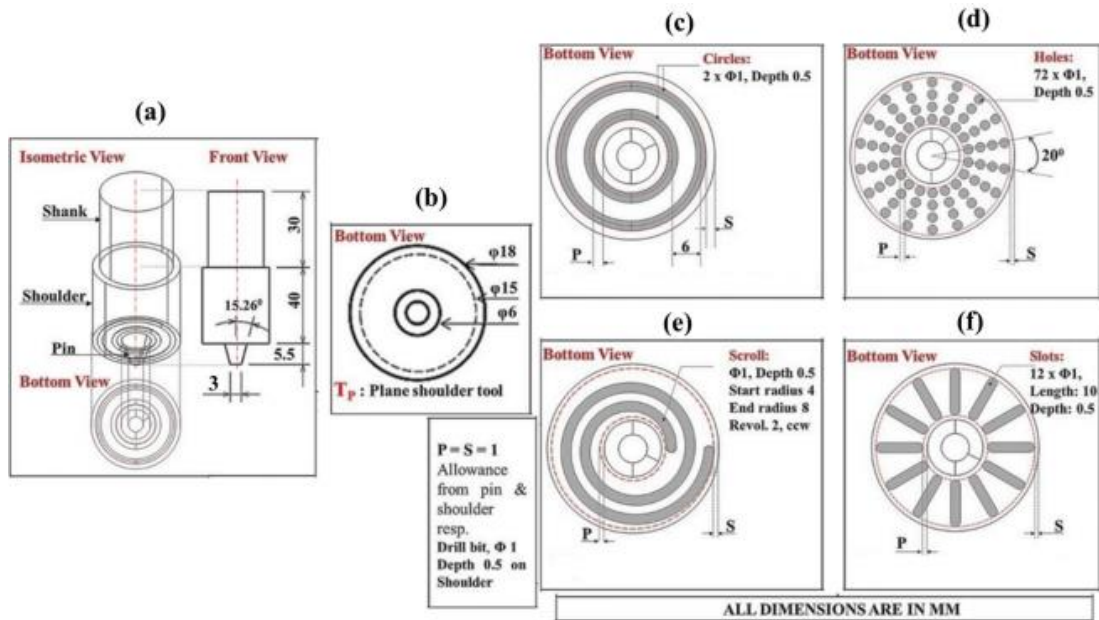


Figure 2-5. View of tools: (a) Front view for all tools; (b) Bottom view of plane shoulder tool (PST); (c) Bottom view of concentric circles shoulder tool (CCST); (d) Bottom view of ridges shoulder tool (RST); (e) Bottom view of knurling shoulder tool (KST); (f) Bottom view of scroll shoulder tool (SST) [51].

More complex features included to weld thicker plates to increase material flow and stirring and decrease process loads. For thicker plate, probe features were selected according to a number of materials, component thicknesses and joint types, as shown in Figure 2-7. The Design of these tools is shown in Figure 2-8 and Figure 2-9.

There are many benefits from using complex features: using very high welding speeds, producing Welding joint with good surface quality, reducing the probe volume and increasing swept rate.

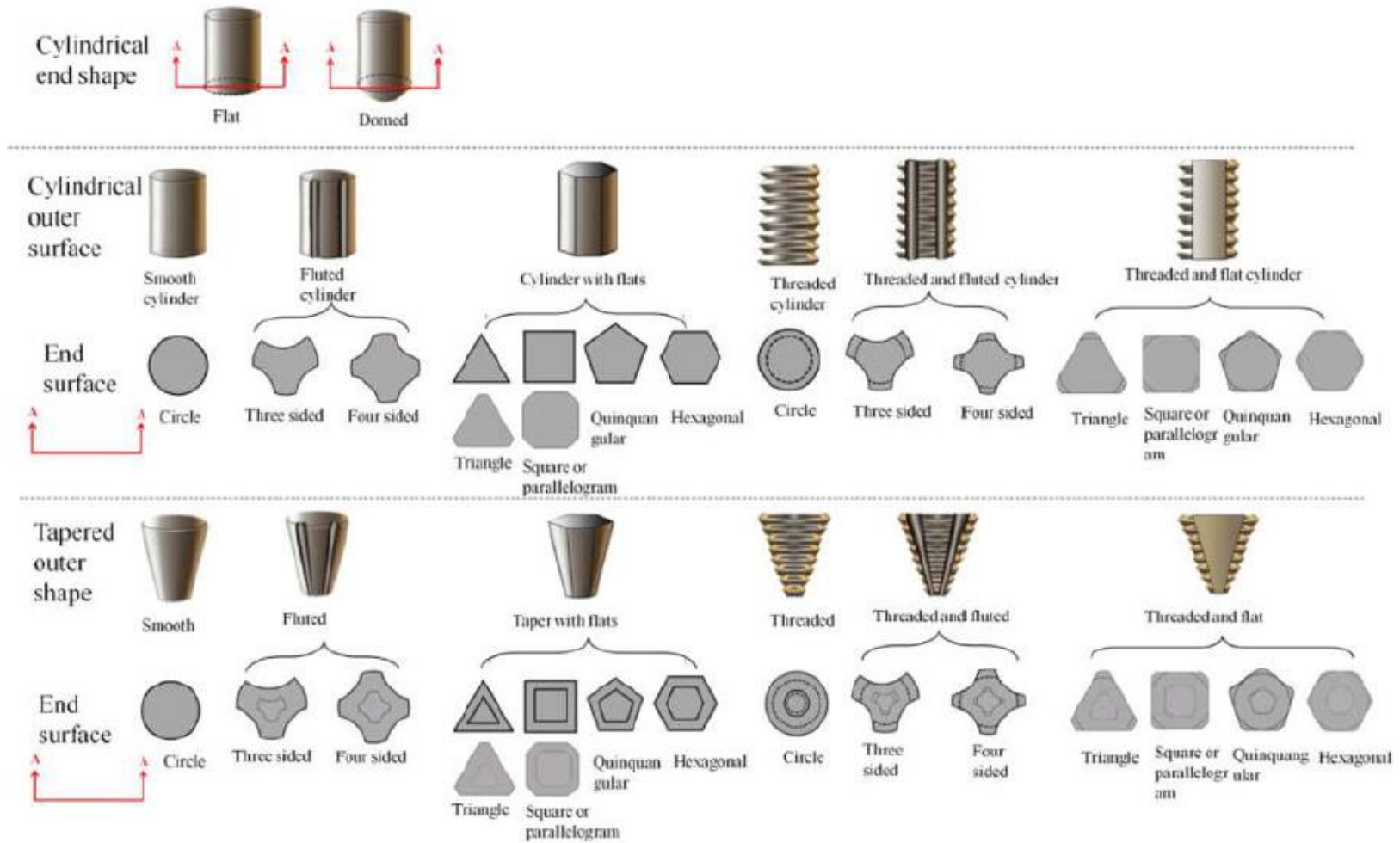


Figure 2-6. Probes features, (A) Probe tip and (B) Probe surface [9].

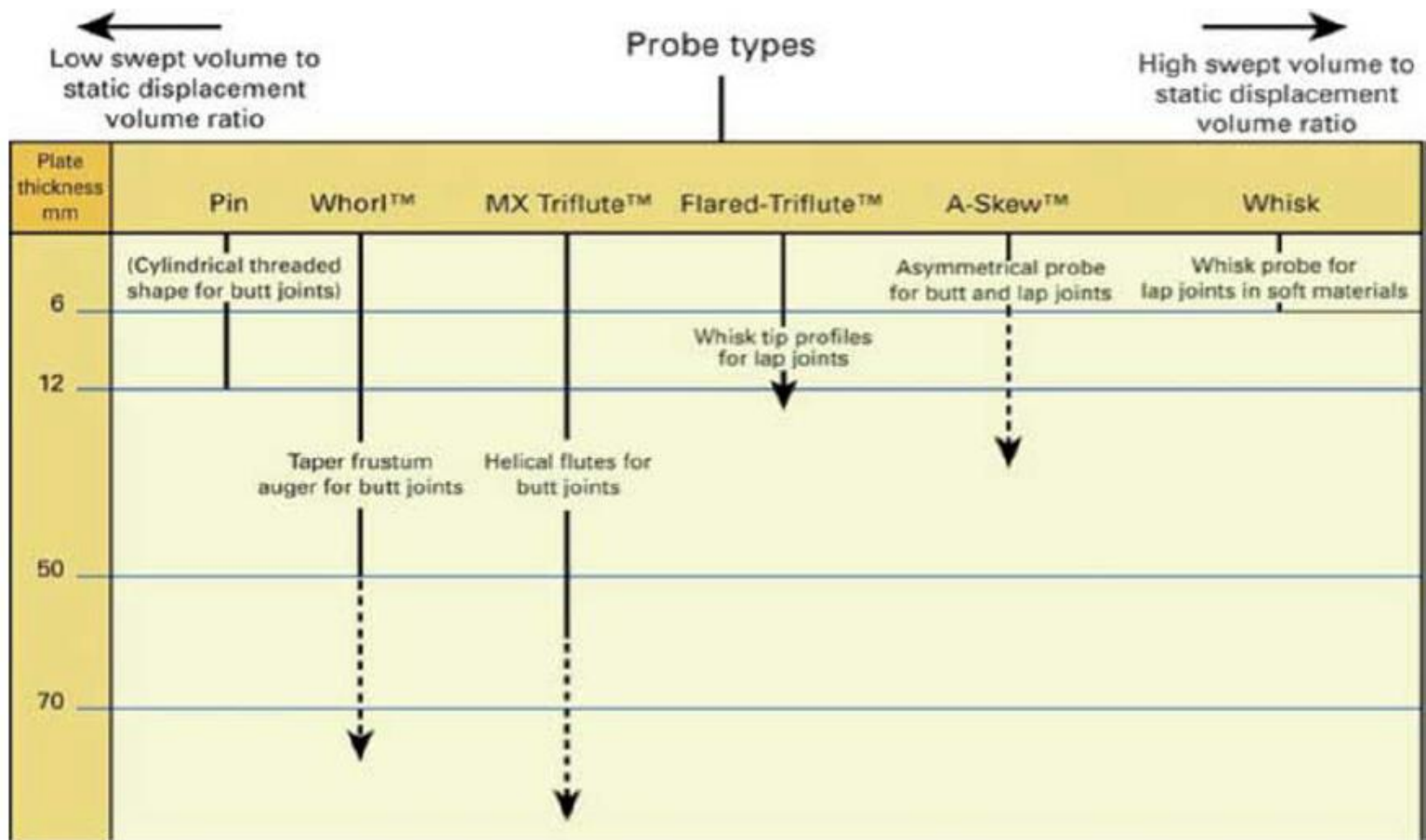


Figure 2-7. Probe types developed at TWI for various material thicknesses and joint types [52].

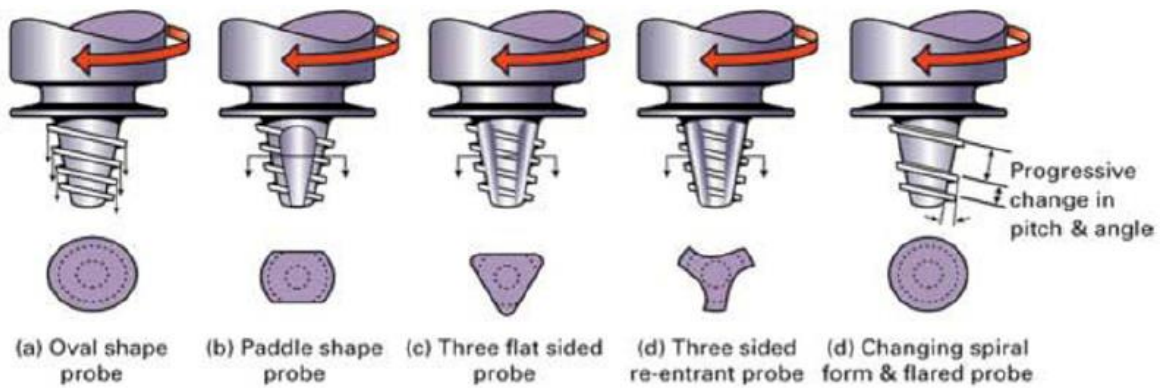


Figure 2-8. Basic variants for the Whorl™ type probes [52].

Zhang, Cao [9] summarised data for different material as shown in Figure 2-10, they found the shoulder diameter is 2.1 time from work piece thickness while it is 3 times from probe diameter. These ratios are recommended to produce sound welding joint.

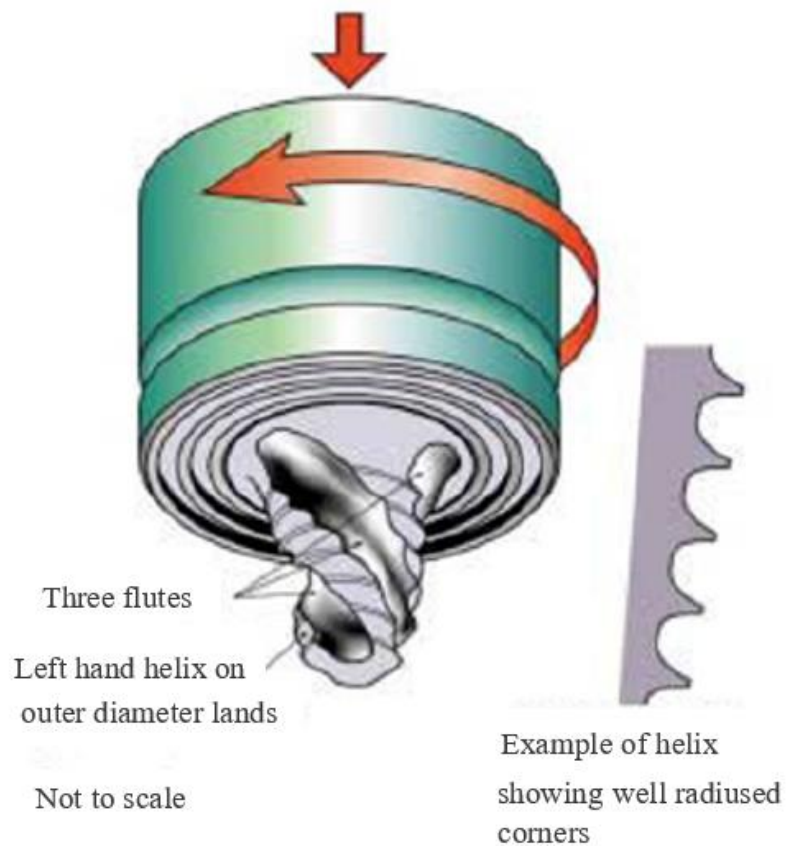


Figure 2-9. Typical MX-Triflute™ probe [52].

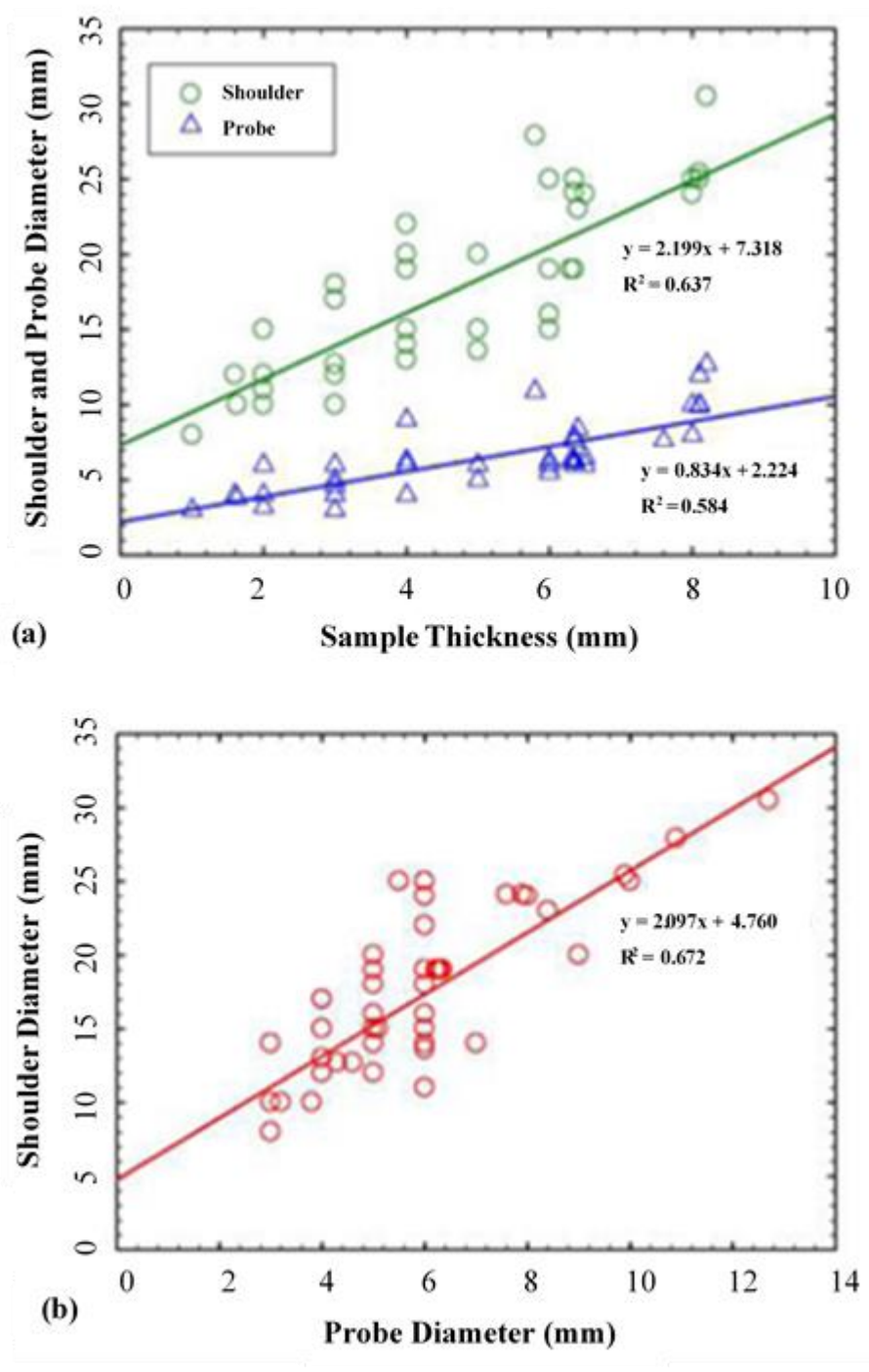


Figure 2-10. (a) Tool diameters versus work piece thickness and (b) Relation between tool diameters [9].

The FSW material are selected according to weld quality and tool wear. Tool material properties may influence on welding quality by affecting on the total heat generation and dissipation. The welding zone microstructure may also be changed when it interacts with eroded tool material. Tool wear occurs when there is the severe heating of the tool during welding cycle or the yield strength of tool material reduces at high temperatures. Table 2-1 list the tool materials, tool geometries and welding variables used to weld some of the common aluminium alloys [53].

Table 2-1. Tool materials, geometries and welding variables used for FSW of several aluminium alloys [53].

Workpiece material	Tool material	Tool shape and size	Operating parameters	Remarks
6111-T4 Al alloy, 0-9 mm thick	H13 steel	SS: flat with scroll; SD: 10 mm; PL: 0-1-6 mm	2000 rev min <sup>-1</sup> ; dwell time: 2-5 s; plunge rate: 2-5 mm s <sup>-1</sup> ; FSSW	Better quality with pinless tool
7075-T7351, 6-35 mm	1. MP159; 2. Dievar tool steel; 3. MP159 pin, H13 shoulder	PS: Triflute, Trivex	394 and 457 rev min <sup>-1</sup> ; 300-540 mm min <sup>-1</sup>	Weld UTS: 470-488 MPa Surface scaling and voiding problems
7075-T7351; 6-35 mm, 16 mm		PS: threaded	190-457 rev min <sup>-1</sup> ; 0-3-1-4 mm rev <sup>-1</sup>	
Al alloys, 5 mm		SS: concave; SD: 15 mm; PS: SC, SCT, triangular; PL: 4-7 mm, 6 mm	600-1500 rev min <sup>-1</sup> ; 25-1000 mm min <sup>-1</sup> ; 3° tilt	Peak joint efficiencies: 70-100%
7020-T6 Al alloy, 4 mm	Steel	SD: 10-20 mm, flat; PD: 3-8 mm; PL: 4-2 mm; PS: frustum and SC	1400 rev min <sup>-1</sup> ; 80 mm min <sup>-1</sup>	Peak joint efficiency: 92%
6082-T6 Al, 1-5 mm		SS: scroll, cavity, fillet; PD: 1-7 mm; PS: SC; PL: 1-2 mm	1810 rev min <sup>-1</sup> ; 460 mm min <sup>-1</sup> ; 2° tilt	Joint efficiencies: ~76%
6061-T6 Al, 9-5 mm and 12-7 mm	H13 steel	SD: 25-4 mm; PD: 5-2-7-6 mm; PL: 1-8-7-1 mm	650 rev min <sup>-1</sup> ; 150 or 200 mm min <sup>-1</sup> ; 3° tilt	
6061-T6 Al, 6-3 mm		SS: concave; SD: 26 mm; PD: 5-6 mm; PL: 5-9 mm; PS: SCT	286-1150 rev min <sup>-1</sup> ; 30-210 mm min <sup>-1</sup>	
5754 Al, 1-32 mm	H13 steel	SS: concave, convex, flat; SD: 12 mm; PD: 5 mm; PL: 1-6 mm	1500 rev min <sup>-1</sup> ; dwell time: 2 s; plunge rate: 20 mm min <sup>-1</sup> ; FSSW	
A319 and A413 Al alloy, 6 mm	Tool steel	PD: 6 mm	1000 rev min <sup>-1</sup> ; 120 mm min <sup>-1</sup>	No property degradation in weld metal
7020-T6 Al, 4 mm	High carbon steel	SS: concave; SD: 13 mm; PS: SC, TC3F; PL: 3-19 mm; PD: 5 mm	300-1620 rev min <sup>-1</sup> ; 100-900 mm min <sup>-1</sup> ; 2-5° tilt	

\*SD: shoulder diameter; PL: pin length; PD: pin diameter; PS: pin shape; SS: shoulder shape; SC: straight circular; SCT: straight circular threaded; TC3F: tapered circular with three flats; UTS: ultimate tensile strength; FSSW: friction stir spot welding. Joint efficiency is the ratio of the tensile strength of the joint to that of the base metal.

### 2.1.3 Microstructures in FSW

High plastic deformation rate and wide range of temperatures in stirred zone during FSW contribute to build welding zones microstructure because of recrystallization, precipitate dissolution and coarsening within and around stirred zone [54, 55]. This lead to formation three regions, stirred (nugget) zone, thermo-mechanically affected zone (TMAZ), and heat-affected zone (HAZ), in addition there is unaffected material or parent metal [56] as shown in Figure 2-11.



Figure 2-11. Microstructural zone classification in a friction stir weld in Al 2024 alloy (A: Parent material, unaffected by process; B: HAZ, thermally affected but with no visible plastic deformation; C: TMAZ, affected by heat and plastic deformation) [57].

### 2.1.4 FSW defects

There are many types of defects in FSW joints as shown in Figure 2-12 .These defects are identified as either flow or geometric related. The lack of penetration defect happens when the probe penetration depth is improper. The flow-related defects happen when welding parameters are selected out of the acceptable processing window because they cause an increase or decrease heat input. With increasing heat input, flash is formed excessively as a result of material flow. While low heat input leads to insufficient flowing material to cause surface lack of fill, wormhole, or lack of consolidation defects on the advancing side [58-61].

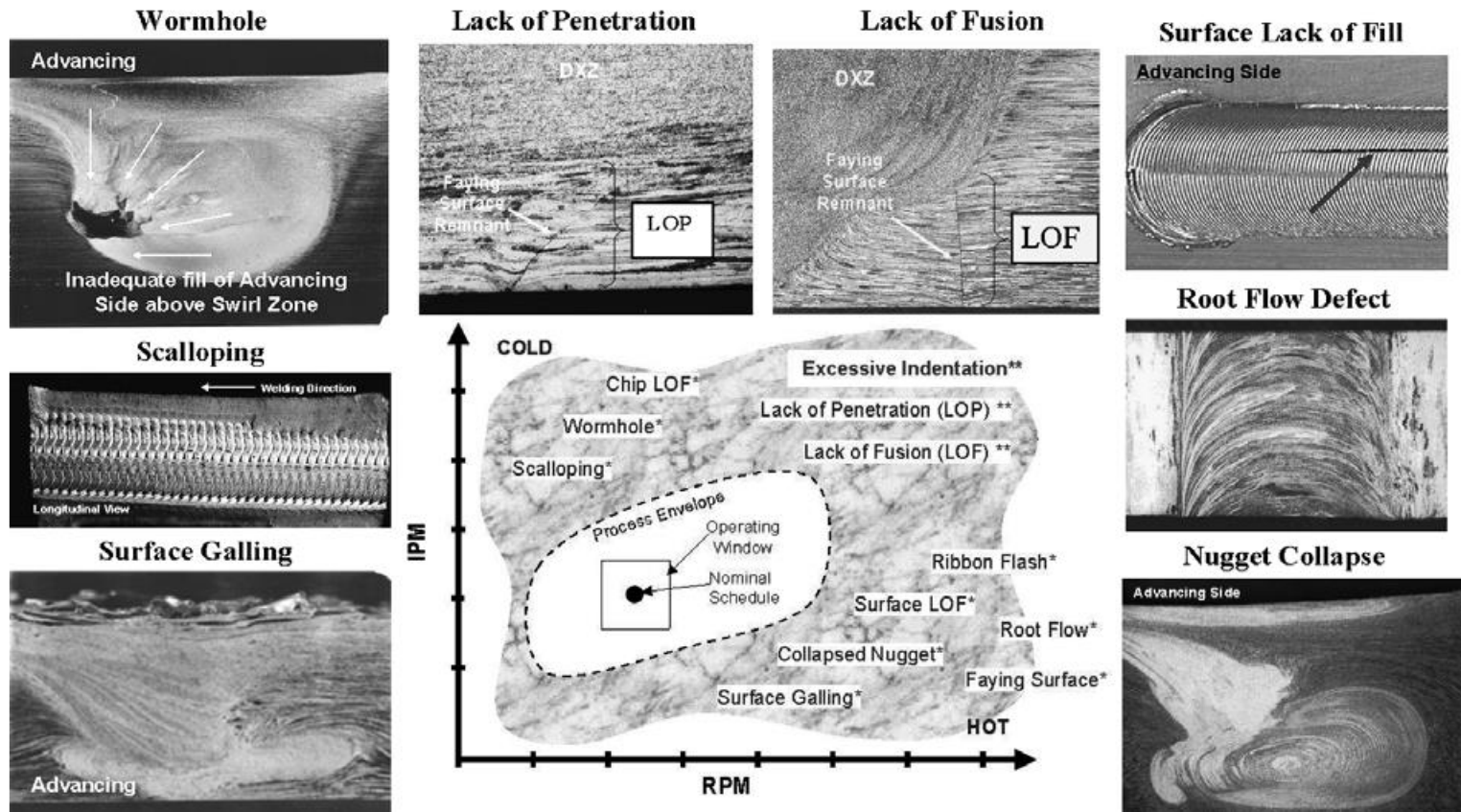


Figure 2-12. Characteristic defect types in friction stir welds [62].

### 2.1.5 Thermal cycle of FSW

FSW cycle as shown in Figure 2-13 is divided into five steps plunging, first dwelling, welding, second dwelling, and extraction [63]. These steps cause thermal sequences during FSW process as shown in Figure 2-14. Thermal cycle can be divided into six periods, first plunge (period I) is a period before shoulder contacts with work piece; second plunge (period II) is a period after shoulder contacts with work piece; first dwell period (period III); weld period (period IV); second dwell period (period V); and cooling period (period VI) [64].

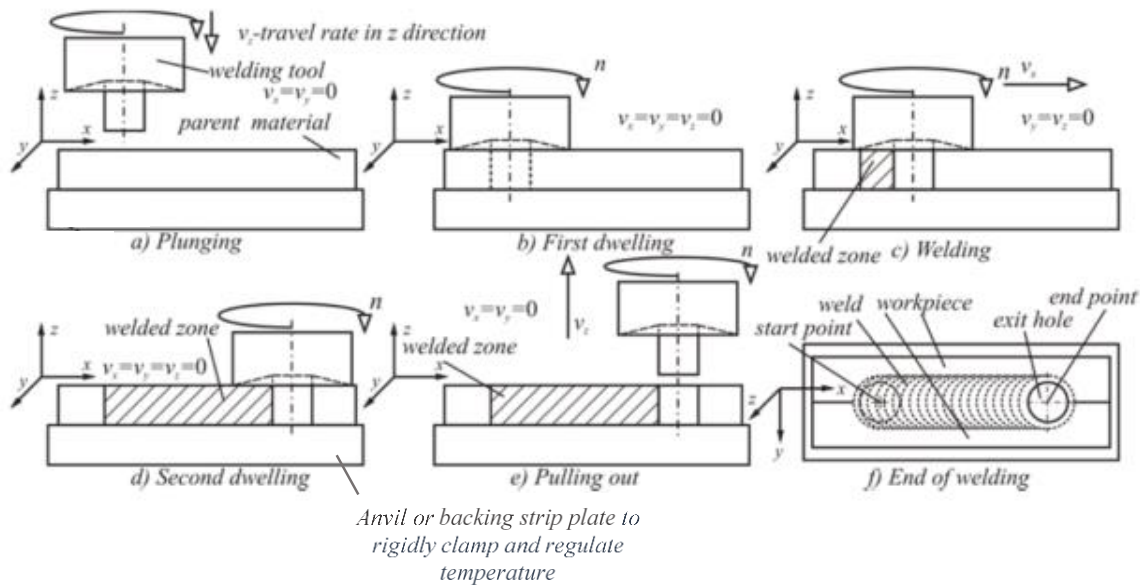


Figure 2-13. Schematic view of FSW steps; plunging, first dwelling, welding, second dwelling, and extraction [13].

The probe heat generation fraction [64] increases remarkably with increasing probe diameter and decrease noticeably with increasing shoulder diameter as shown in Figure 2-15. The previous studies were pointed that the probe heat generation fraction increases from 10 to 40 % [65] with variations of tool profile, Figure 2-15 shows the change of heat generation ratios with variation shoulder and probe radius [66].

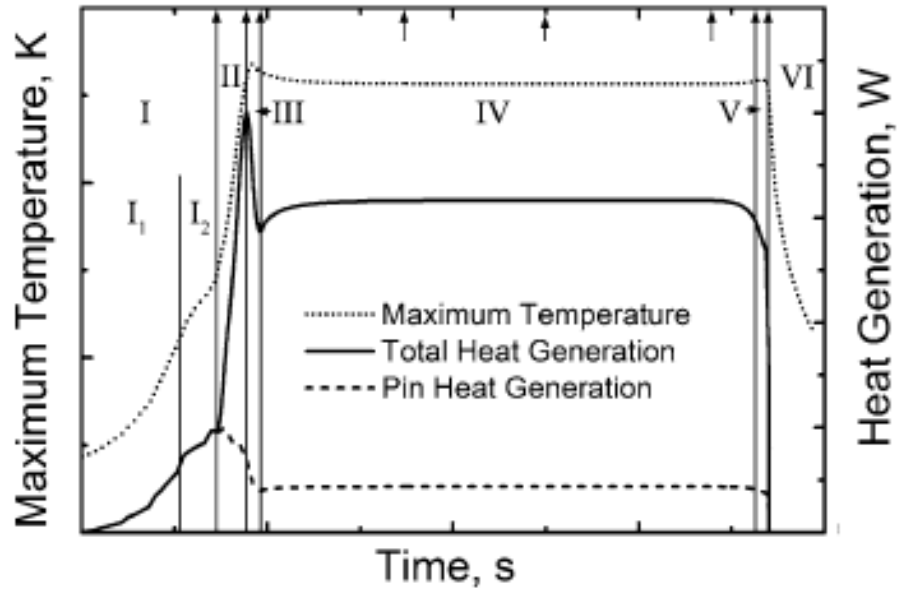


Figure 2-14. Predicted dynamic maximum temperature, total heat generation, and probe heat at FSW steps; plunge (period I); second plunge (period II); first dwell period (period III); weld period (period IV); second dwell period (period V); and cooling period (period VI) [64].

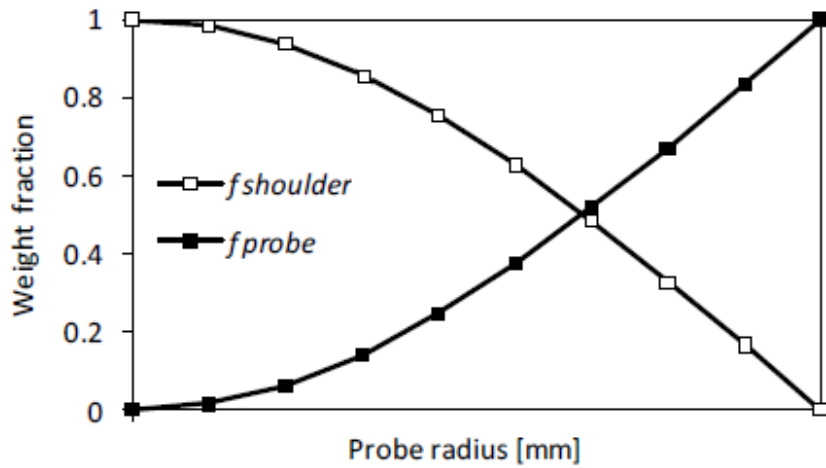


Figure 2-15. Heat fraction generated by the shoulder and probe [66].

## **2.2 FSW of aluminium alloys**

Aluminium alloys are widely used in industries because these alloys have a high strength to weight ratio and stiffness to weight ratio. Modern parts used in industries are joined by welding because these parts have low weight and cost compared with casting parts. For example, the use of welding in airframe structures can save up to 30% of the cost and up to 10% of weight for these structures [1].

However, the joining of aluminium alloys by conventional fusion welding is difficult because it requires a specific technique to remove surface oxidation. 2xxx and 7xxx aluminium series are generally classified as non-weldable because of formation brittle phases and defects in fusion zone [67]. Welding aluminium alloys with other material is so difficult due to the differences in thermal and chemical properties between them.

FSW can be the best solution for all above issues because it is solid state welding process and can use to join most aluminium alloys without needing specific techniques to remove surface oxide.

## **2.3 The heat generation at FSW**

### **2.3.1 Heat generation in FSW**

Heat during FSW is generated by deformational interaction around FSW tool and frictional interaction at the interface between tool and base metal. Both heat sources contribute to increase heat input during FSW and form thermal profile within and around the stirred zone. So, contact condition describes the relation between FSW tool and work piece material.

There are two contact conditions. The first condition is sliding when the contact shear stress (the shear stress between the tool surface and work piece surface) is less than matrix shear stress (the shear stress between the soften layers). The second one is sticking condition when the constant shear stress is greater than matrix shear stress. Many researchers studied the effect of contact condition on total heat generation during FSW. Bastier, Maitournam [5] claimed that plastic deformation contributes 4.4 % from the total heat generation.

So, the most investigations are assumed that the total heat generation is produced by frictional interaction.

### **2.3.2 The effect of welding parameters on heat generation**

Many researchers tried to find a logical relation between heat input and welding parameters. Liu et al [68] studied the effect of welding parameters on the tensile strength of 2017-T351 alloy. This study pointed that fracture positions at an interface between weld nugget and TMAZ on advancing side moved toward weld centre when the ratio of welding speed to rotation rate increases. The mechanical properties for AZ31 magnesium alloy which welded by FSW were studied to show the effect of rotation rate to moving speed ( $\omega/v$ ) ratio on joint quality. The results of this study appeared that increasing weld stirring zone and decreasing partial root penetration with increasing ( $\omega/v$ ) ratio [69].

Kim, Fujii [70] investigated the effects of FSW moving tool speed and rotation rate on aluminium alloy 383 (ADC12) microstructure by calculating Si particle distribution in nugget zone. It was reported that Si particles size decrease with increasing welding speed while rotation speed does not have any effect. Ren et al [71] studied the effect of welding speed and tool rotation on tensile strength and fracture modes for 6061-T651 alloy. Their results pointed that tensile properties and fracture surface varied with welding speed.

### **2.3.3 The effect of FSW tool design on heat generation**

Tool design affects on heat generation ratio for each part of this tool. So, there are many numerical and practical studies which investigated the relation between heat generation rate and friction stir welding tool profile. The most investigations focused on shoulder features (shoulder radius and shoulder surface) because they generate about (60-80) % from heat input at welding zone.

Arora, De [72] offered a numerical heat transfer technique which is used torque to find optimal shoulder diameter. Elangovan and Balasubramanian [73] found from their practical study the optimum shoulder diameter which produced the highest strength for AA6061 joints. Hirasawa, Badarinarayan [14] studied the effect of shoulder surface design on quality of friction spot welding joints. They found that high strength spot welds were produced by using

concave shoulders. The modelling study found that shoulder surface angle influenced on axial force value [74].

In addition, some investigations were focused on the relation of shoulder diameter with probe diameter and plate thickness to produce sound welding joints. This relation has a sound impact on total heat generation and mixing soften material to form welding zone. Join similar materials require shoulder diameter as three times base metal thickness, this point is verified by many researchers such as Prado, Murr [75] and Chen, Da Silva [76], while for dissimilar materials this diameter must be 3.5 times plate thickness because heat input should be higher for suitable material mixing to form sound welding joints [77]. Tang, Guo [78] studied the role of a shoulder on heat generation during FSW by using two kinds of tools (with and without probe). Their results showed that shoulder dominated on heat generation during FSW.

Others researchers studied the effect of variation probe profile on thermal values (the total heat generation and welding temperature). Schmidt, Hattel [79] pointed that probe generated 14% from the total heat generated and 17% in other investigation [80]. While, Colegrove, Painter [81] and Shi, Dickerson [82] their findings pointed that probe generated 20 and 25 % respectively from total heat generation. In recent investigation Zhang, Xiao [65] revealed that probe heat generation fraction varied from 13 to 37% with shoulder diameter and probe diameter variation. Their finding recorded that increase probe diameter from 6 to 10 mm caused rapidly increasing at probe heat generation fraction, while increase shoulder diameter from 16 to 24 mm caused obviously decreasing at probe heat generation fraction.

Recently, many researchers consider the impact of probe shape on welding quality and total heat generation. Suresha, Rajaprakash [83] studied the effect of probe profile changing from square straight to conical on tensile strength at welding zones; they showed that conical tool improves the mechanical properties. Elangovan and Balasubramanian [84] investigated the influence of probe profile on tensile strength for AA2219 aluminium joints which carried out by choosing five different FSW tools. Their results pointed that square probe tool profile recorded superior tensile properties for welding joint.

Ramanjaneyulu, Reddy [85] reported that total heat generation and peak temperature are an increase with increasing number of flats on probe surface (*i.e.*, square to hexagonal probe profile). They pointed that peak temperature increases with decreasing axial force as a result of probe profiles changing which mean rising in total heat input due to highly plastic deformation rate.

The recent investigations are focused on considering the effect of probe shapes and its dimensions on welding quality because the researchers realised the probe contribution in the total heat generation and the flow profile.

#### **2.3.4 Modelling and simulation of FSW thermal cycle**

Although the FSW thermal profile can be measured practically, this procedure has problematic at FW zone due to high plastic deformation which is delivered by the rotating probe in this region. In addition, experimental measurements provide incomplete temperature information. So, there are many investigations which are worked to improve a thermal cycle simulation during FSW by modelling to obtain the optimum results.

3D Finite element is one of the most important methods used to model thermal history of softening layers at welding zone. Ulysse [86] modelled FSW by using 3D finite element (Figure 2-16) to study the effect of welding speed and rotational velocity on FSW temperatures, The results pointed that FSW temperatures increase with reducing welding speed and increasing rotational speed as shown in Figure 2-17 and Figure 2-18.

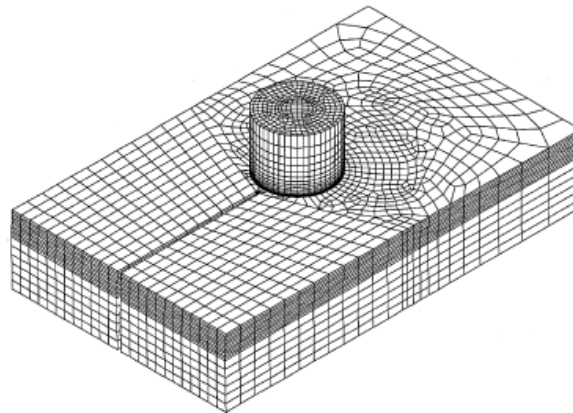


Figure 2-16. Finite element mesh of the welding model [86].

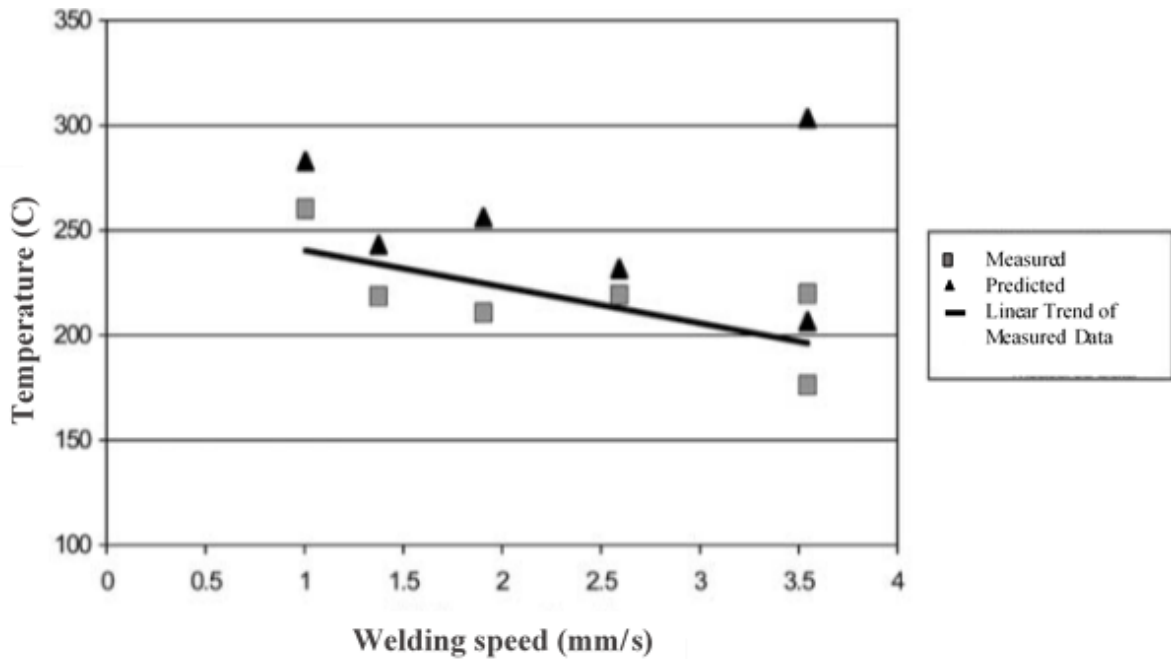


Figure 2-17. Stir-welding temperatures as a function of welding speed [86].

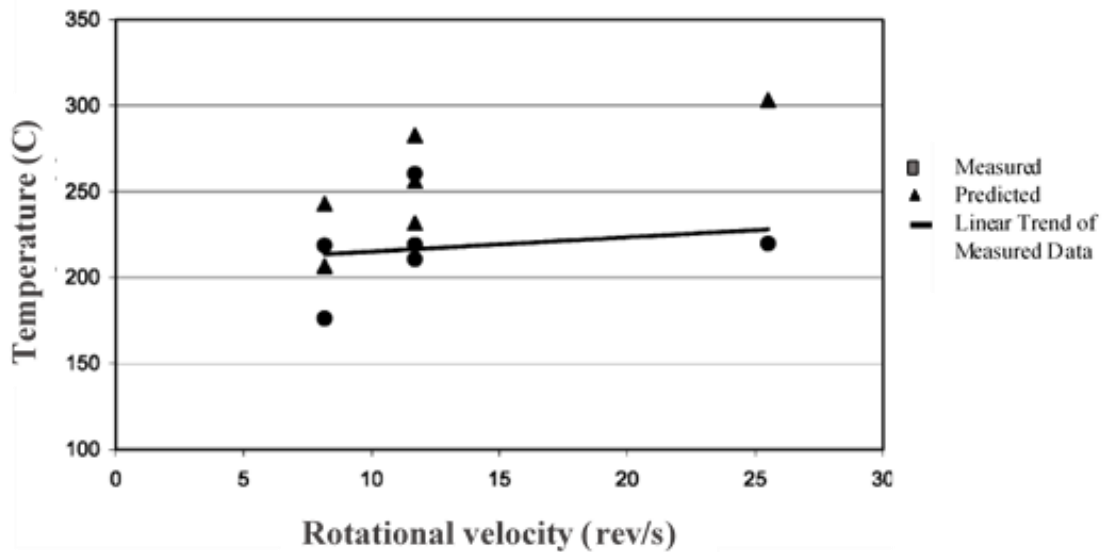


Figure 2-18. Stir-welding temperatures as a function of rotational velocity [86].

Chao, Qi [87] formulated equations (Figure 2-19) to simulate the standard boundary for the FSW tool (equation (2.1)) and workpiece (equation (2.2)) to reduce the gap between experimentally and numerically temperature results for frictional heat generation.

$$Q_3 = Q_4 + q_1 \quad (2.1)$$

Where  $Q_3$  is the heat flux to the tool from the friction between the tool and the workpiece,  $q_1$  is the heat lost from the surface of the tool to the environment through convection and  $Q_4$  is the heat transferred to the machine head in which the tool is mounted.

$$Q_1 = Q_2 + q_2 + Q \quad (2.2)$$

Where  $Q_1$  is the heat flux coming from the friction between the tool and the workpiece,  $Q_2$  is the heat conducted from the bottom surface of the workpiece to the backing plate on the machine,  $q_2$  is the heat lost from the surface of the workpiece to the environment through convection, and  $Q$  is the increase of the heat content in the workpiece.

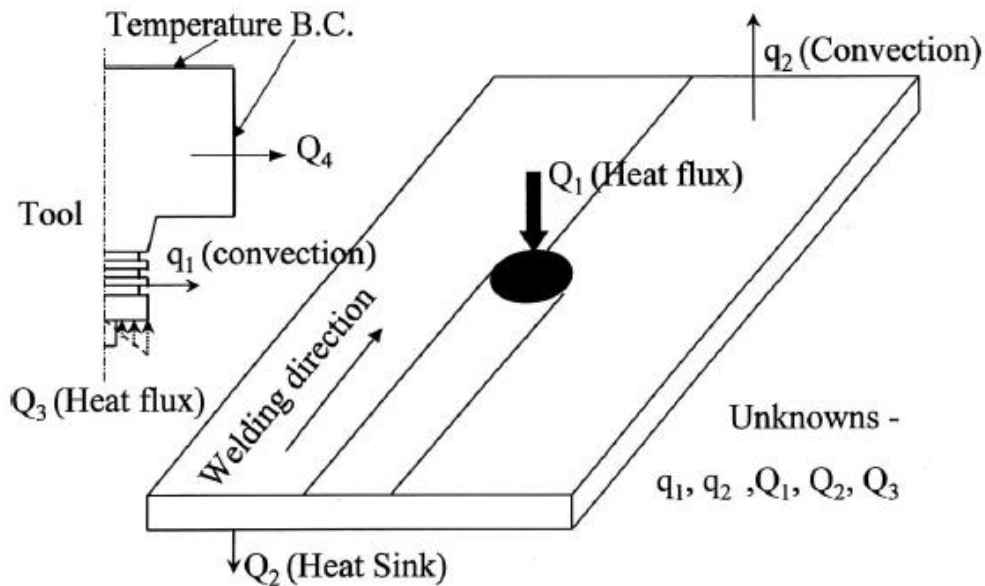


Figure 2-19. Heat transfer in tool and workpiece in friction stir welding (One-half of the tool model is shown due to symmetry) [87].

Schmidt, Hattel [79] defined a contact state variable  $\delta$ , which represent the ratio of the velocity matrix surface to the tool velocity at any contact point (equation (2.3)).

$$\delta = \frac{v_{matrix}}{v_{tool}} = 1 - \frac{\gamma'}{v_{tool}} \quad (2.3)$$

Where  $\gamma'$  is the slip rate and  $v_{tool}$  is the position dependent tool velocity of  $\omega r$ . The relationship between the different contact conditions are listed Table 2-2.

Table 2-2. Definition of contact condition, velocity/shear relationship and state variable

(dimensionless slip rate).

Condition	Matrix velocity	Tool velocity	Shear stress	State variable
Sticking	$v_{matrix} = v_{tool}$	$v_{tool} = \omega r$	$\tau_{friction} > \tau_{yield}$	$\delta = 1$
Sticking/sliding	$v_{matrix} < v_{tool}$	$v_{tool} = \omega r$	$\tau_{friction} \geq \tau_{yield}$	$0 < \delta < 1$
Sliding	$v_{matrix} = 0$	$v_{tool} = \omega r$	$\tau_{friction} < \tau_{yield}$	$\delta = 0$

The sticking condition was assumed by researchers when the shearing occurs in a layer very close to the interface, while the sliding condition was assumed when the shear takes place at the contact interface [79]. According to these contact conditions, the shear contact stresses

( $\tau_{contact}$ ) are introduced:

1. The sticking shear stress ( $\tau_{sticking}$ ) is described the  $\tau_{contact}$  for a sticking condition by von Mises equation under pure shear condition.

$$\tau_{contact} = \tau_{sticking} = \frac{\sigma_y}{\sqrt{3}} \quad (2.4)$$

Where  $\sigma_y$  is the material yield stress.

2. The friction shear stress ( $\tau_{friction}$ ) is described the  $\tau_{contact}$  for a sliding condition by Coulomb's friction law.

$$\tau_{contact} = \tau_{friction} = \mu \cdot P \quad (2.5)$$

Where  $\mu$  is the friction coefficient and  $p$  is the contact pressures.

Graz-Seggau [88] reported that the welding speed is much lower than the peripheral velocity (the linear velocity of the rotating cylinder), so the rotational speed dominates to estimate the FSW heat input.

Đurđanović, Mijajlović [63] modelled the heat generation during FSW. The model assumed that the heat energy was generated by pure sliding, pure sticking and combination of sliding and sticking conditions. Basic heat generation equation of infinitesimal surface in contact with the weld joints is equal to:

$$dQ = \omega \cdot dM \quad (2.6)$$

Where:  $\omega$  tool angular rotation speed,  $\text{rad}^{-1}$ ,  $dM$  – torque of the welding tool.

The  $dM$  is substituted as the perimeter force ( $dF$ ) and radial distance ( $r$ );  $dF$  is substituted as a shear stress  $\tau$  and infinitesimal area of observed surface ( $dA$ ), so the heat generation equation is:

$$dQ = \omega \cdot dM = \omega \cdot r \cdot dF = \omega \cdot r \cdot \tau \cdot dA \quad (2.7)$$

$\tau = \tau_{contact}$  is calculated according to contact condition  $\tau_{friction}$  or  $\tau_{sticking}$ .

Song and Kovacevic [89] presented moving coordinate system (MCS) (equation (2.8)) to simplify modelling of heat transfer from FSW tool to base metal because the heat source moving does not need to model.

$$\frac{d(\rho c T)}{dt} = \frac{d}{dx} \left( k_x \frac{dT}{dx} \right) + \frac{d}{dy} \left( k_y \frac{dT}{dy} \right) + \frac{d}{dz} \left( k_z \frac{dT}{dz} \right) + v_w \frac{d(\rho c T)}{dx} \quad (2.8)$$

Where  $T$  is the temperature,  $c$  is the heat capacity,  $\rho$  is the density,  $k$  is the heat conductivity, and  $v_w$  is the tool moving speed.

AA2524 joints by FSW was modelled to predict the effect of welding speeds and tool rotational speeds on torque, power requirement and the size of the TMAZ [90], their findings pointed that the size of the TMAZ increases with increasing the rotational speed as shown in Figure 2-20 because of higher power and higher peak temperatures.

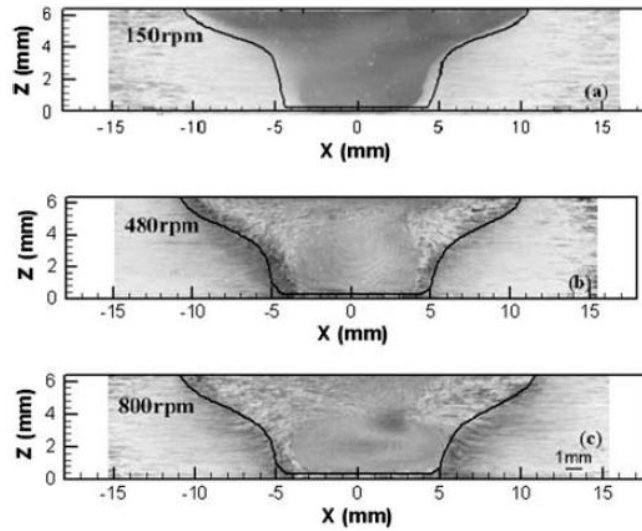


Figure 2-20. Relative comparison of the numerically computed TMAZ with the corresponding experimentally determined geometry. The welding velocity is  $2.11 \text{ mm s}^{-1}$  and the rotation speed was varied: (a) 150 rpm (b) 480 rpm and (c) 800 rpm [90].

Most of the previous investigations studied the effect of probe profiles on joint quality as a result of change total heat generation. Schmidt and Hattel [91] used models to describe the heat source. These models simulated the role of a probe and the effect of contact condition on heat generation during FSW periods.

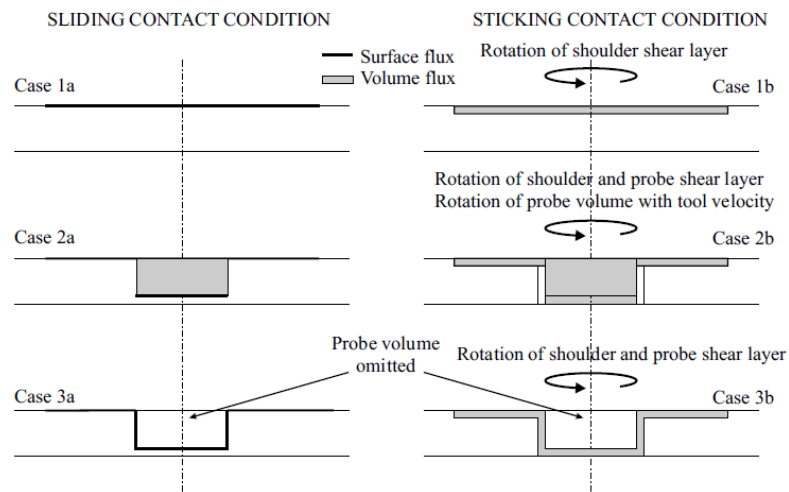


Figure 2-21. Schematic view of configuration of 6 cases: left column = sliding condition, right column = sticking condition. First row: no probe heat generation (HG); second row: with probe H.G; third row: probe volume removed, H.G. in shear layer [91].

Song and Kovacevic [92] used moving heat source to model probe heat generation to explain heat transfer during tool plunges into plates and tool extracts from the work piece. Their results pointed that the peak temperature at the tool shoulder interface could be very close to the base metal melting point if the input heat flux is high enough as shown in Figure 2-22.

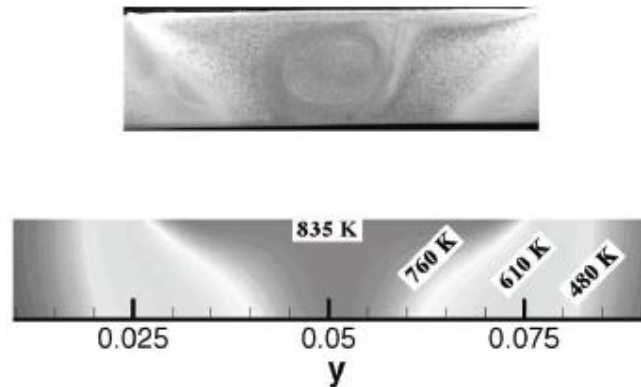


Figure 2-22. Calculated isothermals versus microstructure morphology [92].

Buffa, Hua [22] designed FSW tool (Figure 2-23) by FEM model to study the effect of the change pin angle ( $10^\circ$ ,  $20^\circ$ ,  $30^\circ$  and  $40^\circ$ ) on thermal cycle during FSW process. They found that heat-affected zone and thermal mechanical zone are large in welding zones as a result of increasing taper probe angle as shown in Figure 2-24.

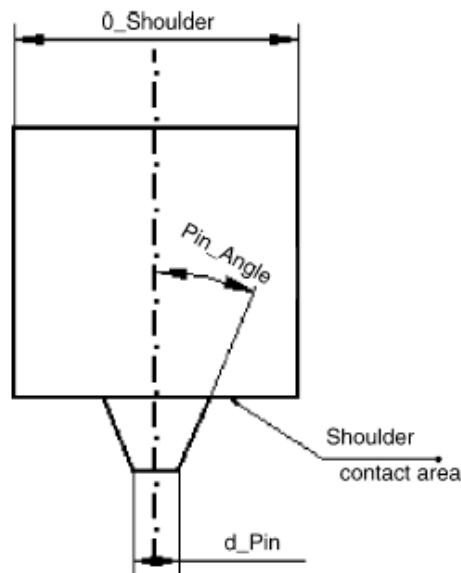


Figure 2-23. Tool design showing geometric parameters [22].

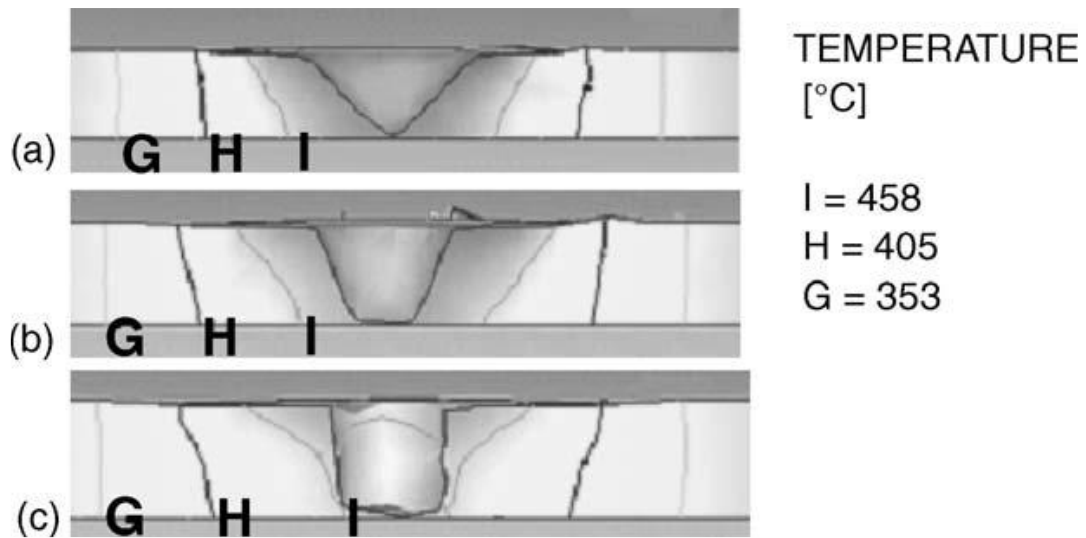


Figure 2-24. Temperature profile in a  $x$ - $z$  section as a function of pin angle  $\alpha$  ( $V_f = 100$  mm/min) (a)  $\alpha = 40^\circ$ , (b)  $\alpha = 20^\circ$  and (c)  $\alpha = 0^\circ$ .

Biswas and Mandal [93] presented 3D finite element model to determine the influence of tool profile variation on heat distribution at weld nugget. Their results showed that the peak temperatures were all closer to or more than 80% of the melting point of AA1100. The tool design with a concave shoulder and conical pin is superior for FSW of AA1100 (Figure 2-25).

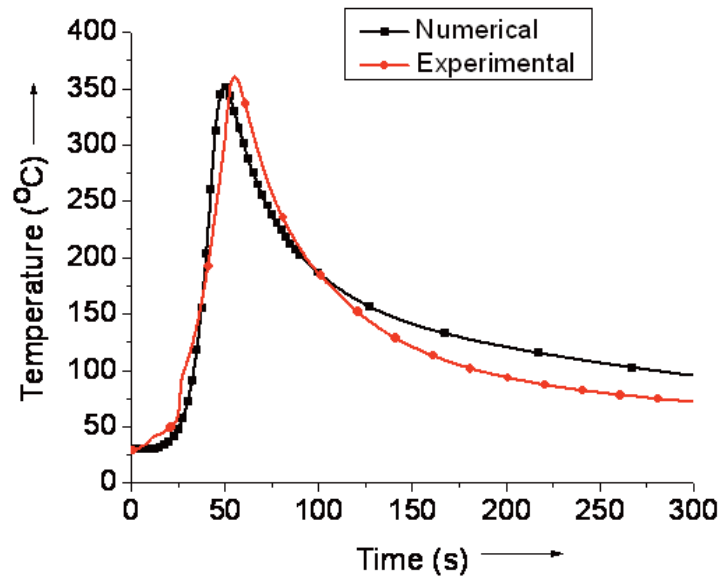


Figure 2-25. Numerical and experimental temperature distribution for welding with conical tool pin [93].

There are many studies focus on the effect of taper probe profile on total heat generation at FSW process. Taper cylindrical probe profile was modelled to predict total heat generation during FSW of Al alloy [94]. The FSW tool was divided into three interfaces (Figure 2-26) to estimate the total heat generation (equation (2.9)) .

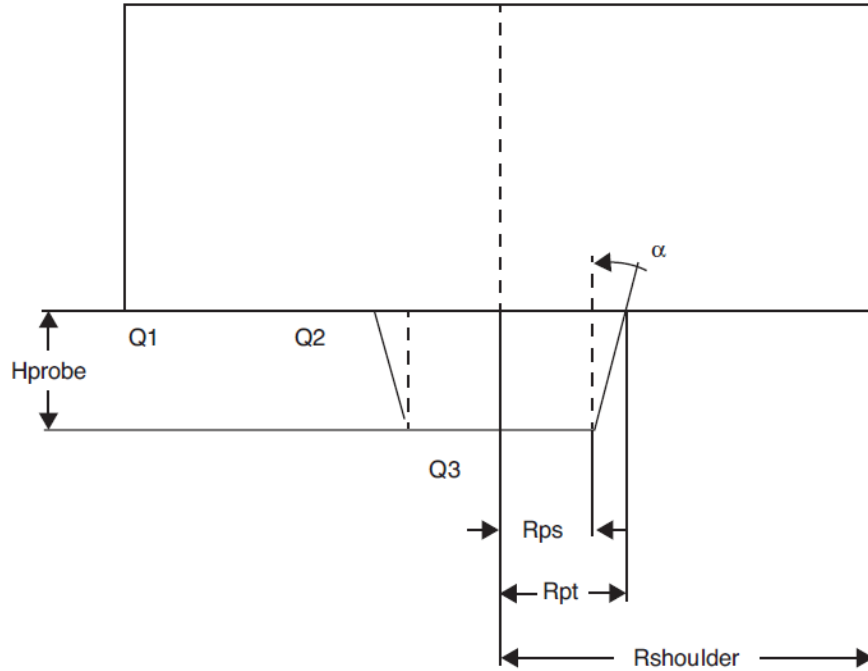


Figure 2-26. Different heat generation regions [94].

$$Q_{total} = Q_1 + Q_2 + Q_3 \quad (2.9)$$

Where  $Q_1$  is heat generated under tool shoulder,  $Q_2$  at the tool pin side, and  $Q_3$  at the tool pin tip.

The taper angle  $\alpha$  was used to characterise the taper pin surface. The general equation (equation (2.10)) for heat generation was used to derive heat generation from each interface.

$$dQ = \omega \cdot dM = \omega \cdot r \cdot dF = \omega \cdot r \cdot \tau_{contact} \cdot dA \quad (2.10)$$

The contact interface between tool and the base metal given by position and orientation relative to the FSW tool axis is shown in Figure 2-27.

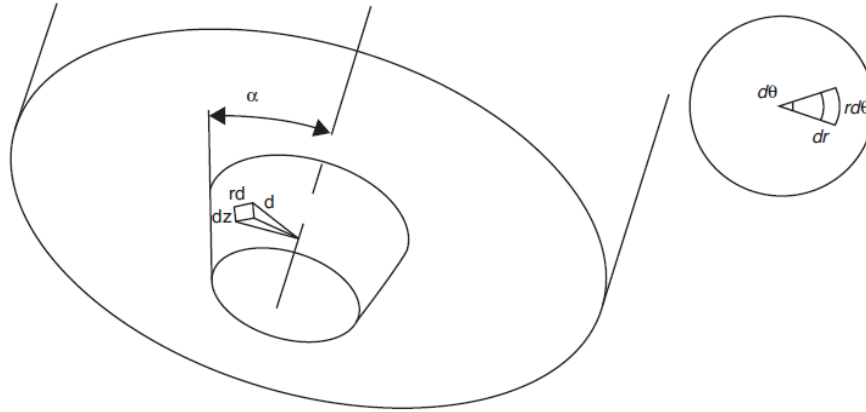


Figure 2-27. Surface orientations and infinitesimal segment area for taper conical profile [94].

There was a good agreement between modelling and experiential results available in literature. The peak temperature decreases with increasing taper angle as shown in Figure 2-28.

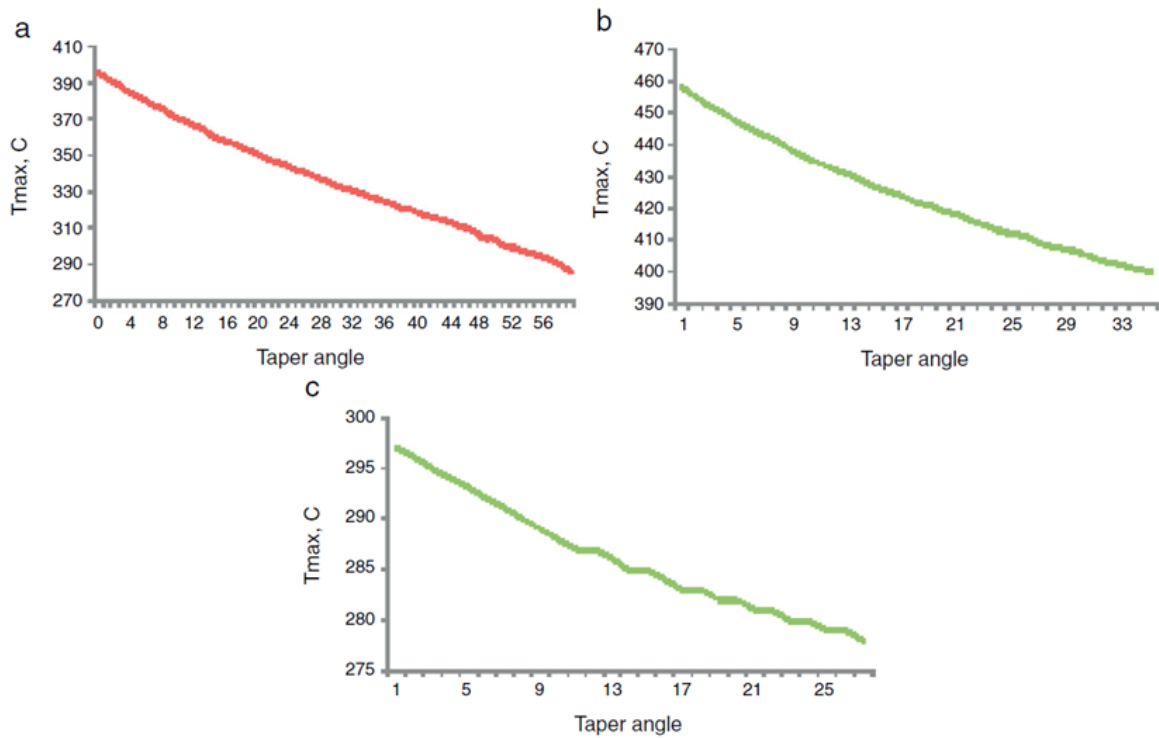


Figure 2-28. Effect of taper angle on peak temperature (a) AA 6061-T6, (b) AA 6061-T651 and (c) AA 6082-T6 [94].

The study of Tikader, Biswas [95] compared between the effect of straight and taper cylindrical probe on FSW heat generation and mechanical properties for AA1100 aluminium alloy. The researchers claimed that straight cylindrical probe profile tool generates high temperature than tapered probe profile tool.

## 2.4 Summary

FSW takes place in the solid phase below the melting point of the materials to be joined. The heat is generated by friction and deformation. Frictional heat is considered the main heat source during FSW because it constitutes more than 95% from the total heat generation.

The heat generation relies on the FSW tool profile, welding parameters and material thermal properties. Although, FSW tool profile has the major effect on the heat generation. The relationship among these factors is important to calculate the heat generation during FSW.

Numerical modelling of heat generation is the best way to study the effect of FSW tool on FSW thermal cycle because practical studies faces two challenges; the first challenge is that the thermocouples cannot be placed in the nugget zone because of high plastic deformation caused by stirring force from the rotating FSW tool. The second one, experimental measurements cannot give the full thermal profile of welding zone.

There are many developments on numerical modelling by previous studies. Basic heat generation equation was used to derive heat generation equations for FSW tool to build thermal modelling of FSW. The  $\tau_{contact}$  was selected according to the contact condition between the FSW tool and the workpiece  $\tau_{frictional}$  for sliding condition and  $\tau_{sticking}$  for sticking condition.

The sticking condition was assumed by researchers when the shearing occurs in a layer very close to the interface, while the sliding condition was assumed when the shear takes place at the contact interface. The MCS can be used to simplify modelling of heat transfer from FSW tool to base metal because the complex moving for the flow material around the tool does not need to model.

The shoulder dominates on the total heat generation during FSW because it constitutes (60-80) % from the total heat generation. The change of probe design has effect on the total heat generation, flow patterns and defect formation.

## **2.5 Gaps in literature**

Little research has been done to study the effect of the change taper polygonal tool profiles on heat generation and distributed during FSW. As a result, no clear analytical methods have been laid out to predict the effect of change FSW tool profiles from straight to taper on the total heat generation. The effect of the change tools profiles on mechanical properties should be studied by finding the relationship between the tools profiles and peak temperature to produce a sound and defect-free weld.

## **2.6 Objectives**

The objective of the proposed research is to improve the understanding of the effect of change FSW tool profiles from taper to straight on the amount of heat generated and distributed in welding joints. The specific objectives are listed below:

1. Derive equations to compute the heat generation at surfaces of shoulder, probe side and probe tip.
2. Perform finite element analysis using COMSOL to compute the heat transfer in FSW.
3. Perform experimental studies including the experimental trials for straight and taper tool profiles were selected according to DOE matrix.
4. Predict the axial force (AF) as a function of welding parameters (N and S) and tool profiles (PFN and  $T_p$ ) by DOE.
5. Measure thermal profiles experimentally by thermocouples placed at 5mm from welding line during experimental trials to validate the modelling results. predictions.
6. Predict the peak temperatures (PT) (calculated by model 2) as a function of welding parameters (N and S) and tool profiles (PFN and  $T_p$ ) by DOE.

7. Predict the tensile strength ( $\sigma_T$ ) as a function of welding parameters (N and S) and tool profiles (PFN and  $Tp$ ) by DOE.
8. Validate the DOE model predictions for AF, PT and  $\sigma_T$ .
9. Predict the optimise tool design and welding parameters to produce the highest tensile strength joint.

## Chapter 3 : Analytical modelling of FSW

In this chapter, equations are derived to calculate the heat input and contribution at surfaces (shoulder, probe side and probe tip) for different tapered tool profiles (triangular (TR), square (SQ), pentagonal (Pen) and hexagonal (Hex)) and straight tool profiles (triangular (STR), square (SSQ), pentagonal (SPen), hexagonal (SHex) and octagonal straight tools (SOct)).

### 3.1 Heat generation equations for FSW tools

The heat during FSW generates at contact interfaces which have a complex profile according to tool shape. In analytical tool interface modelling, FSW tool is divided into a shoulder-base metal interface, vertical probe surface-base metal interface and probe tip-base metal interface. For example, simplified tool design for triangular taper tool (TR) shown in Figure 3-1 , where  $Q_1$  is heat generated under tool shoulder,  $Q_2$  at tool Trapezoidal probe side, and  $Q_3$  at tool probe tip. Total heat generated,  $Q_{total} = Q_1 + Q_2 + Q_3$ .

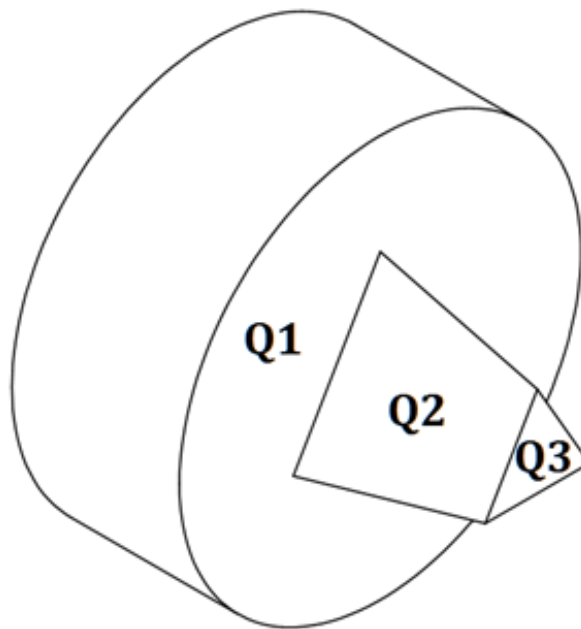


Figure 3-1. TR tool profile.

Heat generated in each contact surface will be computed by using mechanical power equation (3-1) because mechanical energy which provides by FSW machine will convert to heat energy [63].

$$dQ = \omega \cdot dM = \omega \cdot x \cdot dF = \omega \cdot x \cdot \tau_{contact} \cdot dA \quad (3-1) [63]$$

Where  $M$  is a torque of the welding tool,  $F$  is a force,  $\omega$  is angular velocity ( $\omega = 2 \cdot \pi \cdot N$ ),  $A$  is contact area,  $x$  is shear force arm and  $\tau_{contact}$  is a contact shear stress [63].

Note. Contact area ( $dA$ ) and shear force arm ( $x$ ) should be calculated for each surface to calculate the total heat generation.

Contact shear stress value is assumed according to the contact condition. In this work, it is shear friction stress at shoulder surface because the contact condition at shoulder is assumed a sliding, Coulomb's friction law is used to estimate the contact shear stress for a sliding condition  $\tau_{contact} = \tau_{friction} = \mu \cdot P$ , While sticking condition is assumed at the probe and probe tip surfaces, in this case, the contact shear stress  $\tau_{contact} = \tau_{sticking} = \frac{\sigma_y}{\sqrt{3}}$ . According to these assumptions the heat energy is generated by frictional heating at the interface between the FSW tool and work piece.

The element of the contact area at each interface is  $dA$ . This element is expressed by its location and direction relative to tool rotation axis. The shape of element for contact area ( $dA$ ) be selected depending on tool profile.

### 3.1.1 Heat generation equations for taper tools

Equations are derived to calculate the heat input and contribution at surfaces (shoulder, probe surface and probe tip) for different tapered tool profiles (triangular (TR), square (SQ), pentagonal (Pen) and hexagonal (Hex)).

### 3.1.1.1 Heat generation equations for triangular taper tool (TR)

The elements contact area ( $dA$ ) for each interface is expressed by its location and direction relative to tool rotation axis as shown in Figure 3-2. The surface area of probe can be estimated by using isosceles trapezoid elements (Figure 3-2 (b)), while circle and rectangular elements are used to calculate areas for shoulder, probe base and probe tip (Figure 3-2 (a) and (c)).

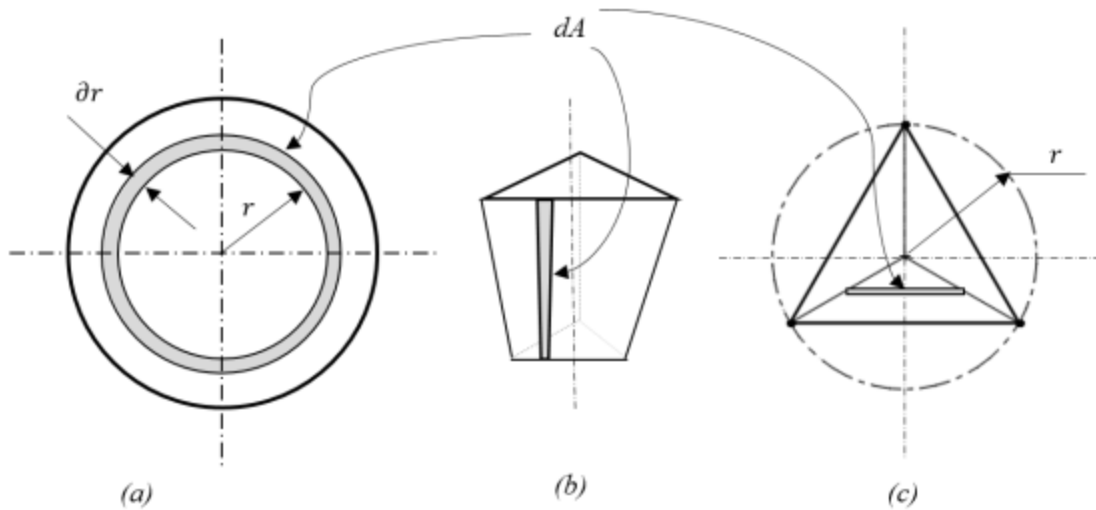


Figure 3-2. Schematic drawing of surface orientations and infinitesimal segment areas for triangular taper tool (TR). (a) Shoulder surface area, (b) Probe surface area and (c) Probe base and tip cross-section area.

#### 3.1.1.1.1 Heat generation from shoulder surface ( $Q_1$ )

It is calculated by subtracting the heat generated for probe base area ( $Q_b$ ) from the heat generated for shoulder ( $Q_{\text{shoulder}}$ ).

Shoulder surface heat generation ( $Q_{\text{shoulder}}$ ) can be expressed by substitution  $dA = 2\pi \cdot r \cdot dr$  (Figure 3-3) and  $x = r$  at equation (3-1).

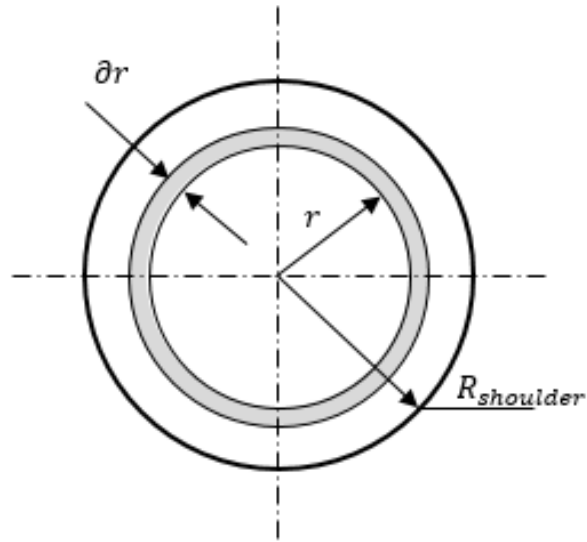


Figure 3-3. Schematic drawing for shoulder segment area.

$$Q_{shoulder} = \int_{r=0}^{r=R_{shoulder}} \omega \cdot \tau_{contact} \cdot r \cdot (2\pi \cdot r \cdot dr)$$

Finally, shoulder surface heat generation ( $Q_{shoulder}$ ) is:

$$Q_{shoulder} = \frac{2}{3} \cdot \pi \cdot \omega \cdot \tau_{contact} \cdot R_{shoulder}^3 \quad (3-2)$$

Where  $R_{shoulder}$  is a shoulder radius.

To calculate probe base area heat generation ( $Q_b$ ), two values should be calculated:

1. Contact element area (dA)

Probe base area can be calculated by dividing this area into three triangles as a shown in Figure 3-4(a) and using a rectangular integral element (dA) (Figure 3-4 (b)).

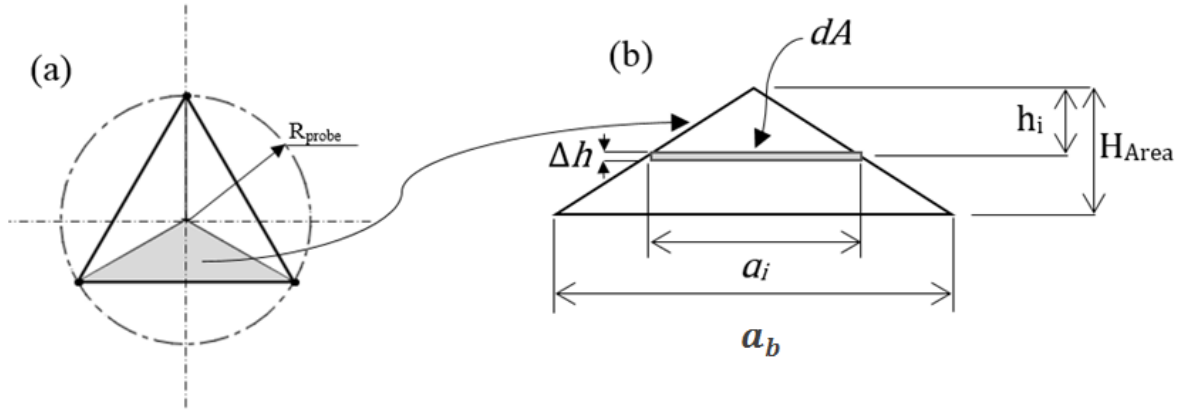


Figure 3-4. Schematic drawing for probe base. (a) The triangular probe base cross section.  
 (b) Schematic drawing for Position and dimensions of segment.

The area for one element ( $dA_{one}$ ) can be calculated by:

$$dA_{one} = a_i \cdot \Delta h \quad (3-3)$$

From Figure 3-4 (b):

$$\frac{h_i}{a_i} = \frac{H_{Area}}{a_b} \quad (3-4)$$

For triangular probe,  $a_b = R_{probe} \cdot \sqrt{3}$ ,  $H_{Area} = \frac{R_{probe}}{2}$  and  $h_i = r$  by substitution these values at equation (3-4):

$$a_i = 2\sqrt{3} \cdot r \quad (3-5)$$

By substituting equation (3-5) into equation (3-3), the area for one element ( $dA_{one}$ ) is:

$$dA_{one} = 2\sqrt{3} \cdot r \cdot \Delta r$$

$A_{one}$  can be calculated by limit equation for  $dA_{one}$ .

$$A_{one} = \lim_{n \rightarrow \infty} \sum_{i=1}^n dA_{one} = \lim_{n \rightarrow \infty} \sum_{i=1}^n 2\sqrt{3}.r.\Delta r = \int_{r=0}^{r=R_{Cb}} 2\sqrt{3}.r.dr \quad (3-6)$$

Where  $R_{Cb}$  is radius of a circumscribed circle at probe base cross section area.

The area of one element ( $dA_{one}$ ) should be as a function of  $R_{probe}$ , therefore the integration limit should be changed from  $R_{Cb}$  to  $R_{probe}$ .

For triangular probe:

$$R_{Cb} = \frac{R_{Probe}}{2}$$

So,

$$dR_{Cb} = \frac{dr_{probe}}{2} \quad (3-7)$$

By using equation (3-7), equation (3-6) can be rewritten as:

$$A_{one} = \int_{r=0}^{r=R_{Probe}} 2\sqrt{3}.\frac{r}{2}.\frac{dr}{2} = \frac{\sqrt{3}}{2} \int_{r=0}^{r=R_{Probe}} r.dr \quad (3-8)$$

Total probe base cross section area ( $A_{Total}$ ) can be calculated as:

$$A_{Total} = PN.A_{one}.$$

Where PN is probe base cross section parts number (Figure 3-4), for triangular probe PN=3.

So,  $A_{Total}$  is:

$$A_{Total} = \frac{3\sqrt{3}}{2} \int_{r=0}^{r=R_{Probe}} r.dr \quad (3-9)$$

2. Shear force arm (x) for probe base area.

At probe base cross section, shear force arm equals to circumscribed radius ( $R_{Cb}$ ) (Figure 3-6) but it should be calculated as a ratio from probe radius ( $R_{probe}$ ) to make probe base heat generation ( $Q_b$ ) as a function of probe radius ( $R_{probe}$ ).

For triangular probe:

$$R_{Cb} = \frac{R_{Probe}}{2}$$

$$\text{So,} \quad x = \frac{r}{2} \quad (3-10)$$

Substituting equation (3-9) and equation (3-10) into equation (3-1) the heat generation from probe base ( $Q_b$ ) is:

$$Q_b = \int_{r=0}^{r=R_{Probe}} \omega \cdot \tau_{contact} \cdot \frac{r}{2} \cdot \frac{3\sqrt{3}}{2} r \cdot dr$$

$$Q_b = \frac{\sqrt{3}}{4} \cdot \omega \cdot \tau_{contact} \cdot R_{probe}^3 \quad (3-11)$$

Therefore,  $Q_1$  is calculated from  $Q_{shoulder} - Q_b$ , i.e. Equations (3-2) and (3-11).

$$Q_1 = \frac{2}{3} \cdot \pi \cdot \omega \cdot \tau_{contact} \cdot (R_{shoulder}^3 - 0.2067 \cdot R_{probe}^3) \quad (3-12)$$

### 3.1.1.1.2 Heat generation from probe surface ( $Q_2$ )

To calculate probe surface heat generation ( $Q_2$ ) from equation (3-1), two values should be calculated:

1. Probe surface area element ( $dA$ )

Polygonal probe lateral surface area relies on a probe flats number. So, probe surface area element ( $dA_{total}$ ) calculates from multiplying integral element for one flat ( $dA_{one}$ ) by a polygon probe flats number (PFN), for triangular probe PFN=3 as shown in equation:

$$dA_{total} = 3 \cdot dA_{one} \quad (3-13)$$

The integral element for one flat ( $dA_{one}$ ) can be expressed as (Figure 3-5):

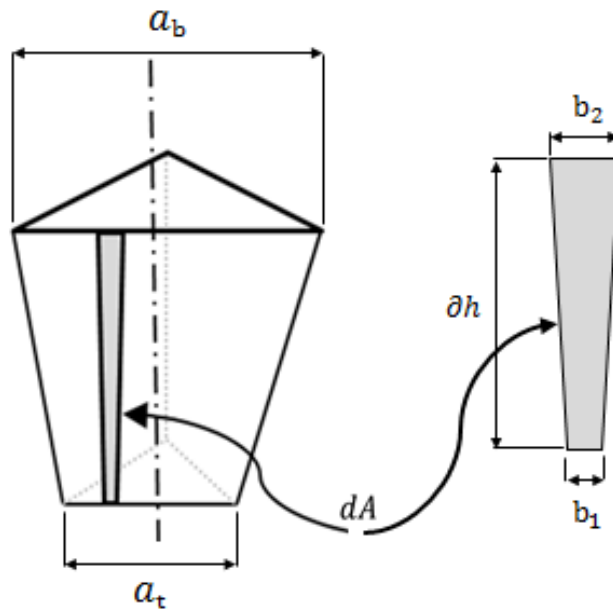


Figure 3-5. Schematic drawing of isosceles trapezoidal elements to probe surface.

$$dA_{one} = \frac{1}{2} \cdot (b_1 + b_2) \cdot dh \quad (3-14)$$

The equation (3-14) can be simplified to:

$$dA_{one} = \frac{1}{2} \cdot n \cdot (b_1 + b_2) \cdot dh = \frac{1}{2} \cdot (n \cdot b_1 + n \cdot b_2) \cdot dh \quad (3-15)$$

Where  $n$  is the number of elements in one flat.

From Figure 3-5 the values of  $n \cdot b_1$  and  $n \cdot b_2$  are equaled to the lower and upper flat sides  $a_t$  and  $a_b$  respectively. The length of these sides depends on probe profile. For triangular probe, they can be calculated as:

$$a_t = \sqrt{3} \cdot R_{tip} \text{ \& } a_b = \sqrt{3} \cdot R_{probe}$$

Where  $R_{tip}$  and  $R_{probe}$  are the values of tip and probe radius respectively.

So, the equation (3-15) can be simplified to:

$$dA_{one} = \frac{\sqrt{3}}{2} (R_{tip} + R_{probe}) \cdot dh \quad (3-16)$$

The ratio between  $R_{probe}$  and  $R_{tip}$  represents the  $Tp$  value which equals 0.7, so the equation (3-16) can be rewritten as:

$$dA_{one} = \frac{\sqrt{3}}{2} (0.7R_{probe} + R_{probe}) \cdot dh = (1.4722) \cdot R_{probe} \cdot dh \quad (3-17)$$

Finally, the probe surface element area ( $dA_{total}$ ) is:

$$dA_{total} = 3 \cdot dA_{one} = 4.4167 \int_{r=0}^{r=R_{probe}} \int_{h=0}^{h=H_{probe}} dr \cdot dh \quad (3-18)$$

Where  $H_{probe}$  is the probe height.

The value of probe geometry factor ( $P_F$ ) is 4.4167.

2. The shear force arm ( $x$ ) for probe surface area.

The shear force arm ( $x$ ) is the normal distance between the centre of element and probe centre line. It can be calculated from:

$$x = F_T \cdot r$$

Where  $F_T$  is taper radius factor, it is the ratio between the average of circumscribed radius for the polygonal tapered probe ( $A_R$ ) and probe base radius ( $R_{Probe}$ ). For triangular probe, the taper radius factor ( $F_T$ ) is:

$$F_T = \frac{A_R}{R_{Probe}}$$

Where  $A_R$  can be calculated by:

$$A_R = \frac{R_{Cb} + R_{Ct}}{2}$$

Where  $R_{Cb}$  and  $R_{Ct}$  are the circumscribed radius at probe base and probe tip respectively (Figure 3-6).

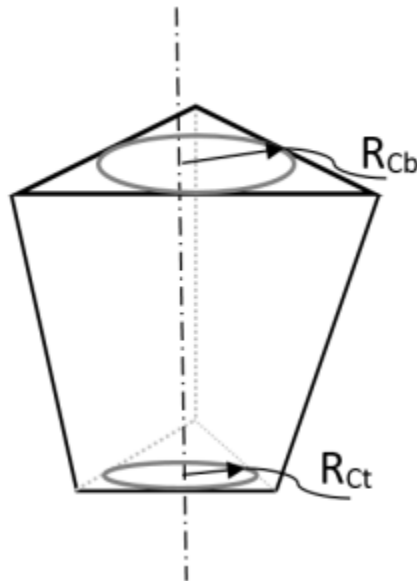


Figure 3-6. The circumscribed radius at probe base and probe tip.

For triangular probe, the values of  $R_{Cb}$  and  $R_{Ct}$  are 1.05 and 1.5 mm, so the value of  $F_T$  is 0.425.

Therefore  $Q_2$  is calculated by substituting probe surface area element (dA) and the shear force arm (x) at equation (3-1):

$$Q_2 = \omega \cdot (0.425) \cdot \tau_{contact} \cdot (4.4167) \cdot \int_{r=0}^{r=R_{probe}} \int_{h=0}^{h=H_{probe}} r \cdot dr \cdot dh$$

Finally, probe surface heat generation ( $Q_2$ ) is:

$$Q_2 = \frac{2}{3} \cdot \pi \cdot \omega \cdot \tau_{contact} \cdot (0.4481) \cdot R_{probe}^2 \cdot H_{probe} \quad (3-19)$$

### 3.1.1.1.3 Heat generation from probe tip surface ( $Q_3$ )

TR has the same profile at probe base and probe tip. The procedure for the deriving heat generation equations of probe base surface ( $Q_b$ ) is used to derive heat generation equations in probe tip ( $Q_3$ ) by replacing  $R_{probe}$  with  $R_{tip}$ .

Therefore, the heat generation from probe tip surface ( $Q_3$ ) is:

$$Q_3 = \frac{\sqrt{3}}{4} \cdot \omega \cdot \tau_{contact} \cdot R_{tip}^3 = \frac{2}{3} \cdot \pi \cdot \omega \cdot \tau_{contact} \cdot (0.2067) \cdot R_{tip}^3 \quad (3-20)$$

From equations (3-12),(3-19) and (3-20),  $Q_{total} = Q_1 + Q_2 + Q_3$

$$Q_{Total} = \frac{2}{3} \cdot \pi \cdot \omega \cdot \tau_{contact} \cdot (R_{shoulder}^3 - (0.2067) \cdot R_{probe}^3 + (0.4481) \cdot R_{probe}^2 \cdot H_{probe} + (0.2067) \cdot R_{tip}^3)$$

The total heat generation equations ( $Q_{Total}$ ) can be presented in a general form:

$$Q_{Total} = \frac{2}{3} \cdot \pi \cdot \omega \cdot \tau_{contact} \cdot (R_{shoulder}^3 - (F_1) \cdot R_{probe}^3 + (F_2) \cdot R_{probe}^2 \cdot H_{probe} + (F_3) \cdot R_{tip}^3)$$

Where  $F_1$ ,  $F_2$  and  $F_3$  are the heat generation equation factors.

### 3.1.1.2 Heat generation equations for square, pentagonal, hexagonal taper tools

The procedure for the deriving heat generation equations of TR tool is used to derive heat generation equations in square (SQ), pentagonal (Pen), hexagonal (Hex) and Octagonal taper tools (Oct). The final factors for heat generation equations are listed in Table 3-1.

Table 3-1. The heat generation equation factors for different taper tool profiles.

Tool profile	F1	F2	F3
TR	0.207	0.448	0.207
SQ	0.450	0.690	0.450
Pen	0.612	0.820	0.612
Hex	0.716	0.896	0.716
Oct	0.832	0.976	0.832

These equations were applied in COMSOL as a heat sources in the interfaces between the FSW tool and the workpiece to analyse the heat transfer in FSW.

### 3.1.2 Heat generation equations for straight tools

Equations are derived to calculate the heat input and contribution at surfaces (shoulder, probe surface and probe tip) for different straight tool profiles (triangular (STR), square (SSQ), pentagonal (SPen), hexagonal (SHex) and octagonal straight tools (SOct)).

#### 3.1.2.1 Heat generation equations for straight triangular tool (STR)

The elements contact area ( $dA$ ) for each interface is expressed by its location and direction relative to tool rotation axis as shown in Figure 3-2. The surface area of probe can be estimated by using isosceles trapezoid elements (Figure 3-2 (b)), while circle and rectangular elements are used to calculate areas for shoulder, probe base and probe tip (Figure 3-2 (a) and (c)).

### 3.1.2.1.1 Heat generation from shoulder surface ( $Q_1$ )

STR has the same profile at probe base of TR. So, the procedure for the deriving heat generation equations of shoulder surface ( $Q_1$ ) for TR is used to derive heat generation equations from shoulder surface ( $Q_1$ ) for STR.

$$Q_1 = \frac{2}{3} \cdot \pi \cdot \omega \cdot \tau_{contact} \cdot (R_{shoulder}^3 - 0.2067 \cdot R_{probe}^3) \quad (3-21)$$

### 3.1.2.1.2 Heat generation from probe surface ( $Q_2$ )

To derive heat generation equation from probe surface ( $Q_2$ ), the same produce for the deriving heat generation equation of  $Q_2$  for TR is used to derive heat generation equation in probe surface ( $Q_2$ ) by substituting:

1.  $b_1 = b_2$
2.  $a_t = a_b = \sqrt{3} \cdot R_{probe}$
3.  $x = \frac{R_c}{R_{probe}} \cdot r$

Finally, probe surface heat generation ( $Q_2$ ) is:

$$Q_2 = \frac{2}{3} \cdot \pi \cdot \omega \cdot \tau_{contact} \cdot (0.620) \cdot R_{probe}^2 \cdot H_{probe} \quad (3-22)$$

### 3.1.2.1.3 Heat generation from probe tip surface ( $Q_3$ )

STR has the same cross section at probe base and probe tip, so the heat generation from probe tip surface ( $Q_3$ ) is equal to the heat generation from probe base ( $Q_b$ ).

Therefore the heat generation from probe tip surface ( $Q_3$ ) is:

$$Q_3 = \frac{2}{3} \cdot \pi \cdot \omega \cdot \tau_{contact} (0.2067 \cdot R_{probe}^3) \quad (3-23)$$

From equations (3-21),(3-22) and (3-23),  $Q_{total} = Q_1 + Q_2 + Q_3$

$$Q_{Total} = \frac{2}{3} \cdot \pi \cdot \omega \cdot \tau_{contact} \cdot (R_{shoulder}^3 + (0.620) \cdot R_{probe}^2 \cdot H_{probe})$$

The total heat generation equations ( $Q_{Total}$ ) can be presented in a general form:

$$Q_{Total} = \frac{2}{3} \cdot \pi \cdot \omega \cdot \tau_{contact} \cdot (R_{shoulder}^3 - (F_1) \cdot R_{probe}^3 + (F_2) \cdot R_{probe}^2 \cdot H_{probe} + (F_3) \cdot R_{tip}^3)$$

Where  $F_1$ ,  $F_2$  and  $F_3$  are the heat generation equation factors.

### 3.1.2.2 Heat generation equations for square, pentagonal, hexagonal straight tools

The procedure for the deriving heat generation equations of STR tool is used to derive heat generation equations for square (SSQ), pentagonal (SPen), hexagonal (SHex) and octagonal straight tools (SOct). The final factors for heat generation equations are listed in Table 3-2.

Table 3-2. The heat generation equation factors for different straight tool profiles.

<b>Tool profile</b>	<b>F1</b>	<b>F2</b>	<b>F3</b>
<b>STR</b>	0.207	0.620	0.207
<b>SSQ</b>	0.450	0.955	0.450
<b>SPen</b>	0.612	1.135	0.612
<b>SHex</b>	0.716	1.240	0.716
<b>SOct</b>	0.832	1.350	0.832

These equations were applied in COMSOL as a heat sources in the interfaces between the FSW tool and the workpiece to analyse the heat transfer in FSW.

## Chapter 4 : Numerical modelling of heat generation during FSW

### 4.1 Introduction

The current project, computational heat transfer in solids (HTS) embedded in COMSOL is used to simulate heat generation and heat distribution in FSW by using both straight and taper tool profiles (TR, SQ, Pen, Hex and Oct) with different values of welding parameters. HTS modelling is built by finite element method (FEM) using a MCS which fixed on tool axis. The main aim of utilising MCS is to model FSW tool which moves along welding line because this movement requires a complex model to simulate this tool as a moving heat source [89]. Heat transfer control equation for base metal in a MCS with a positive the x-direction moving tool can be written as:

$$\frac{d(\rho c_p T)}{dt} = \frac{d}{dx} \left( k_x \frac{dT}{dx} \right) + \frac{d}{dy} \left( k_y \frac{dT}{dy} \right) + \frac{d}{dz} \left( k_z \frac{dT}{dz} \right) + S \frac{d(\rho c_p T)}{dx} \quad (4.1) [89]$$

Where  $T$  is the temperature,  $c_p$  is the heat capacity,  $\rho$  is the density,  $k$  is the heat conductivity, and  $S$  is the welding speed mm/min. The last term of the equation represents the moving of FWS tool by MCS in a positive x-direction for the base metal.

Using HTS requires dividing geometry into small elements to simplify simulation for this geometry. These small elements are known as meshes or cells use to solve equations of heat energy and heat transfer during welding cycle.

This chapter presents the methodology of developing a thermal model to predict thermal cycle; a 3D transient thermal model is simulated by using COMSOL to predict a temperature distribution during FSW of aluminium alloy 6061-T6. The main steps of the FSW thermal model in COMSOL are described in **Appendix 3**.

## 4.2 Physical models

Physical model has been built for the welding joint and FSW tool as defined below.

### 4.2.1 Welding joint

Welding joint geometry is symmetric around welding line. So, it is enough to model one aluminium plate. Dimensions of this plate are 320 mm length, 102 mm width, and 6.35 mm thickness with two infinite domains in the x-direction. Figure 4-1 shows this model geometry:

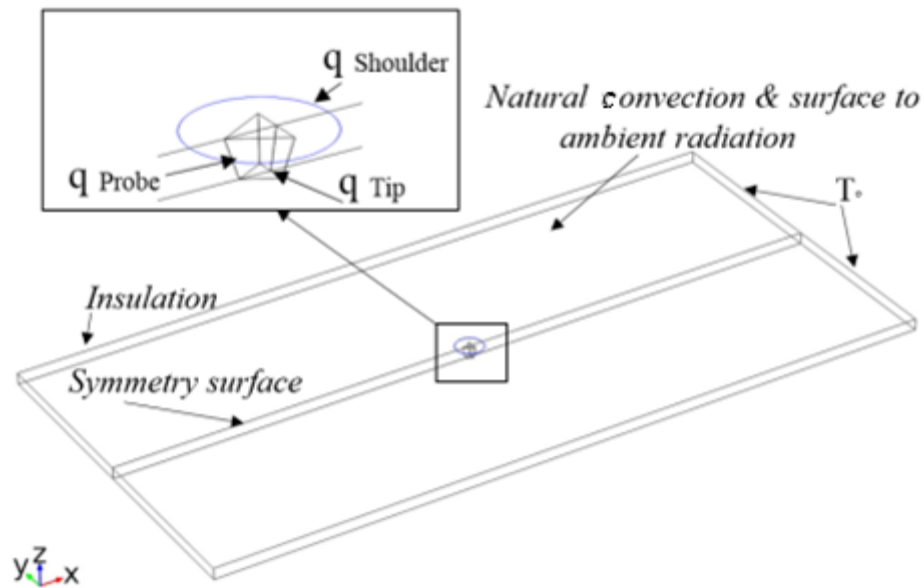


Figure 4-1. FSW Model geometry.

### 4.2.2 FSW tool

FSW tool has two active parts, shoulder and probe. The shoulder has one active surface. While, Probe has two active surfaces, probe surface and probe tip surface. These surfaces contribution in a total heat generation will represent at modelling as:

Heat flux boundary condition at tool shoulder-base metal interface is:

$$k \frac{\delta T}{\delta n} \Big|_{\Gamma} = Q_1 \quad (4.2)$$

Heat flux boundary condition at tool probe surface-base metal interface is:

$$k \frac{\delta T}{\delta n} \Big|_{\Gamma} = Q_2 \quad (4.3)$$

Heat flux boundary condition at tool probe tip-base metal interface is:

$$k \frac{\delta T}{\delta n} \Big|_{\Gamma} = Q_3 \quad (4.4)$$

Where  $k$  is heat conductivity,  $T$  is temperature, and  $n$  is normal direction vector of boundary  $\Gamma$ .

### 4.3 Heat generation equation

Heat during welding process generates as a result of mechanical interaction between FSW tool and the work piece. This energy transfers to the base metal and causes an increase base metal temperature, but this temperature is not enough to melt base metal. So, HTS will be used to model heat transfer during FSW by governing equation, this equation is [96]:

$$\rho \cdot C_p \cdot S \cdot \nabla T = \nabla \cdot (k \cdot \nabla T) + Q \quad (4.5)$$

Where  $\rho$  is density,  $C_p$  is specific heat,  $S$  is velocity vector,  $k$  is thermal conductivity,  $T$  is temperature, and  $Q_{total}$  is internal heat generation rate  $Q_{total} = Q_1 + Q_2 + Q_3$

There is no specific condition in heat transfer even the model temperature increases to the base metal melting point (855 K).

### 4.4 Modelling assumptions

In the first stage of modelling, density, thermal conductivity, thermal capacity and friction coefficient are assumed as constant. In the second stage of modelling, density, thermal conductivity and thermal capacity will be calculated as a function of temperature.

Friction coefficient is a constant because it is difficult to measure it at elevated temperature [63]. These assumptions are listed in Table 4-1.

Table 4-1. Welding parameters and materials properties used in Models 1 and 2.

		Model 1	Model 2
Friction coefficient ( $\mu$ )		$\mu = 0.3$	$\mu = 0.3$
Shear contact ( $\tau_{\text{contact}}$ )	Shoulder	$\tau_{\text{sliding}} = \mu * (Fn/A_{\text{shoulder}})^{(1)}$	$\tau_{\text{sliding}} = \mu * (Fn/A_{\text{shoulder}})^{(1)}$
	Probe and tip surfaces	$\tau_{\text{sticking}} = \frac{\sigma_y^{(2)}(T)}{\sqrt{3}}$	$\tau_{\text{sticking}} = \frac{\sigma_y^{(2)}(T)}{\sqrt{3}}$
Material properties	Density ( $\rho$ ) (kg/m <sup>3</sup> )	2700	$\rho_{(T)}^{(3)}$
	Thermal conductivity (K) (W/(m*K))	167	$K_{(T)}^{(4)}$
	Heat Capacity (Cp) (J/(kg*K))	896	$Cp_{(T)}^{(5)}$

<sup>(1)</sup> Shear contact stress under sliding condition ( $\tau_{\text{sliding}}$ ) in model 1 and 2 is constant during FSW cycle.

<sup>(2)</sup> Shear contact stress under sticking condition ( $\tau_{\text{sticking}}$ ) in model 1 and 2 is a function of temperature according to yield stress as a function of temperature ( $\sigma_y(T)$ ) as shown in Figure 4-2.

<sup>(3)</sup> Density in model 2 is a function of temperature ( $\rho_{(T)}$ ) calculated using JMatPro as shown in Figure 4-3.

<sup>(4)</sup> Thermal conductivity in model 2 is a function of temperature ( $K_{(T)}$ ) calculated using JMatPro as shown in Figure 4-4

<sup>(5)</sup> Heat Capacity in model 2 is a function of temperature ( $Cp_{(T)}$ ) calculated using JMatPro as shown in Figure 4-5.

JMatPro software is used to predict material properties for alloys as a function of their composition and heat treatment.

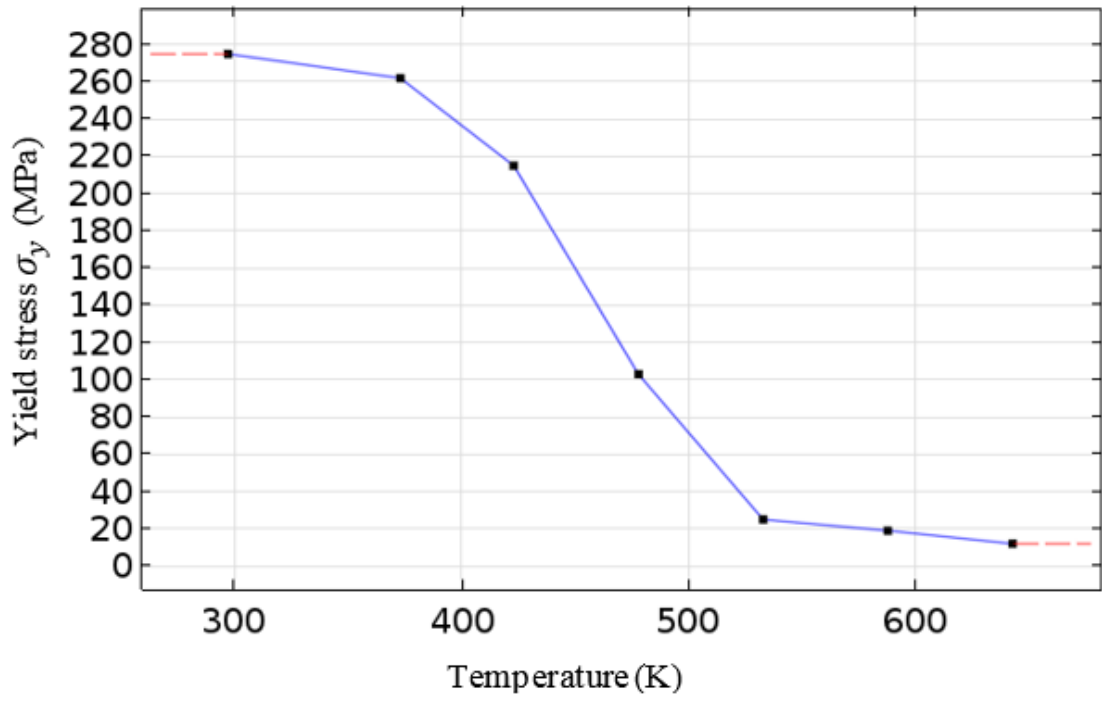


Figure 4-2. Temperature-dependent 0.2% offset yield strength for AA 6061-T6 [97].

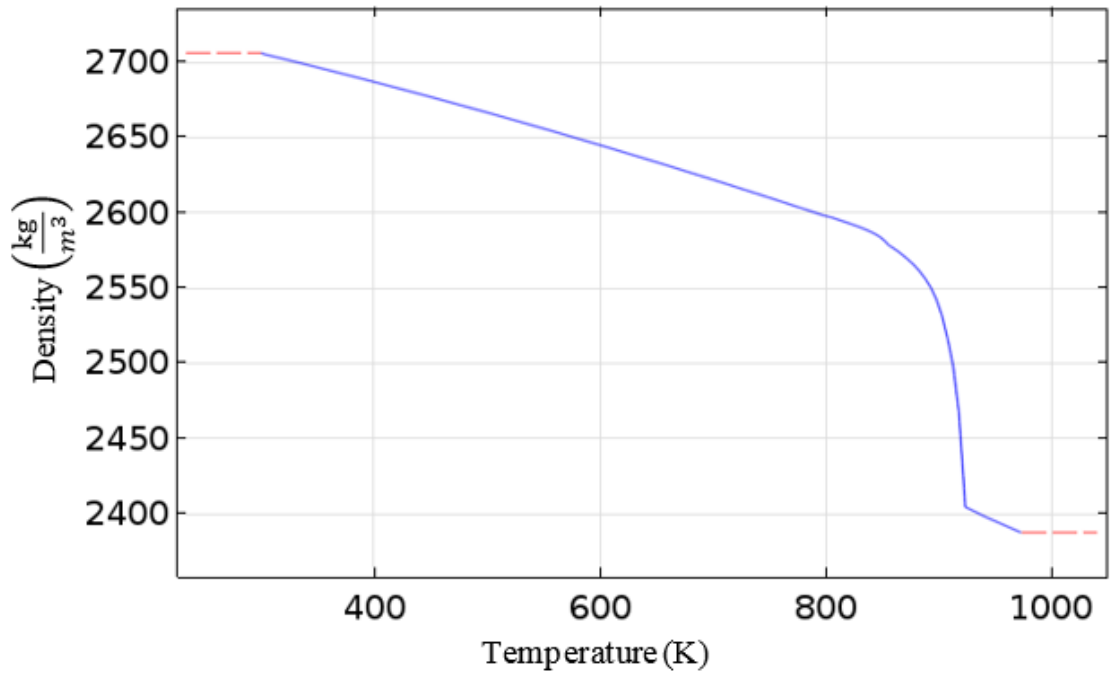


Figure 4-3. Density as a function of temperature.

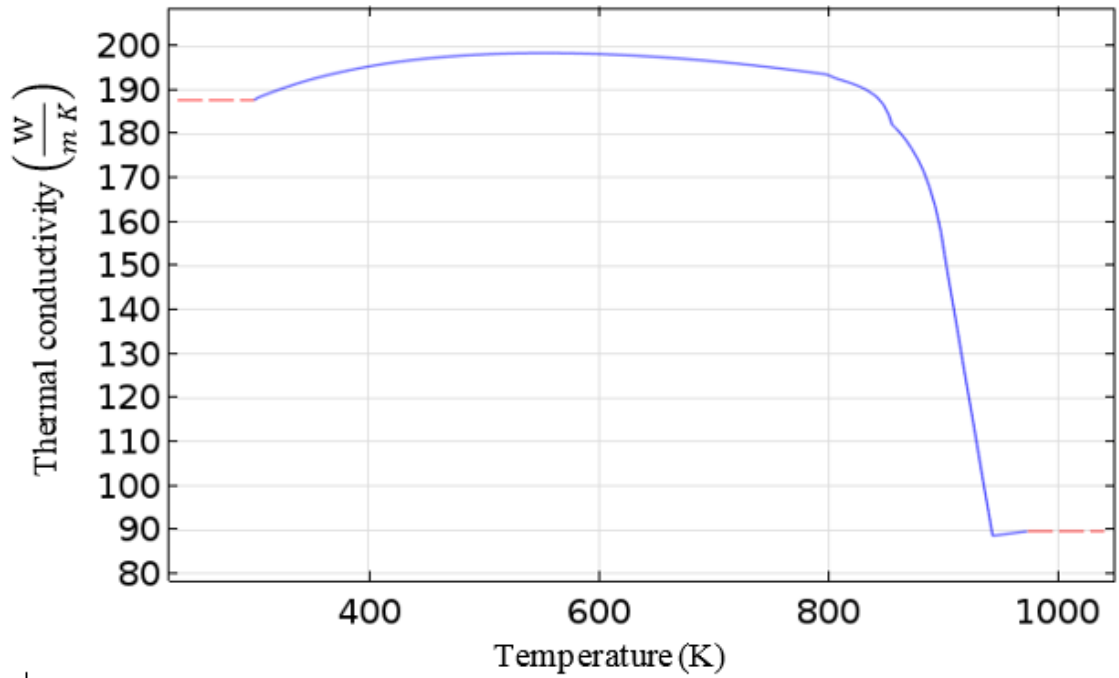


Figure 4-4. Thermal conductivity as a function of temperature.

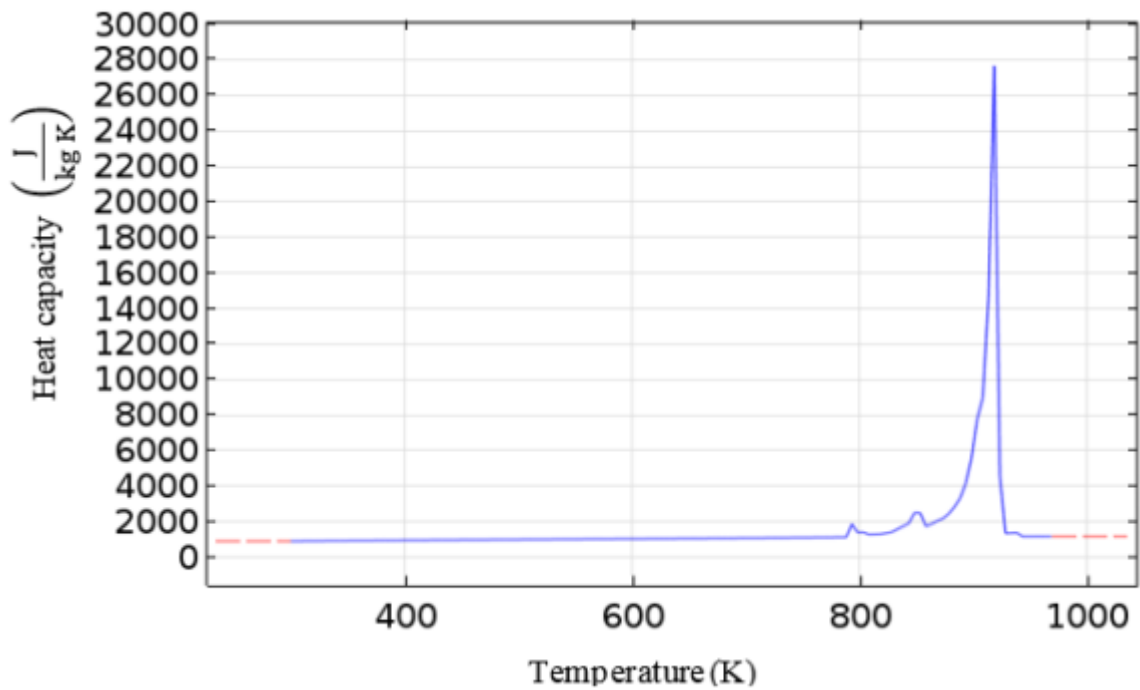


Figure 4-5. Heat capacity as a function of temperature.

## 4.5 Boundary conditions and initial condition

### 1. Convection and radiation boundary conditions

The heat loss from upper plate's surface due convection and radiation, it can be expressed as:

$$k \frac{\delta T}{\delta n} \Big|_{\Gamma} = \varepsilon S_B (T_i^4 - T^4) + h_{up} (T - T_i) \quad (4.6)$$

Convection boundary condition for lower-base metal surface contacts with backup plate can be expressed as:

$$k \frac{\delta T}{\delta n} \Big|_{\Gamma} = h_{down} (T - T_i) \quad (4.7)$$

Where  $k$  is heat conductivity,  $T$  is temperature,  $n$  is a normal direction vector of boundary  $\Gamma$ ,  $S_B$  is The Stefan-Boltzmann constant ( $5.67E - 5 \text{ W/m}^2 \cdot \text{k}^4$ ).  $h_{up}$  and  $h_{down}$  are convection coefficients for lower and upper-base metal surfaces and  $T_i$  is Initial temperature.

In present project,  $h_{up}$  and  $h_{down}$  have different values because there is a contact between lower surface and backup plate. In the present study, it is considered as 12.25 and 6.25  $\text{W/m}^2 \cdot \text{K}$ , respectively. The emissivity ( $\varepsilon$ ) was assumed 0.3.

### 2. Initial condition

The initial condition for the calculation is:

$$T(x, y, z, 0) = T_i \quad (4.8)$$

Where  $T$  is temperature,  $T_i$  is Initial temperature. The  $T_i$  was assumed 300 K.

## Chapter 5 Methodology experimental work

### 5.1 Introduction

FSW experimental trials were carried out according to DOE matrix to validate the numerical modelling results and study the effect of welding parameters and tool design on mechanical properties.

### 5.2 DOE parameters and their levels

Five FSW tool profiles have been selected to create DOE matrix as a shown in Table 5-1, tools dimensions are: shoulder diameter (12mm), probe diameter (6mm) and probe length (6mm).

Welding parameters coded into five levels (Table 5-1). The code of the upper limit welding parameters is 2 and -2 for the lower limit. The intermediate codes are calculated from the following equation:

$$X_i = 2[2X - (X_{\max} + X_{\min})] / (X_{\max} - X_{\min}) \quad (5.1)$$

Where  $X_i$  is the required code value for a variable  $X$ ;  $X$  is any value of the variable from  $X_{\min}$  to  $X_{\max}$ ;  $X_{\min}$  is the lower limit of the variable;  $X_{\max}$  is the upper limit of the variable.

The upper (+1) and lower (-1) values of the factor ranges are the DOE input levels for welding parameters, while the upper limit (2), lower limit (-2) and centre point (0) levels of welding parameters are calculated by equation (5.1).

The axial force was not included in the DOE input levels for welding parameters because its value is determined automatically by FWS machine.

Table 5-1. Levels of welding parameters and tool profiles for DOE matrix.

Variables	Levels				
	-2	-1	0	1	2
<b>N (rpm)</b>	500	725	950	1175	1400
<b>S (mm/min)</b>	150	200	250	200	350
<b>PFN</b>	TR	SQ	Pen	Hex	Oct
<b>Tp</b>	0.4	0.6	0.7	0.8	1

### 5.2.1 Experimental design matrix

DOE uses the RSM in DESIGN EXPERT 10.0.3 software packages to find the mathematical relationship between process variables and the response. CCD is an experimental design which uses in RSM to build a second order model for the response variable without needing to use a complete three level factorial experiment. The developed experimental design matrix in the DOE empirical model was investigated the effect of welding parameters and tool profiles on the peak temperature and tensile strength. The selected experimental design matrix shows in Table 5-2.

A four-factor five-level central composite rotatable matrix design consists 30 sets of experimental points (16 factorial points, 8 axial points, and 6 centre points). So, nine FSW tools were manufactured.

Table 5-2. FSW process variables for DOE matrix.

Run no.	FSW process variables			
	Rotational speed N (r/min)	Welding speed S (mm/min)	PFN	Taper ratio
<b>Factorial points</b>				
1	-1(725)	-1(200)	-1(SQ)	-1(0.6)
2	1(1175)	-1(200)	-1(SQ)	-1(0.6)
3	-1(725)	1(300)	-1(SQ)	-1(0.6)
4	1(1175)	1(300)	-1(SQ)	-1(0.6)
5	-1(725)	-1(200)	1(Hex)	-1(0.6)
6	1(1175)	-1(200)	1(Hex)	-1(0.6)
7	-1(725)	1(300)	1(Hex)	-1(0.6)
8	1(1175)	1(300)	1(Hex)	-1(0.6)
9	-1(725)	-1(200)	-1(SQ)	1(0.8)
10	1(1175)	-1(200)	-1(SQ)	1(0.8)
11	-1(725)	1(300)	-1(SQ)	1(0.8)
12	1(1175)	1(300)	-1(SQ)	1(0.8)
13	-1(725)	-1(200)	1(Hex)	1(0.8)
14	1(1175)	-1(200)	1(Hex)	1(0.8)
15	-1(725)	1(300)	1(Hex)	1(0.8)
16	1(1175)	1(300)	1(Hex)	1(0.8)
<b>Axial points</b>				
17	-2(500)	0(250)	0(Pen)	0(0.7)
18	2(1400)	0(250)	0(Pen)	0(0.7)
19	0(950)	-2(150)	0(Pen)	0(0.7)
20	0(950)	2(350)	0(Pen)	0(0.7)
21	0(950)	0(250)	-2(TR)	0(0.7)
22	0(950)	0(250)	2(OCT)	0(0.7)
23	0(950)	0(250)	0(Pen)	-2(0.4)
24	0(950)	0(250)	0(Pen)	2(1)
<b>Centre points</b>				
25	0(950)	0(250)	0(Pen)	0(0.7)
26	0(950)	0(250)	0(Pen)	0(0.7)
27	0(950)	0(250)	0(Pen)	0(0.7)
28	0(950)	0(250)	0(Pen)	0(0.7)
29	0(950)	0(250)	0(Pen)	0(0.7)
30	0(950)	0(250)	0(Pen)	0(0.7)

### 5.3 Materials selection

#### 5.3.1 Plate material

AA6061-T6 aluminium alloy was selected for DOE experiential trials. The chemical composition and mechanical properties for this alloy are shown in Table 5-3 and Table 5-4 respectively.

Table 5-3. Chemical composition (wt%) of AA6061-T6 aluminium alloy.

	<b>Si</b>	<b>Fe</b>	<b>Cu</b>	<b>Mn</b>	<b>Mg</b>	<b>Cr</b>	<b>Zn</b>	<b>Ti</b>	<b>Al</b>
Specification (weight %) [97]	0.4-0.8	0.7	0.15-0.4	0.15	0.8-1.2	0.04-0.35	0.25	0.15	Bal.
Actual (weight %)	0.63	0.31	0.2	0.06	1	0.06	0.1	0.08	Bal.

Table 5-4. Mechanical properties of AA6061-T6 aluminium alloy.

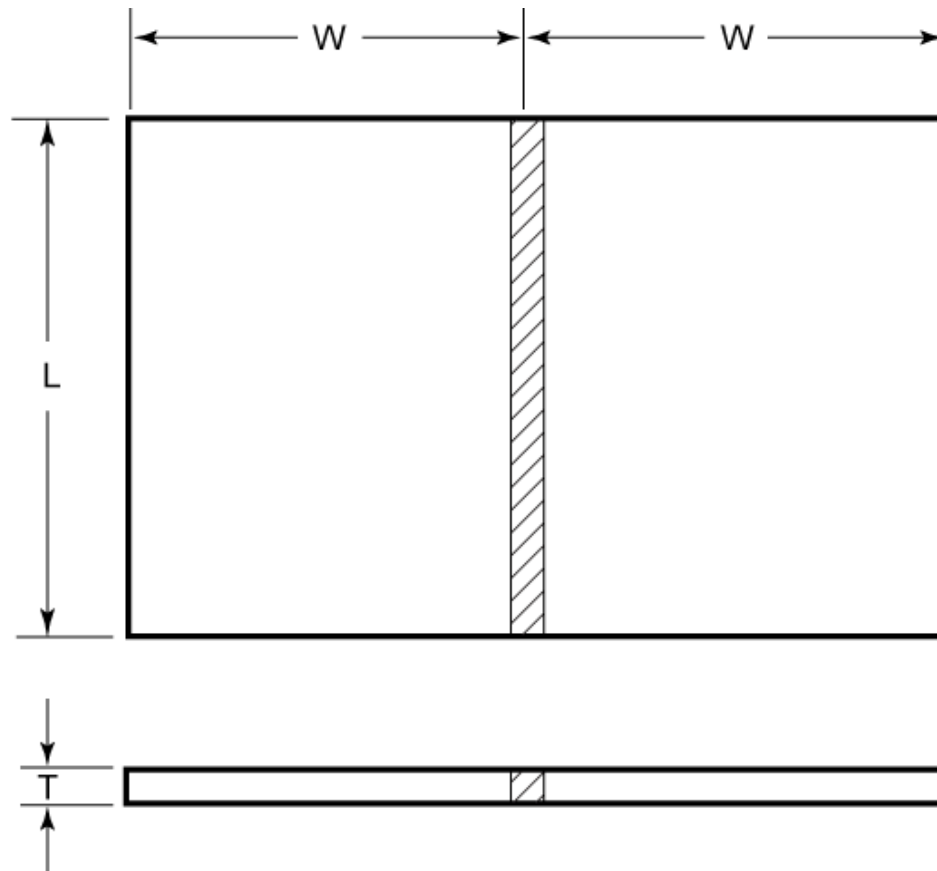
	<b>Tensile strength</b> N/mm <sup>2</sup>	<b>Yield strength</b> N/mm <sup>2</sup>	<b>Elongation</b> %
Specification [97]	310	275	12
Actual	320	294	13.8

#### 5.3.2 Tools Material

H13 tool steel was used to manufacture FSW tools by using computer numerical control machine (CNC) at the University of Leicester workshops and then heat treated to obtain hardness more than 42 HRC.

#### 5.4 FSW joints fabrication

Square groove butt joints from AA6061-T6 aluminium alloy rolled plate (320mm 102mm x 6.35mm) were welded at the TWI Ltd. The dimensions of welding joint shown in Figure 5-1 were selected according to the AWS (D17.3/D17.3:2016) specification for friction stir welding of aluminium alloys for aerospace applications [98].



Base Metal Thickness	Minimum Dimension in [mm]	
	W	L
All	4 [102]	12 [305]

Figure 5-1. Square groove welding joint [98].

## 5.5 Tools manufacturing

### 5.5.1 DOE tools

Friction stir welding tools manufactured from annealed H13 tool steel by using CNC machine, and then hardening to improve the mechanical properties. The required numbers of each part listed at Table 5-5. Figures ((5-2)-(5-11)) show the dimensions for each part.

Table 5-5. The required parts.

parts		Numbers of each part
PFN	TP	
TR	0.7	2
SQ	0.6	4
SQ	0.8	4
Pen	0.4	1
Pen	0.7	4
Pen	1	1
Hex	0.6	4
Hex	0.8	4
Oct	0.7	1
Holder		6

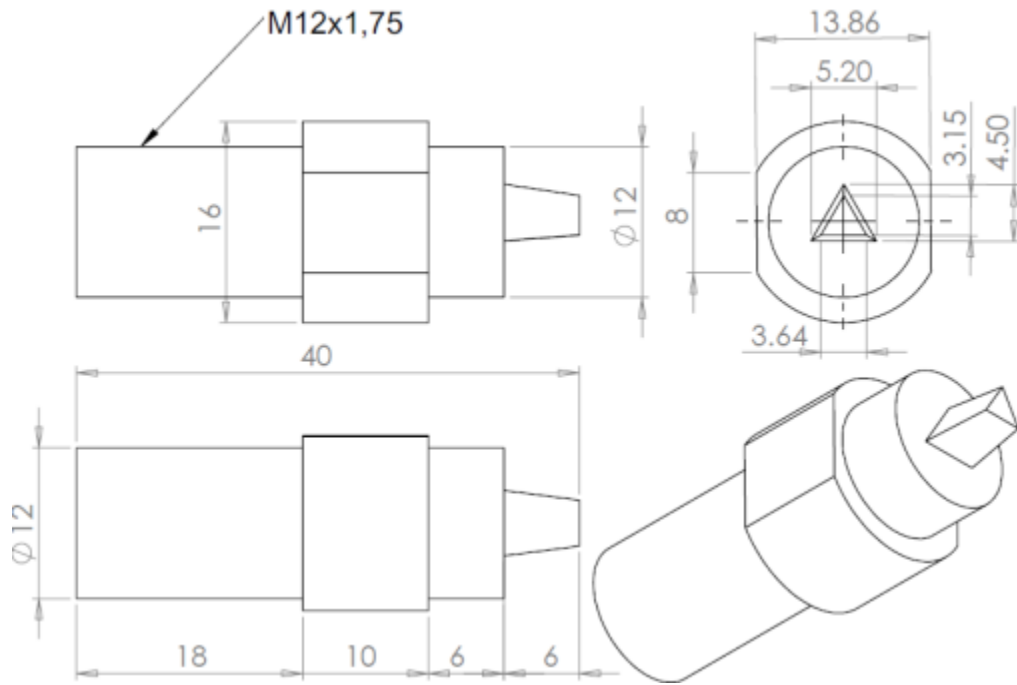


Figure 5-2. Triangular tool 0.7 taper ratio.

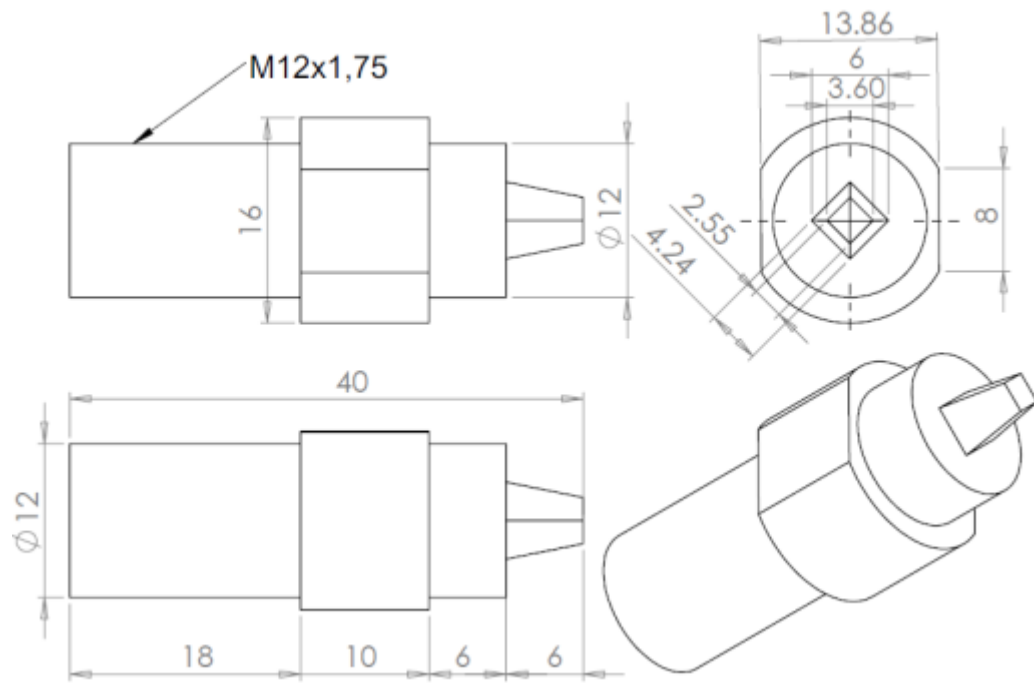


Figure 5-3. Square tool 0.6 taper ratio.

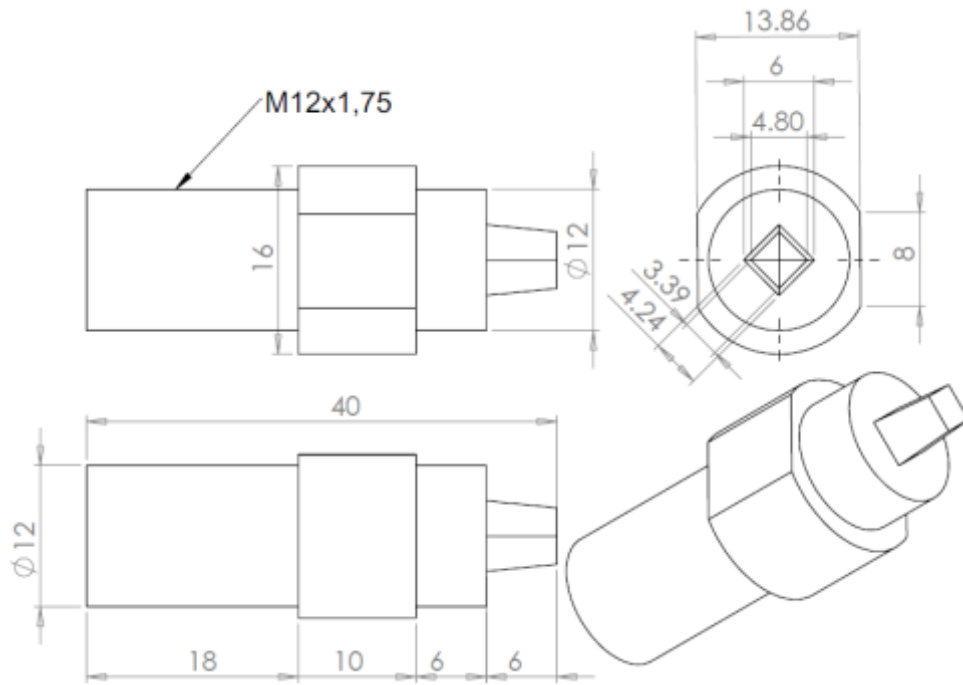


Figure 5-4. Square tool 0.8 taper ratio.

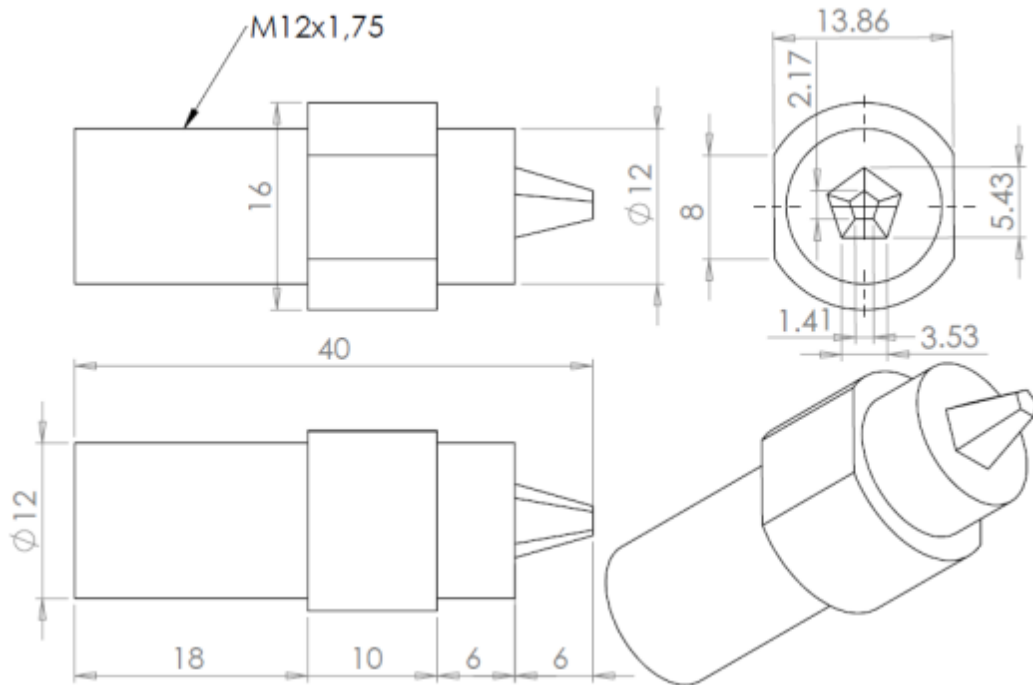


Figure 5-5. Pentagonal tool 0.4 taper ratio.

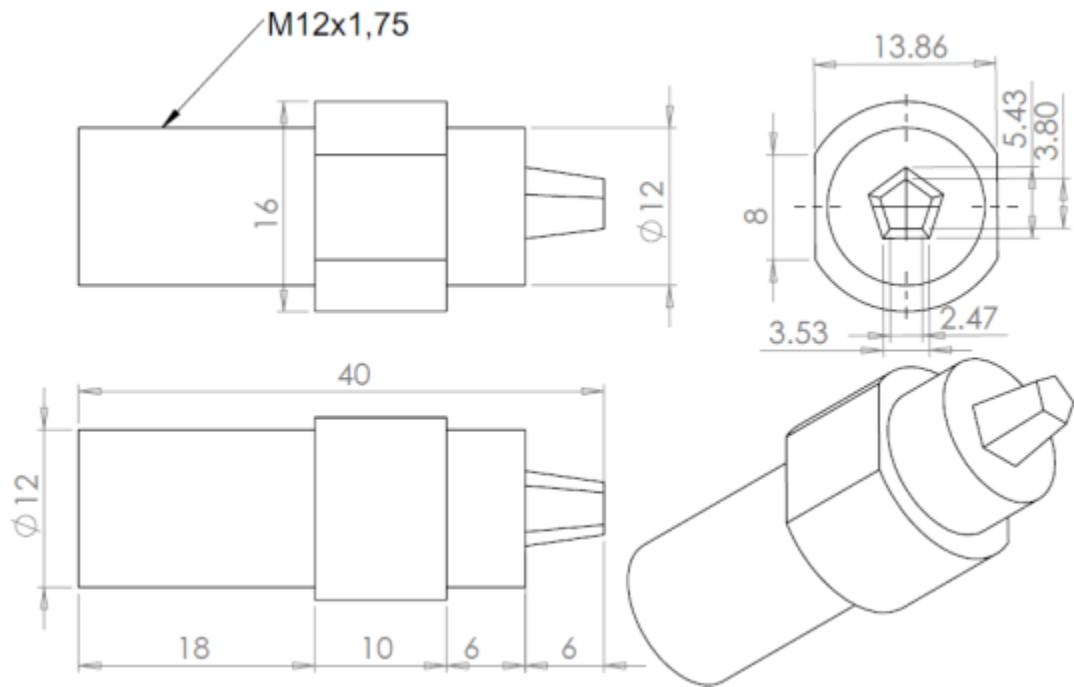


Figure 5-6. Pentagonal tool 0.7 taper ratio.

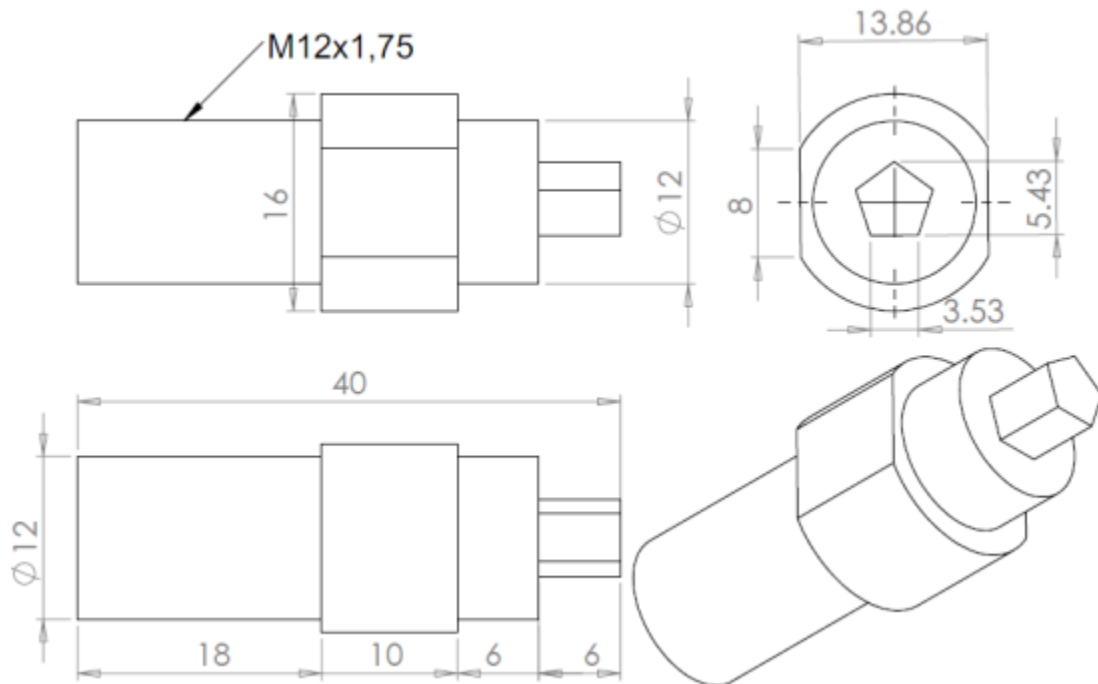


Figure 5-7. Straight pentagonal tool.

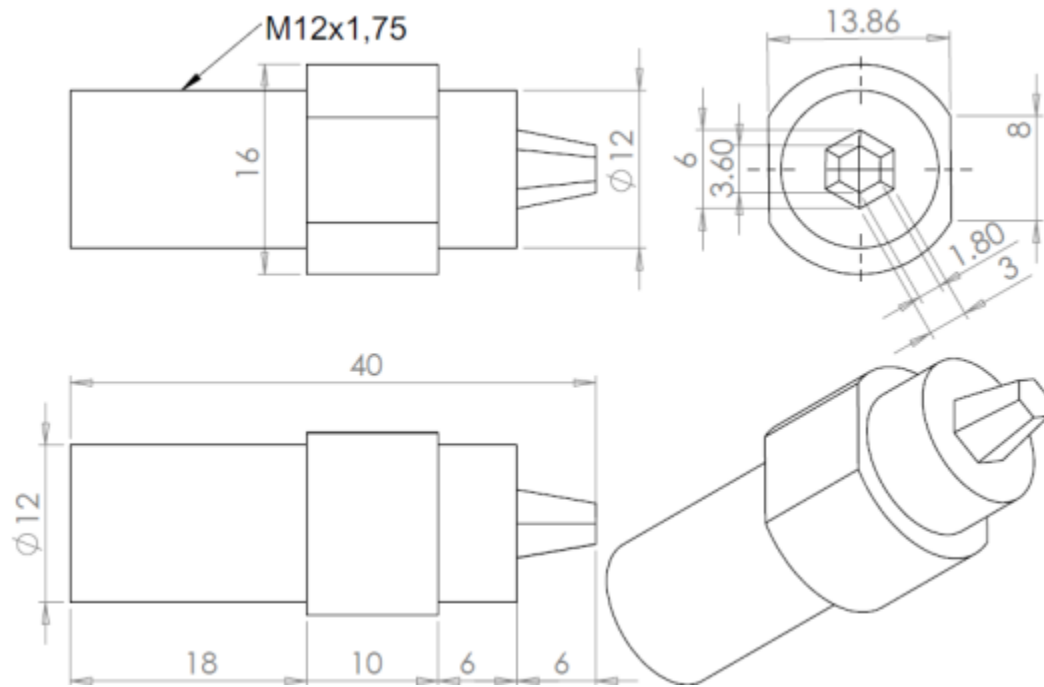


Figure 5-8. Hexagonal tool 0.6 taper ratio.

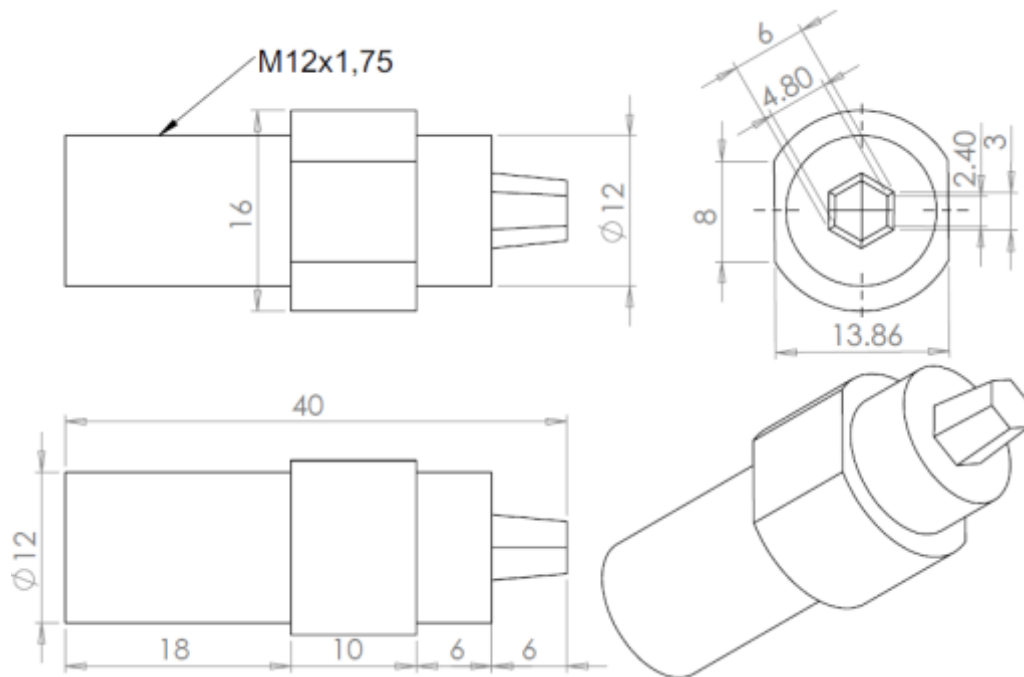


Figure 5-9. Hexagonal tool 0.8 taper ratio.

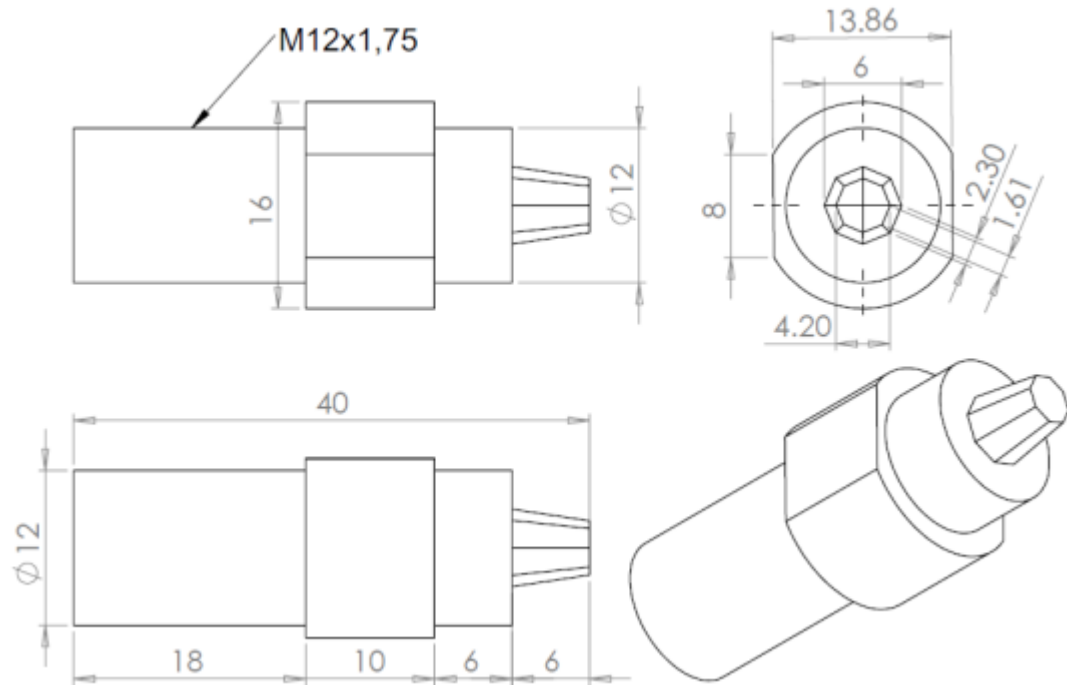


Figure 5-10. Octagonal tool 0.7 taper ratio.

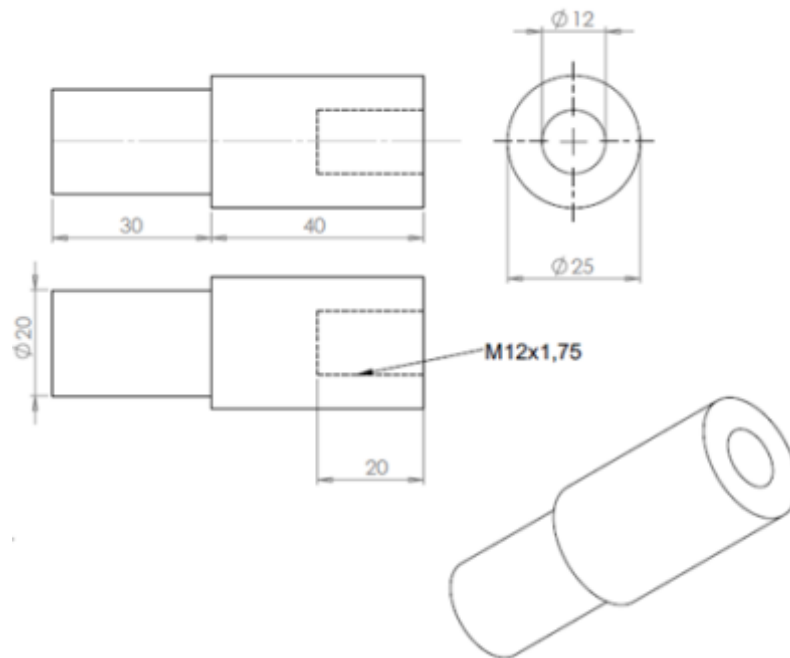


Figure 5-11. Tool holder.

### 5.5.2 DOE validation tools

According to DOE model result, extra straight tools (square tool (SSQ), Hexagonal (SHex), and Octagonal (SOct)) manufactured to validate the adequacy of the DOE model. Figures ((5-12)-(5-14)) show the dimensions for each part while Figure 5-15 shows the assembly of parts to produce the various Tools.

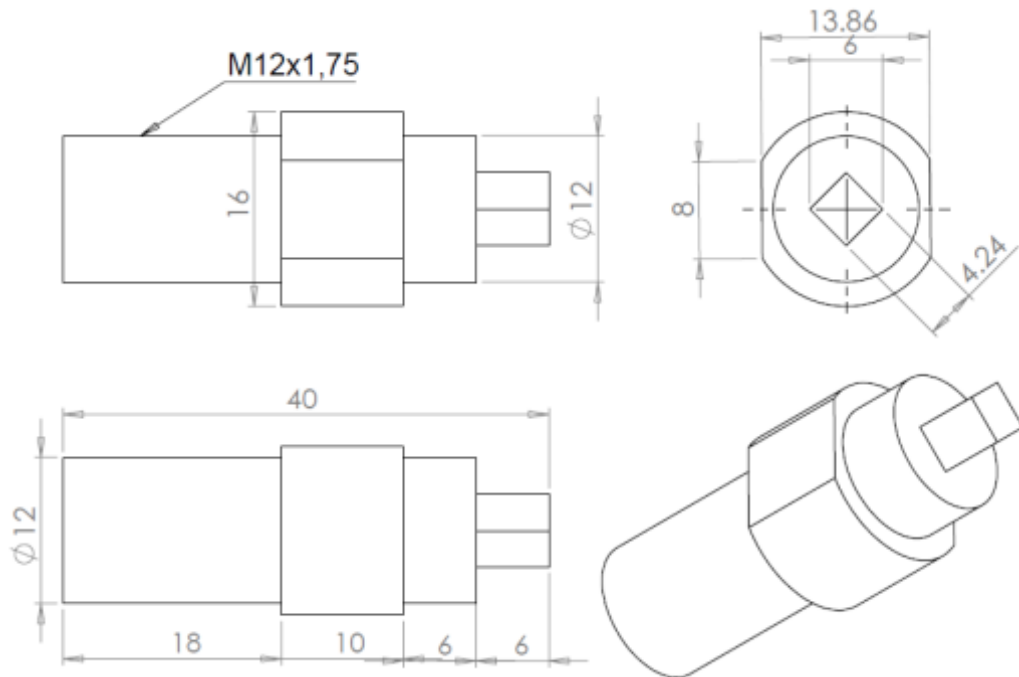


Figure 5-12. Straight square tool.

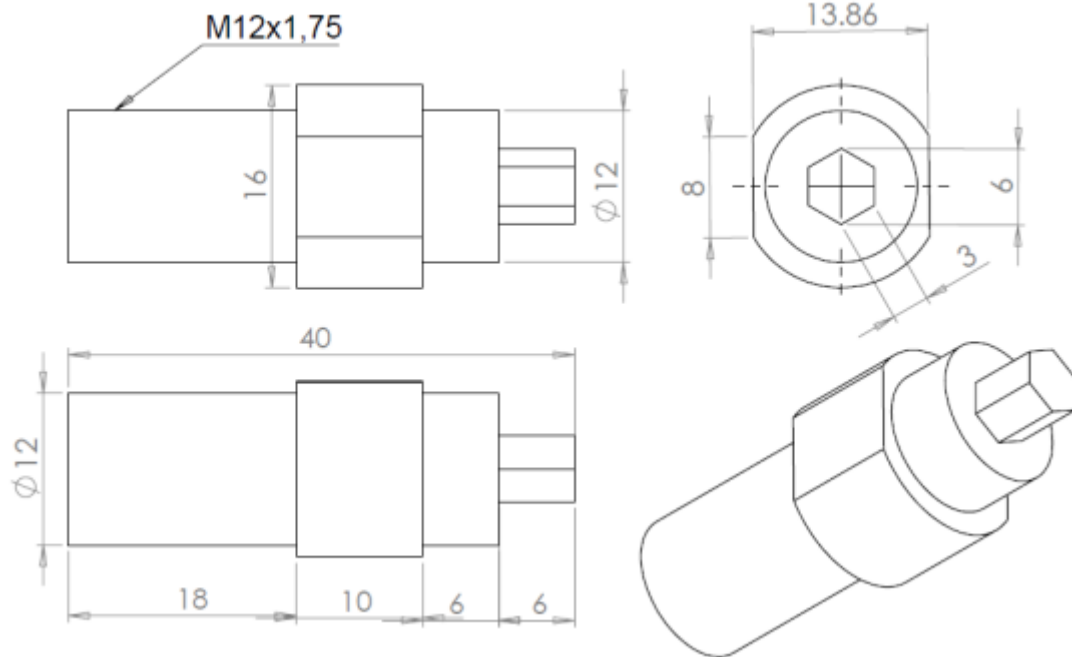


Figure 5-13. Straight hexagonal tool.

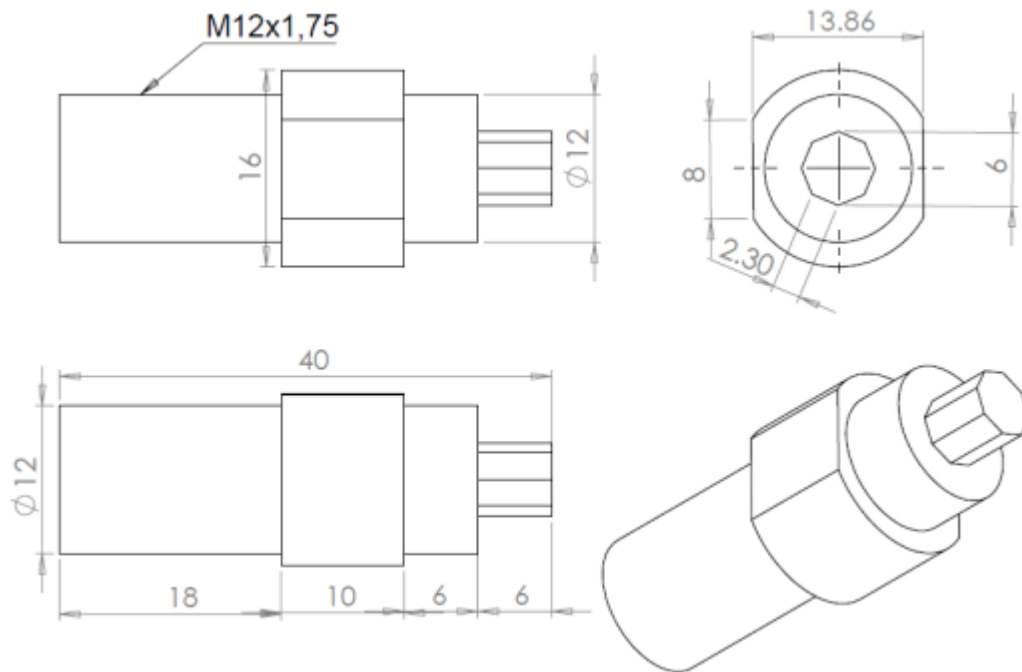


Figure 5-14. Straight octagonal tool.

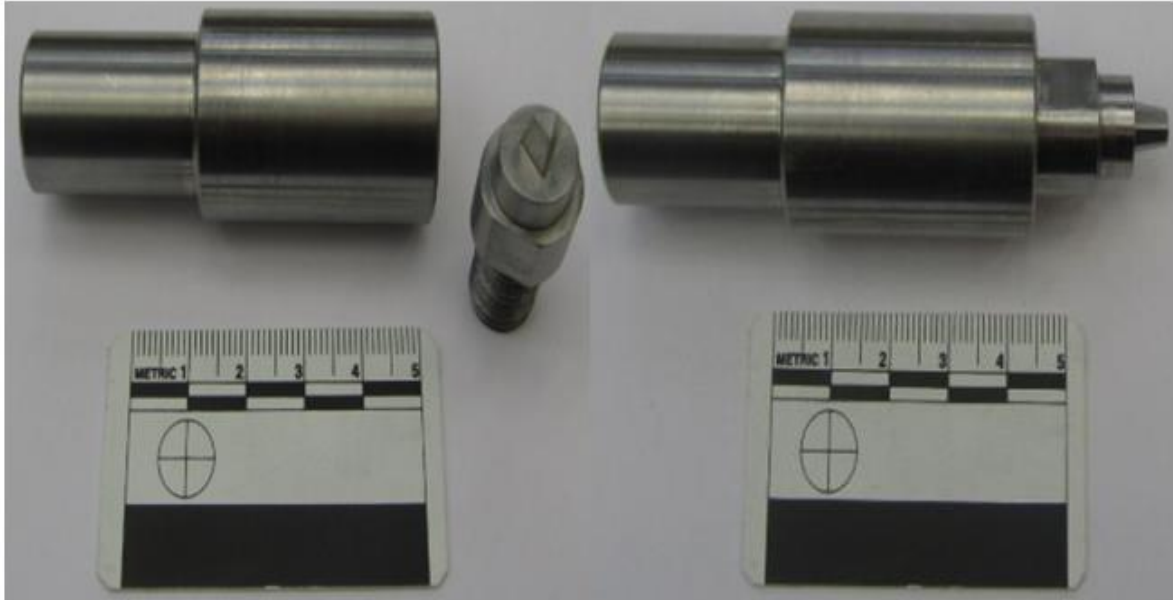


Figure 5-15. The assembly tool and its parts.

### 5.5.3 FSW tools heat treatment

FSW tools manufactured from H13 steel in the annealed condition. Three heat treatments were done to improve the tools mechanical properties. Stress relieving is important to reduce internal stress which generates during manufacturing steps. Hardening process is used to increase the hardness value while tempering is carried out to improve the toughness value by reducing the internal stress which generates during hardening process.

#### 5.5.3.1 Stress Relieving

The stress relieving was done after manufacturing the tools to reduce the possibility of distortion. So, all parts heated to 700°C, and then soaked at this temperature (soaking time calculates according to the dimension of each part (two hours per 25mm of ruling section)) and then cooled in the furnace [99].

### **5.5.3.2 Hardening**

FSW tools were preheated to 780°C, soaked around thirty minutes and the steel were heated to the hardening temperature 1030°C followed by holding for thirty minutes. The tools were then oil quenched [99].

### **5.5.3.3 Tempering**

All parts were heated to 500°C, soaked around two hours and then cooled in air. Second tempering was done to obtain Vickers hardness of 42 [99].

## **5.6 Experiential work**

The experimental work including measured the thermal profile to validate the COMSOL modelling results and studied the effect of welding parameters and tool design on the peak temperature and mechanical properties.

### **5.6.1 Temperature measurement**

The thermal profile was measured by thermocouples during FSW for DOE joints to validate COMSOL model results.

To measure the temperature profile at specific points 5mm from welding line, six K-type thermocouples 1 mm diameter were embedded on the advancing and retreating side in the mid thickness of the plates (Figure 5-16). The experimental set up for temperature measurement is shown in Figure 5-17.

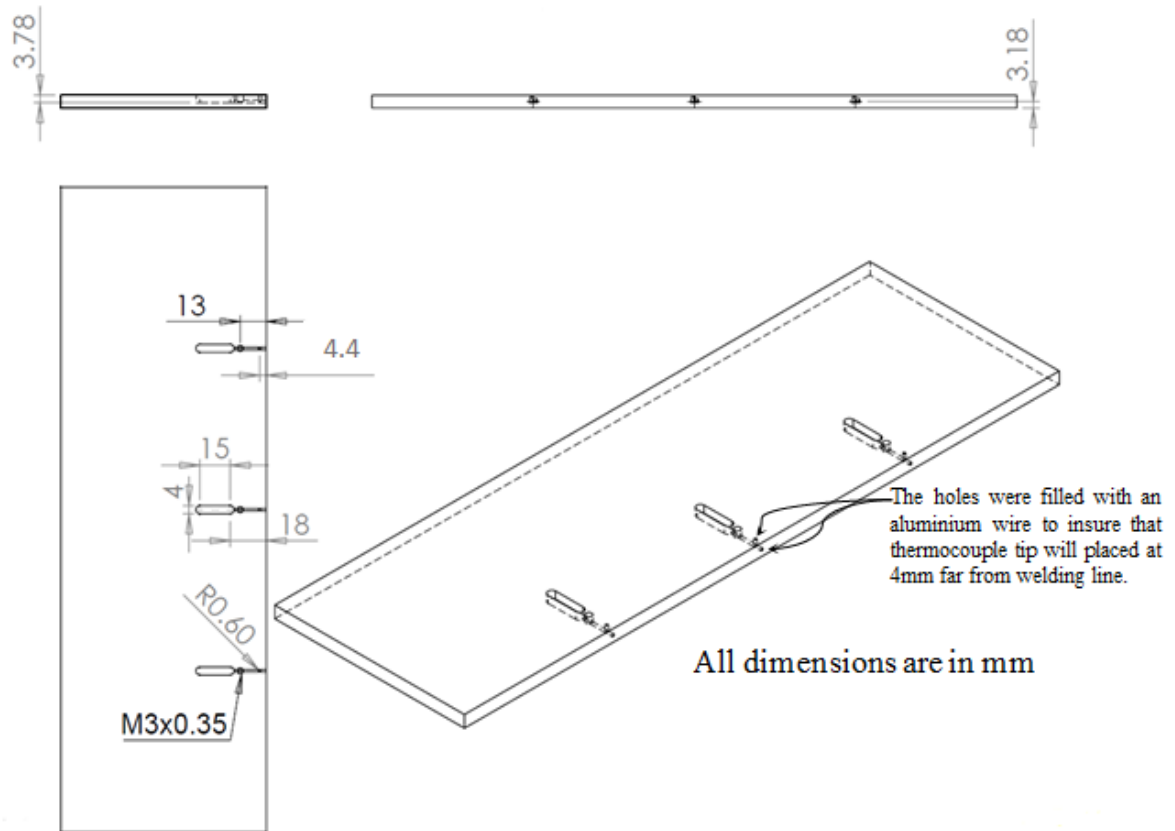


Figure 5-16. Thermocouple locations.

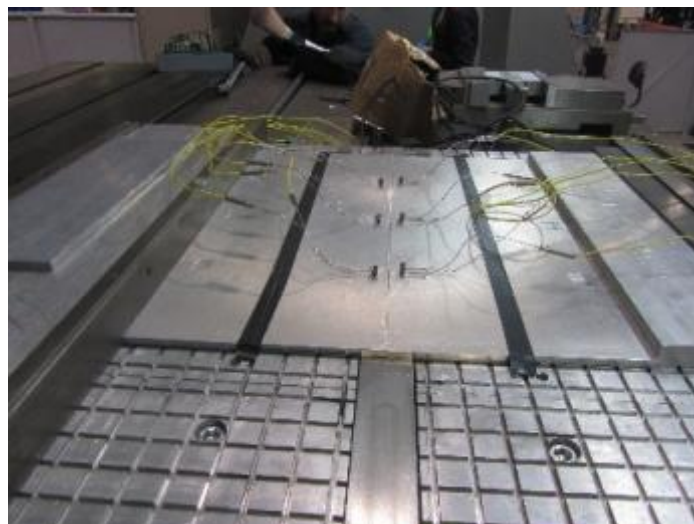


Figure 5-17. Experimental set up for temperature measurements.

## 5.7 Welding quality

### 5.7.1 X-ray radiography

Two dimensions image was taken to each welding joint by using computed tomography (CT) to check any possible defects in the welding joints.

### 5.7.2 Macroscopic and Microscopic Evaluation

Macroscopic and microscopic samples were cut from the welding joints as a shown in Figure 5-18. Macroscopic samples were examined on the cross-sectional face.

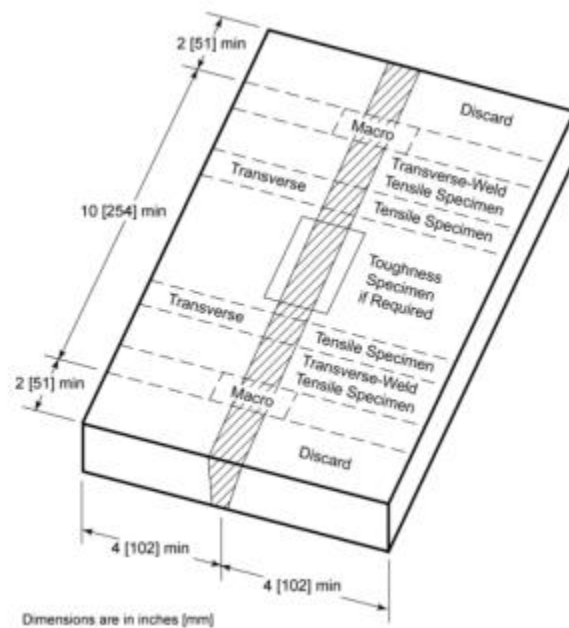


Figure 5-18. Location of the weld test specimens [98].

Samples were cut using the automatic cutting machine with 0.015 mm feed rate and using cooling liquid to prevent heat effect which generate during cutting and then the samples were prepared for macro and microstructure test by grinding and polishing. The microstructure samples were etched by using Keller's [100] while NaOH H<sub>2</sub>O [101] used for macroscopic examination.

### 5.7.3 Microhardness test

Microhardness test was undertaken using a Buehler 1600-6100 microhardness tester. Figure 5-19 shows the measuring positions. 100 gf was applied for 10 seconds.

Vickers hardness is calculated by following formula:

$$HV = 1.854 \times 10^3 \times F/d^2$$

Where F = loading force, 100 gf, d = mean value of the two diagonals of the indentation ( $\mu\text{m}$ )

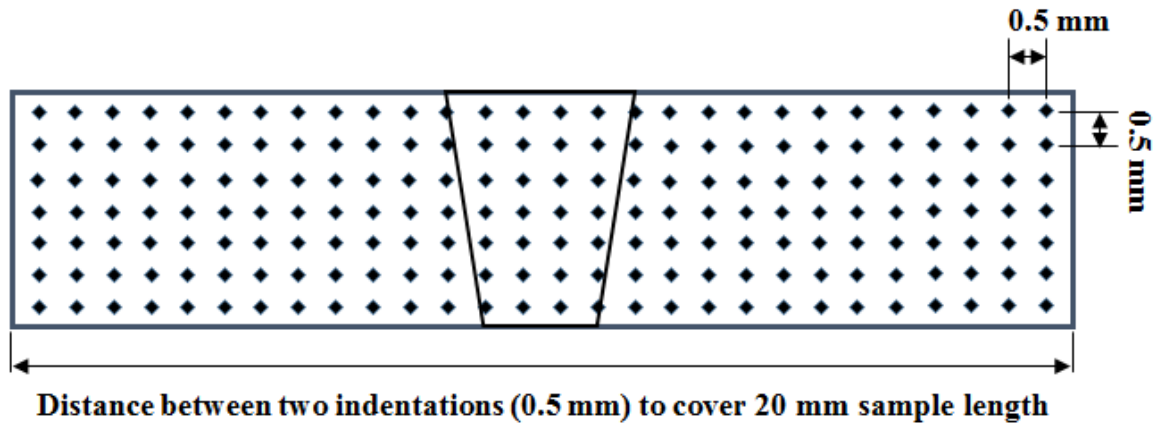


Figure 5-19. Positions of microhardness test indentations.

### 5.7.4 Tensile test

Transverse welding samples were used to measure the tensile strength for DOE joints and DOE validation joints while welding metal samples were used to measure the tensile strength for DOE validation joints.

### 5.7.5 Transverse and welding zone tensile test

Three transverse welding samples (Figure 5-20) and three welding zone samples (Figure 5-21) specimens were manufactured according to the American Society for Testing of Materials standards [102]. The testing was carried out according to the same standard at a rate 5 mm/min.

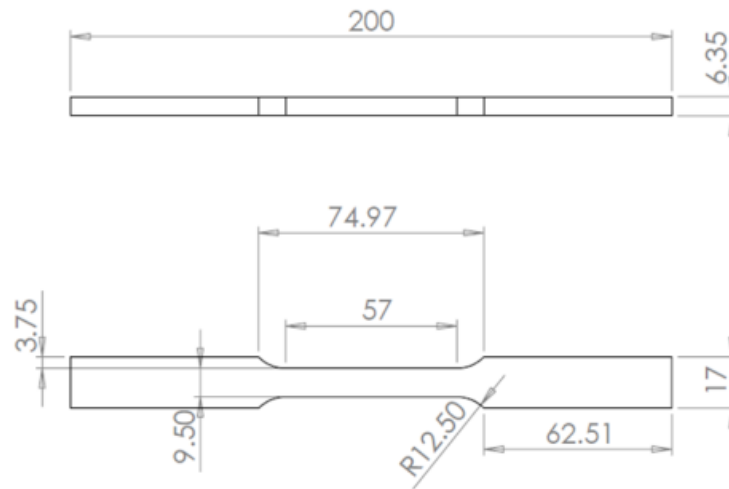


Figure 5-20. Dimensions of transverse welding tensile specimen [102].

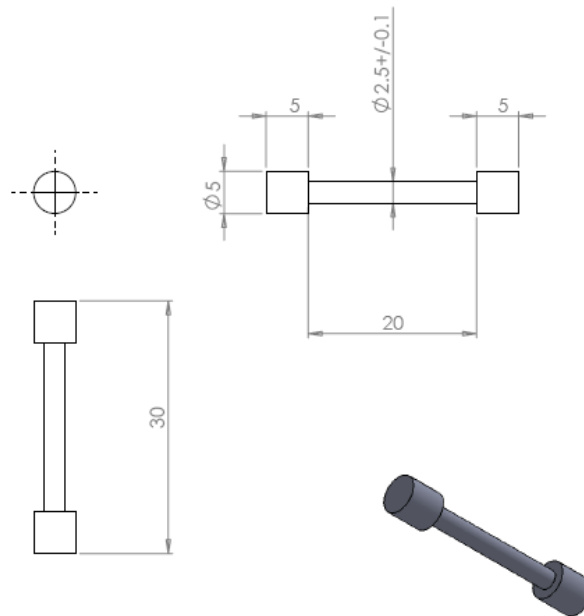


Figure 5-21. Dimensions of a welding zone tensile specimen [102].

# Chapter 6 : Effect of welding parameters and tool profile on axial force

## 6.1 Introduction

Axial force ( $AF$ ) is the essential parameter to calculate heat generation for shoulder interface. Although, it is automatically applied by FWS machine, its value changes according to welding parameters ( $N$  and  $S$ ) and tool profile ( $PFN$  and  $Tp$ ). The axial force value can be predicted as a function to tool profile and welding parameters.

## 6.2 Axial force DOE matrix

The average of axial force during weld period (which calculated from the output machine data for each trial (DOE run)) was considered as an axial force for FSW cycle. Design matrix for AF is shown in Table 6-1. It is a four-factor five-level central composite rotatable design consisting 30 sets of coded conditions composed of a full factorial  $2^4 = 16$ , plus 6 center points and 8 star points.

### 6.2.1 Data driven model for axial force

Axial force is a function of rotational speed, welding speed, tool profile and taper ratio. It can be expressed as:

$$AF = (N, S, PFN, Tp) \quad (6.1)$$

Where  $AF$  is axial force (kN);  $N$  is rotational speed (rpm);  $S$  is welding speed, (mm/min);  $PFN$  is the polygon probe flats number;  $Tp$  is taper ratio.

Table 6-1. Design matrix for experimental value and predicted value of axial force.

Run no.	FSW process variables				AF (kN)	
	<i>N</i> (rpm)	<i>S</i> (mm/min)	<i>PFN</i>	<i>Tp</i>	Experimental value	Predicted value
<b>Factorial points</b>						
1	-1(725)	-1(200)	-1(SQ)	-1(0.6)	7	6.98
2	1(1175)	-1(200)	-1(SQ)	-1(0.6)	5.2	5.14
3	-1(725)	1(300)	-1(SQ)	-1(0.6)	7.34	7.32
4	1(1175)	1(300)	-1(SQ)	-1(0.6)	5.45	5.47
5	-1(725)	-1(200)	1(Hex)	-1(0.6)	7.37	7.38
6	1(1175)	-1(200)	1(Hex)	-1(0.6)	5.56	5.56
7	-1(725)	1(300)	1(Hex)	-1(0.6)	7.63	7.64
8	1(1175)	1(300)	1(Hex)	-1(0.6)	5.85	5.81
9	-1(725)	-1(200)	-1(SQ)	1(0.8)	7.1	7.13
10	1(1175)	-1(200)	-1(SQ)	1(0.8)	5.4	5.39
11	-1(725)	1(300)	-1(SQ)	1(0.8)	7.58	7.58
12	1(1175)	1(300)	-1(SQ)	1(0.8)	5.85	5.83
13	-1(725)	-1(200)	1(Hex)	1(0.8)	7.65	7.63
14	1(1175)	-1(200)	1(Hex)	1(0.8)	5.9	5.91
15	-1(725)	1(300)	1(Hex)	1(0.8)	7.95	8.01
16	1(1175)	1(300)	1(Hex)	1(0.8)	6.25	6.28
<b>Axial points</b>						
17	-2(500)	0(250)	0(Pen)	0(0.7)	8.95	8.91
18	2(1400)	0(250)	0(Pen)	0(0.7)	5.32	5.34
19	0(950)	-2(150)	0(Pen)	0(0.7)	6.03	6.04
20	0(950)	2(350)	0(Pen)	0(0.7)	6.78	6.74
21	0(950)	0(250)	-2(TR)	0(0.7)	5.97	6
22	0(950)	0(250)	2(OCT)	0(0.7)	6.9	6.85
23	0(950)	0(250)	0(Pen)	-2(0.4)	6	6.03
24	0(950)	0(250)	0(Pen)	2(1)	6.7	6.64
<b>Centre points</b>						
25	0(950)	0(250)	0(Pen)	0(0.7)	6.22	6.24
26	0(950)	0(250)	0(Pen)	0(0.7)	6.26	6.24
27	0(950)	0(250)	0(Pen)	0(0.7)	6.27	6.24
28	0(950)	0(250)	0(Pen)	0(0.7)	6.22	6.24
29	0(950)	0(250)	0(Pen)	0(0.7)	6.26	6.24
30	0(950)	0(250)	0(Pen)	0(0.7)	6.24	6.24

For the four factors, the selected polynomial could be expressed as:

$$AF = b_0 + b_1 * N + b_2 * S + b_3 * PFN + b_4 * Tp + b_{11} * N^2 + b_{22} * S^2 + b_{33} * PFN^2 + b_{44} * Tp^2 + b_{12} * N * S + b_{13} * N * PFN + b_{14} * N * Tp + b_{23} * S * PFN + b_{24} * S * Tp + b_{34} * PFN * Tp \quad (6.2)$$

Where  $b_0$  is the free term of the regression equation; the coefficients  $b_1, b_2, b_3$  and  $b_4$  are linear terms; the coefficients  $b_{11}, b_{22}, b_{33}$  and  $b_{44}$  are quadratic terms; the coefficients,  $b_{12}, b_{13}, b_{14}, b_{23}, b_{24}$ , and  $b_{34}$ , are interaction terms.

DESIGN EXPERT 10.0.3 software packages were used to calculate the values of these coefficients for different responses and the results are presented in Table 6-2. The final mathematical equation is:

$$AF = 13.94 - 0.01 * N - 3.819E - 3 * S + 0.29 * PFN - 0.09 * Tp - 2.22E - 7 * N * S + 2.22E - 5 * N * PFN + 1.11E - 4 * N * Tp - 4E - 4 * S * PFN + 5.5E - 4 * S * Tp + 0.025 * PFN * Tp + 4.35E - 6 * N^2 + 1.51E - 5 * S^2 + 0.05 * PFN^2 + 0.02 * Tp^2 \quad (6.3)$$

Table 6-2. Calculated regression coefficients of axial force mathematical model.

Factor	Calculated coefficient
	+13.94
N	-0.01
S	-3.81E-3
PFN	+0.29
Tp	-0.09
N*S	-2.22E-7
N*PFN	+2.22E-5
N*Tp	+1.11E-4
S*PFN	-4E-4
S*Tp	+5.5E-4
PFN*Tp	+0.025
N <sup>2</sup>	+4.35E-6
S <sup>2</sup>	+1.51E-5
PFN <sup>2</sup>	+0.05
Tp <sup>2</sup>	+0.02

### 6.2.2 Adequacy of DOE model for AF

The adequacy of the model developed was then tested by using the analysis of variance technique (ANOVA). The results of the ANOVA are given in Table 6-3. The Model F-value of 956.87 implies the model is significant. There is only a 0.01% chance that an F-value could occur due to noise. The P-value less than 0.05 indicate that model terms are significant. In this case, linear, quadratic and some of interaction terms (N\*Tp, S\*Tp and PFN\*Tp) are significant model terms. Values greater than 0.1 indicate the model terms are not significant, so interaction terms for N\*S and N\*PFN are not significant. The lack of fit F-value of 4.95 implies that the lack of fit is significant. There is 4.57% chance that a lack of fit F-value.

The determined values of the developed model are presented in Table 6-4. The  $R^2$  value is always between 0 and 1, and its value indicates the accuracy of the model. For a good model,  $R^2$  value should be close to 1. In this model, the calculated  $R^2$  is 0.9989. This implies that 99.89% of experimental data confirms the compatibility with the data predicted by the developed model. The value of the adjusted  $R^2$  of 0.9978 is also high to adhere for a high significance of the model. The predicted  $R^2$  of 0.994 is in reasonable agreement with the adjusted  $R^2$  of 0.9978. Adequate precision measures the signal-to-noise ratio. A ratio greater than 4 is desirable. In this study, the ratio is 128.923, which indicates an adequate signal. This model can be used to navigate the design space. The normal probability plot for the axial force shown in Figure 6-1 reveals that the residuals are scattered close to straight line, which means the errors are distributed normally. A typical scatter diagram of the model is presented in Figure 6-2. The observed values and predicted values of the responses are falling on the 45° line, indicating an almost perfect fit of the developed empirical models.

Table 6-3. Axial force ANOVA tests results.

Source	Sum of squares	Degree of freedom	Mean square	F value	p-value	Result
					Prob > F	
<b>Model</b>	<b>22.89</b>	<b>14</b>	<b>1.63</b>	<b>956.87</b>	<b>&lt; 0.0001</b>	<b>significant</b>
<i>N</i>	<i>19.12</i>	<i>1</i>	<i>19.12</i>	<i>11190.64</i>	<i>&lt; 0.0001</i>	
<i>S</i>	<i>0.74</i>	<i>1</i>	<i>0.74</i>	<i>434.35</i>	<i>&lt; 0.0001</i>	
<i>PFN</i>	<i>1.08</i>	<i>1</i>	<i>1.08</i>	<i>634.39</i>	<i>&lt; 0.0001</i>	
<i>Tp</i>	<i>0.56</i>	<i>1</i>	<i>0.56</i>	<i>330.30</i>	<i>&lt; 0.0001</i>	
<i>N*S</i>	<i>1.000E-004</i>	<i>1</i>	<i>1.000E-004</i>	<i>0.059</i>	<i>0.8121</i>	
<i>N*PFN</i>	<i>4.000E-004</i>	<i>1</i>	<i>4.000E-004</i>	<i>0.23</i>	<i>0.6355</i>	
<i>N*Tp</i>	<i>1.000E-002</i>	<i>1</i>	<i>1.000E-002</i>	<i>5.85</i>	<i>0.0287</i>	
<i>S*PFN</i>	<i>6.400E-003</i>	<i>1</i>	<i>6.400E-003</i>	<i>3.75</i>	<i>0.0720</i>	
<i>S*Tp</i>	<i>0.012</i>	<i>1</i>	<i>0.012</i>	<i>7.08</i>	<i>0.0178</i>	
<i>PFN*Tp</i>	<i>1.000E-002</i>	<i>1</i>	<i>1.000E-002</i>	<i>5.85</i>	<i>0.0287</i>	
<i>N<sup>2</sup></i>	<i>1.33</i>	<i>1</i>	<i>1.33</i>	<i>778.57</i>	<i>&lt; 0.0001</i>	
<i>S<sup>2</sup></i>	<i>0.039</i>	<i>1</i>	<i>0.039</i>	<i>22.83</i>	<i>0.0002</i>	
<i>PFN<sup>2</sup></i>	<i>0.056</i>	<i>1</i>	<i>0.056</i>	<i>32.81</i>	<i>&lt; 0.0001</i>	
<i>Tp<sup>2</sup></i>	<i>0.016</i>	<i>1</i>	<i>0.016</i>	<i>9.22</i>	<i>0.0083</i>	
<b>Residual</b>	<b>0.026</b>	<b>15</b>	<b>1.63</b>			
<i>Lack of Fit</i>	<i>0.023</i>	<i>10</i>	<i>1.708E-003</i>	<i>4.95</i>	<i>0.0457</i>	<b>significant</b>
<i>Pure Error</i>	<i>2.350E-003</i>	<i>5</i>	<i>2.328E-003</i>			
<b>Cor Total</b>	<b>22.91</b>	<b>29</b>	<b>4.700E-004</b>			

Table 6-4. Coefficient of determination values for axial force model.

R-Squared	Adj R-Squared	Pred R-Squared	Adeq Precision
<b>0.9989</b>	<b>0.9978</b>	<b>0.994</b>	<b>128.923</b>

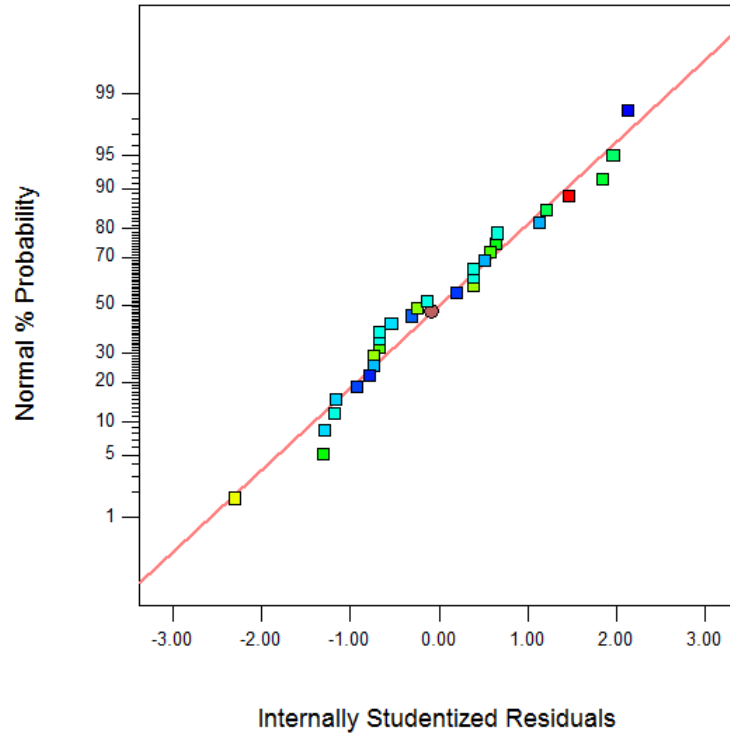


Figure 6-1. Axial force normal probability plot.

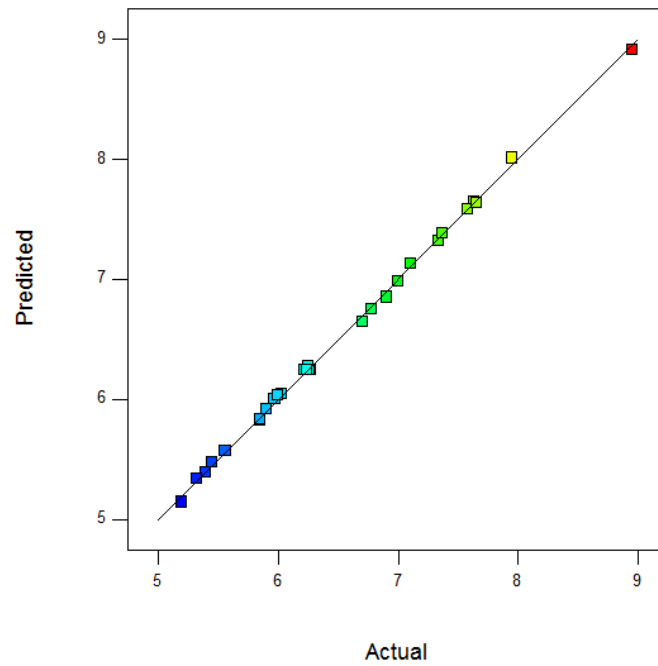


Figure 6-2. Scatter diagram of axial force (KN).

### 6.2.3 Effect of welding parameters and tool profile on axial force

The effects of process parameters and welding tool profiles on axial force were predicted by the data driven model presented in Figures ((6.3)–(6.6)), showing the general trends between cause and effect. From Figure 6-3 and Figure 6-4, it can be seen that the AF decreases when the S decreases and N increases as a result of increasing heat input. The AF increases about 66.84% when the N reduces from 1400 to 500 rpm while it decreases around 10.42% by reducing S from 350 to 150 mm/min.

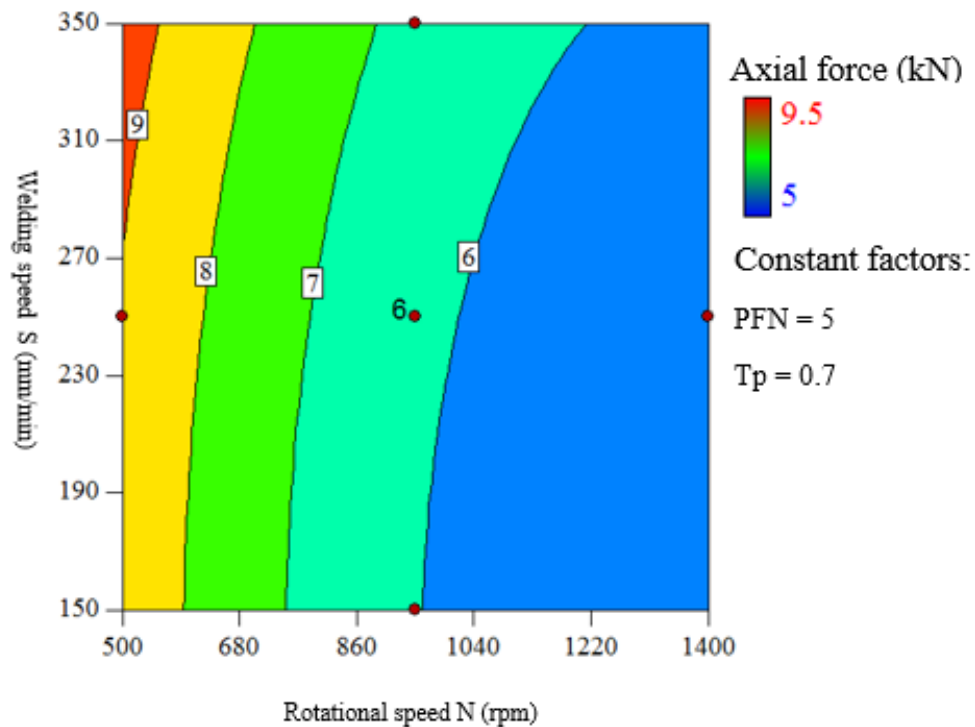


Figure 6-3. Contour plots for the effect of rotational speed and welding speed on axial force.

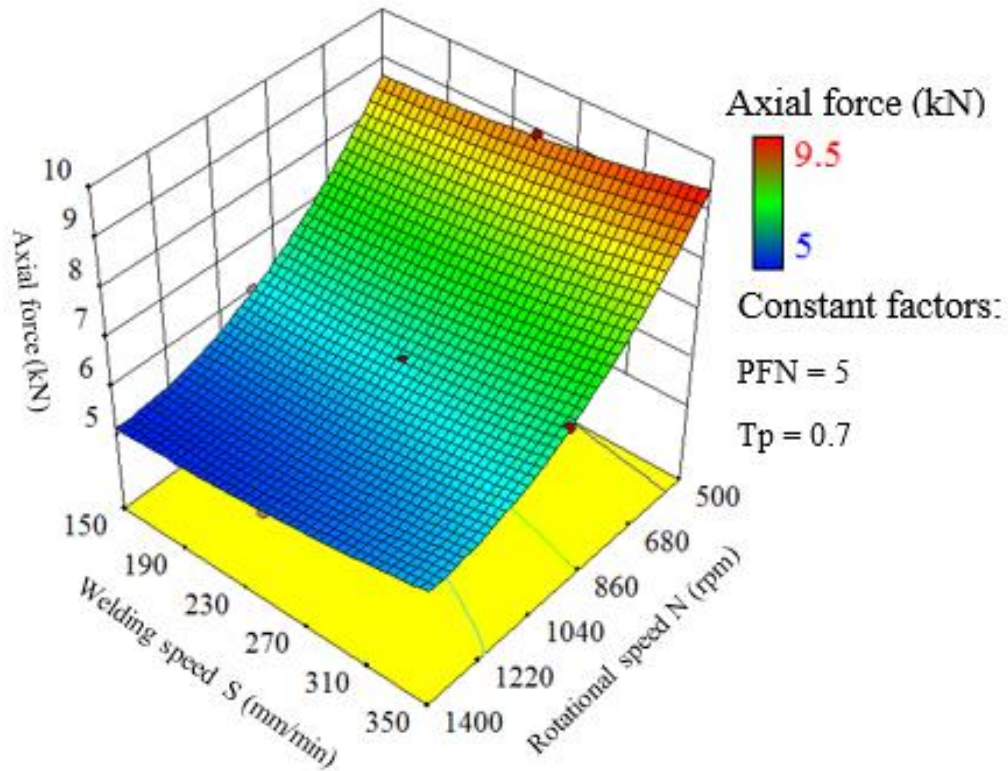


Figure 6-4. Response surface graphs for the effect of rotational speed and welding speed on axial force.

From Figure 6-5 and Figure 6-6, it is evident that axial force increases by increasing number of flats on probe lateral surface and increasing taper ratio, as a result of decreasing shoulder surface area and increasing lateral probe surface area with increasing flats number from 3 to 8.

The AF increases up to 14.16% by change friction stir welding tool from TR to Oct while it increases up to 10.16% by increasing the taper ratio from 0.4 to 1. Change tool profile lead to increasing the total heat generation by increasing frictional heat as a result of increasing AF.

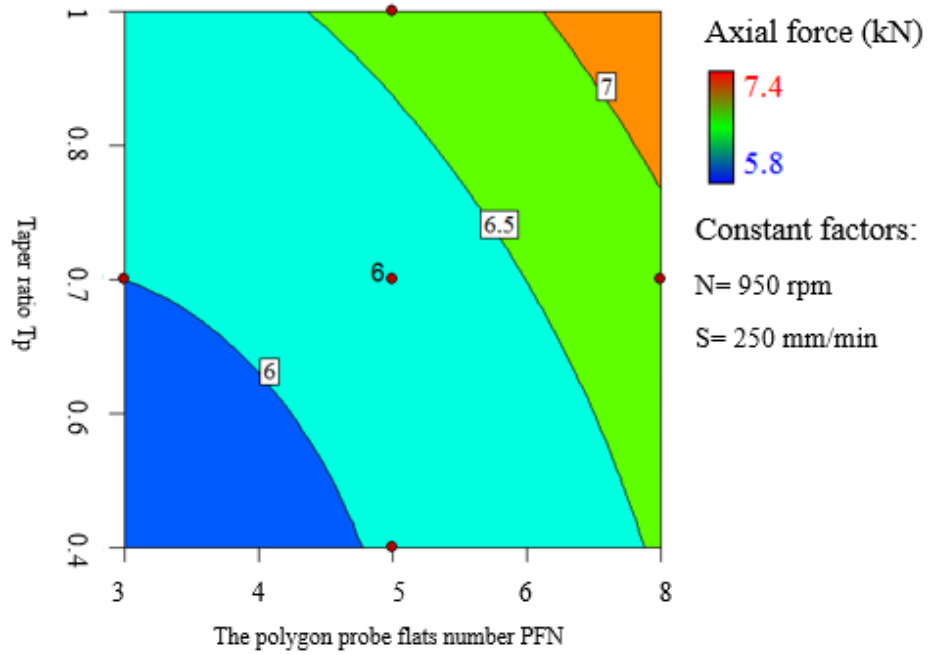


Figure 6-5. Contour plots for the effect of tool profile (PFN and  $T_p$ ) on axial force.

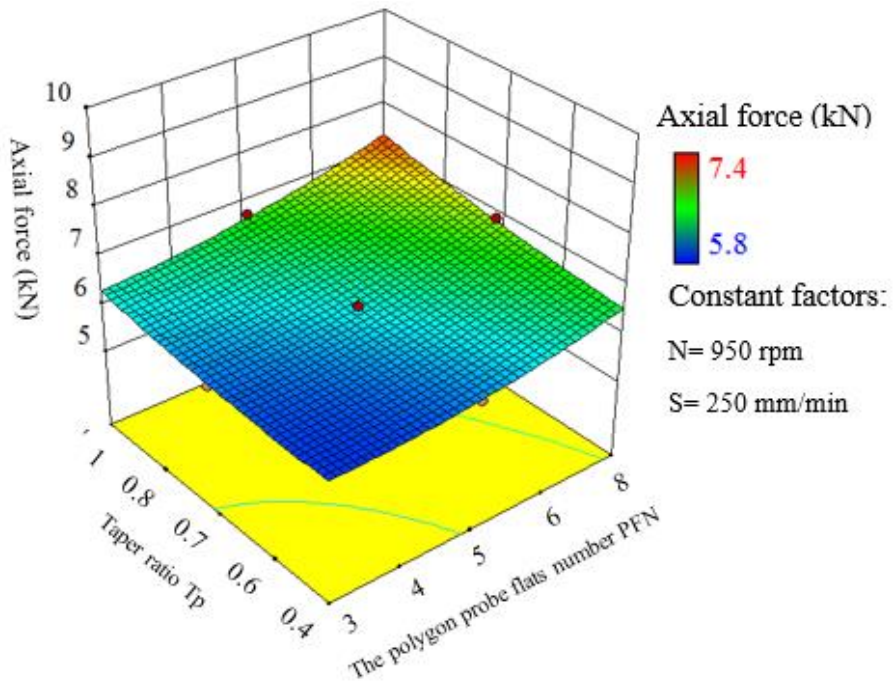


Figure 6-6. Response surface graphs for the effect of tool profile (PFN and  $T_p$ ) on axial force.

### 6.3 Conclusion

The DOE model developed seemed to be a right technique for the prediction of the AF as a function of DOE variables (welding parameters and tool profiles). A significant fitness of this model with the experimental AF data within the range of the DOE variables. The effects of these variables on AF are:

- 1- The AF increases around 77.26% by changing welding parameters (N and S) about 86.5% comes by reducing the N value from 1400 to 500 rpm and 13.5% by increasing S from 150 to 350 mm/min.
- 2- The AF increases around 24.33% by changing tool profile (PFN, Tp) about 58.22% comes by change the PFN from 3 to 8 and 41.78% by increasing Tp from 0.4 to 1.

The DOE predicted equation can be used to calculate the AF within the range of welding parameters and tool profiles to predict the peak temperature by COMSOL model. The COMSOL results will be analysed to evaluate the effect of change tool profile on the peak temperature and heat distribution by increasing the AF.

## Chapter 7 : Effect of tool profiles on thermal profile

Modelling results are simulation of friction stir welding for 6061-T6 aluminium alloy by using different taper tool profiles TR, SQ, Pen, Hex and Oct with  $T_p$  is 0.7. The tool dimensions ( $R_{shoulder}$  6 mm,  $R_{probe}$  3mm and  $H_{probe}$  6mm). Two simulations for each tool were carried out under model 1&2 assumptions which are listed in Table 4-1. Rotational speed and welding speed are constant ( $N= 1000$  rpm,  $S=200$  mm/min). The axial force for each tool was calculated according to  $N$ ,  $S$  and tool design (PFN and  $T_p$ ) by using equation (6.3), welding parameters for each tool are listed in Table 7-1.

Table 7-1. Values of welding parameters for different taper tool profiles.

<b>Tool profile</b>	<b>PFN</b>	<b><math>T_p</math></b>	<b>N (rpm)</b>	<b>S (mm/min)</b>	<b>AF (kN)</b>
<b>TR</b>	3	0.7	1000	200	5.63
<b>SQ</b>	4	0.7	1000	200	5.73
<b>Pen</b>	5	0.7	1000	200	5.92
<b>Hex</b>	6	0.7	1000	200	6.20
<b>Oct</b>	8	0.7	1000	200	6.57

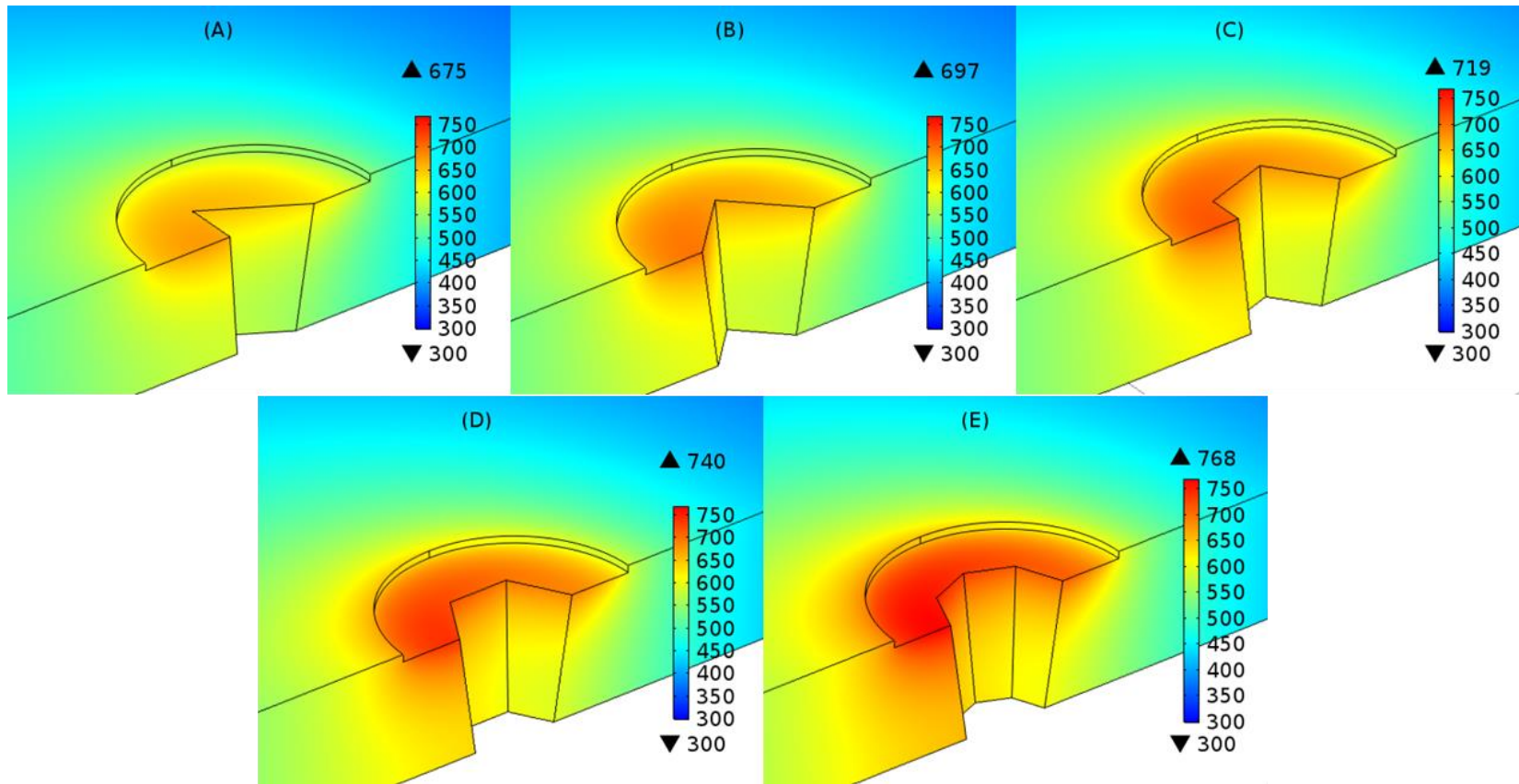


Figure 7-1. Isotherms temperature distribution (K) for different probe profiles: A-TR, B- SQ, C- Pen, D- Hex and E- Oct (model 1).

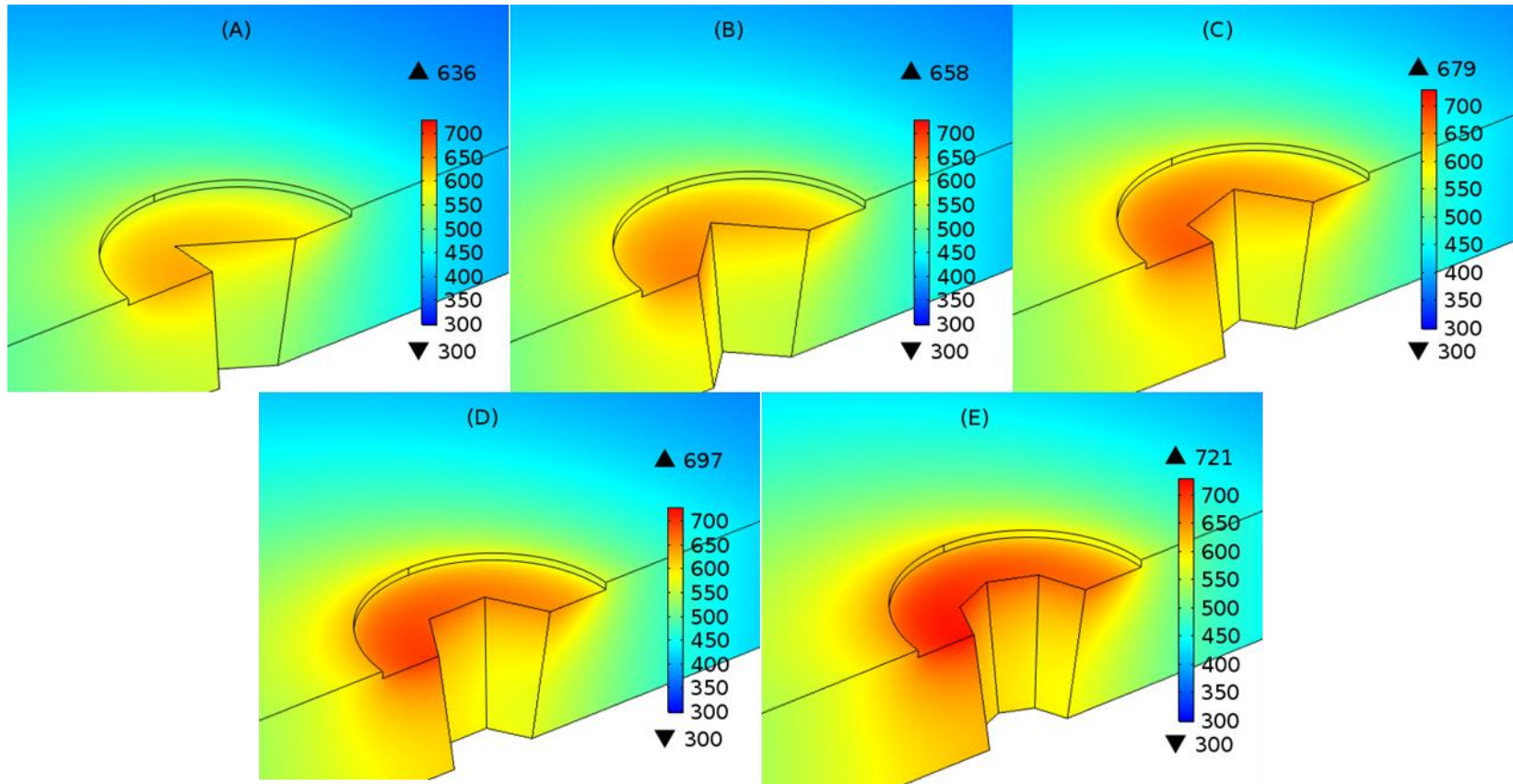


Figure 7-2. Isotherms temperature distribution (K) for different probe profiles: A-TR, B- SQ, C- Pen, D- Hex and E- Oct

(model 2).

Figure 7-1 shows isotherms temperature distribution under model 1 assumptions. It can be seen that the peak temperature increases by increasing number of flats on probe lateral surface (TR (675K), and SQ (697K) Pen (719K), Hex (740K) and Oct (768K)) that because increasing the number of flats increase the heat generation fraction for probe surface and probe tip which increase the total heat generation, although the fraction of the shoulder heat generation is decreased.

From Figure 7-3, an increase of probe interface areas (PIAS) (probe lateral and probe tip interface) with increasing PFN led to increase the frictional heating contribution of sticking condition in the total heat generation. Decreasing shoulder interface area (SIA) causes reducing the frictional heating contribution of sliding condition. SIA reduces 13.59% by increasing PFN from 3 to 8, while PIAS increase up to 25.30%.

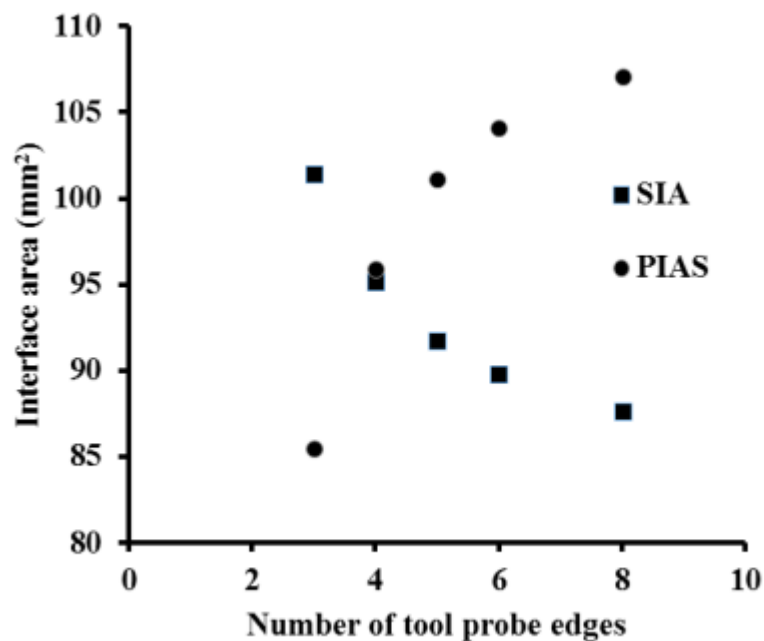


Figure 7-3. Change interfaces area by increasing flats number.

Figure 7-2 shows isotherms temperature distribution with model 2 assumptions. It can be seen that the peak temperature increases with number of flats TR (636K), and SQ (658K), PEN (679K), HEX (697K) and Oct (721K). The peak temperature for TR is 74.39% form melting point of base metal, this ratio increases to 84.33% by using Oct. Oct tool has the

highest peak temperature because of increasing the deformational heating. Decreasing effective stir dimension (the difference between inside and outside polygon radius for probe cross section) lead to increase the deformational heating by increasing stirring interaction and reducing the thickness of rotating layer [85].

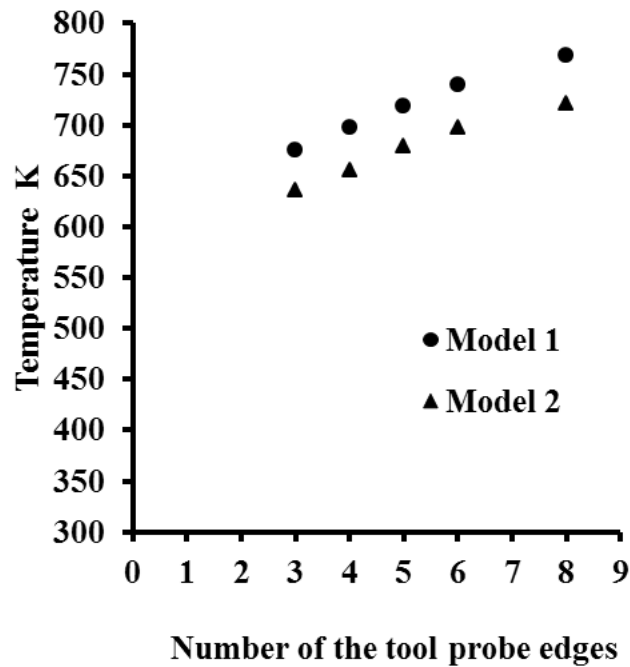


Figure 7-4. Comparison between modelling results for present work.

In contrast, model 2 results showed the lowest peak temperatures compared with model 1 results as shown in Figure 7-4. Model 2 was considered effect the change in physical material properties (density, thermal conductivity and heat capacity) with temperature on the thermal profile during welding cycle. Increasing thermal conductivity and heat capacity at elevated temperature lead to a decrease in peak temperature while decreasing in density causes increasing the peak temperature.

The variation of peak temperature by change probe profile from triangular to octagonal has slightly reducing form 13.78% in Model 1 to 13.36% in Model 2. Peak temperature reduction rate between model 1 and model 2 is an approximately stable at 6% with increasing number of flats on probe surface from 3 to 8.

## 7.1 Modelling results validation

Modelling results (Model 2) for present work are compared with experimental data measured by calculating temperature at specific point 5mm from welding line (L5) at mid thickness of plate as shown in Figure 7-5. This specific point is selected because average experimental temperature (AET) was measured by six K-type thermocouples which were embedded on the plate at the mid thickness of the plates on 5mm from welding line.

Four runs from the complete central composite design matrix were compared L5 with AET the welding parameters and FSW tools for selected runs reported in Table 7-2.

Figure 7-6 shows experimental temperature data for Run 1 measured by six thermocouples. Run 5, 9 and 13 are presented in Appendix 1. There is a slightly variation among the thermal profiles which recorded by different thermocouples.

T- and P- calculated values for maximum temperatures recorded by thermocouples list in Table 7-3 for selected runs.

The P value is less than 0.01%, This difference is considered to be extremely statistically significant. So, AET can be adopted in comparison with L5.

Table 7-2. FSW process variables for selected runs.

Run No.	FSW process variables			
	N (r/min)	S (mm/min)	PFN	TP
1	-1(725)	-1(200)	-1(SQ)	-1(0.6)
5	-1(725)	-1(200)	1(Hex)	-1(0.6)
9	-1(725)	-1(200)	-1(SQ)	1(0.8)
13	-1(725)	-1(200)	1(Hex)	1(0.8)

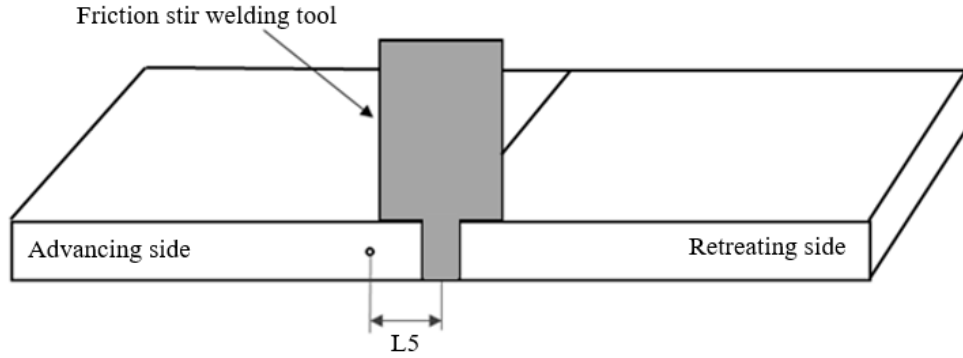


Figure 7-5. A schematic diagram illustrating the L5 position.

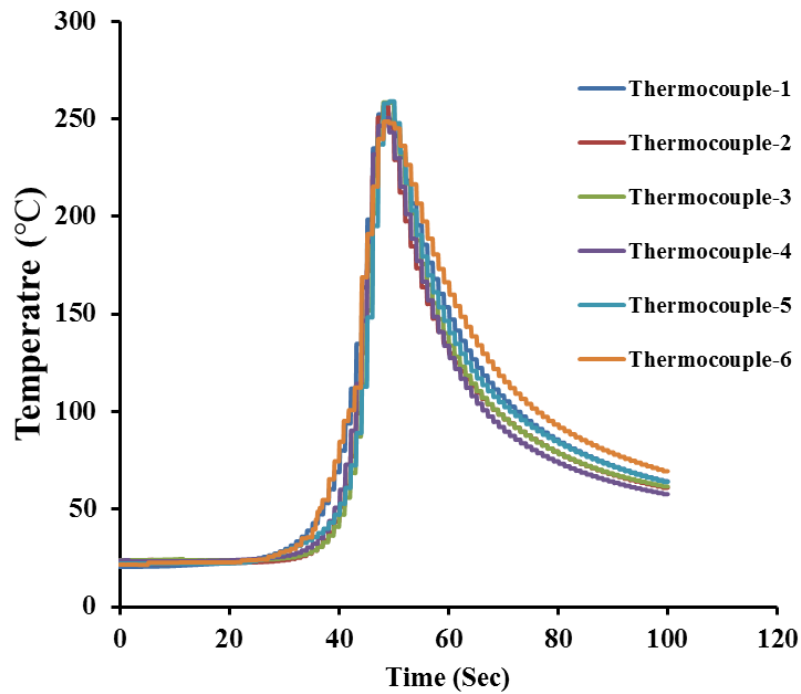


Figure 7-6. Experimental temperature data for Run 1.

Table 7-3. Maximum temperatures and P&T values for selected runs.

Run No.	Maximum Temperature according to thermocouple number (°C)						AET (°C)	T-value	P-value
	1	2	3	4	5	6			
<b>1</b>	253.21	256.6	258.52	250.67	259.05	248.83	254.5	147.1266	<0.0001
<b>5</b>	276	272.04	277.93	274.44	278.15	274.27	275.5	286.2636	<0.0001
<b>9</b>	261.95	262.69	268.44	267.38	265.02	268.14	265.6	230.5601	<0.0001
<b>13</b>	288.21	292.97	292.84	286.93	292.04	288.8	290.3	270.3792	<0.0001

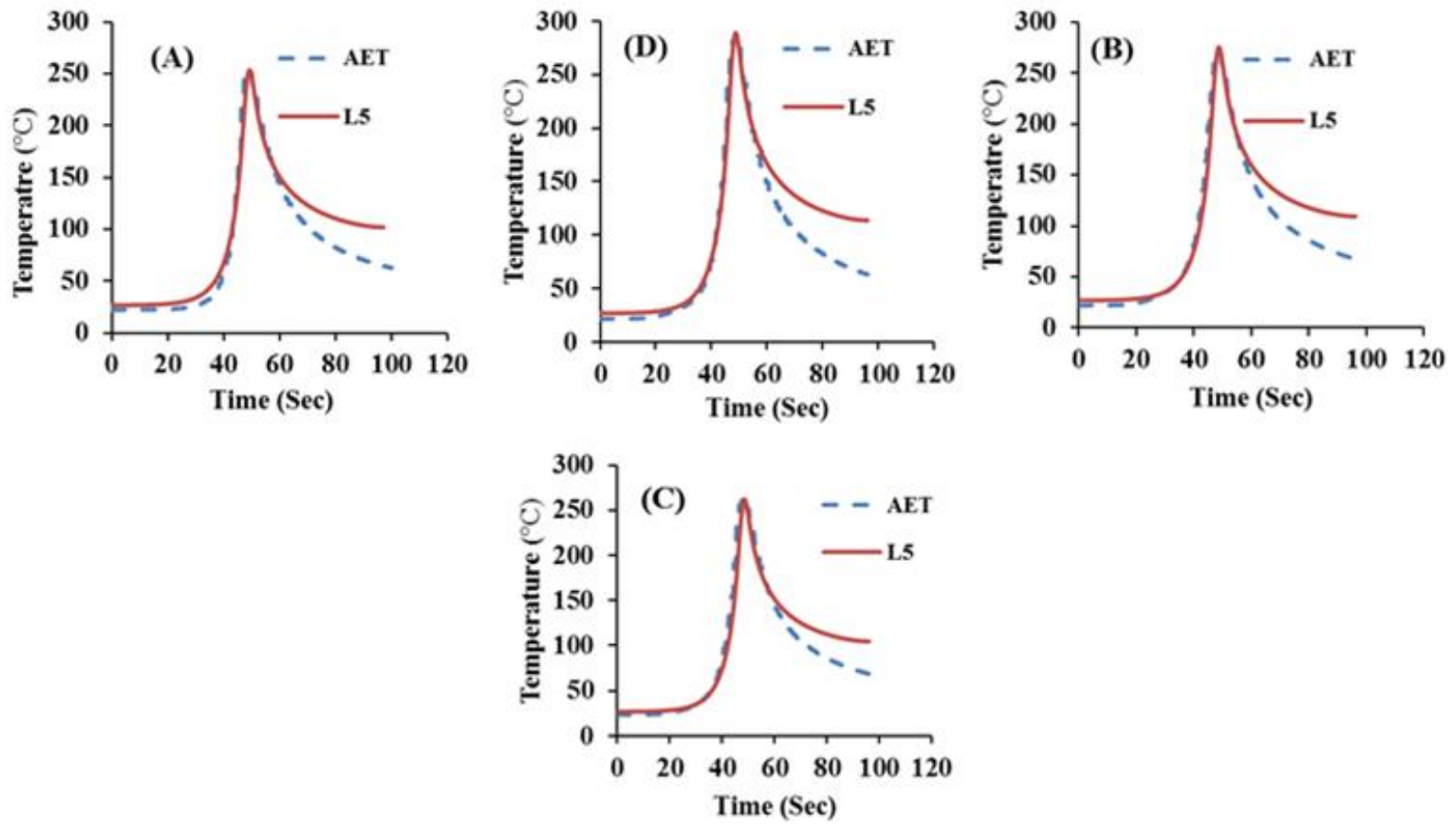


Figure 7-7. Comparison the average experimental temperatures (AET) with calculated temperature (L5) for (A) Run1, (B) Run5, (C) Run9 and (D) Run13.

Figure 7-7 depicts the thermal profiles of L5 and AET for each selected run. For all runs, good agreement can be observed between AET and L5 during the heat build-up, peak temperature and the first part of heat dispersion. However, there is a significant difference in a cooling rate between L5 and AET that is because the convection coefficient does not calculate as a function of temperature in modelling [103]. T- and P- calculated values for L5 and AET are listed in Table 7-4. The P value is 0.0041, this difference is considered to be statistically significant. Therefore modelling results (Model 2) can be adopted to predict peak temperature for DOE matrix.

Table 7-4. The variation between maximum temperatures for L5 and AET.

Run No.	Maximum Temperature according to thermocouple number		T-value	P-value
	AET	L5		
1	254.5	253.9	847.33	0.0008
5	275.5	275.5	0	0
9	265.6	262.2	155.2353	0.0041
13	290.3	288.9	413.71	0.0015

## 7.2 Peak temperature DOE

COMSOL model is used to calculate peak temperature for each trial (DOE run) of friction stir welding (Appendix 2) to predict mathematical equation for the effect of welding parameter and tool profile on peak temperature. Design matrix for the peak temperature is shown in Table 7-5. It is a four-factor five-level central composite rotatable design consisting 30 sets of coded conditions composed of a full factorial  $2^4 = 16$ , plus 6 centre points and 8 star points.

Table 7-5. Design matrix for modelling and predicted values of peak temperature.

Run no.	FSW process variables				Peak temperature (K)	
	<i>N</i> (rpm)	<i>S</i> (mm/min)	<i>PFN</i>	<i>Tp</i>	Modelling value	Predicted value
<b>Factorial points</b>						
1	-1(725)	-1(200)	-1(SQ)	-1(0.6)	614	613.875
2	1(1175)	-1(200)	-1(SQ)	-1(0.6)	676	674.1666
3	-1(725)	1(300)	-1(SQ)	-1(0.6)	597	594.3334
4	1(1175)	1(300)	-1(SQ)	-1(0.6)	649	650.375
5	-1(725)	-1(200)	1(Hex)	-1(0.6)	644	643.1666
6	1(1175)	-1(200)	1(Hex)	-1(0.6)	713	715.2082
7	-1(725)	1(300)	1(Hex)	-1(0.6)	621	619.375
8	1(1175)	1(300)	1(Hex)	-1(0.6)	686	687.1666
9	-1(725)	-1(200)	-1(SQ)	1(0.8)	626	625.8334
10	1(1175)	-1(200)	-1(SQ)	1(0.8)	697	699.875
11	-1(725)	1(300)	-1(SQ)	1(0.8)	611	610.0418
12	1(1175)	1(300)	-1(SQ)	1(0.8)	678	679.8334
13	-1(725)	-1(200)	1(Hex)	1(0.8)	662	661.875
14	1(1175)	-1(200)	1(Hex)	1(0.8)	744	747.6666
15	-1(725)	1(300)	1(Hex)	1(0.8)	639	641.8334
16	1(1175)	1(300)	1(Hex)	1(0.8)	717	723.375
<b>Axial points</b>						
17	-2(500)	0(250)	0(Pen)	0(0.7)	585	587.9584
18	2(1400)	0(250)	0(Pen)	0(0.7)	738	729.7916
19	0(950)	-2(150)	0(Pen)	0(0.7)	695	693.2916
20	0(950)	2(350)	0(Pen)	0(0.7)	650	649.4584
21	0(950)	0(250)	-2(TR)	0(0.7)	618	618.9584
22	0(950)	0(250)	2(OCT)	0(0.7)	695	691.7916
23	0(950)	0(250)	0(Pen)	-2(0.4)	635	637.2916
24	0(950)	0(250)	0(Pen)	2(1)	693	685.4584
<b>Centre points</b>						
25	0(950)	0(250)	0(Pen)	0(0.7)	658	659.5
26	0(950)	0(250)	0(Pen)	0(0.7)	660	659.5
27	0(950)	0(250)	0(Pen)	0(0.7)	658	659.5
28	0(950)	0(250)	0(Pen)	0(0.7)	658	659.5
29	0(950)	0(250)	0(Pen)	0(0.7)	660	659.5
30	0(950)	0(250)	0(Pen)	0(0.7)	660	659.5

### 7.2.1 Data driven model for peak temperature

Peak temperature as a function of rotational speed, welding speed, tool profile and taper ratio can be expressed as:

$$PT = (N, S, PFN, Tp) \quad (7.1)$$

Where  $PT$  is peak temperature (K);  $N$  is rotational speed (rpm);  $S$  is welding speed, (mm/min);  $PFN$  is the polygon probe flats number;  $Tp$  is taper ratio.

For the four factors, the selected polynomial could be expressed as:

$$\begin{aligned} PT = & b_0 + b_1 * N + b_2 * S + b_3 * PFN + b_4 * Tp + b_{11} * N^2 + b_{22} * S^2 + b_{33} \\ & * PFN^2 + b_{44} * Tp^2 + b_{12} * N * S + b_{13} * N * PFN + b_{14} * N \\ & * Tp + b_{23} * S * PFN + b_{24} * S * Tp + b_{34} * PFN * Tp \end{aligned} \quad (7.2)$$

Where  $b_0$  is the free term of the regression equation; the coefficients  $b_1$ ,  $b_2$ ,  $b_3$  and  $b_4$  are linear terms; the coefficients  $b_{11}$ ,  $b_{22}$ ,  $b_{33}$  and  $b_{44}$  are quadratic terms; the coefficients,  $b_{12}$ ,  $b_{13}$ ,  $b_{14}$ ,  $b_{23}$ ,  $b_{24}$  and  $b_{34}$ , are interaction terms.

DESIGN EXPERT 10.0.3 software packages were used to calculate the values of these coefficients for different responses and the results are presented in Table 7-6. The final mathematical equation is:

$$\begin{aligned} PT = & +613.58 + 0.19 * N - 0.72 * S + 11.12 * PFN - 7.16 * -9.44E \\ & - 5 * N * S + 0.01 * N * PFN + 0.02 * N * Tp - 0.02 * S \\ & * PFN + 0.02 * S * Tp + 1.69 * PFN * Tp - 3.09E - 6 * N^2 \\ & + 1.19E - 3 * S^2 - 1.03 * PFN^2 + 0.47 * Tp^2 \end{aligned} \quad (7.3)$$

Table 7-6. Calculated regression coefficients of peak temperature mathematical model.

Factor	Calculated coefficient
	+613.58
N	+0.19
S	-0.72
PFN	+11.12
Tp	-7.16
N*S	-9.44E-5
N*PFN	+0.01
N*Tp	+0.02
S*PFN	-0.02
S*Tp	+0.02
PFN*Tp	+1.69
N <sup>2</sup>	-3.09E-6
S <sup>2</sup>	+1.19E-3
PFN <sup>2</sup>	-1.03
Tp <sup>2</sup>	+0.47

### 7.2.2 Adequacy of DOE model for the peak temperature

The adequacy of the model developed was then tested by using the analysis of variance technique (ANOVA). The results of the ANOVA are given in Table 7-7. The model F-value of 342.24 implies the model is significant. There is only a 0.01% chance that an F-value could occur due to noise. The P value less than 0.05 indicates that model terms are significant. In this case, linear, some of interaction terms (N\*PFN, N\*Tp and PFN\*Tp) and quadratic term for S are significant model terms.

Values greater than 0.1 indicate the model terms are not significant, so interaction terms for N\*S, S\*PFN, S\*Tp quadratic terms N and Tp are not significant. The lack of fit F-value of 8.94 implies that the lack of fit is significant. There is 1.3% chance that a lack of fit F-value could as a result of high agreement between the actual and predicted values.

The determined values of the developed model are presented in Table 7-8. The R<sup>2</sup> value is always between 0 and 1, and its value indicates the accuracy of the model. For a good model, R<sup>2</sup> value should be close to 1. In this model, the calculated R<sup>2</sup> is 0.9969. This implies that 99.69% of COMSOL modelling results confirms the compatibility with the data predicted by

the developed model. The value of the adjusted  $R^2$  of 0.994 is also high to adherent for a high significance of the model. The predicted  $R^2$  of 0.9827 is in reasonable agreement with the adjusted  $R^2$  of 0.9969.

Adequate precision measures the signal-to-noise ratio. A ratio greater than 4 is desirable. In this study, the ratio is 73.516, which indicates an adequate signal. This model can be used to navigate the design space. The normal probability plot for the peak temperature shown in Figure 7-8 reveals that the residuals are scattered close to straight line, which means the errors are distributed normally. A typical scatter diagram of the model is presented in Figure 7-9. The observed values and predicted values of the responses are falling on the 45° line, indicating an almost perfect fit of the developed empirical models.

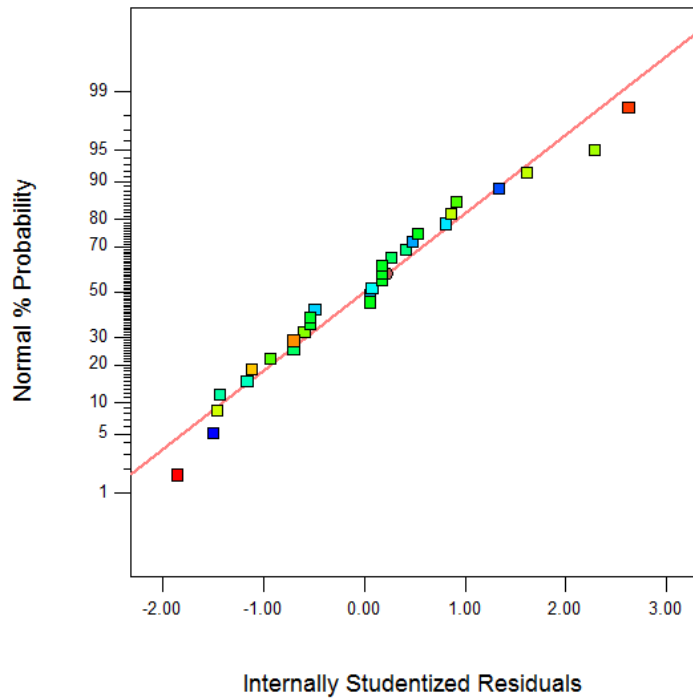


Figure 7-8. Peak temperature normal probability plot.

Table 7-7. Peak temperature ANOVA test results.

Source	Sum of squares	Degree of freedom	Mean square	F value	p-value	Result
					Prob > F	
<b>Model</b>	<i>45224.72</i>	<i>14</i>	<i>3230.34</i>	<i>342.24</i>	<i>&lt; 0.0001</i>	<b>significant</b>
<i>N</i>	<i>30175.04</i>	<i>1</i>	<i>30175.04</i>	<i>3196.88</i>	<i>&lt; 0.0001</i>	
<i>S</i>	<i>2882.04</i>	<i>1</i>	<i>2882.04</i>	<i>305.34</i>	<i>&lt; 0.0001</i>	
<i>PFN</i>	<i>7957.04</i>	<i>1</i>	<i>7957.04</i>	<i>843.01</i>	<i>&lt; 0.0001</i>	
<i>Tp</i>	<i>3480.04</i>	<i>1</i>	<i>3480.04</i>	<i>368.69</i>	<i>&lt; 0.0001</i>	
<i>N*S</i>	<i>18.06</i>	<i>1</i>	<i>18.06</i>	<i>1.91</i>	<i>0.1868</i>	
<i>N*PFN</i>	<i>138.06</i>	<i>1</i>	<i>138.06</i>	<i>14.63</i>	<i>0.0017</i>	
<i>N*Tp</i>	<i>189.06</i>	<i>1</i>	<i>189.06</i>	<i>20.03</i>	<i>0.0004</i>	
<i>S*PFN</i>	<i>18.06</i>	<i>1</i>	<i>18.06</i>	<i>1.91</i>	<i>0.1868</i>	
<i>S*Tp</i>	<i>14.06</i>	<i>1</i>	<i>14.06</i>	<i>1.49</i>	<i>0.2411</i>	
<i>PFN*Tp</i>	<i>45.56</i>	<i>1</i>	<i>45.56</i>	<i>4.83</i>	<i>0.0441</i>	
<i>N<sup>2</sup></i>	<i>0.67</i>	<i>1</i>	<i>0.67</i>	<i>0.071</i>	<i>0.7936</i>	
<i>S<sup>2</sup></i>	<i>241.74</i>	<i>1</i>	<i>241.74</i>	<i>25.61</i>	<i>0.0001</i>	
<i>PFN<sup>2</sup></i>	<i>29.17</i>	<i>1</i>	<i>29.17</i>	<i>3.09</i>	<i>0.0991</i>	
<i>Tp<sup>2</sup></i>	<i>6.03</i>	<i>1</i>	<i>6.03</i>	<i>0.64</i>	<i>0.4367</i>	
<b>Residual</b>	<i>141.58</i>	<i>15</i>	<i>9.44</i>			
<i>Lack of Fit</i>	<i>134.08</i>	<i>10</i>	<i>13.41</i>	<i>8.94</i>	<i>0.0130</i>	<b>significant</b>
<i>Pure Error</i>	<i>7.50</i>	<i>5</i>	<i>1.5</i>			
<b>Cor Total</b>	<i>45366.30</i>	<i>29</i>				

Table 7-8. Coefficient of determination values for peak temperature.

R-Squared	Adj R-Squared	Pred R-Squared	Adeq Precision
<i>0.9969</i>	<i>0.994</i>	<i>0.9827</i>	<i>73.516</i>

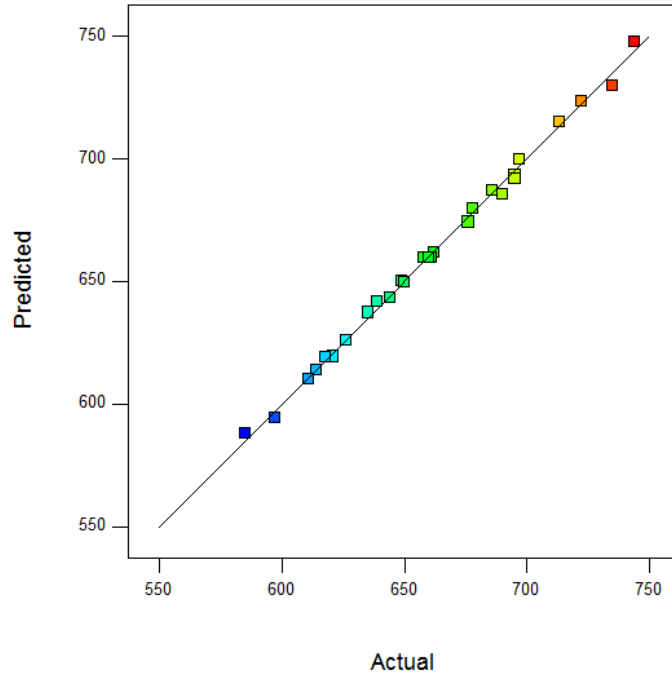


Figure 7-9. Scatter diagram of peak temperature (K).

### 7.2.3 Effect of welding parameters and tool profile on peak temperature

The effects of process parameters and welding tool profiles on the peak temperature were predicted by data driven model for the peak temperature presented in Figures ((7.10)–(7.13)), showing the general trends between cause and effect.

From Figure 7-10 and Figure 7-11, it can be seen that the peak temperature decreases when welding speed increases and rotational speed decreases as a result of decreasing heat input. The PT increases about 24.12% when the N increases from 500 to 1400 rpm while it decreases around 6.45% by increasing S from 150 to 350 mm/min.

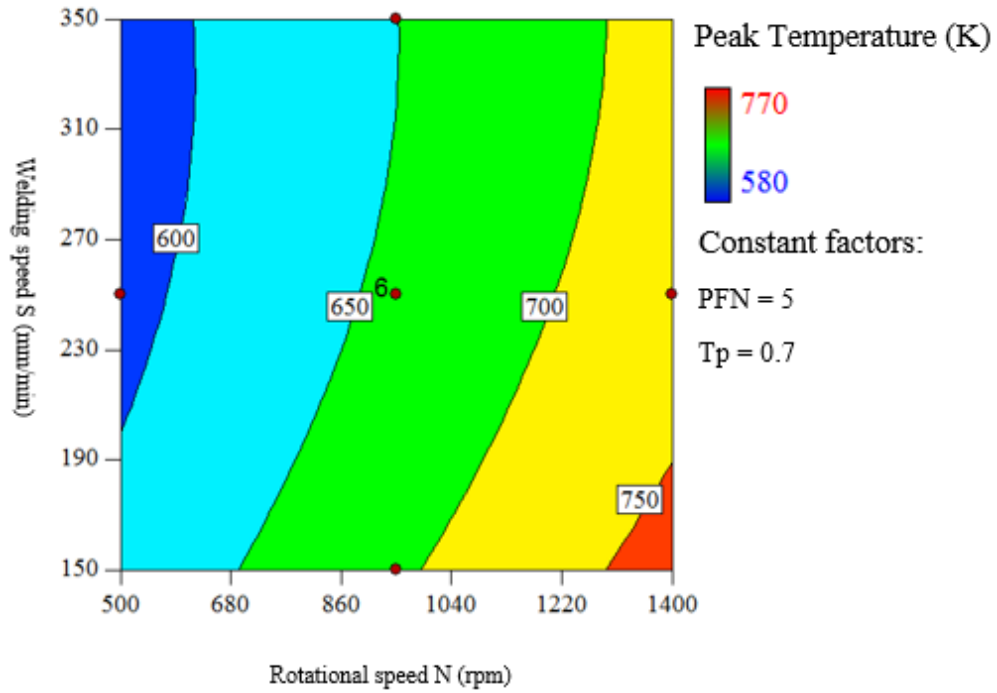


Figure 7-10. Contour plots for the effect of rotational speed and welding speed on peak temperature.

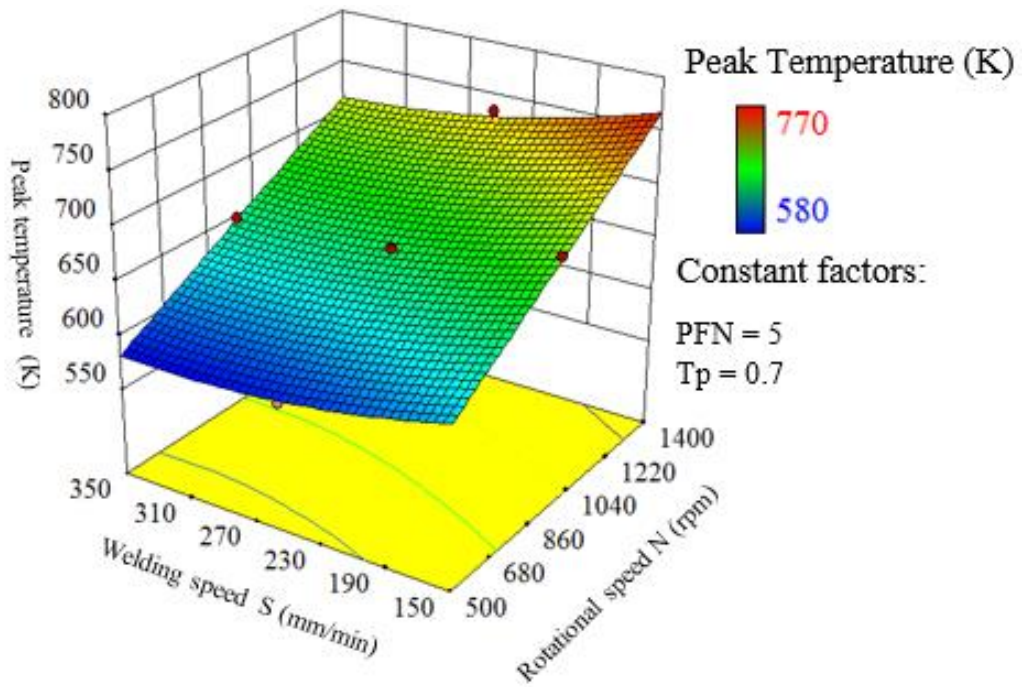


Figure 7-11. Response surface graphs for the effect of rotational speed and welding speed on peak temperature.

From Figure 7-12 and Figure 7-13, it is evident that peak temperature increases by change tool profile (PFN and  $T_p$ ) as a result of increasing contribution of probe in the total heat generation. Peak temperature increases up to 19.2% by changing tool design, 11.63% comes from increasing PFN from 3 to 8 increases while change the taper ratio from 0.4 to 1 increases 7.57%.

According to this variation in peak temperature, the heat input can be controlled by change tool profile without change welding parameters to improve mechanical properties of welding joint.

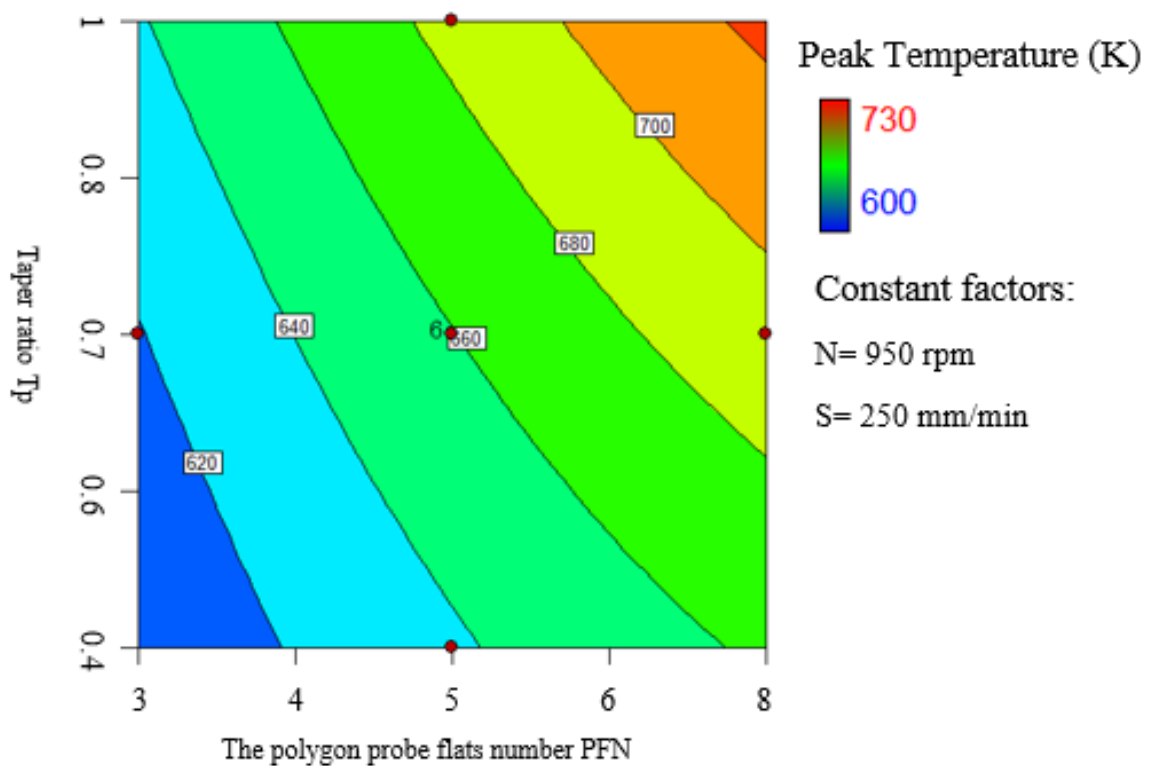


Figure 7-12. Contour plots for the effect of tool profile (PFN and  $T_p$ ) on peak temperature.

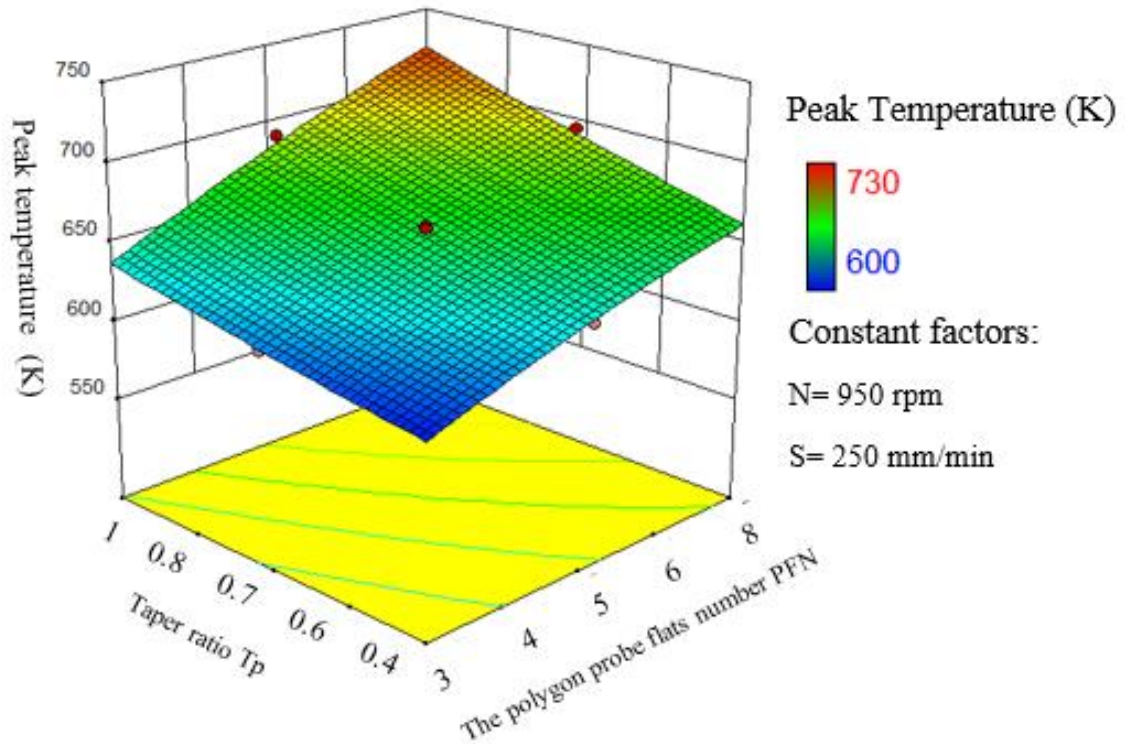


Figure 7-13. Response surface graph for the effect of tool profile (PFN and  $T_p$ ) on peak temperature.

### 7.3 Conclusion

#### ❖ Equations for heat generation

Equations of heat generation during FSW for taper and straight polygonal tool profiles have been derived. The major finding from the present work can be summarized as follow:

- The amount of heat generation from shoulder surface decrease with increasing of flats on the probe surface as a result of increase probe base area.
- The contribution of probe surface at total heat generation increases with increasing of flats on the probe surface as a result of increase the flow rate of the soft material around the probe and contact area.
- The contribution of probe tip at total heat generation increases with increasing of flats on the probe surface as a result of increase contact area.

### ❖ **Modelling results**

An analytical model for heat generation in FSW of aluminium alloy type AA 6061-T6 using different taper and straight polygonal tool profiles are developed. The major finding from the present work can be summarized as follow:

- The amount of heat generated as well as peak temperature is relatively high in non-circular taper probe profiles, they increase by increasing the number of edges to reach maximum values in the Oct tool profile.
- The effective stir dimension is decreased by increasing number of flats on surface probe profile.
- An increase in the number of effective stir dimension with increasing the number of flats on probe surface lead to increasing the total heat generation.

### ❖ **DOE results**

DOE model uses to predict the effect of welding parameters (N and S) and tool profile (PFN and Tp). The major finding from the present work can be summarized as follow:

- The PT increases around 30.57% by changing welding parameters (N and S), about 78.91% comes by increasing the N value from 500 to 1400 rpm and 21.09% by decreasing S from 350 to 150 mm/min.
- The PT increases around 19.21% by changing tool profile (PFN and Tp), about 60.57% comes by increasing the PFN from 3 to 8 and 39.43% by increasing Tp from 0.4 to 1.

## Chapter 8 : Mechanical performance

### 8.1 Tensile strength DOE

Three transverse tensile specimens for each trial (DOE run) of friction stir welding were tested to predict mathematical equation for the effect of welding parameter and tool profile on tensile strength. The tensile test results for each trial was checked by calculating the mean transverse tensile strength results (MTTR), standard deviation (SD), the standard error of the mean (SEM), T-value and level of significance (P-value), all results are listed in Table 8-1. The differences for the results are considered to be extremely statistically significant that because the maximum P-value is 0.0005 which is less than 0.05. Although, there is statistically significant variation in SD because of the effect of defect size on all DOE runs which causes differences in tensile results for each DOE run. The tensile test results were considered to study the adequacy of DOE model to predict optimum conditions.

Design matrix for the tensile strength is shown in Table 8-2. It is a four-factor five-level central composite rotatable design consisting 30 sets of coded conditions composed of a full factorial  $2^4 = 16$ , plus 6 centre points and 8 star points.

#### 8.1.1 Data driven model for tensile strength

Tensile strength as a function of rotational speed, welding speed, tool profile and taper ratio can be expressed as:

$$\sigma_T = (N, S, PFN, Tp) \quad (8.1)$$

Where  $\sigma_T$  is the tensile strength (MPa);  $N$  is rotational speed (rpm);  $S$  is welding speed, (mm/min);  $PFN$  is the polygon probe flats number;  $Tp$  is taper ratio.

Table 8-1. MTTR, paired SD& SEM difference, T-value and level of significance.

Run No.	Tensile test results (MPa)			MTTR (MPa)	Paired difference		Paired T-value	Level of significance
	1	2	3		SD	SEM		P-Value
1	192.2	186.5	181.4	186.7	5.403	3.119	59.8533	0.0003
2	201.5	196.4	191.6	196.5	4.951	2.858	68.7466	0.0002
3	166.3	161.7	157.4	161.8	4.451	2.57	62.9647	0.0003
4	176.5	171.2	166.8	171.5	4.857	2.804	61.1591	0.0003
5	171.7	176.7	182.3	176.9	5.303	3.062	57.7804	0.0003
6	182.1	188.1	195	188.4	6.455	3.727	50.551	0.0004
7	148.7	152.3	156.5	152.5	3.904	2.254	67.6609	0.0002
8	167.2	162.7	157.9	162.6	4.651	2.685	60.5554	0.0003
9	196.1	191.9	186.2	191.4	4.969	2.869	66.7178	0.0002
10	199.4	205	214.2	206.2	7.473	4.314	47.7944	0.0004
11	169.4	164.9	158.9	164.4	5.268	3.041	54.0544	0.0003
12	174.8	178.8	181.6	178.4	3.418	1.973	90.4137	0.0001
13	184.6	180.1	177.4	180.7	3.637	2.1	86.0476	0.0001
14	187.4	191.2	197.1	191.9	4.888	2.822	68.0029	0.0002
15	158.3	155.4	153.4	155.7	2.464	1.422	109.4599	0.0001
16	160.8	164.9	168.1	164.6	3.659	2.113	77.9112	0.0002
17	139.3	133.9	129.1	134.1	5.103	2.946	45.5165	0.0005
18	158.2	154.1	151.5	154.6	3.378	1.95	79.2734	0.0002
19	196.8	200.2	205.7	200.9	4.491	2.593	77.4796	0.0002
20	143.5	146.9	150.6	147	3.551	2.05	71.7002	0.0002
21	198.3	202.8	205.2	202.1	3.503	2.022	99.932	0.0001
22	184.9	180.7	174.7	180.1	5.126	2.96	60.8502	0.0003
23	196.6	192.6	187.1	192.1	4.77	2.754	69.7585	0.0002
24	199.7	203.1	207.7	203.5	4.015	2.318	87.7895	0.0001
25	201.1	200.8	198.7	200.2	1.308	0.755	265.1714	0.0001
26	198.4	199	201.1	199.5	1.418	0.819	243.728	0.0001
27	202.5	200.8	197.6	200.3	2.488	1.436	139.4429	0.0001
28	197.9	199.1	202.1	199.7	2.163	1.249	159.888	0.0001
29	204.1	200.7	195.5	200.1	4.331	2.501	80.0187	0.0002
30	196.9	199.2	203.3	199.8	3.242	1.872	106.7468	0.0001

Table 8-2. Design matrix for experimental and predicted values of tensile strength.

Run no.	FSW process variables				Tensile strength (MPa)	
	<i>N</i> (rpm)	<i>S</i> (mm/min)	<i>PFN</i>	<i>Tp</i>	MMTR	Predicted value
<b>Factorial points</b>						
1	-1(725)	-1(200)	-1(SQ)	-1(0.6)	186.7	185.77
2	1(1175)	-1(200)	-1(SQ)	-1(0.6)	196.5	197.112
3	-1(725)	1(300)	-1(SQ)	-1(0.6)	161.8	160.67
4	1(1175)	1(300)	-1(SQ)	-1(0.6)	171.5	170.89
5	-1(725)	-1(200)	1(Hex)	-1(0.6)	176.9	177.62
6	1(1175)	-1(200)	1(Hex)	-1(0.6)	188.4	187.31
7	-1(725)	1(300)	1(Hex)	-1(0.6)	152.5	153.09
8	1(1175)	1(300)	1(Hex)	-1(0.6)	162.6	161.63
9	-1(725)	-1(200)	-1(SQ)	1(0.8)	191.4	192.03
10	1(1175)	-1(200)	-1(SQ)	1(0.8)	206.2	205.32
11	-1(725)	1(300)	-1(SQ)	1(0.8)	164.4	165.21
12	1(1175)	1(300)	-1(SQ)	1(0.8)	178.4	177.35
13	-1(725)	-1(200)	1(Hex)	1(0.8)	180.7	181.02
14	1(1175)	-1(200)	1(Hex)	1(0.8)	191.9	192.67
15	-1(725)	1(300)	1(Hex)	1(0.8)	155.7	154.75
16	1(1175)	1(300)	1(Hex)	1(0.8)	164.6	165.24
<b>Axial points</b>						
17	-2(500)	0(250)	0(Pen)	0(0.7)	134.1	133.74
18	2(1400)	0(250)	0(Pen)	0(0.7)	154.6	155.57
19	0(950)	-2(150)	0(Pen)	0(0.7)	200.9	200.51
20	0(950)	2(350)	0(Pen)	0(0.7)	147	148.01
21	0(950)	0(250)	-2(TR)	0(0.7)	202.1	200.04
22	0(950)	0(250)	2(OCT)	0(0.7)	180.1	179.77
23	0(950)	0(250)	0(Pen)	-2(0.4)	192.1	193.17
24	0(950)	0(250)	0(Pen)	2(1)	203.5	203.04
<b>Centre points</b>						
25	0(950)	0(250)	0(Pen)	0(0.7)	200.2	199.93
26	0(950)	0(250)	0(Pen)	0(0.7)	199.5	199.93
27	0(950)	0(250)	0(Pen)	0(0.7)	200.3	199.93
28	0(950)	0(250)	0(Pen)	0(0.7)	199.7	199.93
29	0(950)	0(250)	0(Pen)	0(0.7)	200.1	199.93
30	0(950)	0(250)	0(Pen)	0(0.7)	199.8	199.93

For the four factors, the selected polynomial could be expressed as:

$$\begin{aligned} \sigma_T = & b_0 + b_1 * N + b_2 * S + b_3 * PFN + b_4 * Tp + b_{11} * N^2 + b_{22} * S^2 + b_{33} \\ & * PFN^2 + b_{44} * Tp^2 + b_{12} * N * S + b_{13} * N * PFN + b_{14} * N \\ & * Tp + b_{23} * S * PFN + b_{24} * S * Tp + b_{34} * PFN * Tp \end{aligned} \quad (8.2)$$

Where  $b_0$  is the free term of the regression equation; the coefficients  $b_1$ ,  $b_2$ ,  $b_3$  and  $b_4$  are linear terms; the coefficients  $b_{11}$ ,  $b_{22}$ ,  $b_{33}$  and  $b_{44}$  are quadratic terms; the coefficients,  $b_{12}$ ,  $b_{13}$ ,  $b_{14}$ ,  $b_{23}$ ,  $b_{24}$ , and  $b_{34}$ , are interaction terms.

DESIGN EXPERT 10.0.3 software packages were used to calculate the values of those coefficients for different responses and the results are presented in Table 8-3. The final mathematical equation is:

$$\begin{aligned} \sigma_T = & -170.37 + 0.55 * N + 1.04 * S - 4.01 * PFN + 2.60 * Tp - 2.56E \\ & - 5 * N * S - 1.83E - 3 * N * PFN + 2.17E - 3 * N * Tp \\ & + 2.75E - 3 * S * PFN - 8.75E - 3 * S * Tp - 0.71 * PFN * Tp \\ & - 2.73E - 4 * N^2 - 2.57E - 3 * S^2 - 2.51 * PFN^2 - 0.46 \\ & * Tp^2 \end{aligned} \quad (8.3)$$

Table 8-3. Calculated regression coefficients of tensile strength mathematical model.

Factor	Calculated coefficient
	-170.37
N	+0.55
S	+1.04
PFN	-4.01
Tp	+2.60
N*S	-2.56E-5
N*PFN	-1.83E-3
N*Tp	+2.17E-3
S*PFN	+2.75E-3
S*Tp	-8.75E-3
PFN*Tp	-0.71
N <sup>2</sup>	-2.73E-4
S <sup>2</sup>	-2.57E-3
PFN <sup>2</sup>	-2.51
Tp <sup>2</sup>	-0.46

### 8.1.2 Adequacy of DOE model for tensile strength

The adequacy of the model developed was then tested by using the analysis of variance technique (ANOVA). The results of the ANOVA are given in Table 8-4. The Model F-value of 781.09 implies the model is significant. There is only a 0.01% chance that an F-value could occur due to noise. The P-value less than 0.05 indicates that model terms are significant.

In this case, linear, quadratic and one of interaction terms (PFN\*Tp) are significant model terms. Values greater than 0.1 indicate the model terms are not significant, so interaction terms for N\*S, N\*PFN, S\*PFN and S\*Tp are not significant. The lack of fit F-value of 15.55 implies that the lack of fit is insignificant. There is 0.37% chance that a lack of fit F-value could as a result of noise.

The determined values of the developed model are presented in Table 8-5. The  $R^2$  value is always between 0 and 1, and its value indicates the accuracy of the model. For a good model,  $R^2$  value should be close to 1. In this model, the calculated  $R^2$  is 0.9986. This implies that 99.86% of experimental results confirm the compatibility with the data predicted by the developed model.

The value of the adjusted  $R^2$  of 0.9974 is also high to adherent for a high significance of the model. The predicted  $R^2$  of 0.9923 is in reasonable agreement with the adjusted  $R^2$  of 0.9974 because the difference is less than 0.2. Adequate precision measures the signal-to-noise ratio. A ratio greater than 4 is desirable. In this study, the ratio is 98.524, which indicates an adequate signal. This model can be used to navigate the design space.

The normal probability plot for the tensile strength shown in Figure 8-1 reveals that the residuals are scattered close to straight line, which means the errors are distributed normally. A typical scatter diagram of the model is presented in Figure 8-2. The observed values and predicted values of the responses are falling on the 45° line, indicating an almost perfect fit of the developed empirical models.

Table 8-4. Tensile strength ANOVA test results.

Source	Sum of squares	Degree of freedom	Mean square	F value	p-value	Result
					Prob > F	
<i>Model</i>	<i>11545.24</i>	<i>14</i>	<i>824.66</i>	<i>781.09</i>	<i>&lt; 0.0001</i>	<i>significant</i>
<i>N</i>	<i>715.04</i>	<i>1</i>	<i>715.04</i>	<i>677.27</i>	<i>&lt; 0.0001</i>	
<i>S</i>	<i>4134.38</i>	<i>1</i>	<i>4134.38</i>	<i>3915.95</i>	<i>&lt; 0.0001</i>	
<i>PFN</i>	<i>616.11</i>	<i>1</i>	<i>616.11</i>	<i>583.56</i>	<i>&lt; 0.0001</i>	
<i>Tp</i>	<i>146.03</i>	<i>1</i>	<i>146.03</i>	<i>138.31</i>	<i>&lt; 0.0001</i>	
<i>N*S</i>	<i>1.32</i>	<i>1</i>	<i>1.32</i>	<i>1.25</i>	<i>0.2807</i>	
<i>N*PFN</i>	<i>2.72</i>	<i>1</i>	<i>2.72</i>	<i>2.58</i>	<i>0.1292</i>	
<i>N*Tp</i>	<i>3.80</i>	<i>1</i>	<i>3.80</i>	<i>3.60</i>	<i>0.0771</i>	
<i>S*PFN</i>	<i>0.30</i>	<i>1</i>	<i>0.30</i>	<i>0.29</i>	<i>0.6003</i>	
<i>S*Tp</i>	<i>3.06</i>	<i>1</i>	<i>3.06</i>	<i>2.90</i>	<i>0.1092</i>	
<i>PFN*Tp</i>	<i>8.12</i>	<i>1</i>	<i>8.12</i>	<i>7.69</i>	<i>0.0142</i>	
<i>N<sup>2</sup></i>	<i>5237.70</i>	<i>1</i>	<i>5237.70</i>	<i>4960.99</i>	<i>&lt; 0.0001</i>	
<i>S<sup>2</sup></i>	<i>1130.07</i>	<i>1</i>	<i>1130.07</i>	<i>1070.36</i>	<i>&lt; 0.0001</i>	
<i>PFN<sup>2</sup></i>	<i>172.29</i>	<i>1</i>	<i>172.29</i>	<i>163.18</i>	<i>&lt; 0.0001</i>	
<i>Tp<sup>2</sup></i>	<i>5.71</i>	<i>1</i>	<i>5.71</i>	<i>5.41</i>	<i>0.0345</i>	
<i>Residual</i>	<i>15.84</i>	<i>15</i>	<i>1.06</i>			
<i>Lack of Fit</i>	<i>15.34</i>	<i>10</i>	<i>1.53</i>	<i>15.55</i>	<i>0.0037</i>	<i>significant</i>
<i>Pure Error</i>	<i>0.49</i>	<i>5</i>	<i>0.099</i>			
<b>Cor Total</b>	<i>11561.08</i>	<i>29</i>				

Table 8-5. Coefficient of determination values for tensile strength.

R-Squared	Adj R-Squared	Pred R-Squared	Adeq Precision
<i>0.9986</i>	<i>0.9974</i>	<i>0.9923</i>	<i>98.524</i>

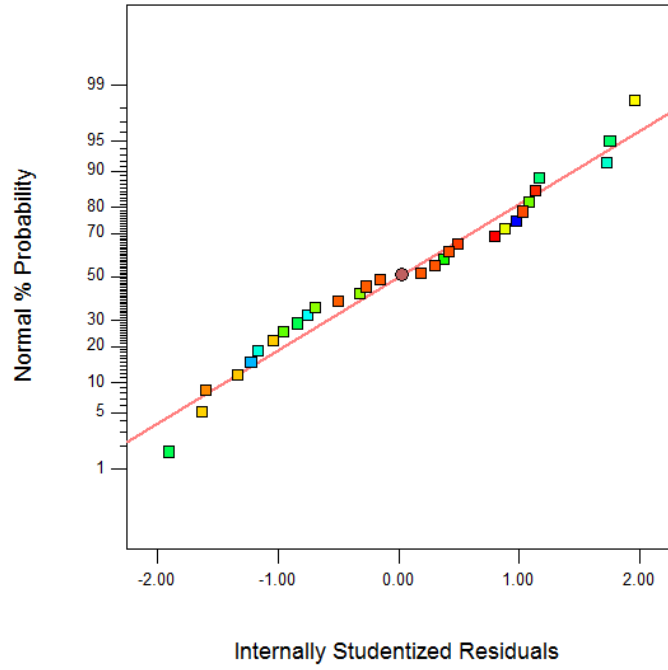


Figure 8-1. Tensile strength normal probability plot.

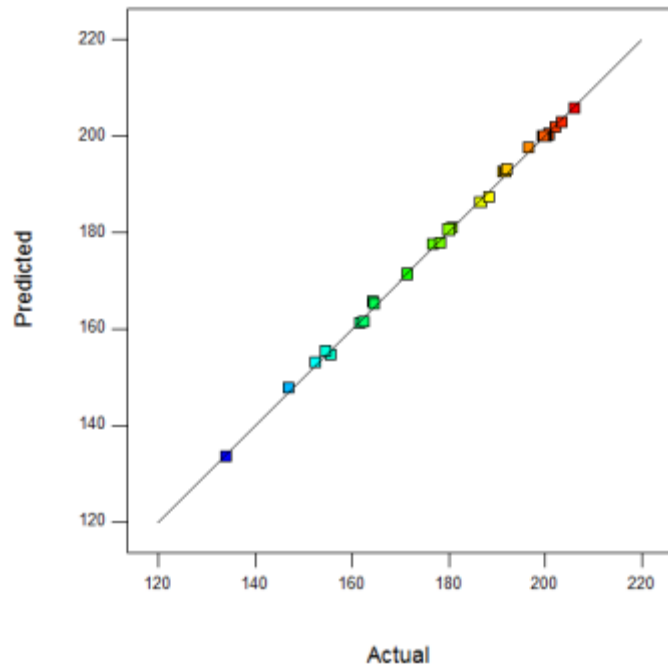


Figure 8-2. Scatter diagram of tensile strength (MPa).

### 8.1.3 Effect of welding parameters and tool profile on tensile strength

The effects of welding parameters and tool profiles on the tensile strength were predicted by data driven model for the tensile strength presented in Figures ((8.3)–(8.6)), showing the general trends between cause and effect.

From Figure 8-3 and Figure 8-4, it can be seen that the tensile strength increases when welding and rotational speed increase up to optimum welding conditions ( $N=1000$  rpm,  $S=200$  mm/min) because they generate sufficient heat energy and perfect flow profile

And then the tensile strength decreases because excess heat input causes by increasing rotational speed and nonhomogeneous flow profile. The tensile strength increases up to 49.89% with changing rotational speed while it increases 28.37% with changing welding speed.

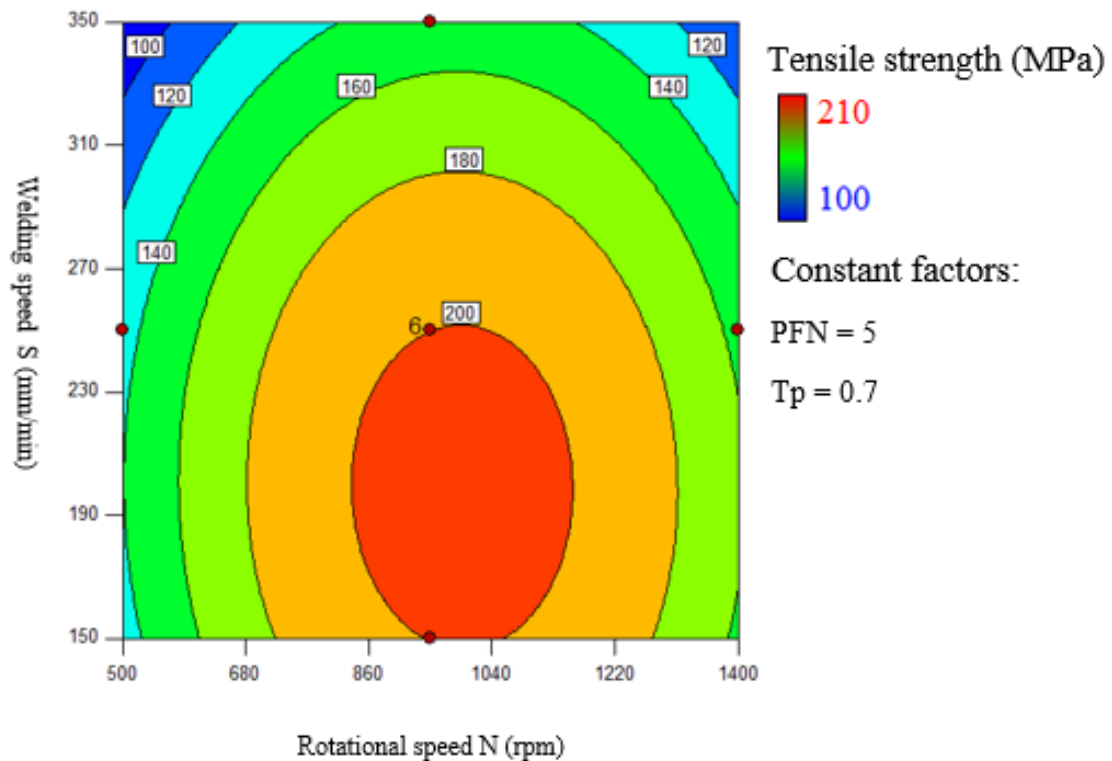


Figure 8-3. Contour plots for the effect of rotational speed and welding speed on tensile strength.

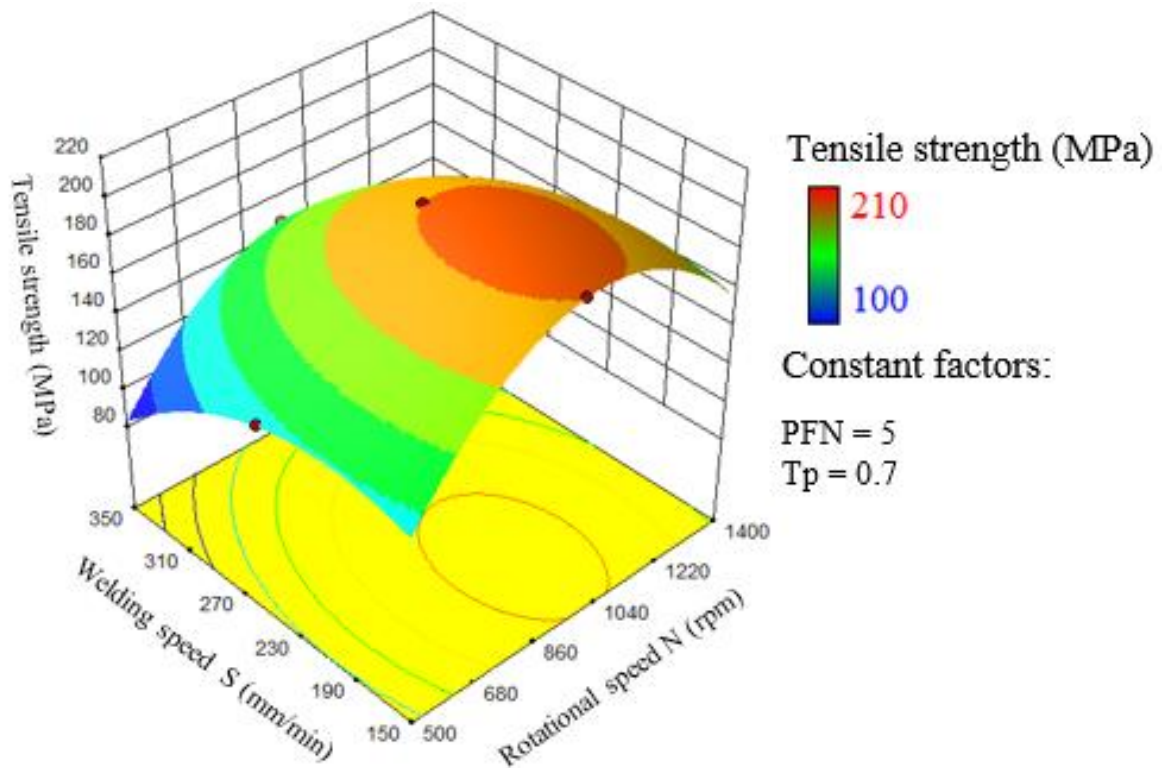


Figure 8-4. Response surface graphs for the effect of rotational speed and welding speed on tensile strength.

From Figure 8-5 and Figure 8-6, it is evident that tensile strength slightly increases about 1.21% by increasing number of flats from 3 to 4 on probe lateral surface and then decrease about 11.22 % by increasing number of flats from 4 to 8. The increase taper ratio from 0.4 to 1 causes 4.86% increasing in tensile strength. Total increasing of tensile strength is around 16.08% by changing tool profile at welding parameters (N=950 rpm, S=250 mm/min).

From equation (8.3), with optimum welding parameters ( N=1000 rpm, S=200 mm/min), the maximum tensile strength is an approximately 215.65 MPa by using straight square tool profile (SSQ) while the minimum tensile strength is about 187.97 MPa by using straight octagonal tool profile (SOct). Total increasing of tensile strength is an approximately 22.15% by changing tool profile at optimum welding parameters.

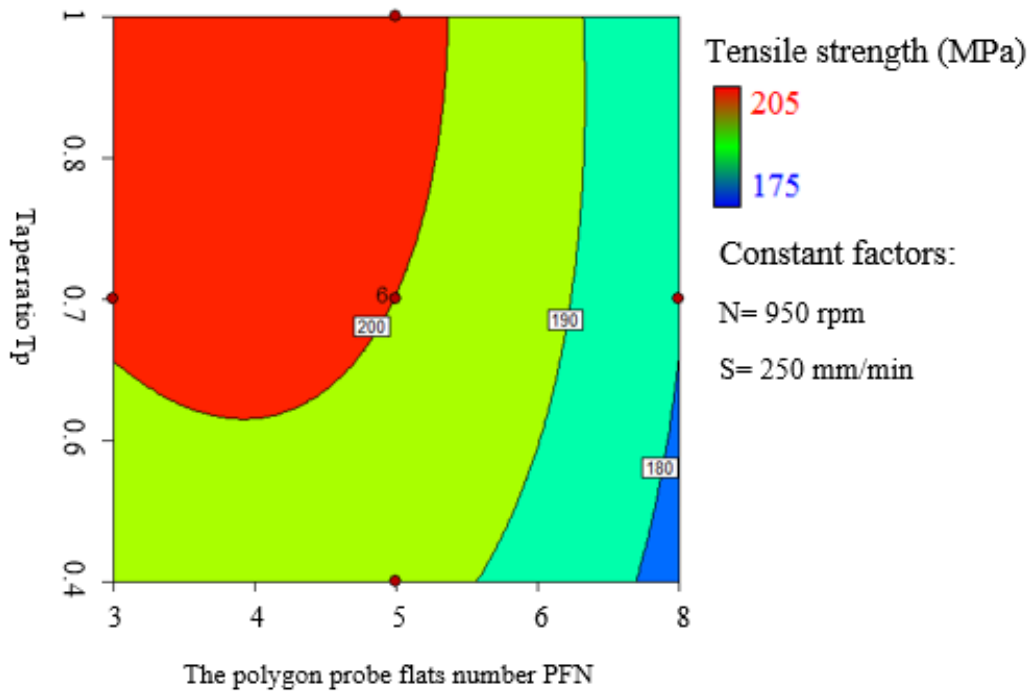


Figure 8-5. Contour plots for the effect of tool profile (PFN and Tp) on tensile strength.

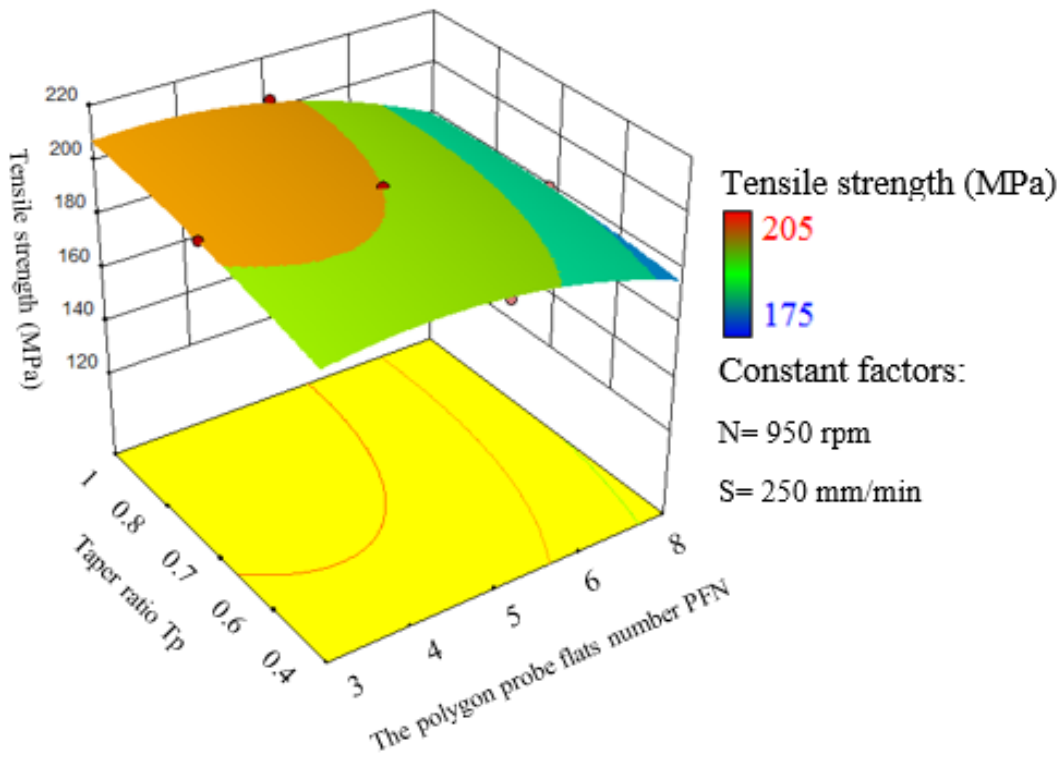


Figure 8-6. Response surface graphs for the effect of tool profile (PFN and Tp) on tensile strength.

## 8.2 Conclusion

DOE results for the effect of welding parameters and tool profiles on the transverse tensile strength have been analysed. The major finding from the present work can be summarized as follows:

1. It is evident that as welding speed increases from 150 mm/min to 200 mm/min, the tensile strength of the FSW welded aluminium alloy 6061-T6 increases and then decreases. At the highest welding speed (350 mm/min), lower tensile strength is observed due to increasing the flow rate of the soft material which leads to excess flash metal formation and large defect size.
2. It is obvious that rotational speed increases from 500 rpm to 1000 rpm, the transverse tensile strength of the FSW joint increases and then decreases. At the lowest welding rotational speed (500 rpm) and highest welding speed (1400 rpm), lower tensile strength is observed due to the insufficient frictional heat and increasing frictional heat generation respectively.
3. The tensile strength is increased by reducing PFN from 8 to 4 and then decreases. The lower tensile strength is observed when PFN is 8. Increasing PFN causes increasing the total heat generation and the flow rate of the soft material around the probe.
4. The tensile strength is slightly increased with increasing the taper ratio from 0.4 to 1 due to increasing the total heat generation.

## Chapter 9 : Validation of DOE results

### 9.1 Introduction

To validate the DOE results for axial force, peak temperature and tensile strength, extra work pieces welded by FSW with optimization levels of welding parameters and tool profile (straight square tool (SSQ), S = 200 mm/min, N= 1000 rpm). Straight tools (Hexagonal (SHex) and Octagonal (SOct)) were tested at the same welding parameters to validate DOE results. Friction stir welding simulation was carried out by using model 2 assumptions.

### 9.2 Validation axial force DOE results

The difference between the experimental and predicted (calculated value by equation (6.3)) axial force was checked by calculating SD, SEM, T-value and level of significance (P-value), all results are listed in Table 9-1. The differences for the results are considered to be very statistically significant that because the maximum P-value is 0.01 which is less than 0.05. So, the axial force DOE equation can be adopted to predict axial force at the design space.

Table 9-1. Paired SD, SEM difference, T-value and level of significance of the axial force.

Tool profile	Axial force (KN)		Paired difference		Paired T-value	Level of significance
	Experimental	Predicted	SD	SEM		P-Value
<b>SSQ</b>	6.06	6.04	0.0141	0.0100	605	0.0011
<b>SHex</b>	6.82	6.61	0.1485	0.1050	63.9524	0.01
<b>SOct</b>	7.19	7.03	0.1131	0.0800	88.8750	0.0072

### 9.3 Validation peak temperature DOE results

The difference between the modelling (COMSOL results in Figure 9-1) and predicted (calculated value by equation(7.3)) peak temperature was checked by calculating standard SD, SEM, T-value and level of significance (P-value), all results are listed in Table 9-2. These differences are considered to be very statistically significant that because the maximum

P-value is 0.0063, this value is less than 0.05. So, the peak temperature DOE equation can be adopted to predict the peak temperature at the design space.

Table 9-2. Paired SD, SEM difference, T-value and level of significance of the peak temperature.

Tool profile	Peak temperature (K)		Paired difference		Paired T-value	Level of significance
	Modelling	Predicted	SD	SEM		P-Value
<b>SSQ</b>	688	685	2.12	1.50	457.6667	0.0014
<b>SHex</b>	734	730	2.83	2.00	366.0000	0.0017
<b>SOct</b>	764	749	10.61	7.50	100.8667	0.0063

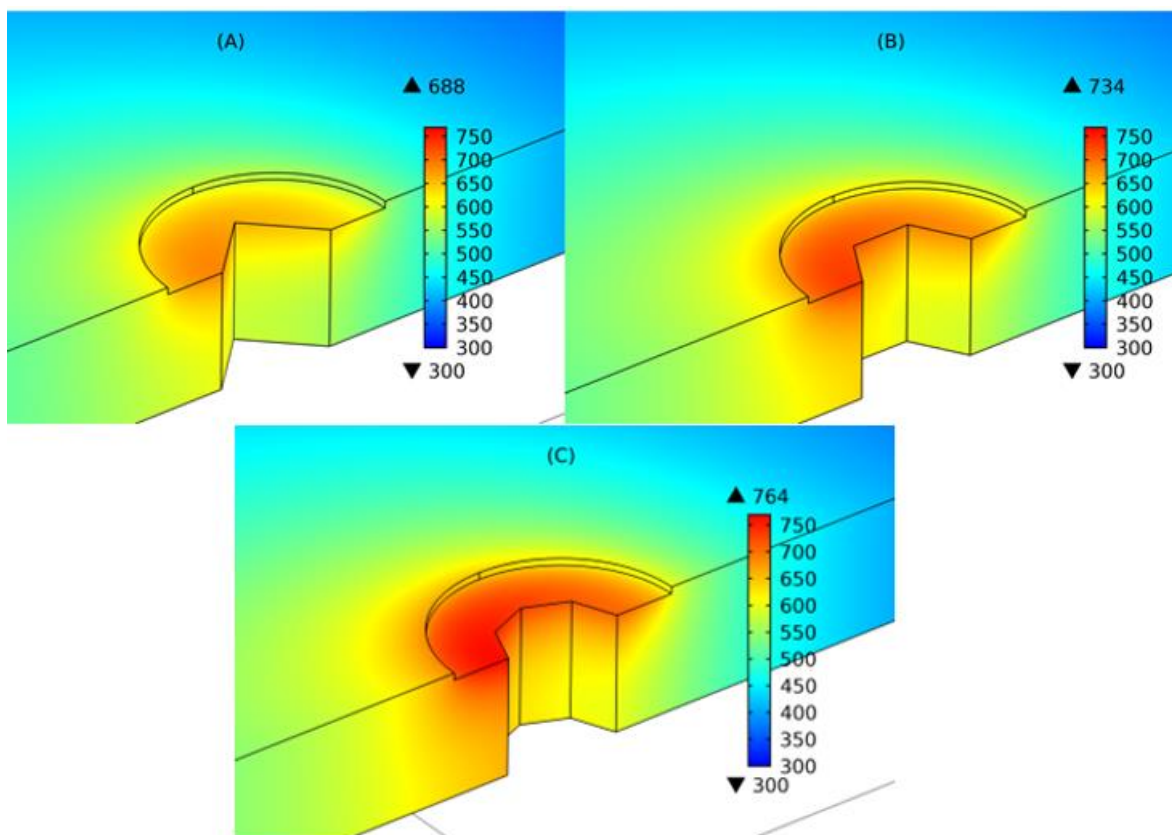


Figure 9-1. Isotherms temperature distribution for different probe profiles: A-SSQ, B- SHex, and C- SOct (model 2).

The peak temperature for SSQ is 80.46% from base metal melting point, this ratio increases to 89.35% by using SOct.

#### 9.4 Validation tensile strength DOE results

The transverse tensile strength results for validation DOE trials show in Figure 9-2. The difference in the transverse tensile test results of each trial was checked by calculating the mean of transverse tensile strength results (MTTS), SD, SEM, T-value and level of significance (P-value), all results are listed in Table 9-3. These differences are considered to be extremely statistically significant that because the maximum P-value is 0.0001 which is less than 0.05.

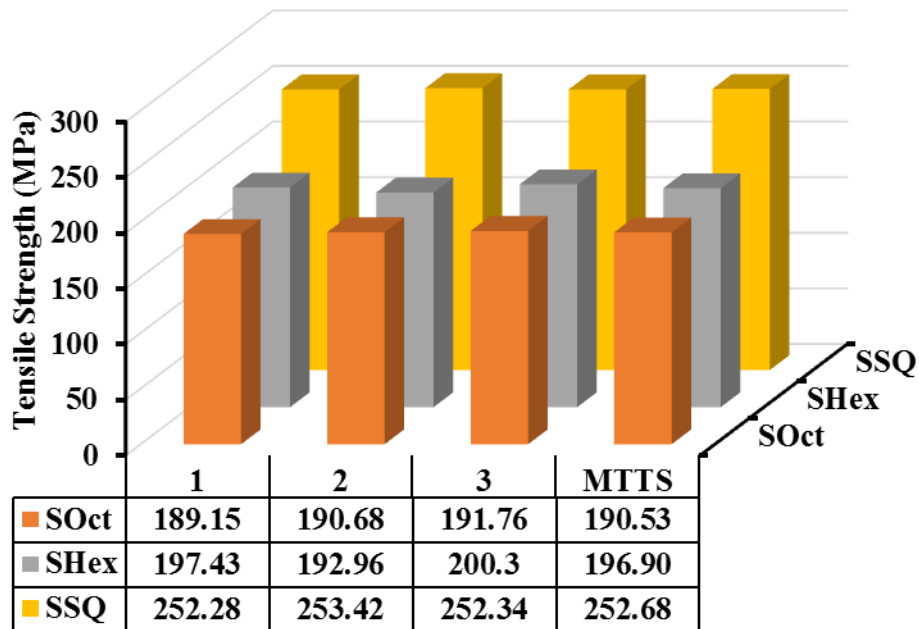


Figure 9-2. Transverse tensile strength for welding joints by SSQ, SHex and SOct tools.

From Figure 9-2, it can be seen the maximum value of MTTs is 252.68 MPa for joint welded by using optimum welding parameters ( $N=1000$  rpm,  $S=200$  mm/min) and tool profile (SSQ) according to predicted equation (8.3) and then decrease about 24.60% by increasing number of flats from 4 to 8.

Table 9-3. Mean, paired difference (SD and SEM), T-value and level of significance of the tensile test results.

Tool profile	Tensile test results (MPa)			MTTS (MPa)	Paired difference		Paired T-value	Level of significance P-Value
	1	2	3		SD	SEM		
<b>SOct</b>	189.15	190.68	191.76	190.53	1.31	0.76	251.64	<0.0001
<b>SHex</b>	197.43	192.96	200.3	196.90	3.70	2.13	92.20	0.0001
<b>SSQ</b>	252.28	253.42	252.34	252.68	0.64	0.37	682.17	<0.0001

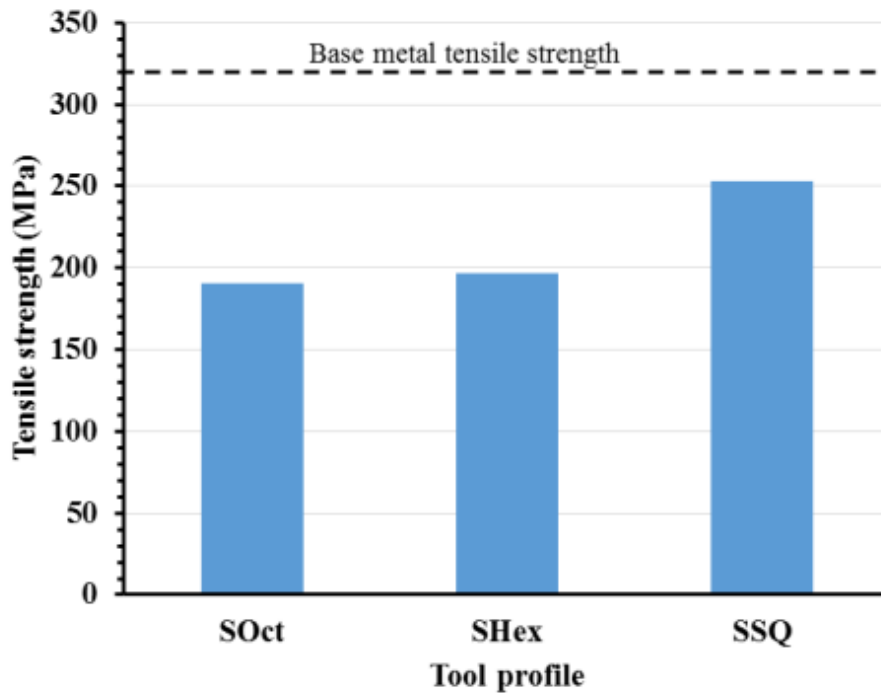


Figure 9-3. Comparison between the MTTTS of the joints welded by different tools with the tensile strength of base metal.

From Figure 9-3, it can be seen that the MTTTS increases 59.54% to 61.53% from the base metal tensile strength by decreasing the number of flats from 8 to 6, while it increases to 79% by decreasing the number of flats from 6 to 4. The MTTTS increases 32.62% by changing tool profile from SOct to SSQ.

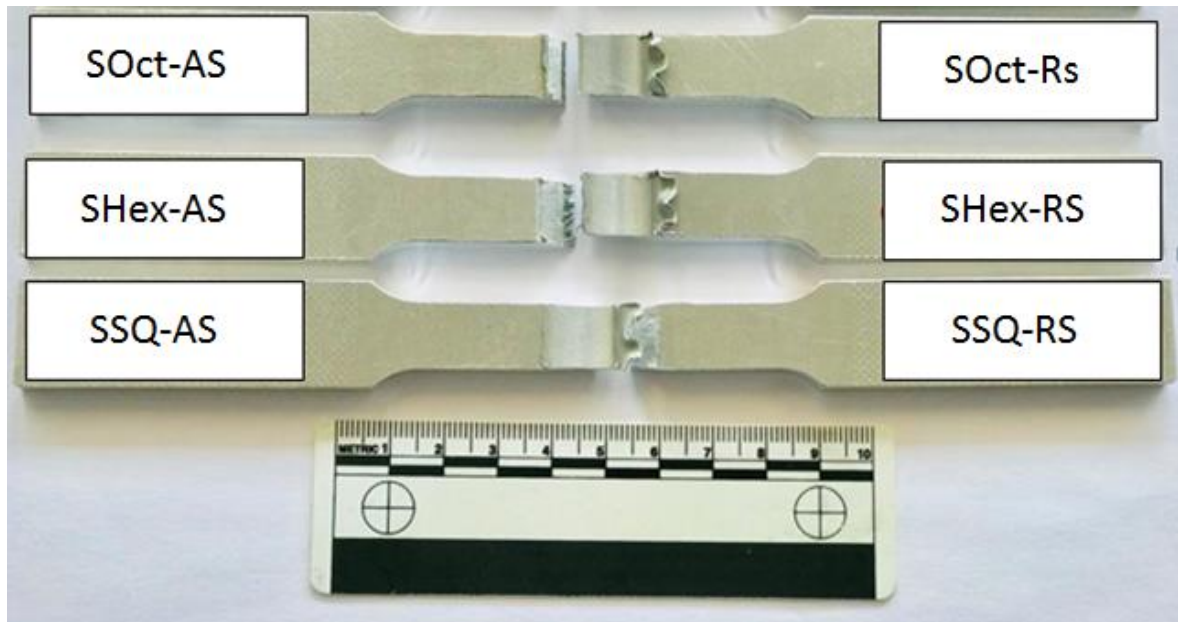


Figure 9-4. Tensile fracture appearances of FSW welds.

The macroscopic fracture appearance of the transverse tensile FSW welds specimens show in Figure 9-4. A typical shear fracture mode is invariably on the advancing side (AS) for SOct and SHex tool due to defect location in weld zone close to AS while the fracture location for SSQ tool is on the retreating side because this joint is free defect.

The difference between MTTs and predicted (calculated value by equation(8.3)) tensile strength was checked by calculating standard deviation SD, the standard error of the mean SEM, T-value and level of significance (P-value), all results are listed in Table 9-4. Although the difference of the SSQ is considered to be statistically significant, this difference is relatively large in comparison with the differences for other tools (SHex and SOct). The variation in P-Value is relatively large because the SSQ joint is free of defect while all other runs have defect.

Other differences are considered to be very statistically significant that because the maximum P-value is 0.0081, this value is less than 0.05. So, the tensile strength DOE model can be adopted to predict the tensile strength at the design space.

Table 9-4. Paired difference (SD and SEM), T-value and level of significance of the transverse tensile strength.

Tool profile	Peak temperature (K)		Paired difference		Paired T-value	Level of significance
	MTTS	Predicted	SD	SEM		P-Value
<b>SSQ</b>	252.68	215.95	25.9720	18.3650	12.7588	0.0498
<b>SHex</b>	196.90	201.97	3.5850	2.5350	78.6726	0.0081
<b>SOct</b>	190.53	188.43	1.4849	1.0500	180.4571	0.0035

## 9.5 Conclusion

The  $AF$ ,  $PT$  and  $\sigma_T$  DOE models results were validated. The major finding from this chapter can be summarized as follow:

- ❖ The differences between the experimental and predicted (calculated values by equation (6.3)) axial force are considered to be very statistically significant. So, the  $AF$  DOE equation can be adopted to predict the axial force.
- ❖ The differences between the modelling and predicted results (calculated values by equation (9.1)) of peak temperature are considered to be very statistically significant. So, the  $PT$  DOE equation can be adopted to predict the peak temperature at the design space.
- ❖ Although the difference between experiential and predicted tensile strength results for the SSQ is relatively large. The DOE equation for  $\sigma_T$  was predicted correct the optimum welding parameters and welding tool.
- ❖ The optimum welding joint results are:
  - The  $PT$  for SSQ is 80.46% form base metal melting point. This percentage is closer to 80% in comparison with SHex and SOct tools. Therefore, SSQ is preferable to join 6061-T6.
  - The MTTTS increases to 32.62% by change tool profile from straight octagonal (SOct) to straight square (SSQ)
  - The MTTTS increases to 79% by decreasing the number of flats from 6 to 4.

# Chapter 10: Effect of tool profile on heat distribution, microstructure and mechanical properties

## 10.1 Introduction

This chapter presents the effect of tool profile on microhardness, macrostructure, microstructure, weld zone tensile strength and heat distribution.

## 10.2 Microhardness results

Figure 10-1 shows microhardness map for DOE validation trials (SOct, SHex and SSQ), it can be seen that the hardness range in the welding centre line of all validation runs is from 87 HV near the shoulder interface to 64 HV near the probe tip interface; in contrast to a mid-thickness of work piece hardness range which is from 67 to 108 HV.

The SSQ joint is free defect joint because it has homogenous hardness distribution at the stirring probe zone. This joint has narrow HAZ and TMAZ in advancing side (AS) comparing with retreating side (RS) that explain the tensile shear fracture in RS.

SHex and SOct joints have nonhomogeneous hardness distribution in the stirring probe zone because of increasing heat input and string action. High string action leads to form defect close to root joint in AS that explain the tensile shear fracture at the edge of welding zone (WZ).

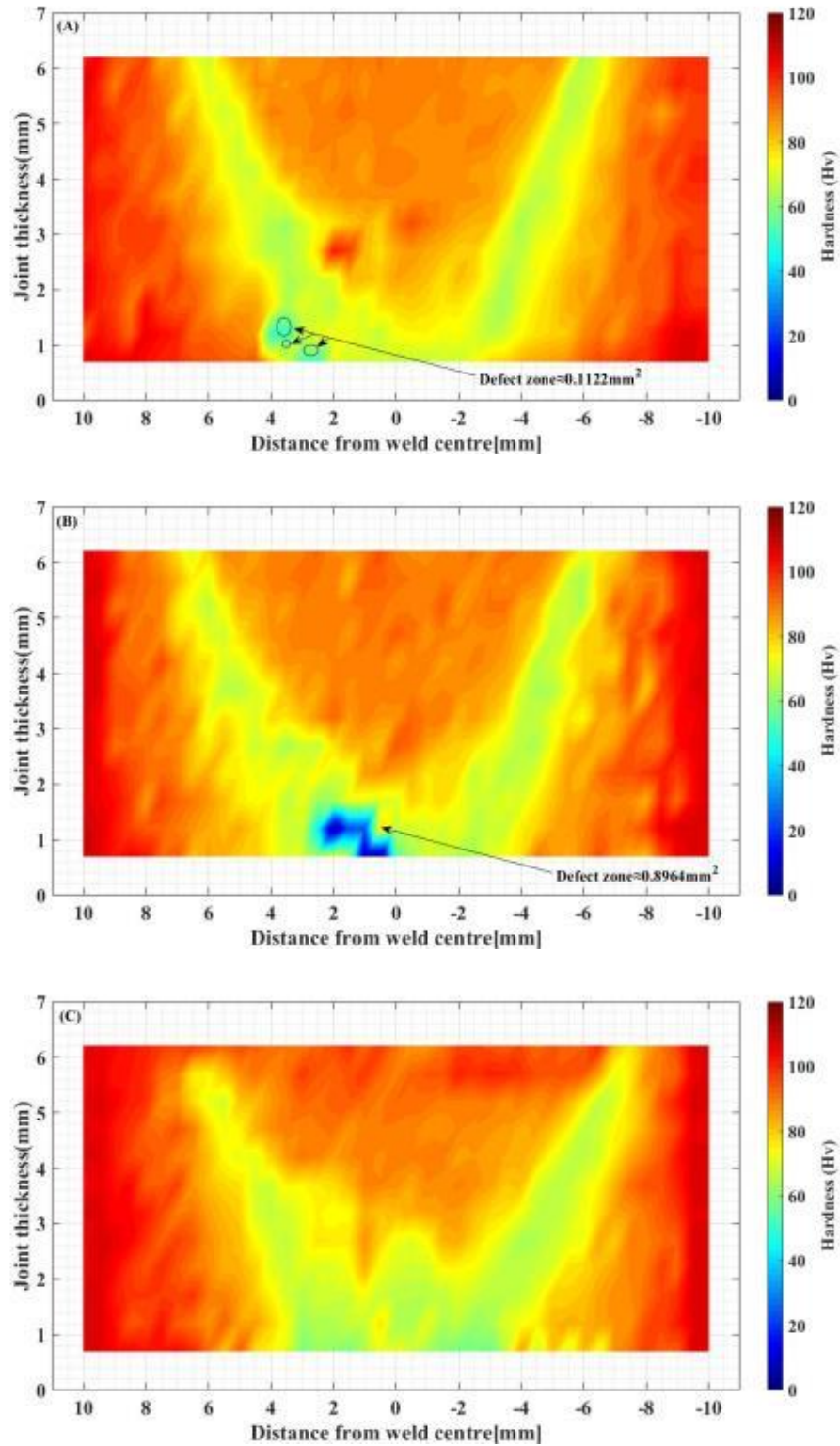


Figure 10-1. Corresponding 2D microhardness map for different tool profiles: (A) SOct, (B) SHex and (C) SSQ.

### 10.3 Macrostructure and CT scan

Macrostructure and CT scan test were carried out to show defect types in practical DOE trial. According to welding parameters and tool profile for DOE trials, there are three possible defect types: insufficient heat input defect, excess heat input defect and abnormal stirring defect. One case from each defect type presents in this section.

Figure 10-2 shows macrostructure and CT scan images for Run2 in DOE matrix. It can be seen that inner defect was formed as a tunnel defect because of an excess heat input which generated with higher rotation speed and lower welding speed.

Figure 10-3 shows macrostructure and CT scan images for Run3 in DOE matrix. It can be seen that inner defect was formed as a wormhole defect because of an insufficient heat input with lower rotation speed and higher welding speed.

Figure 10-4 shows macrostructure and CT scan images for Run18 in DOE matrix. It can be seen that inner defect was formed as a tunnel defect due to the high stir action as a result of higher rotation and welding speed.

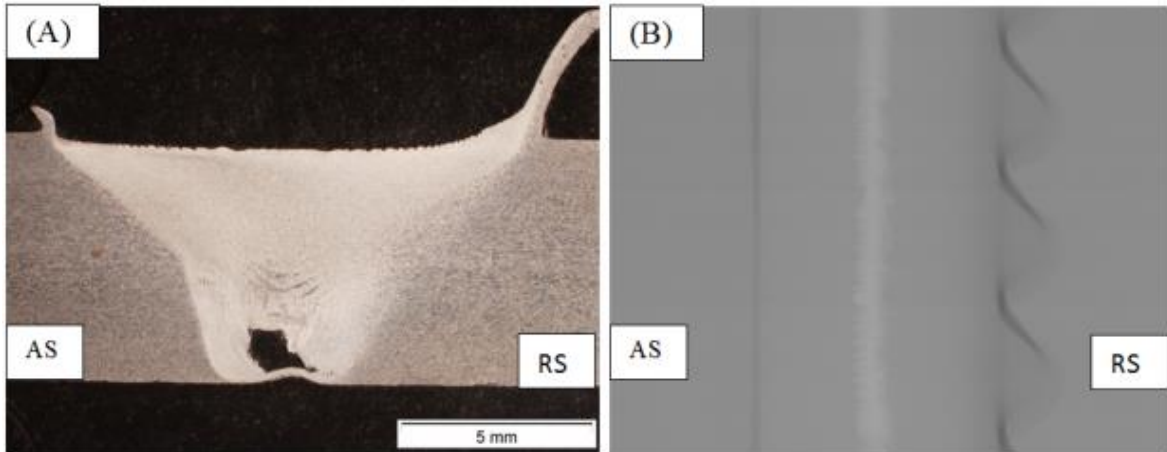


Figure 10-2. 2D images of Run2 (A) Microstructure and (B) CT scan.

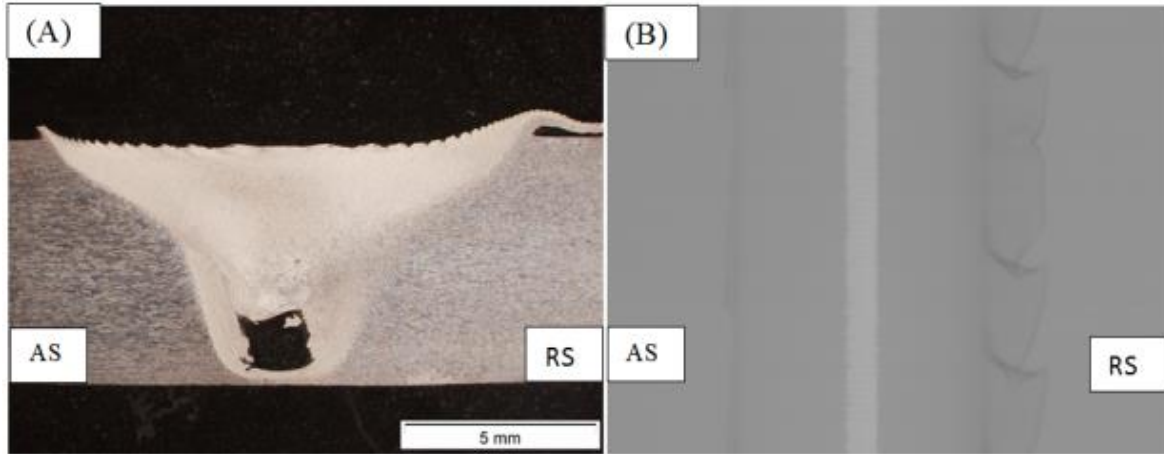


Figure 10-3. 2D images of Run3 (A) Microstructure and (B) CT scan.

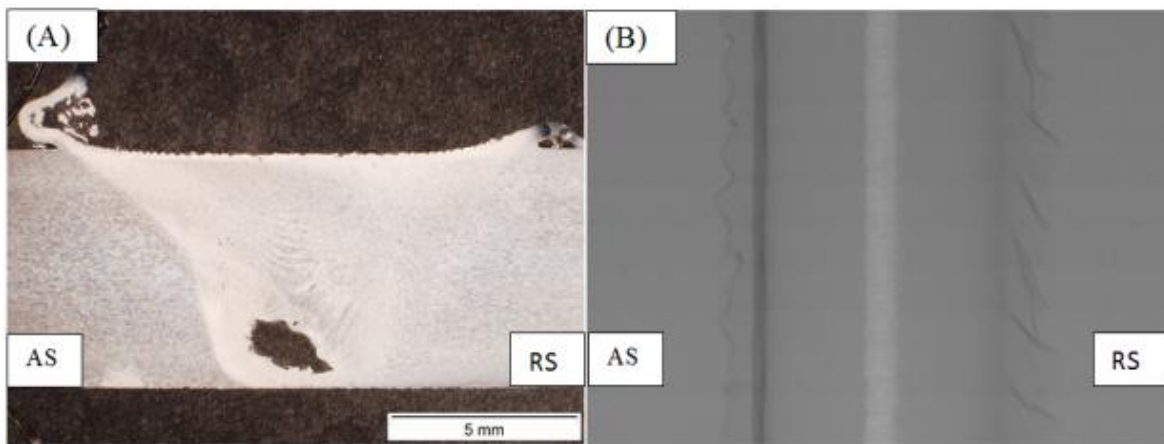


Figure 10-4. 2D images of Run18 (A) Microstructure and (B) CT scan.

For validations trial, Figure 10-5 displays macrostructure and CT scan images for optimum friction stir welding condition ( $N=1000$  rpm,  $S=200$  mm/min and SSQ). It can be seen that this welding joint is a free defect with good surface conditions and homogenous welding zone.

Figure 10-6 displays macrostructure and CT scan images for SHex joint which welded by optimum welding parameters. It can be seen the tunnel defect that because increasing the heat input and stir action. This joint has good surface conditions but there is abnormal stirring in welding zone.

Figure 10-7 displays macrostructure and CT scan images for SOct joint which welded with optimum welding parameters. It can be seen the inner defect because of the high stir action with increasing number of flats to 8. This higher level of stir action causes nonhomogeneous welding zone and observing waves action on the shoulder interface.

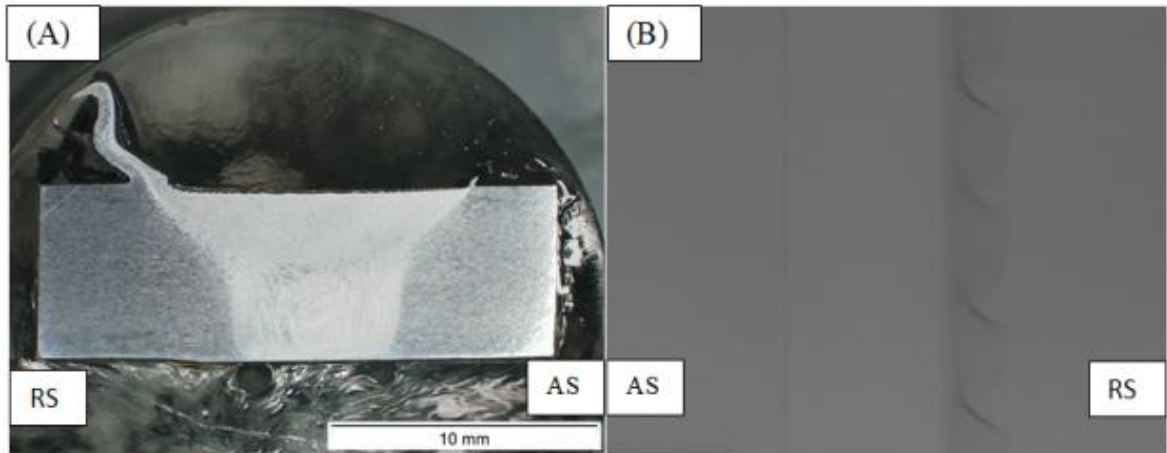


Figure 10-5. 2D images of SSQ joint (A) Microstructure and (B) CT scan.

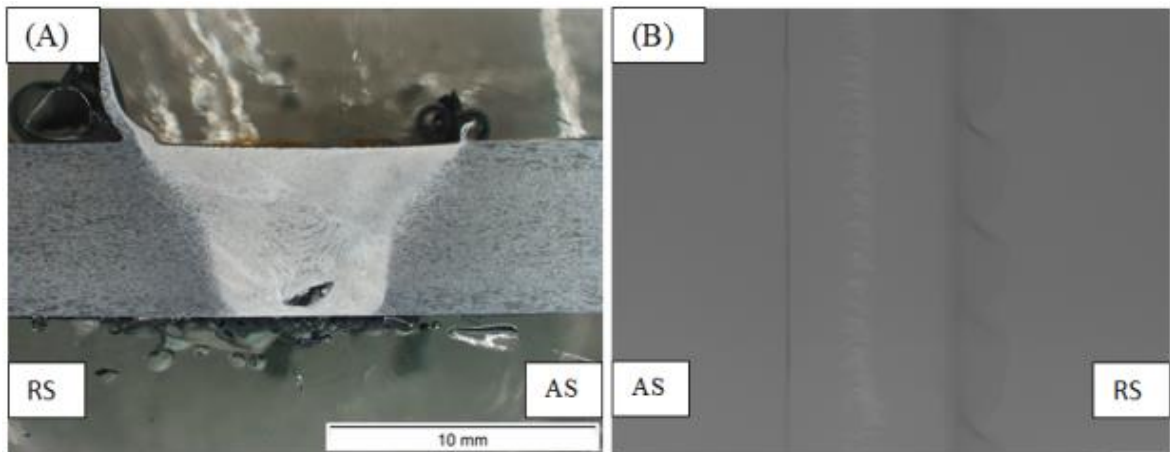


Figure 10-6. 2D images of SHex joint (A) Microstructure and (B) CT scan.

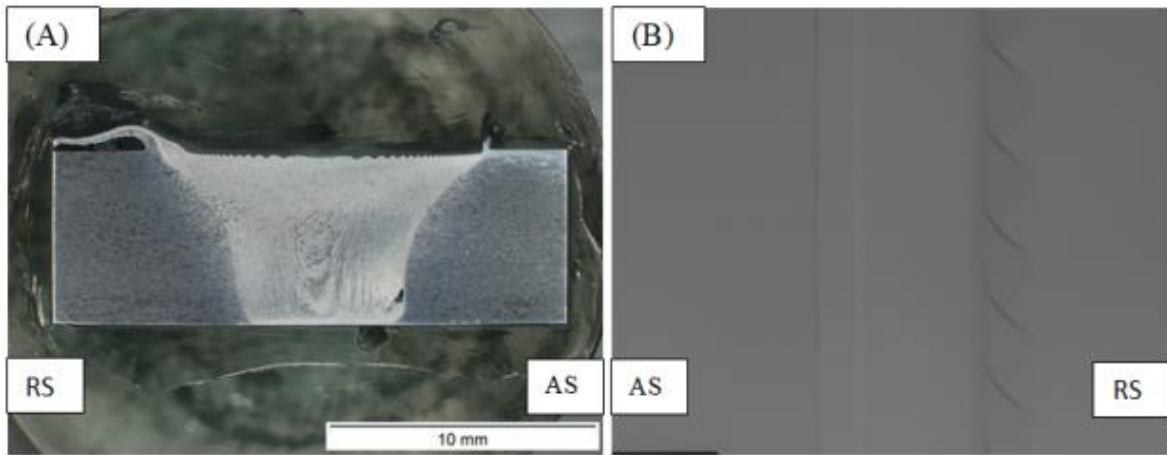


Figure 10-7. 2D images of SOct joint (A) Microstructure and (B) CT scan.

#### 10.4 Microstructure for optimum condition trial

The effect of SSQ tool on the material flow profile, grain size and its orientation detects in Figure 10-8 by using optical microscope.

Figure 10-8 (A) shows the microstructure at the RS region from the effect of shoulder to the base metal. Higher stir action, high heat input and high cooling rate cause finer grains size and narrow HAZ width.

Figure 10-8 (B) shows the microstructure for the effect of change stir action from shoulder to probe at RS region. High stir action, reducing the heat input slightly comparison with region (A) and lower cooling rate produce fine grains size and wider HAZ.

Figure 10-8 (C) shows the microstructure at the RS region from the effect of probe tip to the base metal. The vortexes between different layers were observed as a result of stir action by tool tip. The HAZ was a very narrow.

Figure 10-8 (D) shows the microstructure for the effect of shoulder interface on stir zone centre. A higher heating rate in this region causes a larger grain size.

Figure 10-8 (E) shows the microstructure of WZ region closed to tool tip. A homogenous material flow leads to produce finer grain size.

Figure 10-8 (G) shows the microstructure at the AS region from the effect of shoulder to the base metal. Higher stir action, high heat input and higher cooling rate cause finer grains and very narrow HAZ width.

Figure 10-8 (H) shows the microstructure for the effect of change stir action from shoulder to probe at AS region. A higher stir action in the TMAZ and lower heating rate cause smaller HAZ comparing with the same region in RS

Figure 10-8 (F) shows the microstructure at the AS region from the effect of probe tip to the base metal. A wide range of grains size in the probe tip material flow region was observed because there are many rotation layers which were formed by stirring action.

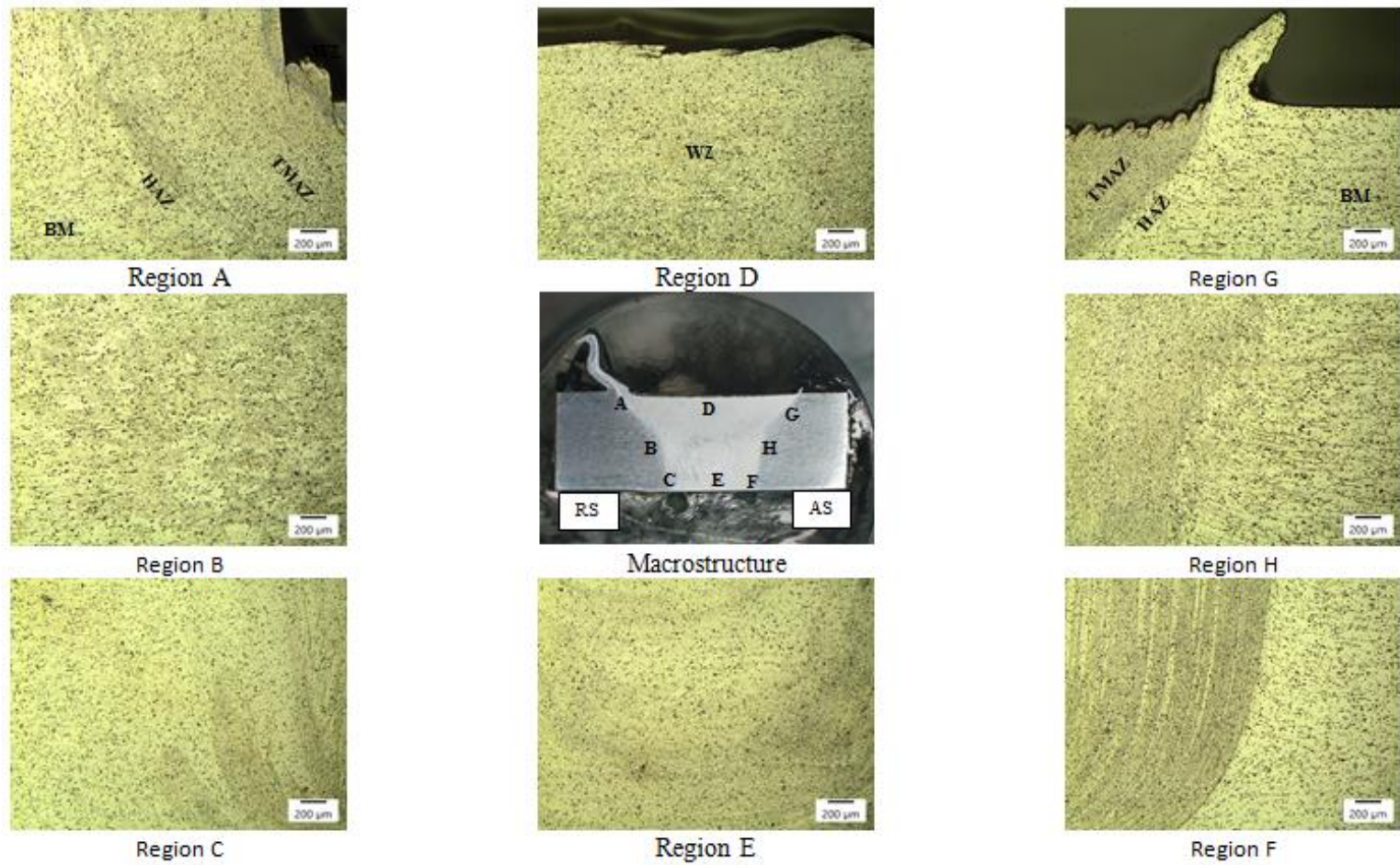


Figure 10-8. Microstructure of SSQ joints.

## 10.5 Weld zone tension testing

Tensile test for Welding zone was carried out to evaluate the effect of welding defect on the tensile strength for DOE validating trials (SSQ, SHex and SOct). The welding zone tensile strength results for validation DOE trials show in Figure 10-9. The difference in the tensile test results of each trial was checked by calculating mean welding zone tensile strength results (MWZTS), SD, the standard error of the mean SEM, T-value and level of significance (P-value), all results are listed in Table 10-1. These differences are considered to be extremely statistically significant as a result of maximum P-value is 0.0003 which is less than 0.05.

Table 10-1. MWZTS, paired difference (SD and SEM), T-value and level of significance.

Tool profile	Tensile test results (MPa)			MWZTS (MPa)	Paired difference		Paired T-value	Level of significance
	1	2	3		SD	SEM		P-Value
<b>SOct</b>	268.46	270.01	269.39	269.29	0.78	0.45	597.86	<0.0001
<b>SHex</b>	279.69	289.79	274.31	281.26	7.86	4.54	61.99	0.0003
<b>SSQ</b>	295.21	293.81	294.39	294.47	0.70	0.41	725.0815	<0.0001

Figure 10-9 shows the welding zone tensile strength for samples welded by different straight tool profiles. It can be seen that the tensile strength increases 4.45% by decreasing the number of flats on pin surface from 8 to 6, while it increases 4.69% by decreasing the number of flats from 6 to 4. So, the defects in SOct and SHex joints have the major effect of variation in MTTs results.

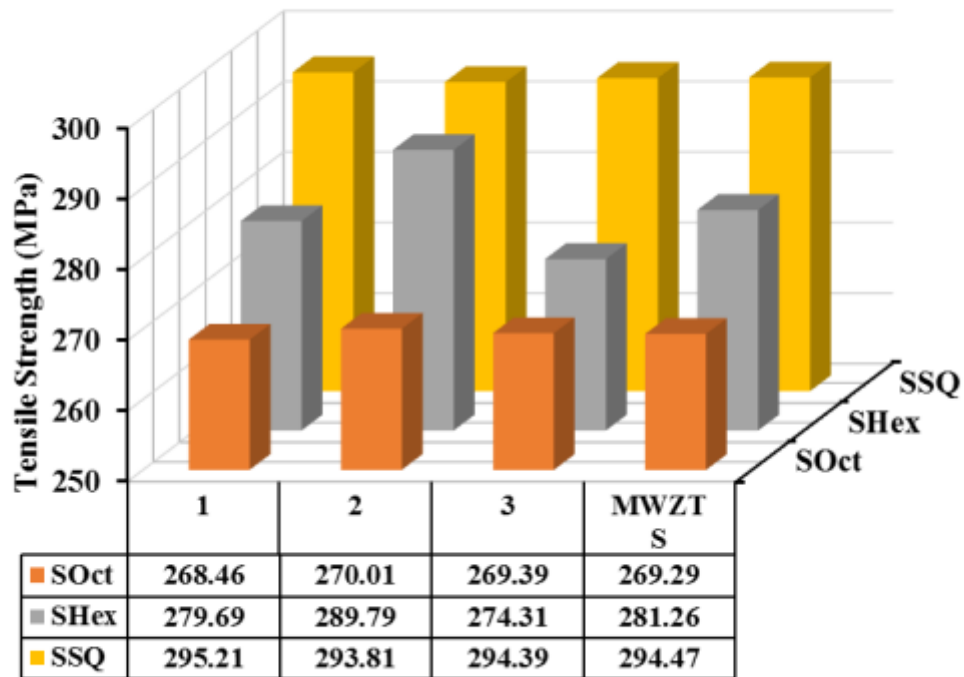


Figure 10-9. Welding zone tensile strength for welding joints by SSQ, SHex and SOct tools.

Figure 10-10 compares the MWZTS of the joints for different straight tool profiles with the tensile strength of the base metal (6060-T6). It can be seen that the tensile strength increases 84.15% to 87.89% from the base metal tensile strength by decreasing the number of flats from 8 to 6, while it increases to 92.02% by decreasing the number of flats from 6 to 4. Figure 10-11 shows the variation between MTTS and MWZTS for DOE validation runs. It can be seen that the variation between the MTTS and MWZTS slightly increases from 41.33% to 42.84% by decreasing number of flats on probe lateral surface from 8 to 6. In contrast, SSQ showed the lowest variation (16.53%) compared with other tools because the SSQ tool generates sufficient heat input and homogenous material flow to produce a sound and defect-free weld.

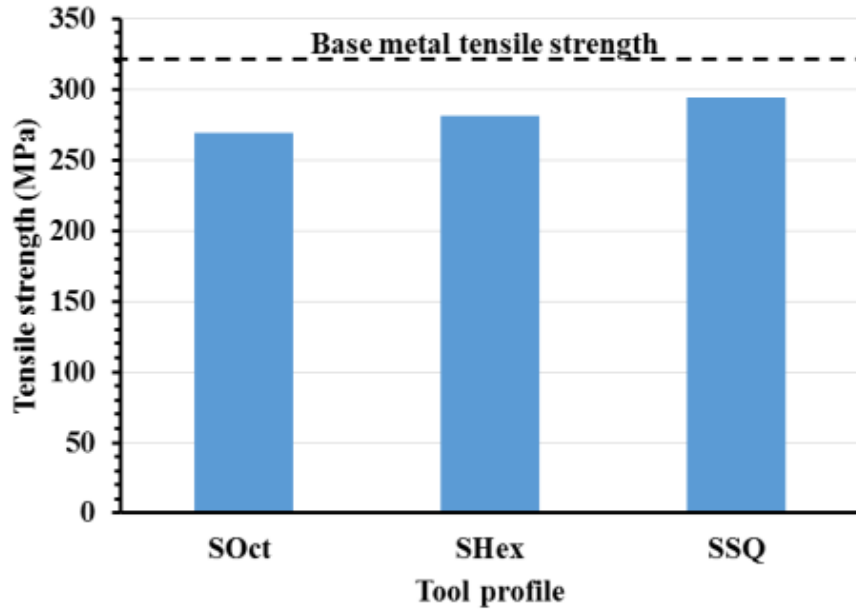


Figure 10-10. Comparison between MWZTS of the joints welded by different tools with the tensile strength of base metal.

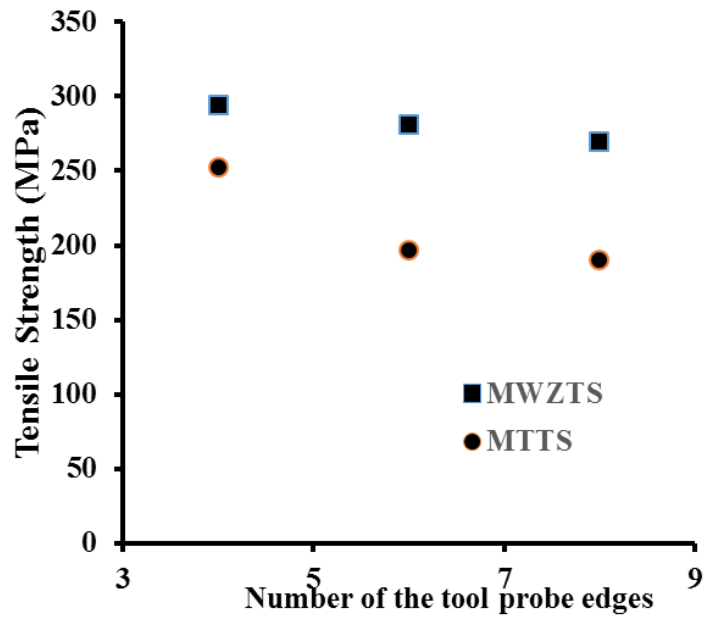


Figure 10-11. Comparison among the MTTS and MWZTS.

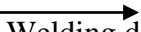
## **10.6 The effect of tool profile on temperature distribution**

Thermal contours on the 6 mm, 3mm and 0mm planes of the welding joint thickness around the STR, SSQ, SPen, SHex and SOct tools are shown in Figures ((10-12)– (10-16)), respectively. The black circle and the black polygonal lines in figures illustrate the outline of the tool. Two important findings can be observed in these figures.

Firstly, there is a difference in density of the isothermal contours between tool leading edge and tool trailing edge. For the 6mm plane, thermal contours are compressed closing to the rear probe edge and expanded at the front edge because of the higher effect for shoulder heat generation.

This effect reduces through the joint thickness, at the tip interface of the tool (the 0mm plane), the contours are expanded closing to the rear probe edge and compressed at the front edge.

Secondly, the contours at shoulder interface are not concentric with the tool outline. The peak temperature of the thermal profile is located at the tool rear between the trailing probe edge and the trailing shoulder edge.

Direction of rotation  Welding direction 

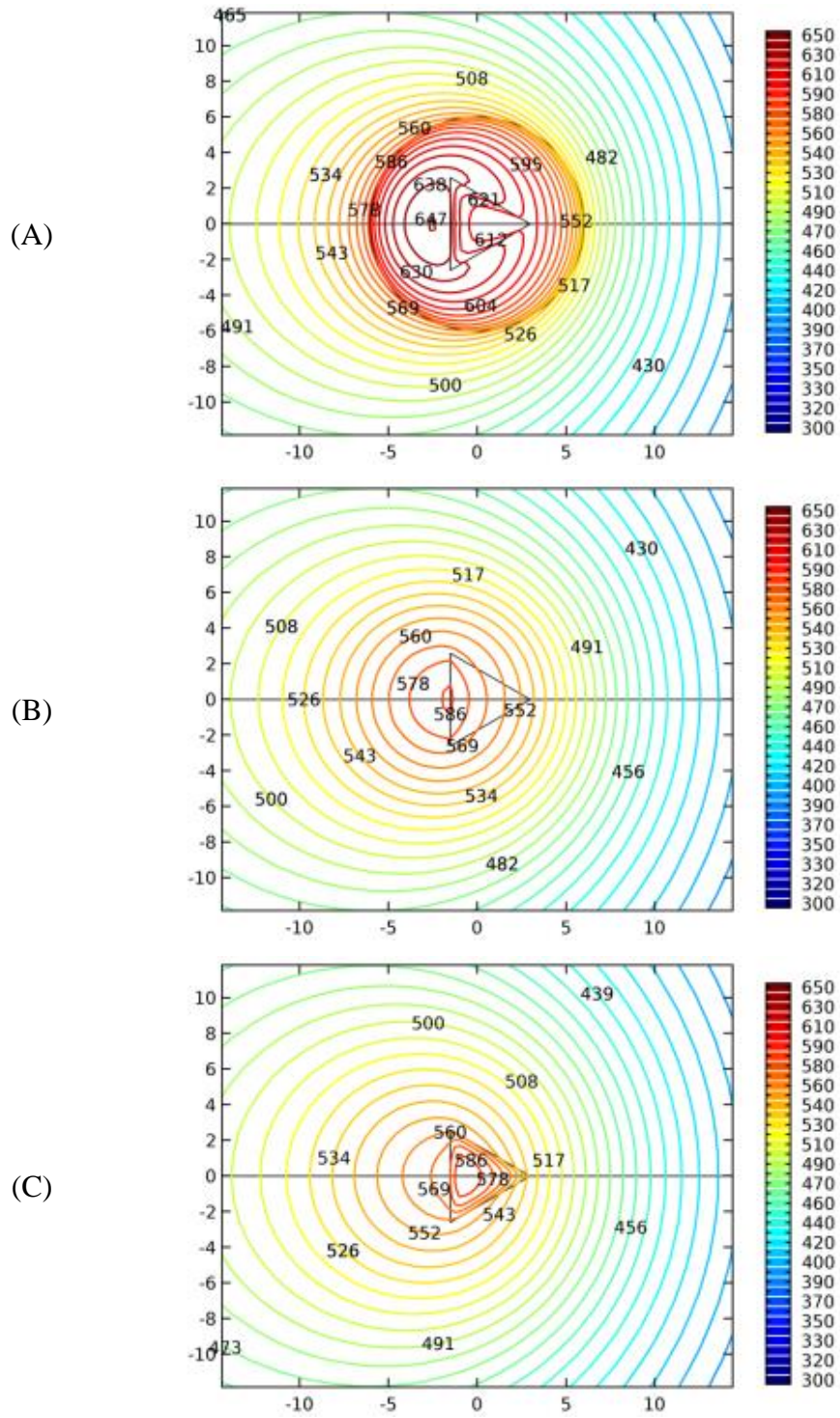
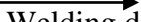


Figure 10-12. Temperature contours for STR joint at different planes in the work piece thickness: (A) 6mm, (B) 3mm and (C) 0 mm.

Direction of rotation  Welding direction 

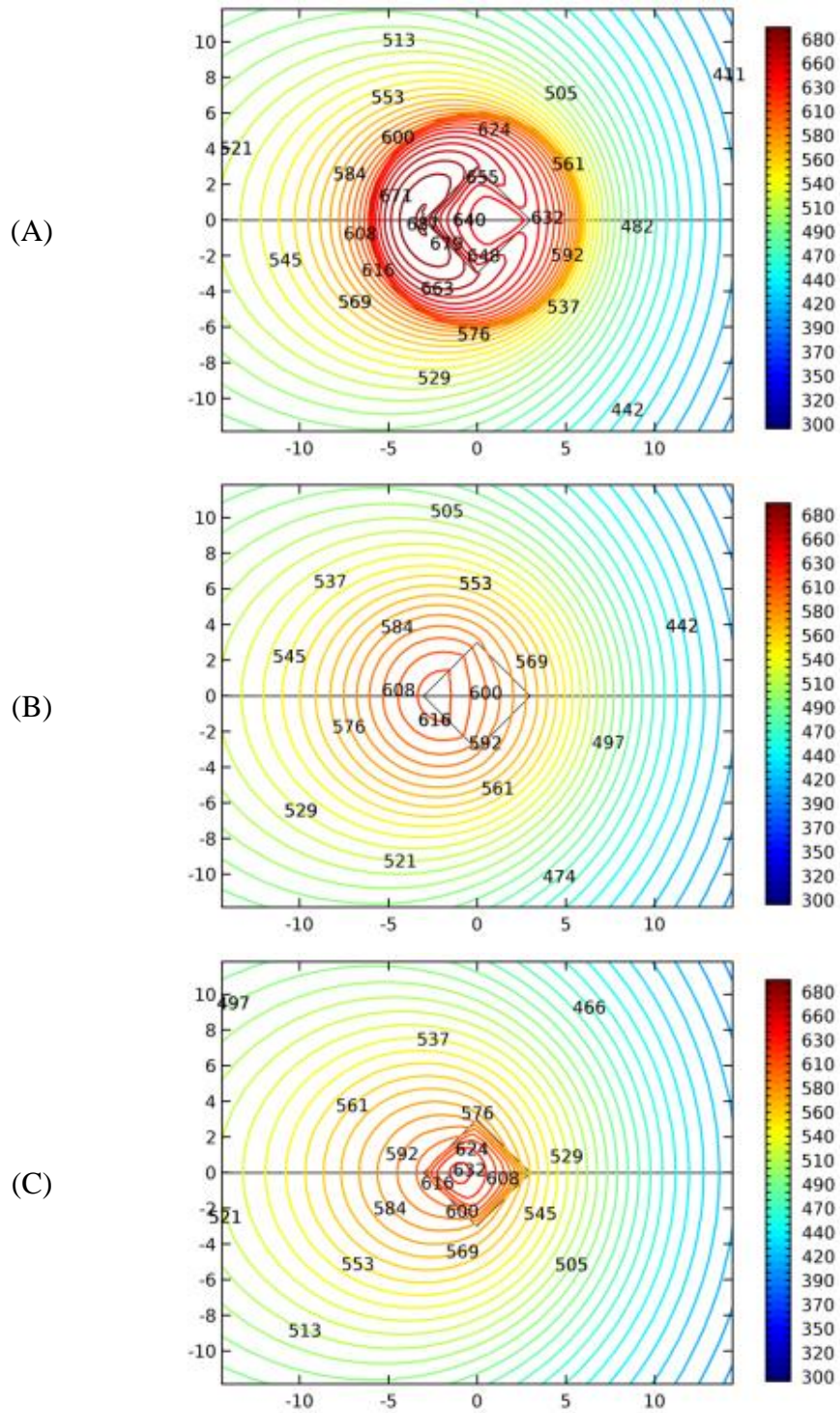
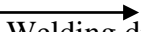


Figure 10-13. Temperature contours for SSQ joint at different planes in the work piece thickness: (A) 6mm, (B) 3mm and (C) 0 mm.

Direction of rotation  Welding direction 

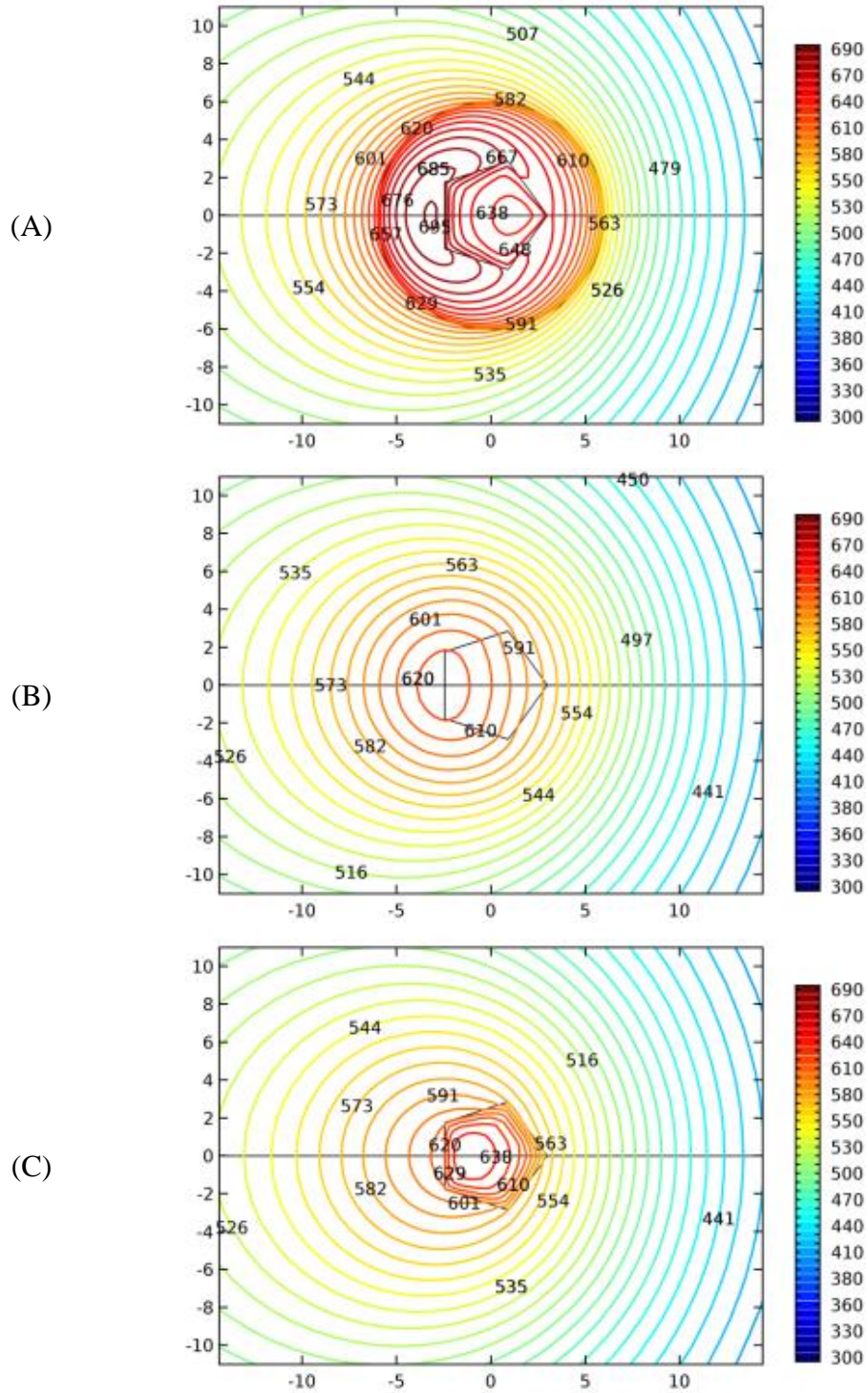
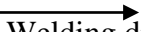


Figure 10-14. Temperature contours for SPen joint at different planes in the work piece thickness: (A) 6mm, (B) 3mm and (C) 0 mm.

Direction of rotation  Welding direction 

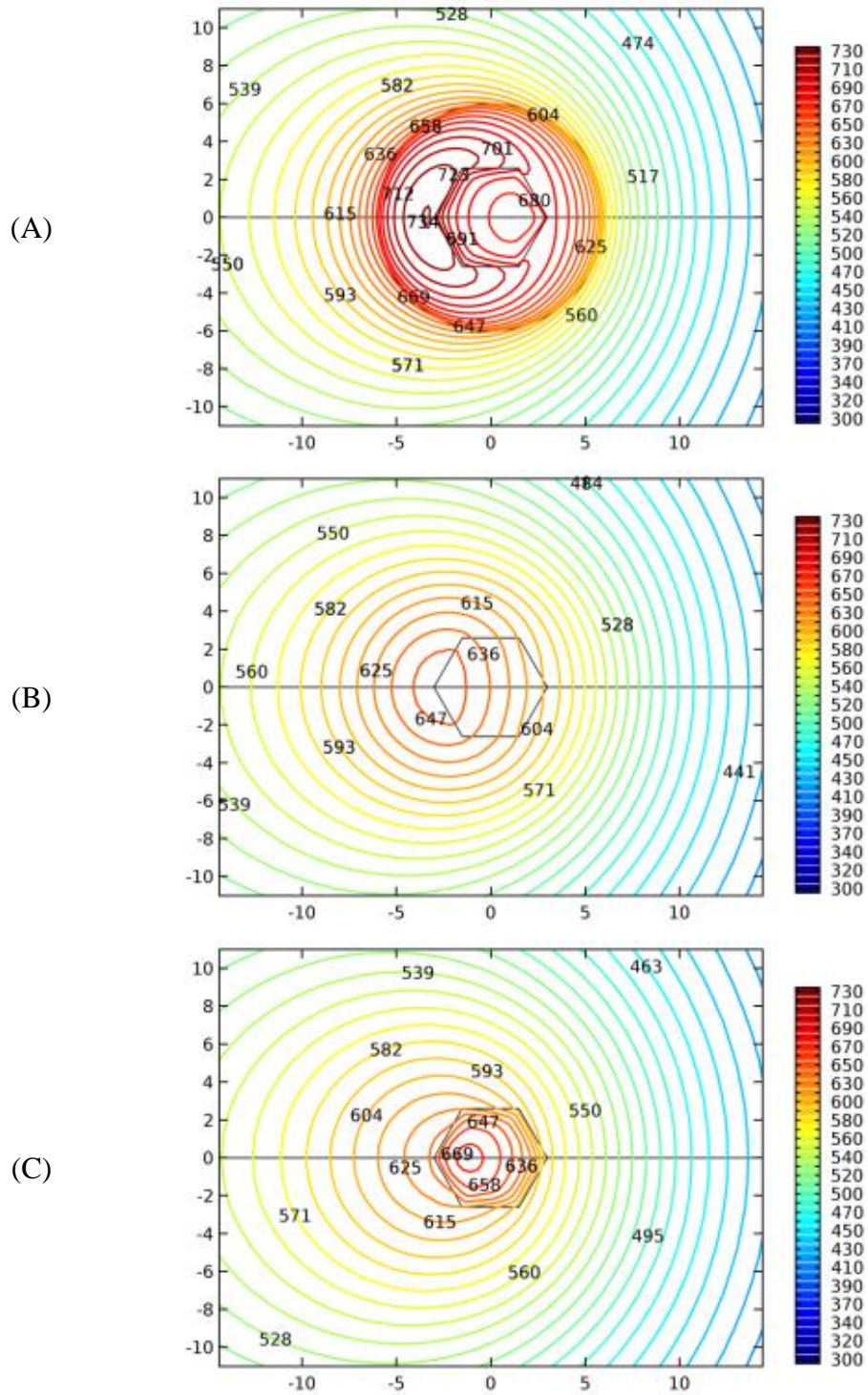


Figure 10-15. Temperature contours for SHex joint at different planes in the work piece thickness: (A) 6mm, (B) 3mm and (C) 0 mm.

Direction of rotation  Welding direction 

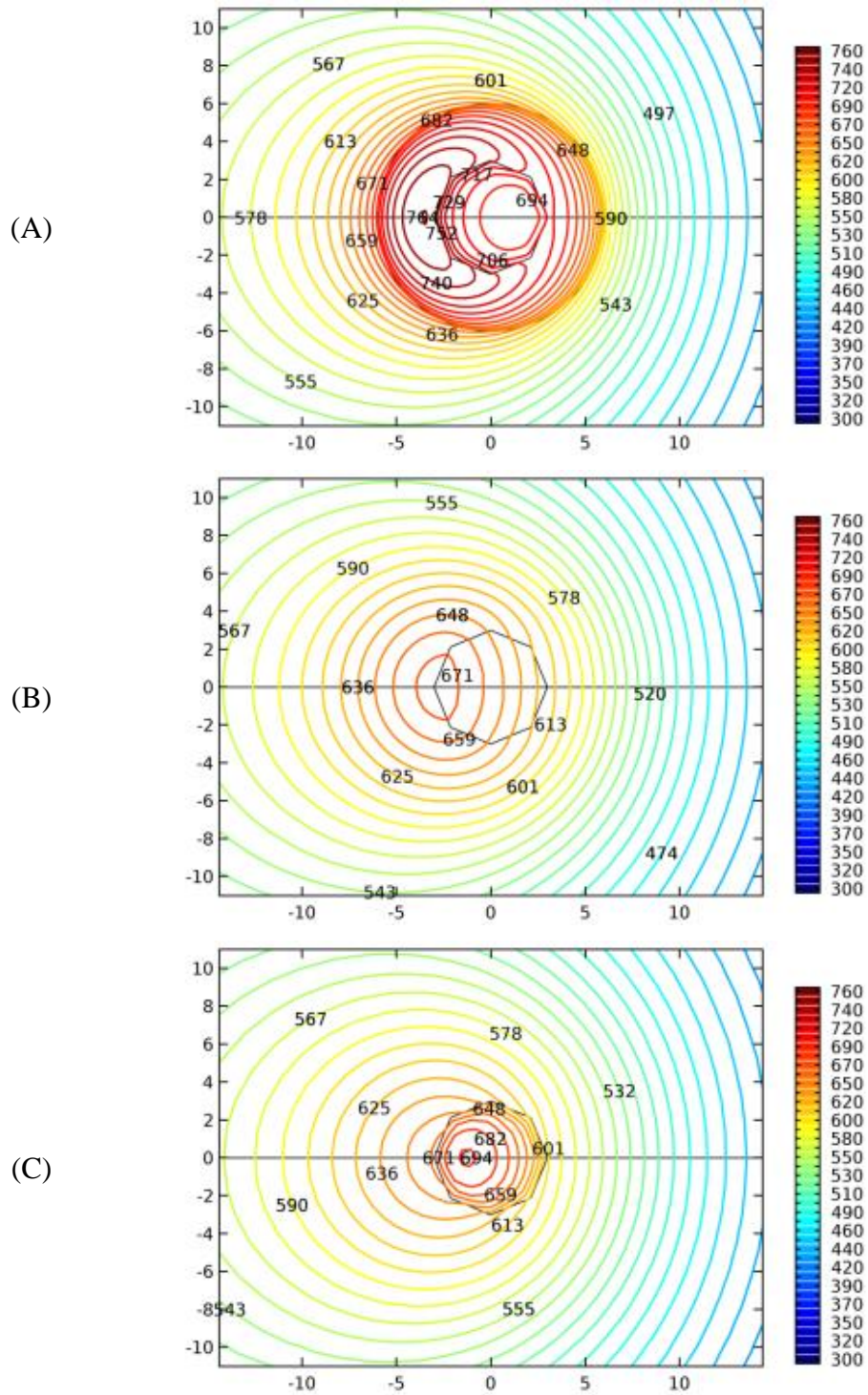


Figure 10-16. Temperature contours for SOct joint at different planes in the work piece thickness: (A) 6mm, (B) 3mm and (C) 0 mm.

## 10.7 Conclusion

This chapter studies the effect of tool geometry on the quality of 6061-T6 aluminium joint.

Important conclusions from this chapter are:

- ❖ SSQ tool profile produced defect free joint because the heat input increases the peak temperature to 80.46% base metal melting point and SSQ tool profile has homogenous material flow leads to reducing formation flash material.
- ❖ For SSQ joint, finer grain size in the prob stir zone compare with shoulder stir zone due to increasing heating rate close to shoulder interface which causes grain growth. The stirring action causes refine the grain size in probe stir zone.
- ❖ SSQ tool produces symmetry in hardness profiles across the welding joint. The welding zone has homogenous hardness distribution in shoulder and probe stirring zones. This joint has narrow HAZ and TMAZ in AS comparing with RS.
- ❖ The joint welded by using SSQ tool with optimum welding parameters showed higher tensile strength in WZ.
- ❖ The peak temperature in the WZ is located at the rear shoulder interface between trailing probe edge and trailing shoulder edge.

# Chapter 11: Conclusion and future work

## 11.1 Conclusion

The geometry of the FSW tool was studied in this work during the FSW of 6061-T6 aluminum alloys. The heat generation equations for taper and straight tools were derived and implemented in COMSOL to investigate the effect of change tool profile on heat generation and distribution. Based on the obtained results, the following conclusions can be outlined.

The welding parameters (N and S) significantly affect on AF. The increase of AF by change tool profile (PFN and Tp) should be considered to prevent the excess heat input. i.e. increasing the AF by increasing PFN and Tp requires adjusting the welding parameters to obtain the appropriate welding temperature to produce a sound and defect-free weld.

The total heat generation increases with increasing the polygon probe flats number from 3 to 8 and the taper ratio from 0.4 to 1 due to increasing the heat generation equation factors for probe side and probe tip (F2 and F3). Despite, the shoulder heat generation conurbation is decreased by increasing the subtracted heat generated of probe base area (F1).

The trend and behaviour of modelling temperature is very close to the experimentally temperature. This implies that heat generation equations, as well as the heat transfer model are adequate to predict heat generation and distribution during FSW of aluminium alloy.

The peak temperature increases around 19% by increasing the number of probe flats from 3 to 8, and the taper ratio changes from 0.4 to 1. So, the peak temperature can be correlated with respective FSW tool profile. This relationship can be used to select the FSW tool to produce the superior mechanical properties for aluminium joint.

The transverse tensile strength increases approximately 33% by changing the tool profile from straight octagonal (SOct) to straight square (SSQ) due to producing defect free joints with symmetric hardness profiles. The tensile strength of SSQ joint is 79% of base metal tensile strength were obtained using rotational speed of 1000 rpm, welding speed of 200 mm/min.

The optimum conditions (N = 1000 rpm, S = 200 mm/min and SSQ) were predicted according to DOE equation of tensile strength to obtain maximum tensile strength because these optimum conditions produce the sufficient peak temperature (80.46% from base metal melting point).

## **11.2 Future work**

1. Further work is needed to study the effect of change FSW tool profiles on heat generation and distribution for aluminium alloy by change the shoulder diameter.
2. More analysis is required to deeply understand the effect of change FSW tool profiles from taper to straight on heat distribution of aluminium alloy.
3. The microstructures associated with the hardness profile in FSW of aluminium alloy need to study by transmission electron microscopy (TEM) and orientation imaging microscopy (OIM).

## References

1. Mishra, R.S. and Z. Ma, *Friction stir welding and processing*. Materials Science and Engineering: R: Reports, 2005. **50**(1): p. 1-78.
2. Threadgill, P., et al., *Friction stir welding of aluminium alloys*. International Materials Reviews, 2013.
3. Tanwar, P. and V. Kumar, *Friction Stir Welding: Review*. International Journal of Enhanced Research in Science Technology & Engineering, 2014. **3**: p. 172-176.
4. Ji, S., et al., *Vertical compensation friction stir welding assisted by external stationary shoulder*. Materials & Design, 2015. **68**: p. 72-79.
5. Bastier, A., et al., *Steady state thermomechanical modelling of friction stir welding*. Science and Technology of Welding and Joining, 2006. **11**(3): p. 278-288.
6. Behnagh, R.A., M. Besharati Givi, and M. Akbari, *Mechanical properties, corrosion resistance, and microstructural changes during friction stir processing of 5083 aluminum rolled plates*. Materials and manufacturing processes, 2012. **27**(6): p. 636-640.
7. Mijajlović, M. and D. Milčić, *Analytical Model for Estimating the Amount of Heat Generated During Friction Stir Welding: Application on Plates Made of Aluminium Alloy 2024 T351*. Welding Processes, 2012: p. 247-274.
8. Nandan, R., T. DebRoy, and H. Bhadeshia, *Recent advances in friction-stir welding—process, weldment structure and properties*. Progress in materials science, 2008. **53**(6): p. 980-1023.
9. Zhang, Y., et al., *Review of tools for friction stir welding and processing*. Canadian Metallurgical Quarterly, 2012. **51**(3): p. 250-261.
10. Meilinger, Á. and I. Török, *The importance of friction stir welding tool*. Production Processes and Systems, 2013. **6**(1): p. 25-34.
11. Mehta, M., et al., *Tool geometry for friction stir welding—optimum shoulder diameter*. Metallurgical and Materials Transactions A, 2011. **42**(9): p. 2716-2722.
12. Xu, X., et al., *Microstructural Investigation of Friction-Stir-Welded 7005 Aluminum Alloy*. Journal of Materials Engineering and Performance, 2015. **24**(11): p. 4297-4306.

13. Tikader, S., P. Biswas, and A.B. Puri, *A study on tooling and its effect on heat generation and mechanical properties of welded joints in friction stir welding*. Journal of The Institution of Engineers (India): Series C, 2018. **99**(2): p. 139-150.
14. Hirasawa, S., et al., *Analysis of effect of tool geometry on plastic flow during friction stir spot welding using particle method*. Journal of Materials Processing Technology, 2010. **210**(11): p. 1455-1463.
15. Galvão, I., et al., *Influence of tool shoulder geometry on properties of friction stir welds in thin copper sheets*. Journal of Materials Processing Technology, 2013. **213**(2): p. 129-135.
16. Casalino, G., S. Campanelli, and M. Mortello, *Influence of shoulder geometry and coating of the tool on the friction stir welding of aluminium alloy plates*. Procedia Eng, 2014. **69**: p. 1541-1548.
17. Palanivel, R., et al., *Effect of tool rotational speed and pin profile on microstructure and tensile strength of dissimilar friction stir welded AA5083-H111 and AA6351-T6 aluminum alloys*. Materials & Design, 2012. **40**: p. 7-16.
18. Leal, R., et al., *Material flow in heterogeneous friction stir welding of thin aluminium sheets: effect of shoulder geometry*. Materials Science and Engineering: A, 2008. **498**(1-2): p. 384-391.
19. Teimurnezhad, J., H. Pashazadeh, and A. Masumi, *Effect of shoulder plunge depth on the weld morphology, macrograph and microstructure of copper FSW joints*. Journal of Manufacturing Processes, 2016. **22**: p. 254-259.
20. Badarinarayan, H., et al., *Effect of tool geometry on hook formation and static strength of friction stir spot welded aluminum 5754-O sheets*. International Journal of Machine Tools and Manufacture, 2009. **49**(11): p. 814-823.
21. Zhang, H., et al., *Microstructure–property characteristics of a novel non-weld-thinning friction stir welding process of aluminum alloys*. Materials & Design, 2015. **86**: p. 379-387.
22. Buffa, G., et al., *Design of the friction stir welding tool using the continuum based FEM model*. Materials Science and Engineering: A, 2006. **419**(1-2): p. 381-388.

23. Mironov, S., Y. Sato, and H. Kokawa, *Influence of welding temperature on material flow during friction stir welding of AZ31 magnesium alloy*. Metallurgical and Materials Transactions A, 2019. **50**(6): p. 2798-2806.
24. Nishihara, T. and Y. Nagasaka. *Development of micro-FSW*. in *Proceedings of the 5th International Symposium on Friction Stir Welding, Metz, France*. 2004.
25. Trueba, L., et al., *Effect of tool shoulder features on defects and tensile properties of friction stir welded aluminum 6061-T6*. Journal of Materials Processing Technology, 2015. **219**: p. 271-277.
26. Lumsden, J., G. Pollock, and M. Mahoney. *Effect of tool design on stress corrosion resistance of FSW AA 7050-T 7451*. in *Friction Stir Welding and Processing III as held at the 2005 TMS Annual Meeting*. 2005.
27. Dubourg, L., et al., *Process window optimization for FSW of thin and thick sheet Al alloys using statistical methods*. 2006.
28. Ahmed, M., et al., *Through-thickness crystallographic texture of stationary shoulder friction stir welded aluminium*. Scripta materialia, 2011. **64**(1): p. 45-48.
29. Li, D., et al., *Effect of welding parameters on microstructure and mechanical properties of AA6061-T6 butt welded joints by stationary shoulder friction stir welding*. Materials & Design, 2014. **64**: p. 251-260.
30. Li, D., et al., *Investigation of stationary shoulder friction stir welding of aluminum alloy 7075-T651*. Journal of Materials Processing Technology, 2015. **222**: p. 391-398.
31. Maltin, C.A., et al., *The potential adaptation of stationary shoulder friction stir welding technology to steel*. Materials & Design, 2014. **64**: p. 614-624.
32. Li, Z., et al., *Joint features and mechanical properties of friction stir lap welded alclad 2024 aluminum alloy assisted by external stationary shoulder*. Materials & Design, 2016. **90**: p. 238-247.
33. Zhou, Z., et al., *Effect of rotating speed on joint morphology and lap shear properties of stationary shoulder friction stir lap welded 6061-T6 aluminum alloy*. The International Journal of Advanced Manufacturing Technology, 2017. **88**(5-8): p. 2135-2141.

34. Jiang, X., B. Wynne, and J. Martin, *Microstructure and texture evolution of stationary shoulder friction stir welded Ti6Al4V alloy*. Science and Technology of Welding and Joining, 2015. **20**(7): p. 594-600.
35. Jiang, X., B.P. Wynne, and J. Martin, *A Microstructure and Crystallographic Texture Investigation of Stationary Shoulder Friction Stir Welding of Ti-6Al-4V*.
36. Saeidi, M., M. Barmouz, and M.K.B. Givi, *Investigation on AA5083/AA7075+ Al<sub>2</sub>O<sub>3</sub> joint fabricated by friction stir welding: characterizing microstructure, corrosion and toughness behavior*. Materials Research, 2015. **18**(6): p. 1156-1162.
37. Zhang, J., et al., *Investigation on dissimilar underwater friction stir lap welding of 6061-T6 aluminum alloy to pure copper*. Materials & Design, 2014. **64**: p. 74-80.
38. Dawes, C., et al., *Development of the new friction stir technique for welding aluminum phase II*. TWI member report, Cambridge, UK, 1995.
39. Hasan, A., et al., *A numerical methodology for predicting tool wear in Friction Stir Welding*. Journal of Materials Processing Technology, 2017. **241**: p. 129-140.
40. Packer, S. *Tool geometries and tool materials for friction stir welding high melting temperature materials*. in *Proceedings of the 1st International Joint Symposium on Joining and Welding*. 2013. Elsevier.
41. Padmanaban, G. and V. Balasubramanian, *Selection of FSW tool pin profile, shoulder diameter and material for joining AZ31B magnesium alloy—an experimental approach*. Materials & Design, 2009. **30**(7): p. 2647-2656.
42. Fujii, H., et al., *Effect of tool shape on mechanical properties and microstructure of friction stir welded aluminum alloys*. Materials Science and Engineering: A, 2006. **419**(1-2): p. 25-31.
43. Azizieh, M., A. Kokabi, and P. Abachi, *Effect of rotational speed and probe profile on microstructure and hardness of AZ31/Al<sub>2</sub>O<sub>3</sub> nanocomposites fabricated by friction stir processing*. Materials & Design, 2011. **32**(4): p. 2034-2041.
44. Mehta, M., et al., *Numerical modeling of friction stir welding using the tools with polygonal pins*. Defence Technology, 2015. **11**(3): p. 229-236.
45. Mugada, K.K. and K. Adepu, *Influence of ridges shoulder with polygonal pins on material flow and friction stir weld characteristics of 6082 aluminum alloy*. Journal of Manufacturing Processes, 2018. **32**: p. 625-634.

46. Patel, V.V., V. Badheka, and A. Kumar, *Effect of polygonal pin profiles on friction stir processed superplasticity of AA7075 alloy*. Journal of materials processing technology, 2017. **240**: p. 68-76.
47. Raturi, M., A. Garg, and A. Bhattacharya, *Joint strength and failure studies of dissimilar AA6061-AA7075 friction stir welds: Effects of tool pin, process parameters and preheating*. Engineering Failure Analysis, 2019. **96**: p. 570-588.
48. Hattingh, D., et al., *Characterization of the influences of FSW tool geometry on welding forces and weld tensile strength using an instrumented tool*. Journal of materials processing technology, 2008. **203**(1-3): p. 46-57.
49. Hasan, M.M., M. Ishak, and M. Rejab, *Effect of pin tool flute radius on the material flow and tensile properties of dissimilar friction stir welded aluminum alloys*. The International Journal of Advanced Manufacturing Technology, 2018. **98**(9-12): p. 2747-2758.
50. Fonda, R.W., J.F. Bingert, and K.J. Colligan, *Texture and grain evolutions in a 2195 friction stir weld*. 2004, Los Alamos National Laboratory.
51. Mugada, K.K. and K. Adepu, *Role of tool shoulder end features on friction stir weld characteristics of 6082 aluminum alloy*. Journal of The Institution of Engineers (India): Series C, 2019. **100**(2): p. 343-350.
52. Thomas, W.M., et al., *Friction stir welding tools and developments*. Welding in the World, 2003. **47**(11-12): p. 10-17.
53. Rai, R., et al., *friction stir welding tools*. 2011. **16**(4): p. 325-342.
54. Ma, Z., R.S. Mishra, and M.W. Mahoney, *Superplastic deformation behaviour of friction stir processed 7075Al alloy*. Acta materialia, 2002. **50**(17): p. 4419-4430.
55. Ma, Z., et al., *High strain rate superplasticity in friction stir processed Al-Mg-Zr alloy*. Materials Science and Engineering: A, 2003. **351**(1): p. 148-153.
56. Su, J.-Q., et al., *Microstructural investigation of friction stir welded 7050-T651 aluminium*. Acta materialia, 2003. **51**(3): p. 713-729.
57. Threadgill, P., et al., *Friction stir welding of aluminium alloys*. International Materials Reviews, 2009. **54**(2): p. 49-93.
58. Arbegast, W.J., *A flow-partitioned deformation zone model for defect formation during friction stir welding*. Scripta materialia, 2008. **58**(5): p. 372-376.

59. Al-Moussawi, M. and A. Smith, *Defects in friction stir welding of steel*. *Metallography, Microstructure, and Analysis*, 2018. **7**(2): p. 194-202.
60. Ajri, A. and Y.C. Shin, *Investigation on the effects of process parameters on defect formation in friction stir welded samples via predictive numerical modeling and experiments*. *Journal of Manufacturing Science and Engineering*, 2017. **139**(11).
61. Kim, Y., et al., *Three defect types in friction stir welding of aluminum die casting alloy*. *Materials Science and Engineering: A*, 2006. **415**(1-2): p. 250-254.
62. Mishra, R.S. and M.W. Mahoney, *Friction stir welding and processing*, *ASM International*. 2007, Materials Park, Ohio.
63. Đurđanović, M., et al., *Heat generation during friction stir welding process*. *Tribology in industry*, 2009. **31**(1-2): p. 8-14.
64. Zhang, X., B. Xiao, and Z. Ma, *A transient thermal model for friction stir weld. Part I: the model*. *Metallurgical and Materials Transactions A*, 2011. **42**(10): p. 3218-3228.
65. Zhang, X., B. Xiao, and Z. Ma, *A transient thermal model for friction stir weld. Part II: Effects of weld conditions*. *Metallurgical and Materials Transactions A*, 2011. **42**(10): p. 3229-3239.
66. Neto, D.M. and P. Neto, *Numerical modeling of friction stir welding process: a literature review*. *The International Journal of Advanced Manufacturing Technology*, 2013. **65**(1-4): p. 115-126.
67. Williams, S.W., *Welding of airframes using friction stir*. *Air & Space Europe*, 2001. **3**(3): p. 64-66.
68. Liu, H., et al., *Tensile properties and fracture locations of friction-stir-welded joints of 2017-T351 aluminum alloy*. *Journal of Materials Processing Technology*, 2003. **142**(3): p. 692-696.
69. Gharacheh, M.A., et al., *The influence of the ratio of “rotational speed/traverse speed”( $\omega/v$ ) on mechanical properties of AZ31 friction stir welds*. *International Journal of Machine Tools and Manufacture*, 2006. **46**(15): p. 1983-1987.
70. Kim, Y., et al., *Effect of welding parameters on microstructure in the stir zone of FSW joints of aluminum die casting alloy*. *Materials Letters*, 2006. **60**(29): p. 3830-3837.

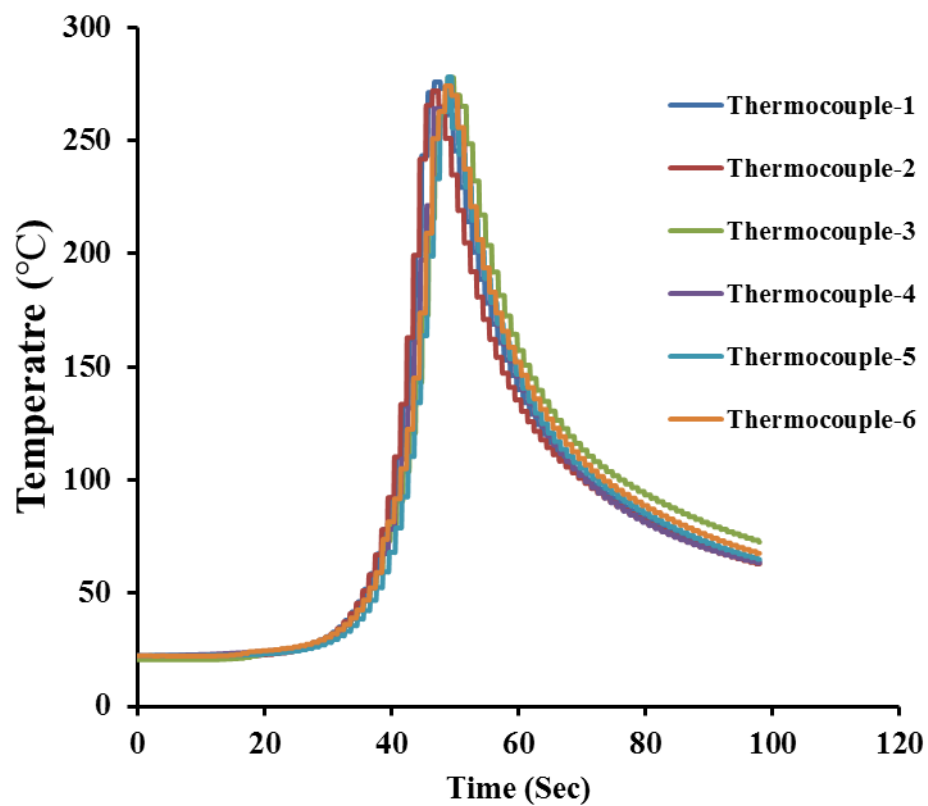
71. Ren, S., Z. Ma, and L. Chen, *Effect of welding parameters on tensile properties and fracture behavior of friction stir welded Al–Mg–Si alloy*. Scripta Materialia, 2007. **56**(1): p. 69-72.
72. Arora, A., A. De, and T. DebRoy, *Toward optimum friction stir welding tool shoulder diameter*. Scripta materialia, 2011. **64**(1): p. 9-12.
73. Elangovan, K. and V. Balasubramanian, *Influences of tool pin profile and tool shoulder diameter on the formation of friction stir processing zone in AA6061 aluminium alloy*. Materials & design, 2008. **29**(2): p. 362-373.
74. Li, H., D. Mackenzie, and R. Hamilton, *Parametric finite-element studies on the effect of tool shape in friction stir welding*. Proceedings of the Institution of Mechanical Engineers, Part B: Journal of Engineering Manufacture, 2010. **224**(8): p. 1161-1173.
75. Prado, R., et al., *Tool wear in the friction-stir welding of aluminum alloy 6061+ 20% Al<sub>2</sub>O<sub>3</sub>: a preliminary study*. Scripta materialia, 2001. **45**(1): p. 75-80.
76. Chen, X.-G., et al., *Microstructure and mechanical properties of friction stir welded AA6063–B 4 C metal matrix composites*. Materials Science and Engineering: A, 2009. **518**(1): p. 174-184.
77. Malarvizhi, S. and V. Balasubramanian, *Influences of tool shoulder diameter to plate thickness ratio (D/T) on stir zone formation and tensile properties of friction stir welded dissimilar joints of AA6061 aluminum–AZ31B magnesium alloys*. Materials & Design, 2012. **40**: p. 453-460.
78. Tang, W., et al., *Heat input and temperature distribution in friction stir welding*. Journal of Materials Processing and Manufacturing Science, 1998. **7**: p. 163-172.
79. Schmidt, H., J. Hattel, and J. Wert, *An analytical model for the heat generation in friction stir welding*. Modelling and Simulation in Materials Science and Engineering, 2003. **12**(1): p. 143.
80. Schmidt, H.B. and J.H. Hattel, *Thermal modelling of friction stir welding*. Scripta Materialia, 2008. **58**(5): p. 332-337.
81. Colegrove, P., et al. *3D Flow and Thermal Modeling of the FSW Process*. in *2nd Int. Symp. of FSW Proc., 2nd Int. Symp. on 'Friction stir welding*. 2000.

82. Shi, Q., T. Dickerson, and H.R. Shercliff. *Thermomechanical FE modelling of friction stir welding of Al-2024 including tool loads*. in *Friction Stir Welding: Proceedings of the 4th International Symposium on Friction Stir Welding*. 2003. TWI Limited.
83. Suresha, C., B. Rajaprakash, and S. Upadhyaya, *A study of the effect of tool pin profiles on tensile strength of welded joints produced using friction stir welding process*. *Materials and Manufacturing Processes*, 2011. **26**(9): p. 1111-1116.
84. Elangovan, K. and V. Balasubramanian, *Influences of pin profile and rotational speed of the tool on the formation of friction stir processing zone in AA2219 aluminium alloy*. *Materials Science and Engineering: A*, 2007. **459**(1): p. 7-18.
85. Ramanjaneyulu, K., et al., *Structure-property correlation of AA2014 friction stir welds: role of tool pin profile*. *Journal of materials engineering and performance*, 2013. **22**(8): p. 2224-2240.
86. Ulysse, P., *Three-dimensional modeling of the friction stir-welding process*. *International Journal of Machine Tools and Manufacture*, 2002. **42**(14): p. 1549-1557.
87. Chao, Y.J., X. Qi, and W. Tang, *Heat transfer in friction stir welding—experimental and numerical studies*. *Journal of manufacturing science and engineering*, 2003. **125**(1): p. 138-145.
88. Graz-Seggau, *Mathematical Modelling of Weld Phenomena 6*. Vol. in: 6th International Seminar on the Numerical Analysis of Weldability. 2001, Institute of Materials, Austria.
89. Song, M. and R. Kovacevic, *Thermal modeling of friction stir welding in a moving coordinate system and its validation*. *International Journal of Machine Tools and Manufacture*, 2003. **43**(6): p. 605-615.
90. Arora, A., et al., *Torque, power requirement and stir zone geometry in friction stir welding through modeling and experiments*. *Scripta Materialia*, 2009. **60**(1): p. 13-16.
91. Schmidt, H.N.B. and J. Hattel, *Heat source models in simulation of heat flow in friction stir welding*. *International Journal of Offshore and Polar Engineering*, 2004. **14**(04): p. 296-304.

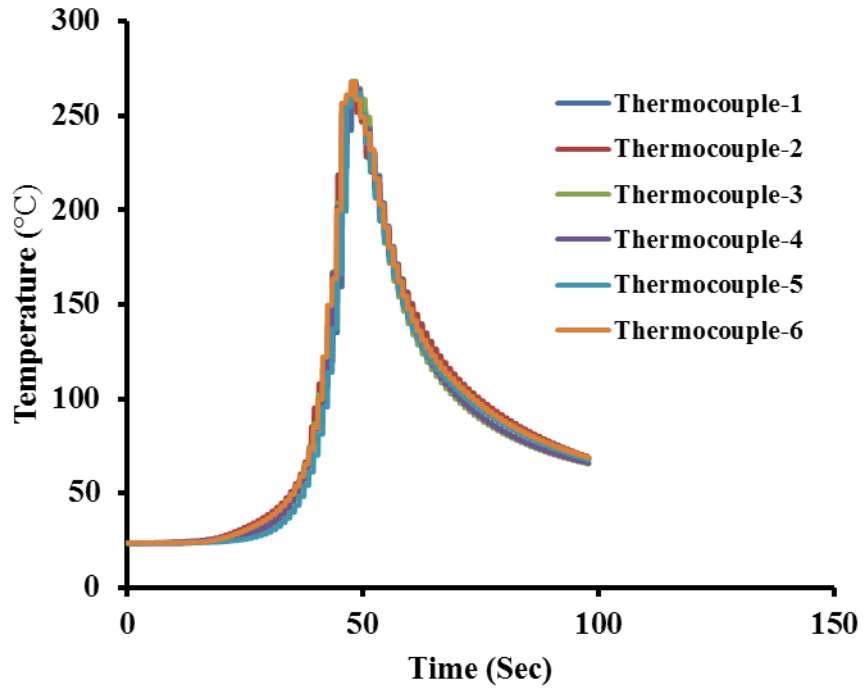
92. Song, M. and R. Kovacevic, *Numerical and experimental study of the heat transfer process in friction stir welding*. Proceedings of the Institution of Mechanical Engineers, Part B: Journal of Engineering Manufacture, 2003. **217**(1): p. 73-85.
93. Biswas, P. and N. Mandal, *Effect of tool geometries on thermal history of FSW of AA1100*. Welding Journal, 2011. **90**(Suppl): p. 129-135.
94. Gadakh, V.S. and K. Adepu, *Heat generation model for taper cylindrical pin profile in FSW*. Journal of Materials Research and Technology, 2013. **2**(4): p. 370-375.
95. Tikader, S., P. Biswas, and A.B. Puri, *A Study on Tooling and Its Effect on Heat Generation and Mechanical Properties of Welded Joints in Friction Stir Welding*. Journal of The Institution of Engineers (India): Series C, 2016: p. 1-12.
96. Crank, J. and P. Nicolson. *A practical method for numerical evaluation of solutions of partial differential equations of the heat-conduction type*. in *Mathematical Proceedings of the Cambridge Philosophical Society*. 1947. Cambridge Univ Press.
97. Properties, A.H., *Selection: Nonferrous Alloys and Special-Purpose Materials, vol. 2*. ASM International, Materials, Park, OH, 1990.
98. Standard, A.A.N., *Specification for Friction Stir Welding of Aluminium Alloys for Aerospace Hardware* American Welding Society. **AWS D17.3/D17.3M:200X**.
99. Committee, A.H. and A.S.f.M.H.T. Division, *Heat treating*. Vol. 10. 1991: ASM International.
100. E407-07, A., *Standard practice for microetching metals and alloys*. 2015, ASTM International West Conshohocken, PA.
101. ASTM, E., *ASTM E340-00-Standard Test Method for Macroetching Metals and Alloys*. Annual Book of ASTM Standards, 2013.
102. ASTM, E., *Standard test methods for tension testing of metallic materials*. Annual book of ASTM standards. ASTM, 2001.
103. Al-Ezzi, S., *Design, Modeling, and Optimization of GTA Spot Welding in Conjunction with Ultrasonic Vibration for Oxygen Free Copper Welding Joint* 2018, Southwest Jiaotong University.

## APPENDICES

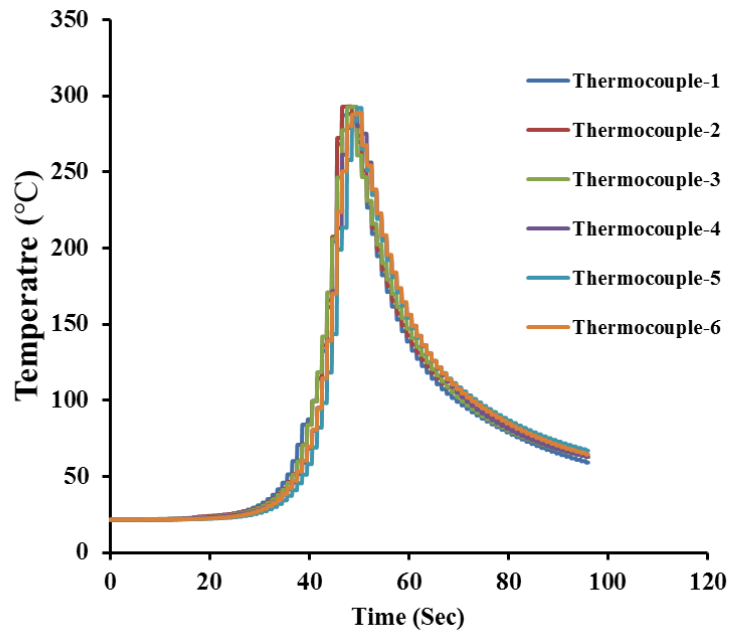
### Appendix 1: Experimental temperature data



Experimental temperature data for Run5.

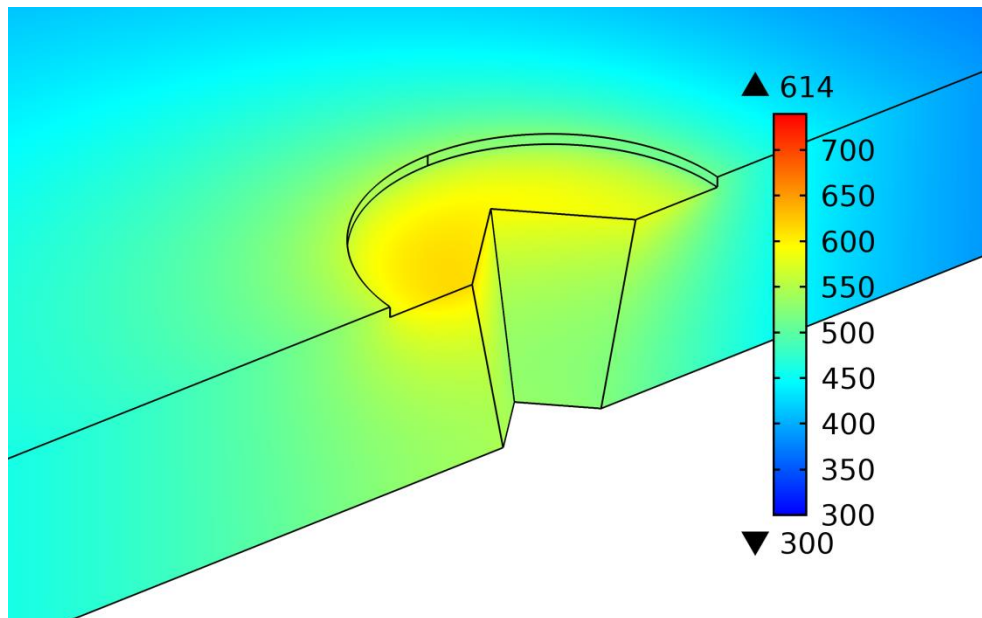


Experimental temperature data for Run9.

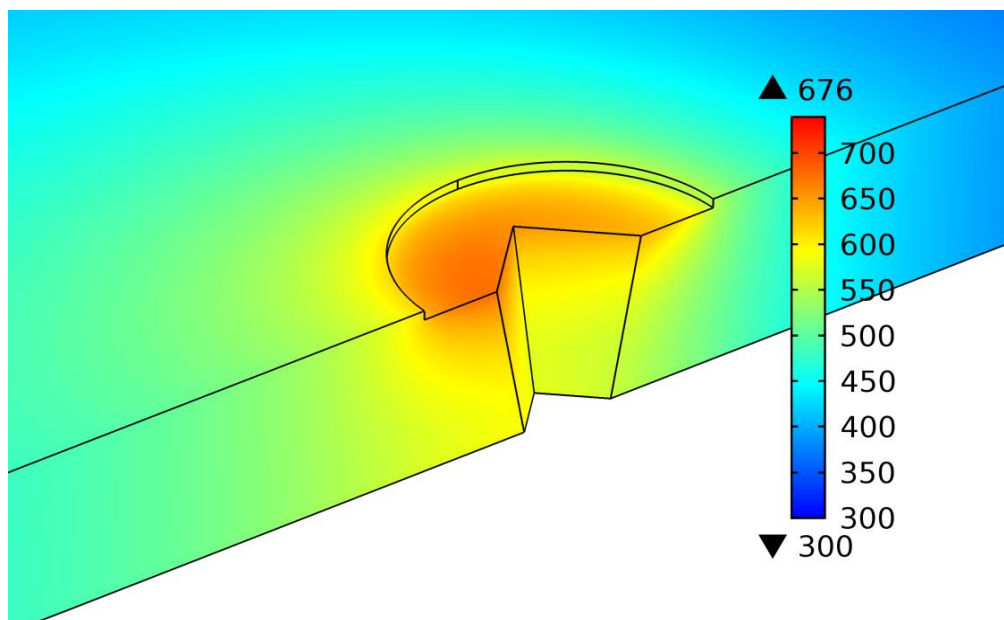


Experimental temperature data for Run13.

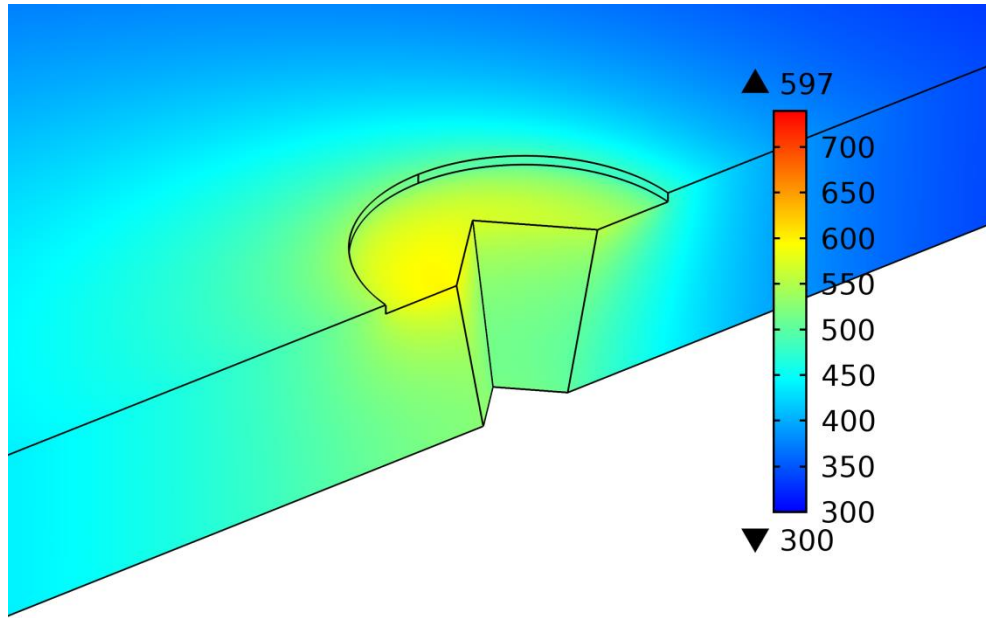
## Appendix 2: Isotherms temperature distribution (K) for DOE Runs



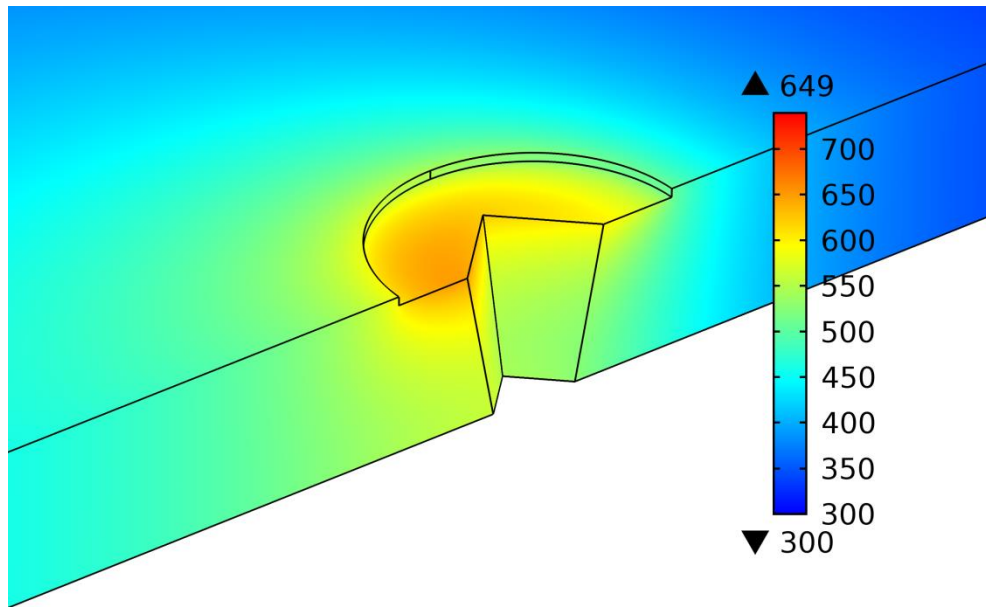
1) Isotherms temperature distribution (K) for Run1 from peak temperature DOE.



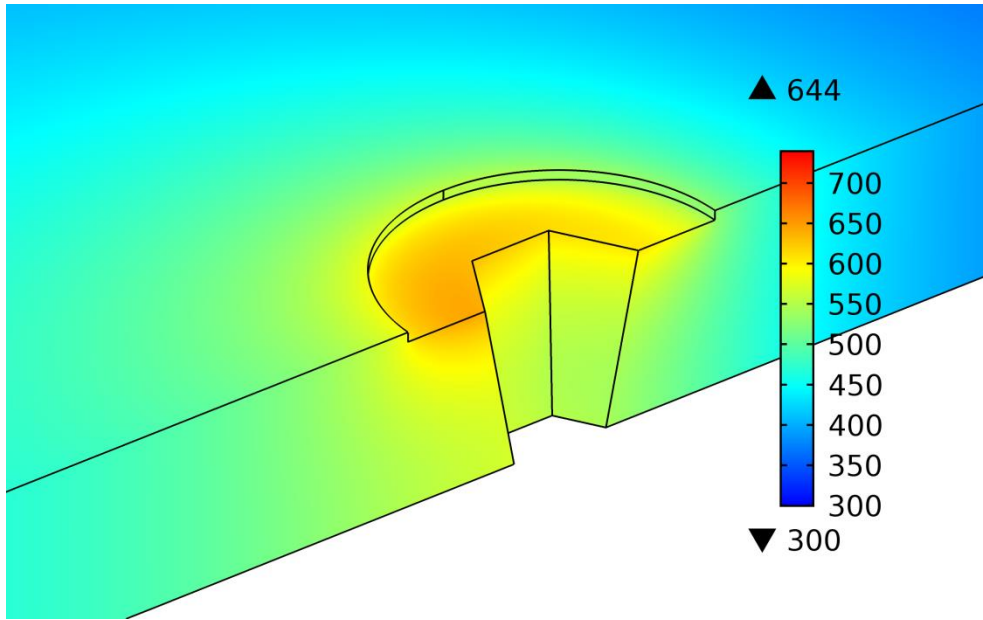
2) Isotherms temperature distribution (K) for Run2 from peak temperature DOE.



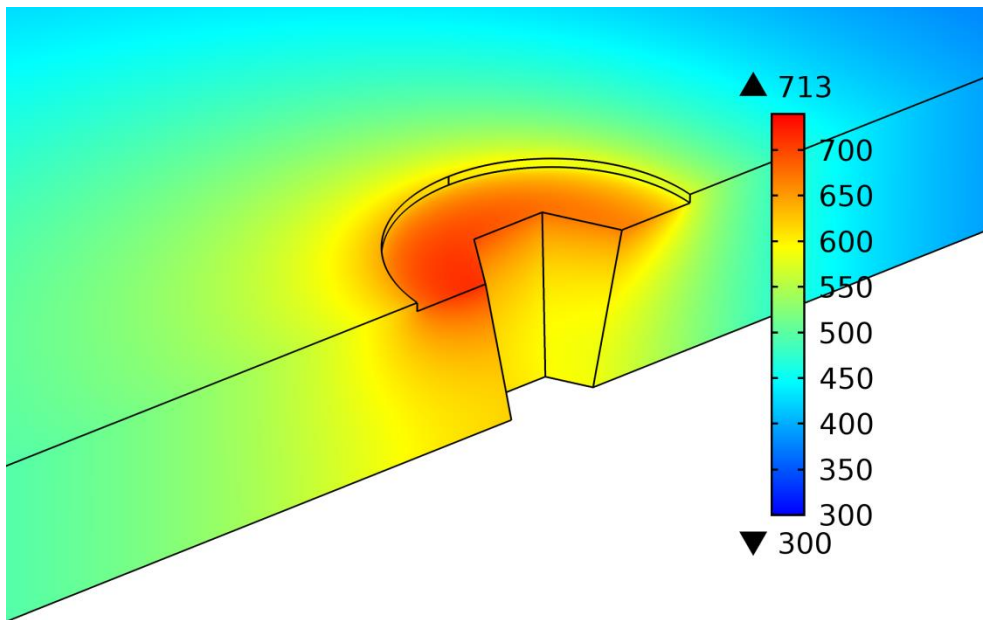
3) Isotherms temperature distribution (K) for Run3 from peak temperature DOE.



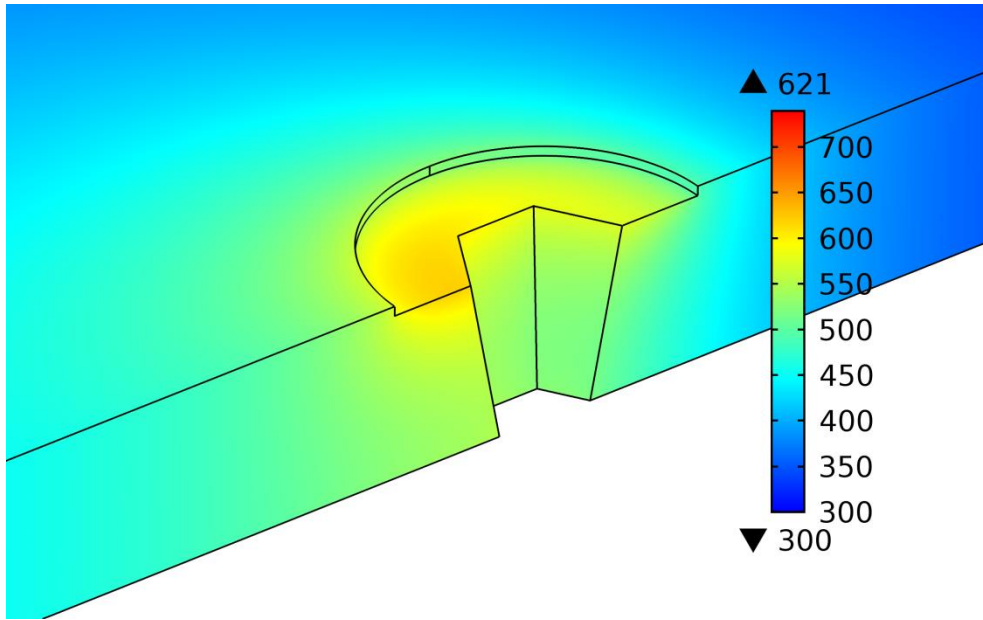
4) Isotherms temperature distribution (K) for Run4 from peak temperature DOE.



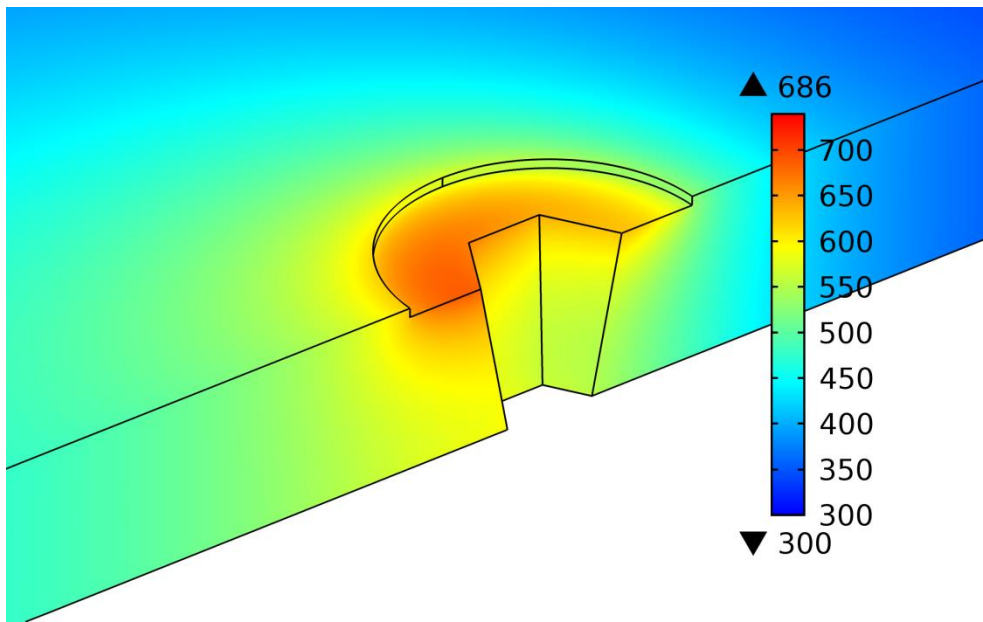
5) Isotherms temperature distribution (K) for Run5 from peak temperature DOE.



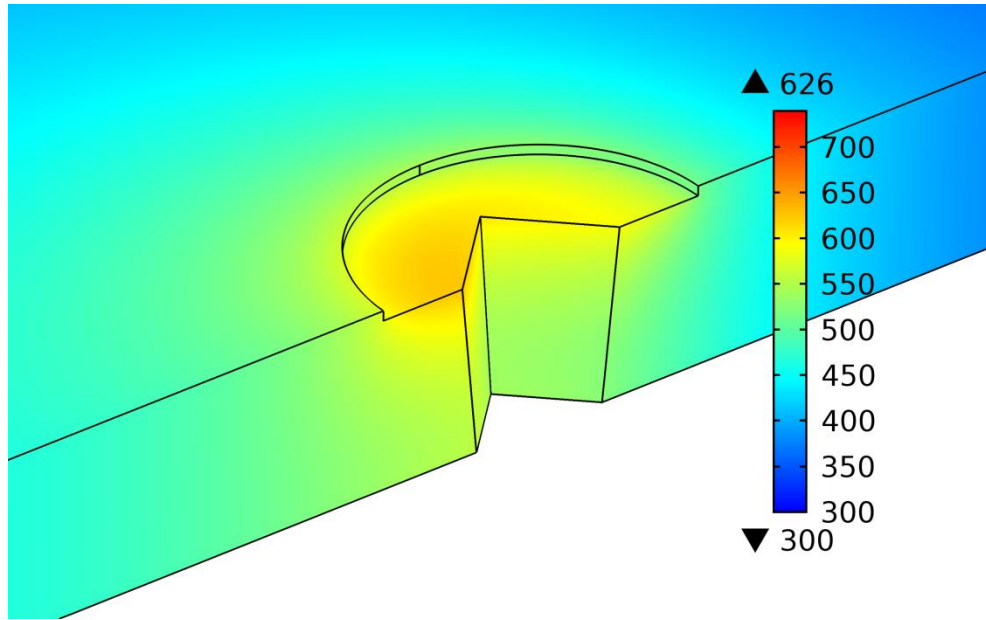
6) Isotherms temperature distribution (K) for Run6 from peak temperature DOE.



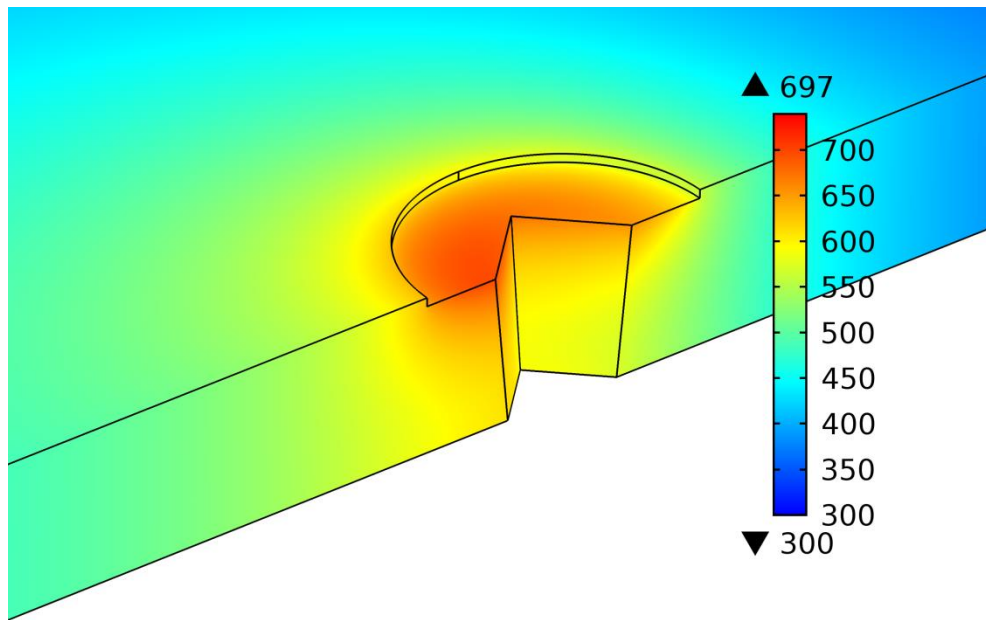
7) Isotherms temperature distribution (K) for Run7 from peak temperature DOE.



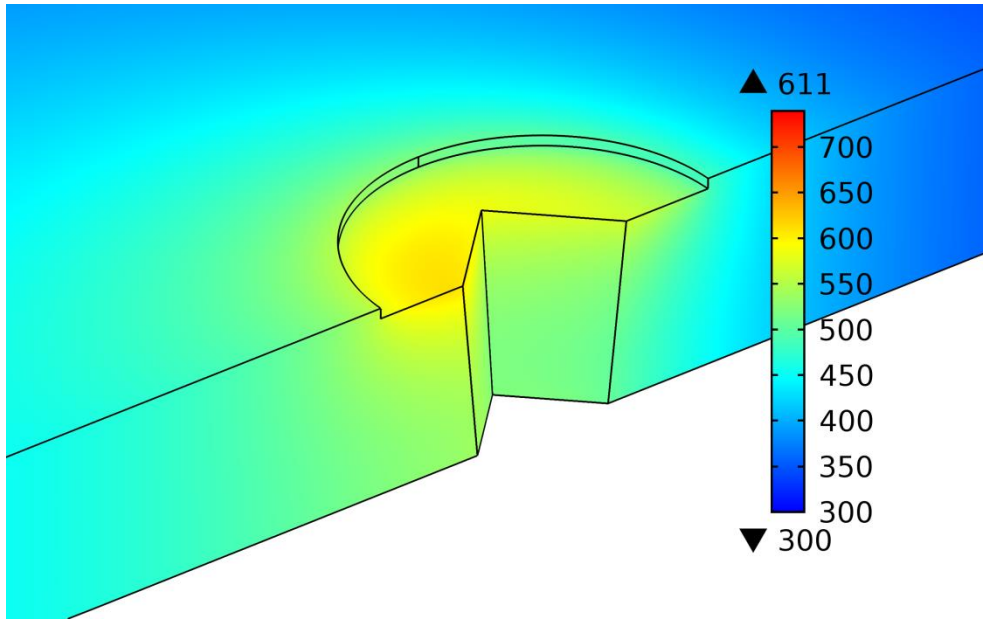
8) Isotherms temperature distribution (K) for Run8 from peak temperature DOE.



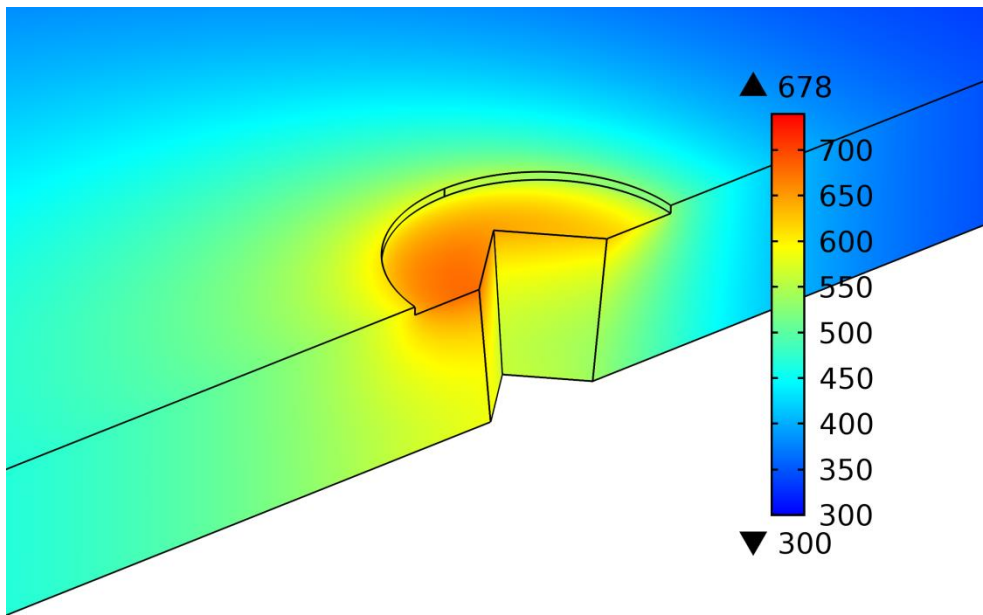
9) Isotherms temperature distribution (K) for Run9 from peak temperature DOE.



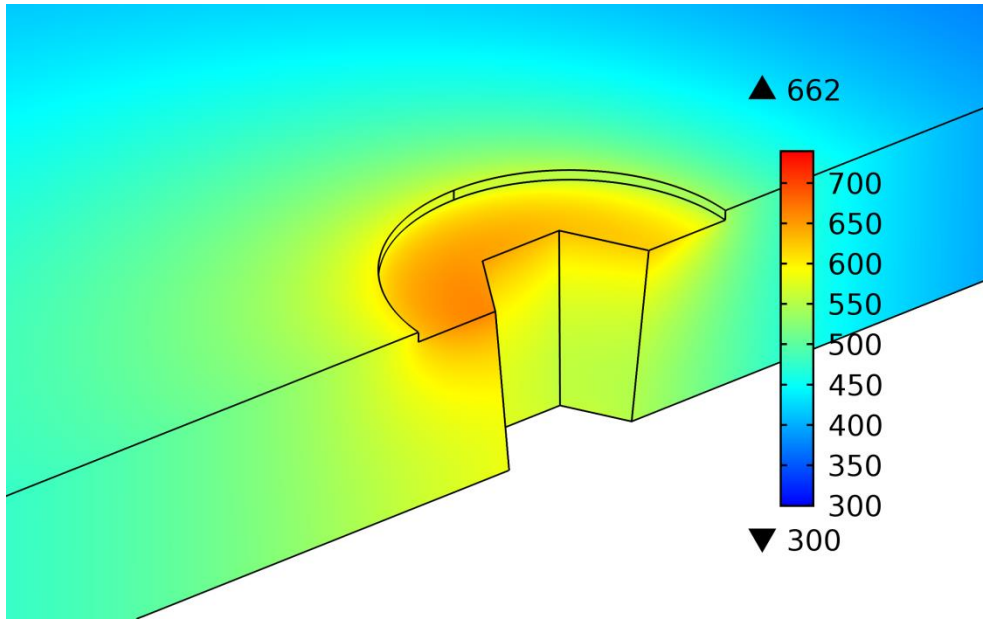
10) Isotherms temperature distribution (K) for Run10 from peak temperature DOE.



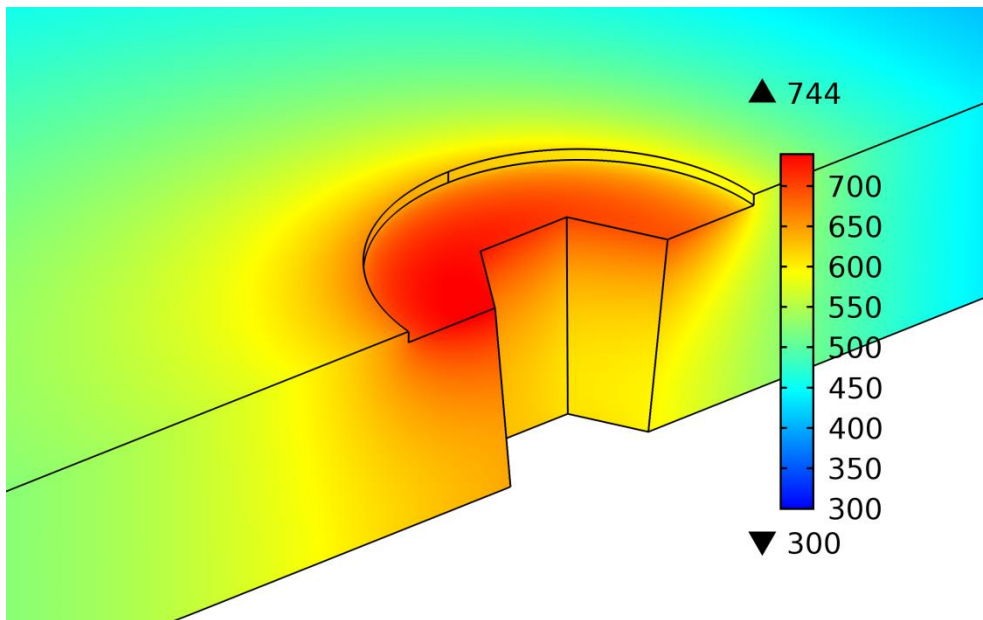
11) Isotherms temperature distribution (K) for Run11 from peak temperature DOE.



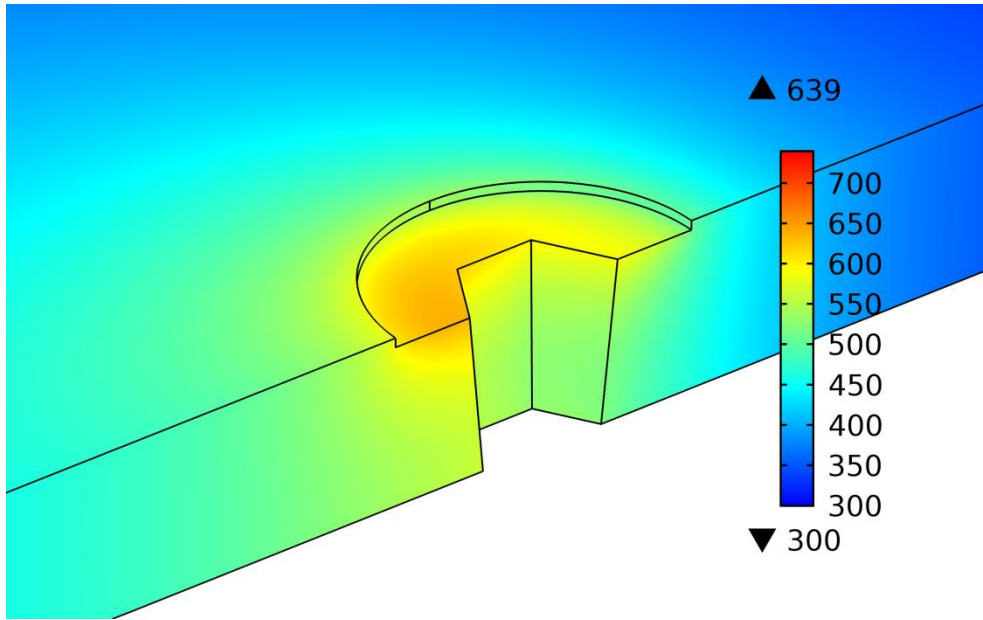
12) Isotherms temperature distribution (K) for Run12 from peak temperature DOE.



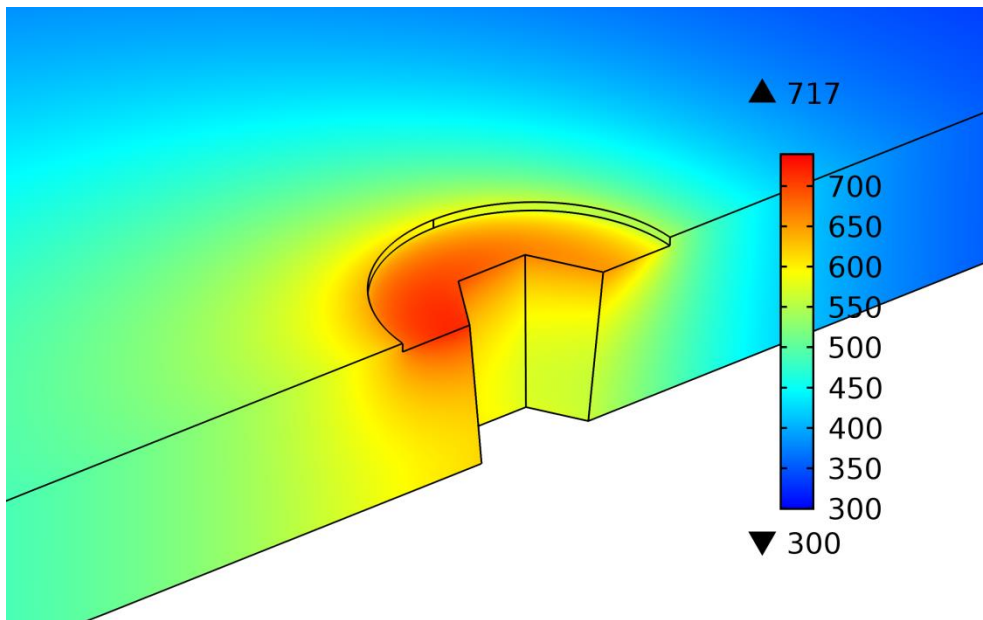
13) Isotherms temperature distribution (K) for Run13 from peak temperature DOE.



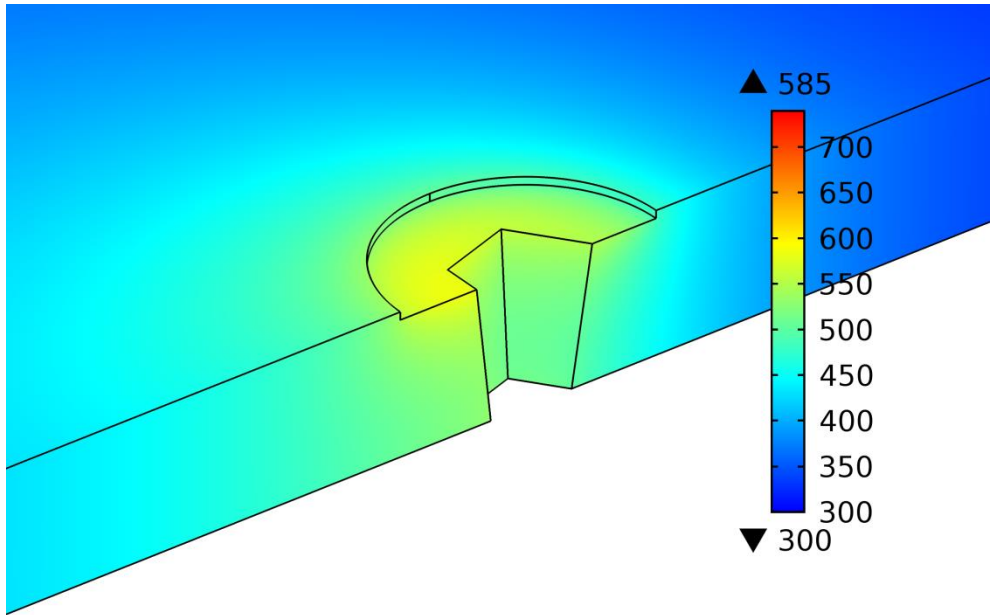
14) Isotherms temperature distribution (K) for Run14 from peak temperature DOE.



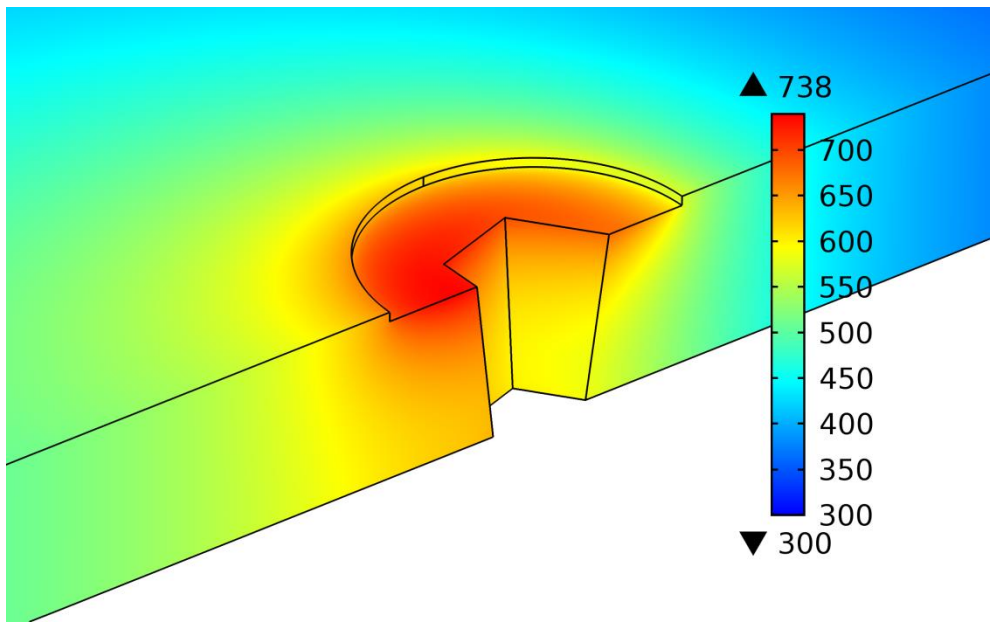
15) Isotherms temperature distribution (K) for Run15 from peak temperature DOE.



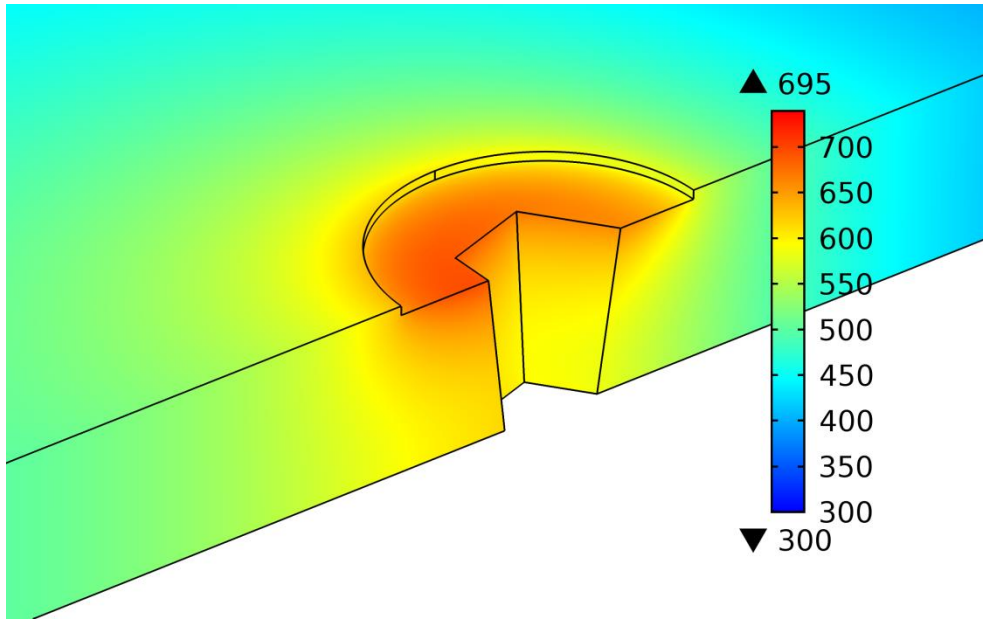
16) Isotherms temperature distribution (K) for Run16 from peak temperature DOE.



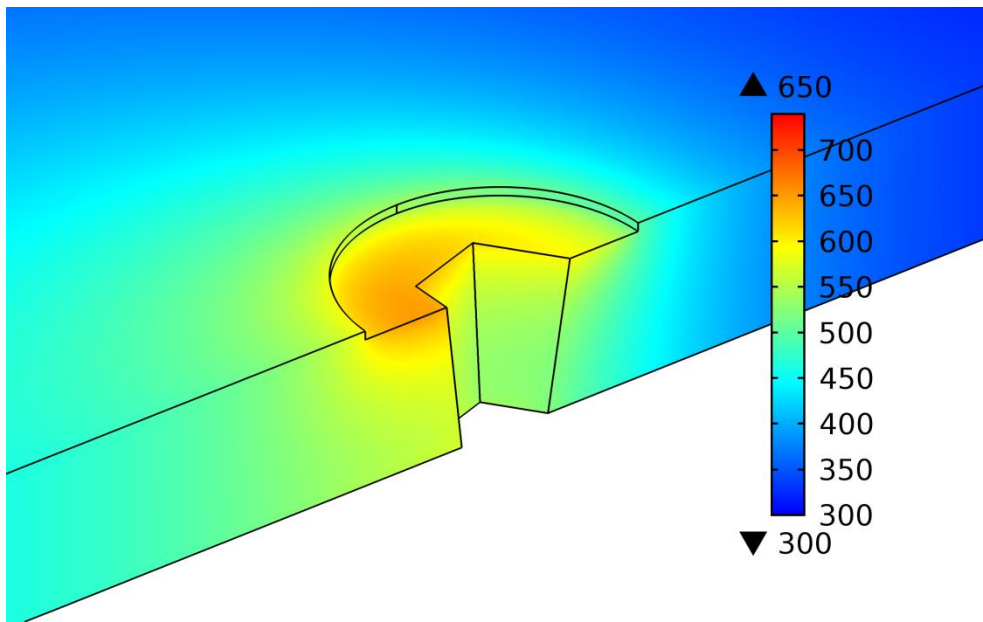
17) Isotherms temperature distribution (K) for Run17 from peak temperature DOE.



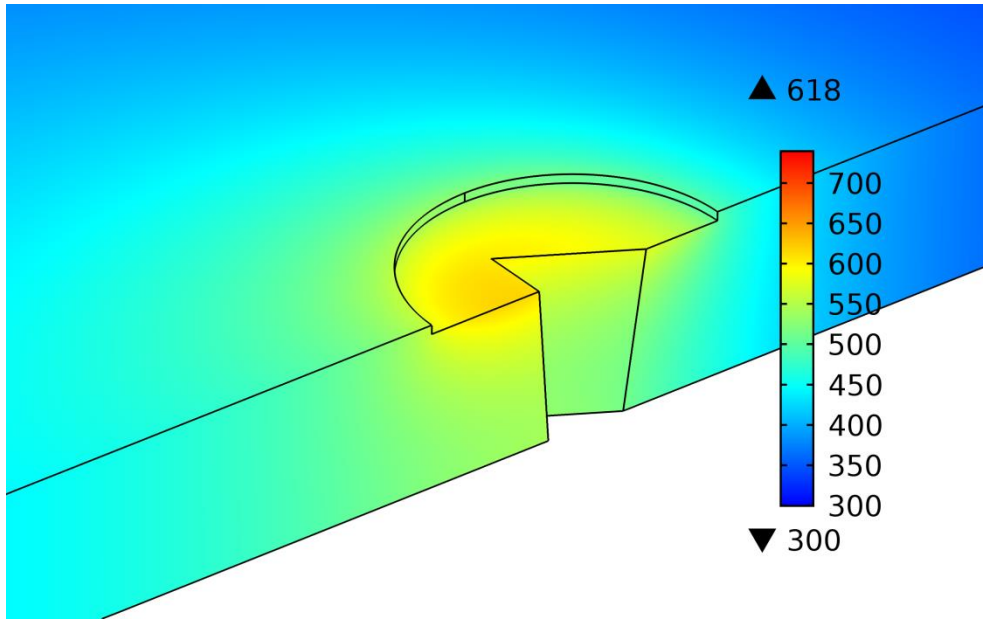
18) Isotherms temperature distribution (K) for Run18 from peak temperature DOE.



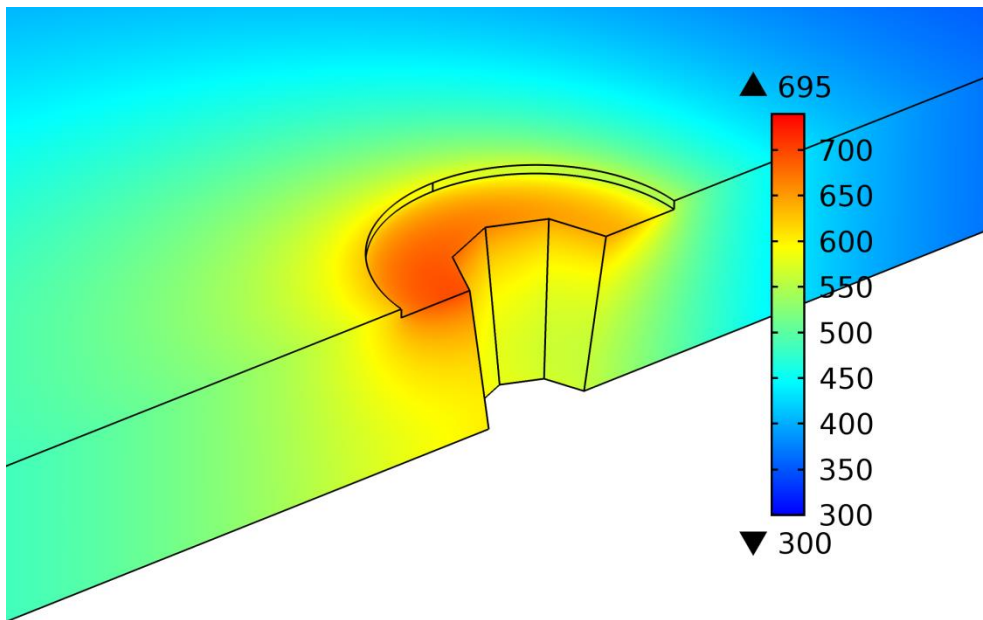
19) Isotherms temperature distribution (K) for Run19 from peak temperature DOE.



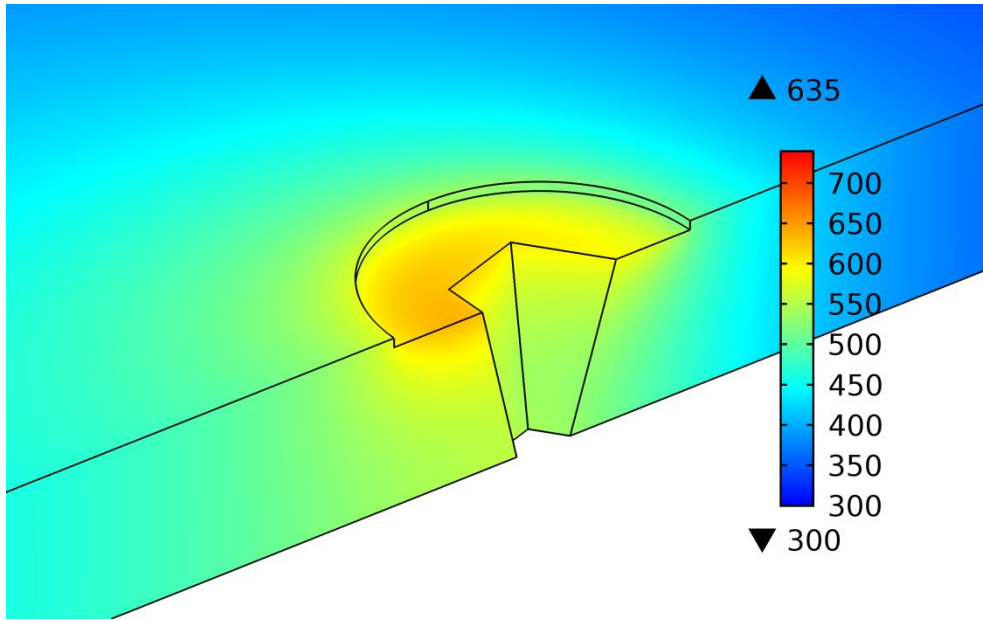
20) Isotherms temperature distribution (K) for Run20 from peak temperature DOE.



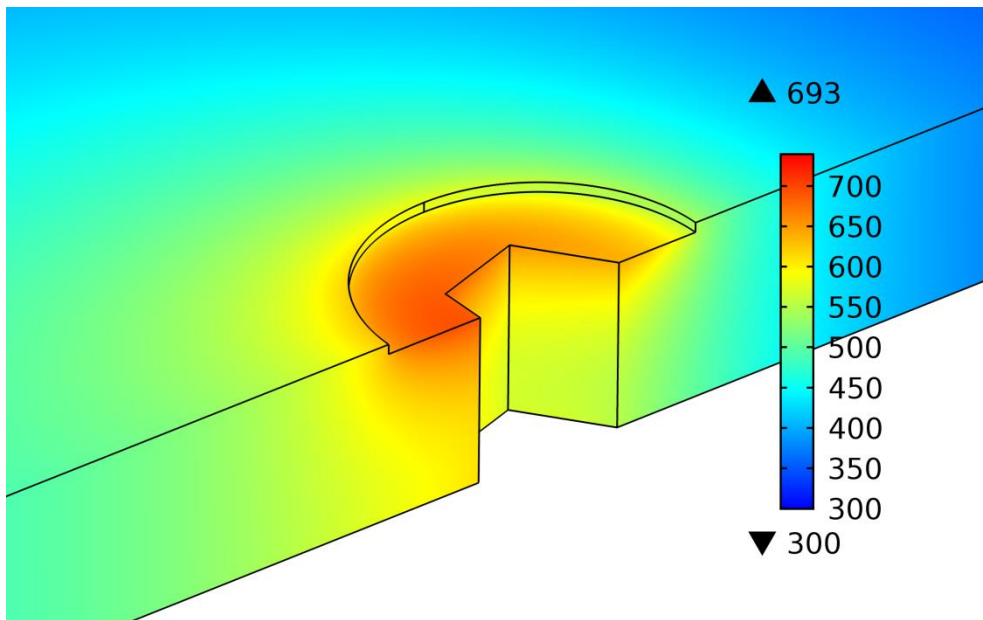
21) Isotherms temperature distribution (K) for Run21 from peak temperature DOE.



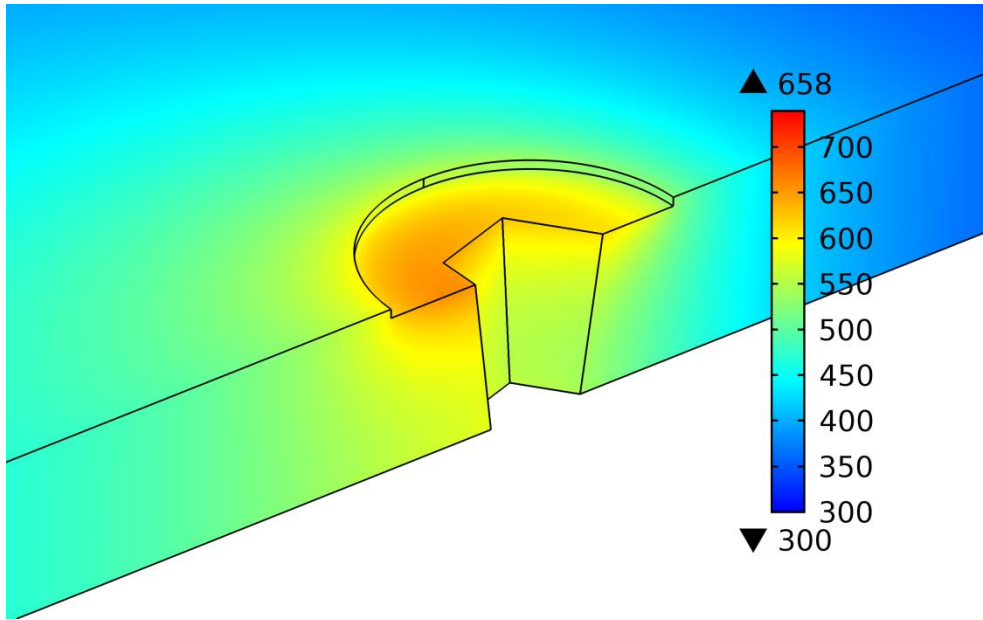
22) Isotherms temperature distribution (K) for Run22 from peak temperature DOE.



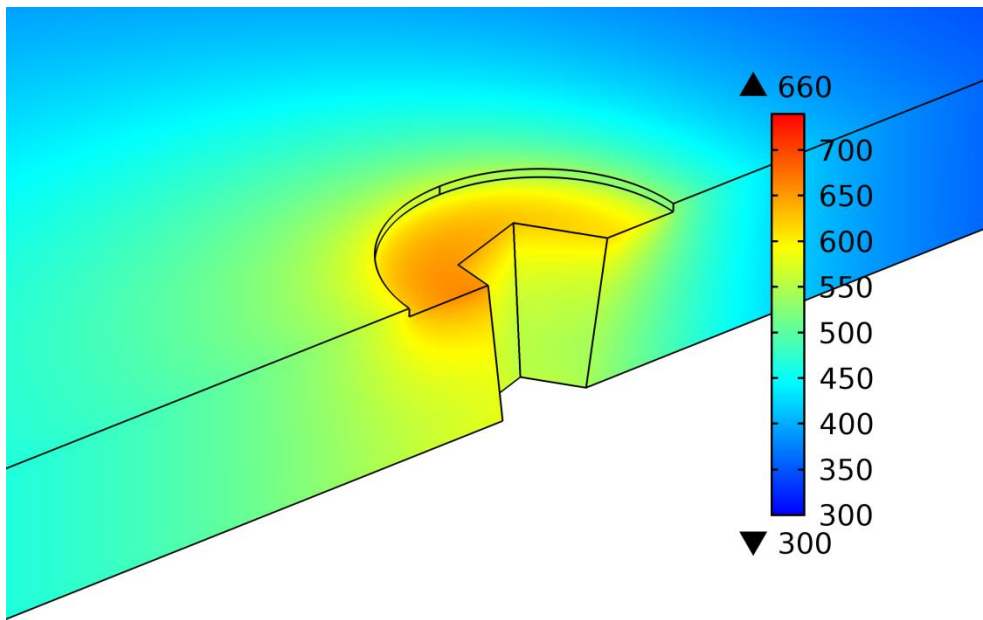
23) Isotherms temperature distribution (K) for Run23 from peak temperature DOE.



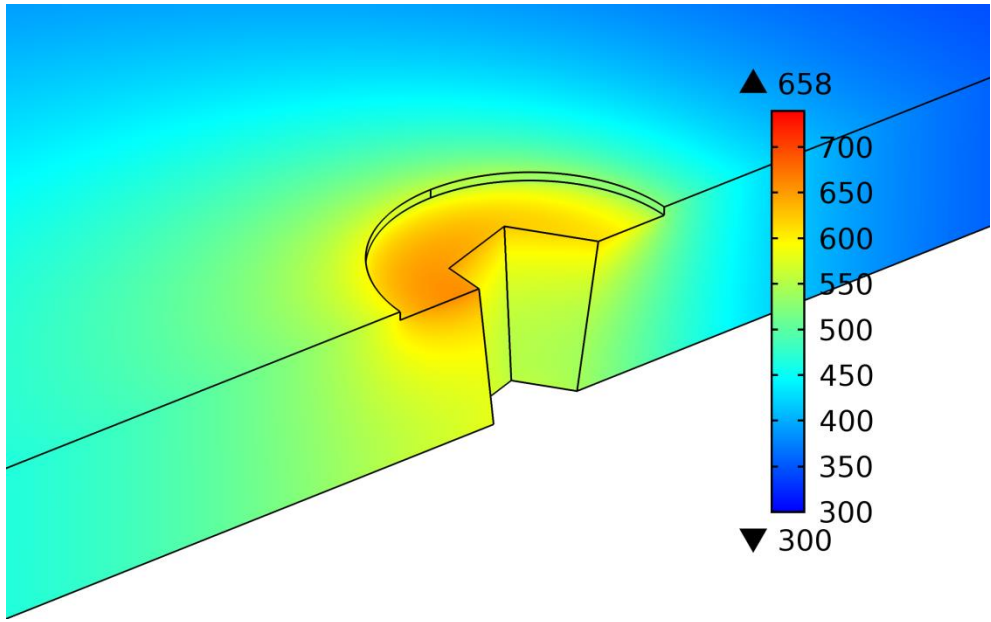
24) Isotherms temperature distribution (K) for Run24 from peak temperature DOE.



25) Isotherms temperature distribution (K) for Run25&28 from peak temperature DOE.



26) Isotherms temperature distribution (K) for Run26, 29 and 30 from peak temperature DOE.



27) Isotherms temperature distribution (K) for Run27 from peak temperature DOE.

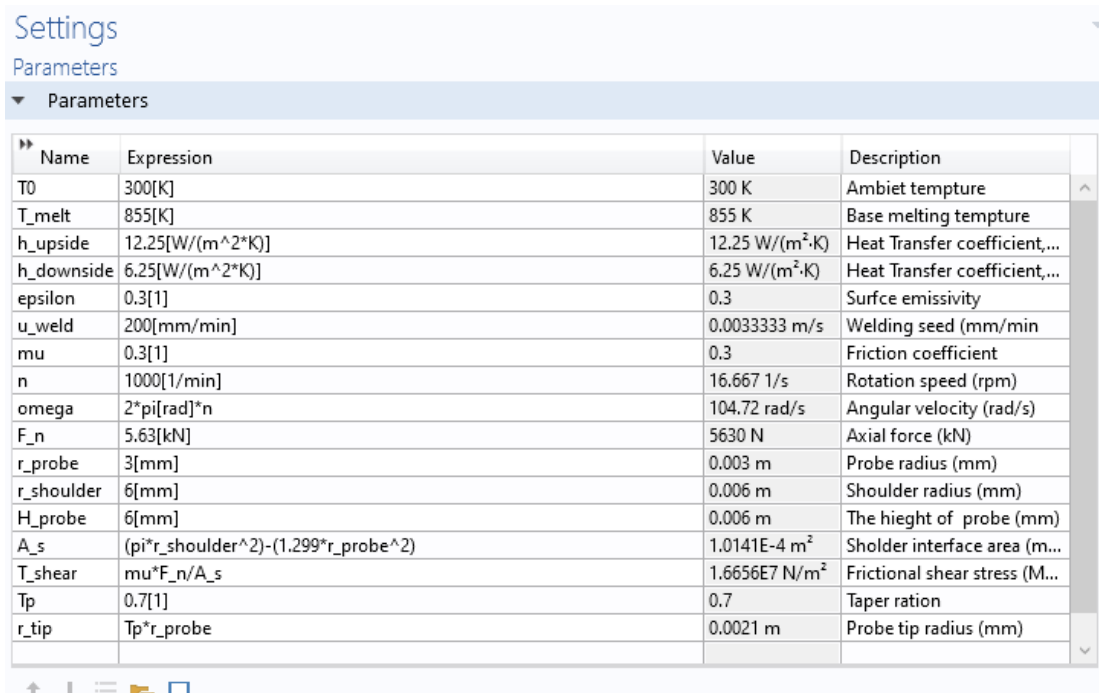
## Appendix 3: The main steps in COMSOL model

Computational heat transfer in solids (HTS) embedded in COMSOL is used to analyse the heat transfer in this welding process. The main steps should be included to finalise FSW model according to a prescribed specification that follows.

### 1. Parameters

The parameters, their units and descriptions are listed in table 1.

Table 1. The parameters, their units.



Name	Expression	Value	Description
T0	300[K]	300 K	Ambient temperature
T_melt	855[K]	855 K	Base melting temperature
h_upside	12.25[W/(m <sup>2</sup> *K)]	12.25 W/(m <sup>2</sup> *K)	Heat Transfer coefficient,...
h_downside	6.25[W/(m <sup>2</sup> *K)]	6.25 W/(m <sup>2</sup> *K)	Heat Transfer coefficient,...
epsilon	0.3[1]	0.3	Surface emissivity
u_weld	200[mm/min]	0.0033333 m/s	Welding speed (mm/min)
mu	0.3[1]	0.3	Friction coefficient
n	1000[1/min]	16.667 1/s	Rotation speed (rpm)
omega	2*pi[rad]*n	104.72 rad/s	Angular velocity (rad/s)
F_n	5.63[kN]	5630 N	Axial force (kN)
r_probe	3[mm]	0.003 m	Probe radius (mm)
r_shoulder	6[mm]	0.006 m	Shoulder radius (mm)
H_probe	6[mm]	0.006 m	The height of probe (mm)
A_s	(pi*r_shoulder^2)-(1.299*r_probe^2)	1.0141E-4 m <sup>2</sup>	Shoulder interface area (m...
T_shear	mu*F_n/A_s	1.6656E7 N/m <sup>2</sup>	Frictional shear stress (M...
Tp	0.7[1]	0.7	Taper ratio
r_tip	Tp*r_probe	0.0021 m	Probe tip radius (mm)

### 2. The FSW tool interfaces contribution in a total heat generation will represent at modelling as variables, the definitions of these variables are:

- Heat flux at tool shoulder-base metal interface (Figure 2) is included as heat generation from shoulder surface ( $Q_1$ ) as shown in Figure 3.
- Heat flux at tool probe surface-base metal interface (Figure 4) is included as heat generation from probe surface ( $Q_2$ ) as shown in Figure 5.
- Heat flux at tool probe tip-base metal interface (Figure 6) is included as heat generation from probe tip surface ( $Q_3$ ) as shown in Figure 7.

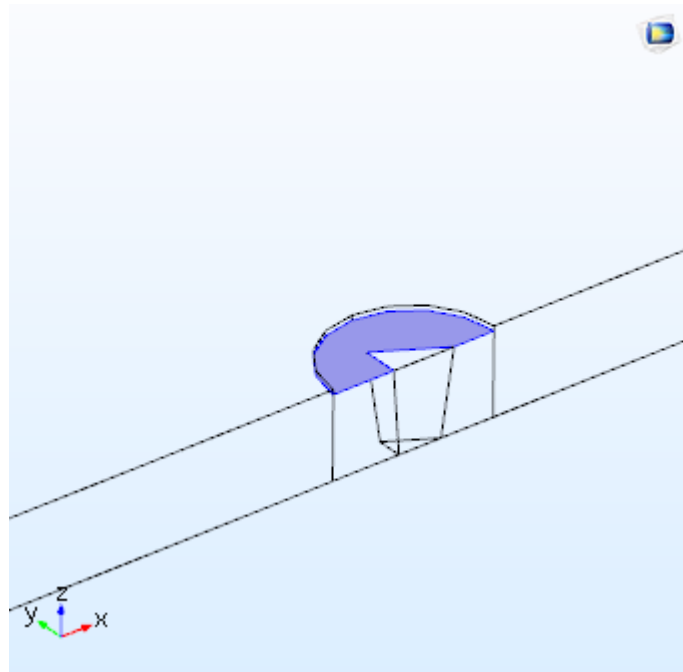


Figure 2. The tool shoulder-base metal interface.

Settings

Variables

Label:

Geometric Entity Selection

Geometric entity level:

Selection:

8  
Active

Variables

Name	Expression	Unit	Description
Q1	$(2/3) \cdot \pi \cdot (\omega) \cdot T_{\text{shear}} \cdot (r_{\text{shoulder}}^3 - 0.2067 \cdot r_{\text{probe}}^3)$	W	

Figure 3. The definition of heat generation from shoulder surface ( $Q_1$ ).

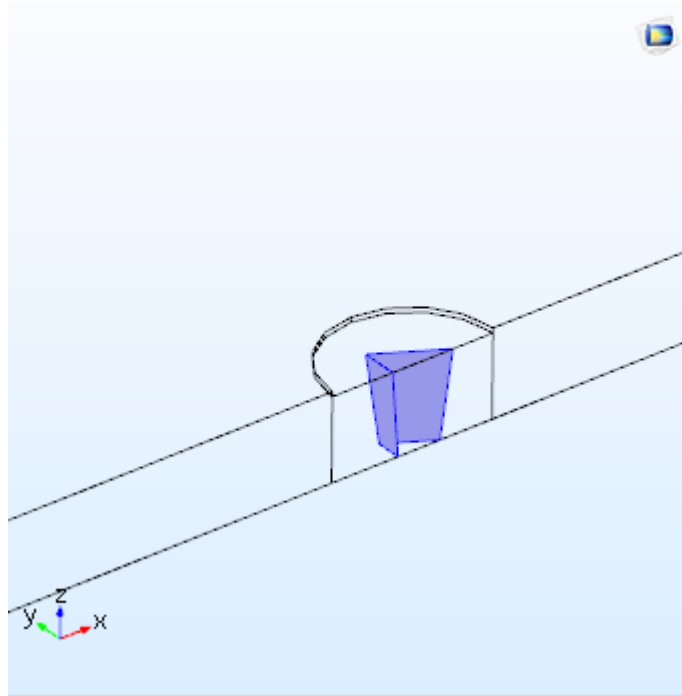


Figure 4. The tool probe surface-base metal interface.

Settings

Variables

Label: Q2

Geometric Entity Selection

Geometric entity level: Boundary

Selection: Manual

Active

9

12

Variables

Name	Expression	Unit	Description
Q2	$(2/(3)) * \pi * ((0.448 * r\_probe^2) * H\_probe * \omega) * ((1/\sqrt{3})) * \bar{V}bar(T[1/K])[MPa]$	W	

Figure 5. The definition of heat generation from probe surface ( $Q_2$ ).

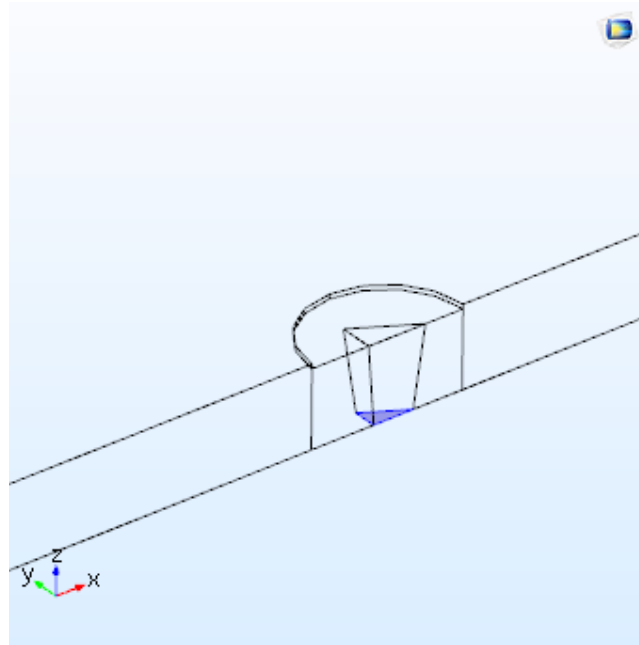


Figure 6. The tool probe tip-base metal interface.

Settings

Variables

Label: Q3

Geometric Entity Selection

Geometric entity level: Boundary

Selection: Manual

ON Active

13

Variables

Name	Expression	Unit	Description
Q3	$(2/3)*\pi*\omega*0.2067*(r_{tip})^3*((1/\sqrt{3}))*\bar{Ybar}(T[1/K])$ [MPa]	W	

Figure 7. The definition of heat generation from probe tip surface ( $Q_3$ ).

### 3. Convection and radiation boundary conditions

- The heat loss from the upper plate's surface due convection and radiation, it can be implemented in COMSOL model as shown in Figures 8, 9 and 10.
- The heat loss form lower plate's surface due convection, it can be implemented in COMSOL model as shown in Figures 11 and 12.

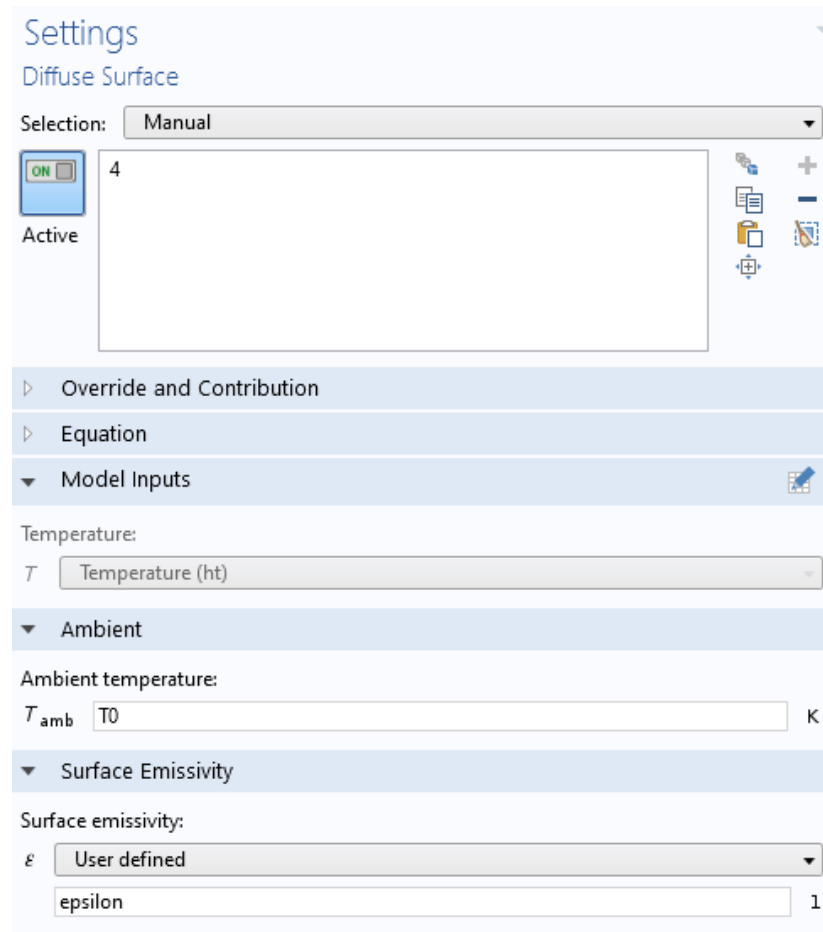


Figure 8. Setting to add radiation boundary condition.

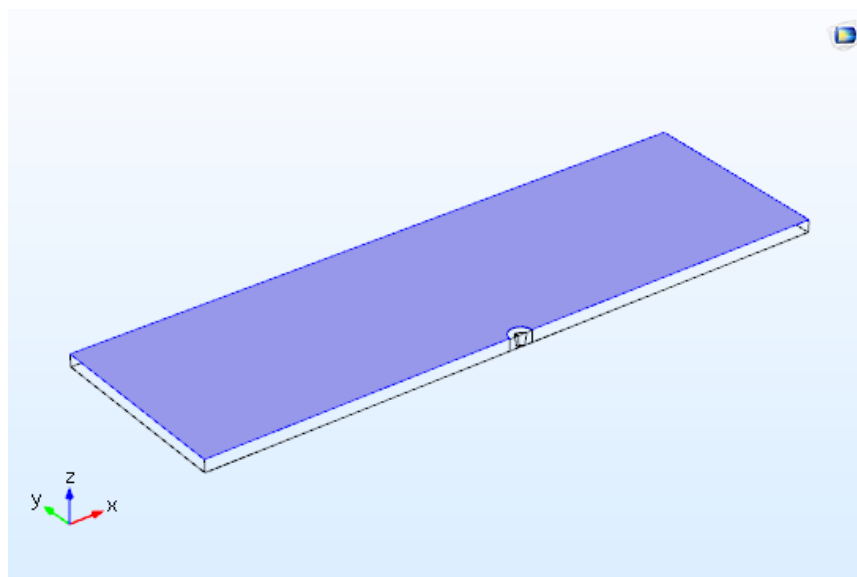


Figure 9. The upper plate's surface.

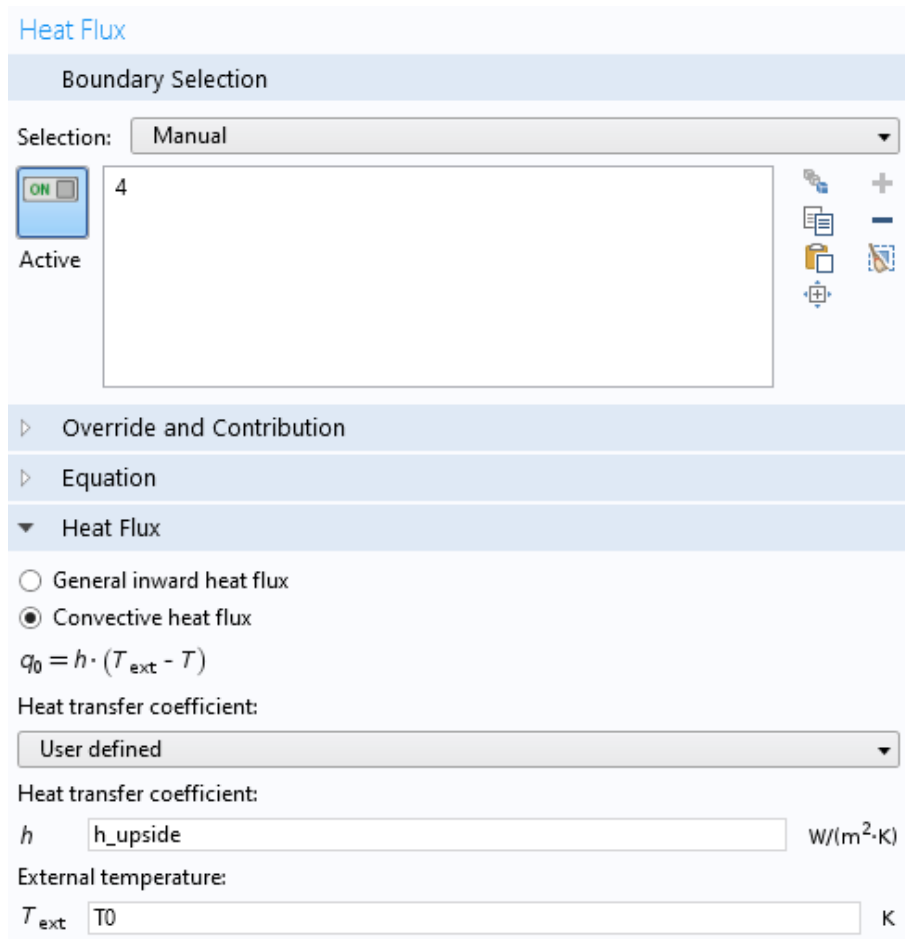


Figure 10. Setting to add upper convection boundary condition.

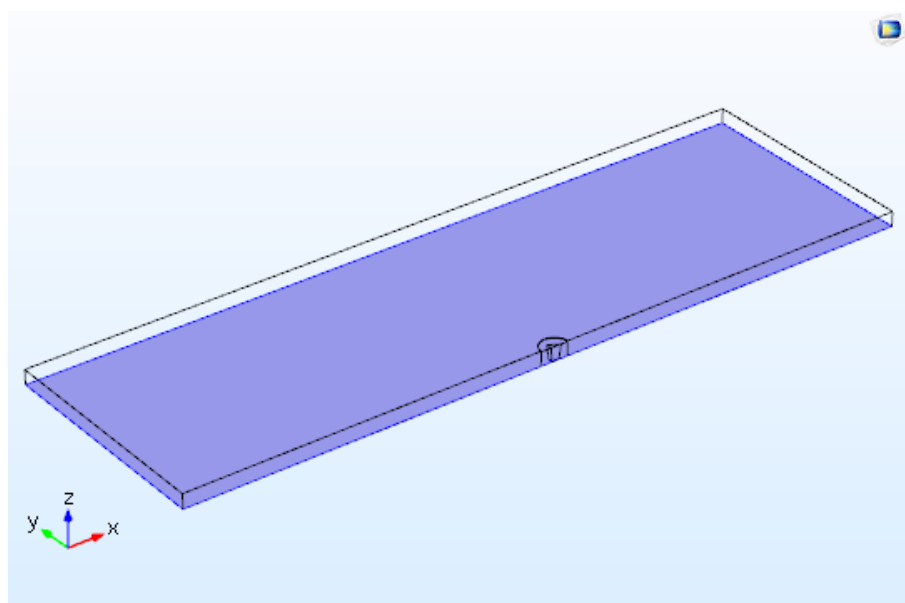


Figure 11. The lower plate's surface.

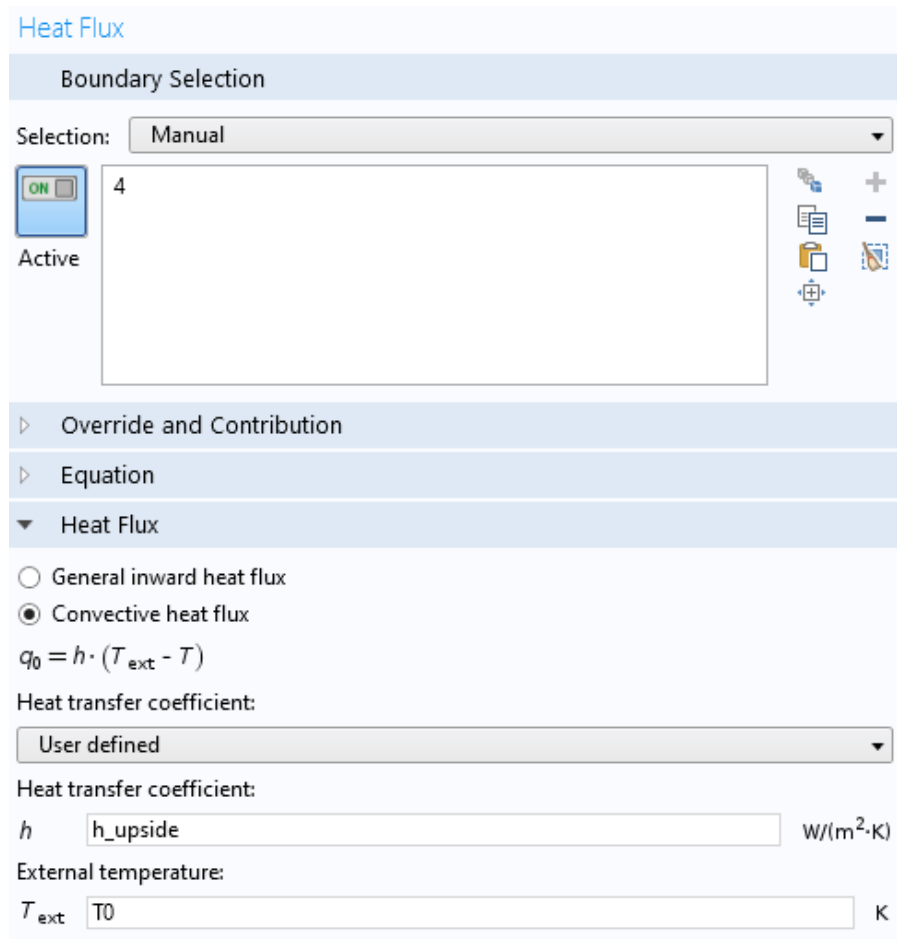


Figure 12. Setting to add lower convection boundary condition.

#### 4. Finite element mesh.

The physics-controlled was selected as the sequence type with extremely fine element size for the mesh as shown in Figures 13 and 14.

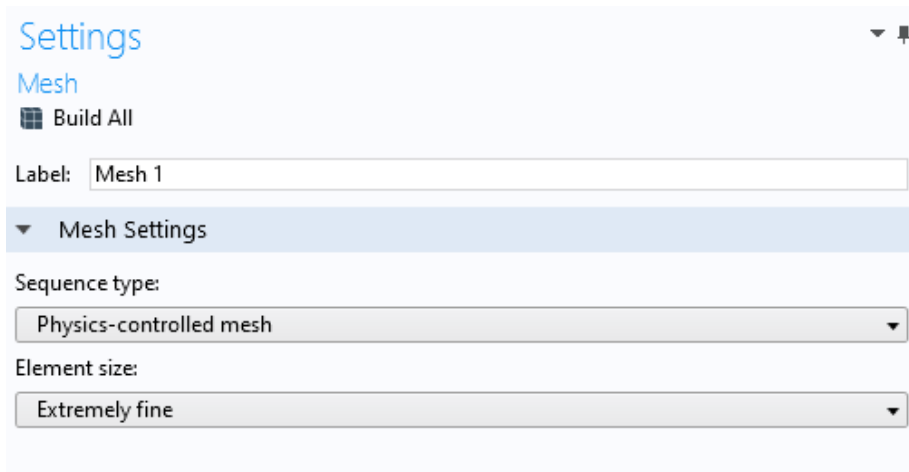


Figure 13. Setting the mesh.

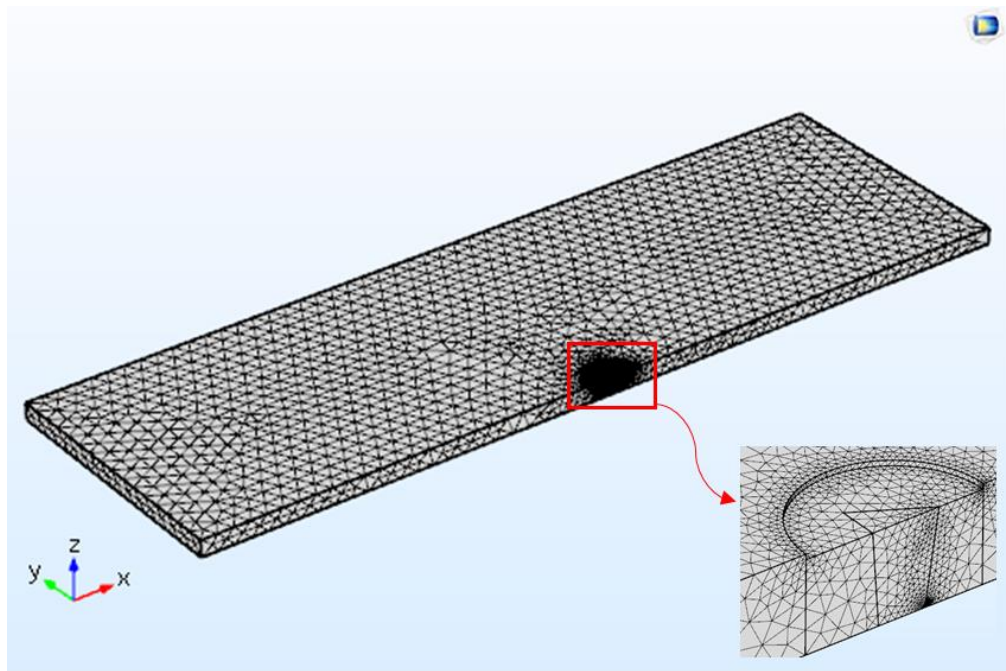


Figure 14. Geometrical mesh of the model.